Modelling the dynamic flight behaviour of birds in different frames of reference



James A. Kempton

Merton College

University of Oxford

A thesis submitted for the degree of

Doctor of Philosophy

Michaelmas 2022

Abstract

In this thesis I consider two aspects – energetics and guidance – of two dynamic flight behaviours performed by birds – dynamic soaring and prey pursuit. Uniting the thesis is the collection and modelling of bird trajectory data in different frames of reference to make inferences on dynamic flight behaviour. In particular, I collect data in a camera-fixed reference frame to model the dynamic soaring flight trajectories of Manx shearwater in an aerodynamic reference frame, whereas I model the attack trajectories of Harris' hawks in both an inertial and a background frame of reference using data collected in an Earth-fixed frame of reference. The output of my investigation into the energetics of dynamic soaring is the first empirical demonstration of dynamic soaring outside the albatrosses, the formulation of a new metric for identifying and quantifying dynamic soaring, and the demonstration that the large-scale distribution of the Manx shearwater is affected by their dynamic soaring behaviour. The output of my investigation into the guidance of prey pursuit is the finding that Harris' hawk attack trajectories are well modelled by the proportional navigation (PN) guidance law commonly used by homing missiles. However, I also show that a guidance law that can be mechanised using only visual information – rather than the inertial and visual information required by PN – also successfully fits attack trajectory data. Finally, I propose a method for analysing eye-in-head movements during dynamic flight in birds, and I find that Harris' hawks limit eye-in-head movement during terminal pursuit, a necessary condition to implement PN guidance. In being reflective about the reference frames in which I model bird behaviour and, in cases, by modelling the same data in different reference frames, I expose the utility of the reference frame concept in analysing biological systems.

Author contributions

The main chapters of this thesis are manuscripts that have been published, have been submitted, or will soon be submitted. Below, I describe the contributions that co-authors on these manuscripts made.

Chapter 2 was published in *Science Advances* in 2022, and I provide the published version of the manuscript in Appendix D. To indicate author contributions, I here provide the author list, the acknowledgements section of the published paper, and, if necessary, the list of any figures created by co-authors. Author list: James A. Kempton, Joe Wynn, James Evry, Annette L. Fayet, Natasha Gillies, Tim Guilford, Marwa Kavelaars, Ignacio Juarez-Martinez, Oliver Padget, Christian Rutz, Martyna Syposz, Graham K. Taylor. As stated in the acknowledgements section of the published paper, individual contributions are as follows – Conceptualization: J.K., J.W., T.G., G.T; Formal analysis: J.K., J.W., G.T.; Investigation: J.K., S.B., J.E., A.F., N.G., T.G., M.K., I.M., O.P., C.R., A.S. and M.S.; Methodology: J.K., J.W., T.G., O.P., C.R., and G.T.; Supervision: T.G. G.T.; Visualization: J.K. and J.W.; Writing (original draft): J.K., J.W., G.T. All authors reviewed and commented on the original draft. Joe Wynn created Figures 2.7, 2.8, and 2.9.

Chapter 3 has been submitted to *eLife*. To indicate author contributions, I here provide the author list, the acknowledgements section of the submitted paper, and, if necessary, the list of any figures created by co-authors. Author list: James A. Kempton, Caroline H. Brighton, Lydia A. France, Marco Klein Heerenbrink, Sofia Miñano, James Shelton, and Graham K. Taylor. As stated in the acknowledgements section of the submitted paper, individual contributions are as follows – Conceptualization: J.A.K., C.H.B., and G.K.T.; Formal analysis: J.A.K., C.H.B., L.A.F., M.K.H., J.S., and G.K.T.; Investigation: J.A.K., C.H.B., M.K.H., and S.M.; Methodology: J.A.K., C.H.B., and G.K.T.; Supervision: G.K.T.; Visualization: J.A.K.; Writing (original draft): J.A.K., and G.K.T.; All authors reviewed and commented on the original draft. Caroline Brighton created Figure 3.9.

Chapter 4 is *in prep*. To indicate author contributions, I here provide the author list, the acknowledgements section of the current manuscript version, and, if necessary, the list of any figures created by co-authors. Author list: James A. Kempton, Oliver Bradley-Baker, Caroline H. Brighton, Sofia Miñano, and Graham K. Taylor. As stated in the acknowledgements section of the current manuscript version, individual contributions are as follows – Conceptualization: J.A.K., O.B, and G.K.T.; Formal analysis: J.A.K. Investigation: J.A.K., O.B, C.H.B., and S.M.; Methodology: J.A.K., C.H.B., and S.M; Supervision: G.K.T.; Visualization: J.A.K.; Writing (original draft): J.A.K.

Acknowledgements

I don't believe that dropping school physics at age 16 aided the execution of my research. I thank those friends of mine that are physicists for those discussions and lessons that have helped me. Similarly, I don't know what Jeremy Kasdin and Derek Paley look like, what nationalities they are, where they work, if they are still alive, or whether these are their real names, but their book – Engineering Dynamics – has been an integral servant to this thesis. My peers in the Oxford Flight Group have also been fundamental to my research, and I thank them for their tolerance of my eccentricities. I wish to thank the head of the Group, my supervisor, Graham Taylor. His keen intellectual insight, his financial assistance in the final year of my DPhil, his support during times of ill health, his backing of my adventures outside the DPhil remit (some of which led to the discovery of new species to science), and his lenience in response to my hand in the closure of the Tinbergen Building, are all greatly appreciated. Tim Guilford played a large role in setting me on the path to this thesis, and I want to thank him for it. Sunetra Gupta has played an important role in my intellectual development, and will continue to do so. I greatly appreciate her contribution, and I also appreciate the marvellous dinners that I have shared with her and Alex Caccia.

The execution of my studies would have been scarcely possible without the staff and owners of the White Hart pub in Wytham, who always provided a quiet table at which I could eat my lunch. I am sorry to see that its doors are now closed, though if there could be a time for such a sad event, it is as its longest serving patron retires from Wytham.

I have now spent many years in Oxford and I have seen the 'City of Dreaming Spires' and the pylons that abut the view. I hope that the institution of Oxford continues to evolve alongside that core spirit that moulds friends as those that I have made. To these friends, and in particular to Leonidas Romanos-Davranoglou and Ben Hopkins, I am most grateful.

There are many reasons that this thesis has been submitted a little later than desired. One is because of the unpleasant bout of Covid-19 that I contracted in Montpellier in the summer of 2022. I should like to thank the Gueroults for their kind hospitality that ensured I was not feverish on the streets. I should also like to thank those people, activities, and ideas that ensured this thesis was not submitted on time, and that have helped me to meet future deadlines.

I should not have been able to complete this research without the generous financial support of the Christopher Welch Scholarship, and I should like to thank the Board of the Scholarship as such. I also want to thank Merton College for its financial assistance, and broader academic and pastoral support these many years. To the Ms, I thank you for such high standards.

I want to thank Elena for making the completion of this thesis so much more fun.

Finally, I would like to thank my father for his generosity and, to Mummy and Miles, I am eternally grateful for your perennial kindness, love, and support.

Contents

List of Figures vii

List of Supplementary Videos ix

1 Introduction 1
- 1.1 Disclaimer . . . 1
- 1.2 Reference frames . . . 2
  - 1.2.1 Inertial Reference Frames . . . 4
  - 1.2.2 Non-inertial reference frames . . . 5
- 1.3 Modelling in different reference frames . . . 5
  - 1.3.1 Tractability . . . 6
  - 1.3.2 Parsimony . . . 7
  - 1.3.3 Physical meaning . . . 9
  - 1.3.4 Explicability . . . 9
- 1.4 Modelling biological systems in different reference frames . . . 10
  - 1.4.1 Dynamic soaring . . . 10
  - 1.4.2 Prey pursuit . . . 11
- 1.5 Conclusion . . . 12
- References . . . 12

2 Optimization of dynamic soaring in a flap-gliding seabird impacts its large-scale distribution at sea 15
- 2.1 Abstract . . . 15
- 2.2 Introduction . . . 16
- 2.3 Theoretical Framework . . . 19
- 2.4 Results . . . 23
- 2.5 Discussion . . . 34
- 2.6 Materials and Methods . . . 45
- References . . . 49

3 Visual guidance by hawks in pursuit of terrestrial prey 53
- 3.1 Abstract . . . 53
- 3.2 Introduction . . . 54
- 3.3 Results . . . 57
- 3.4 Discussion . . . 66
- 3.5 Materials and Methods . . . 73
- References . . . 80

4 The motion of hawk eyes during dynamic flight behaviour **83**
4.1 Abstract . . . 83
4.2 Introduction . . . 84
4.3 Results . . . 85
4.4 Discussion . . . 94
4.5 Materials and Methods . . . 99
References . . . 101

5 Discussion **104**
5.1 The consequences of reference frame choice . . . 104
5.1.1 Tractability . . . 105
5.1.2 Parsimony . . . 108
5.1.3 Physical meaning . . . 109
5.2 Conclusion . . . 111
References . . . 111

Appendices

A Supplementary Material to Chapter 2 **114**
A.1 Supplementary Text . . . 114
References . . . 122

B Supplementary Material to Chapter 3 **123**
B.1 Supplementary Text . . . 123
B.2 Supplementary Figures . . . 127
References . . . 127

C Supplementary Material to Chapter 4 **131**
C.1 Supplementary Figures . . . 131

D Published version of Chapter 2 **140**

List of Figures

2.1 Cyclical basis of dynamic soaring. . . . 17
2.2 Reconstruction of cyclical turning behavior using bird-borne video. . . . 22
2.3 Weaving flight of Manx Shearwaters. . . . 24
2.4 Optimization of the phasing of the vertical and horizontal components of each flight. . . . 27
2.5 Optimization of horizontal flight trajectories with respect to the wind. . . . 30
2.6 Influence of the wind on the effectiveness of dynamic soaring. . . . 31
2.7 At-sea distribution of Manx Shearwaters. . . . 32
2.8 Association of wind direction and flight direction in Manx Shearwaters. . . . 34
2.9 Association of wind speed and flight direction in Manx Shearwaters. . . . 35
2.10 Performance space of dynamic soaring. . . . 36

3.1 Pursuit geometry. . . . 57
3.2 Harris' hawk attack geometry with background point. . . . 60
3.3 Simulated trajectories for a single flight under two different guidance models and optimal parameter values. . . . 63
3.4 Comparison of the prediction error, N, and K distributions under inertial-PNP and background-PNP guidance. . . . 64
3.5 Both PNP guidance laws are successful models of the data, but background-PNP is more sensitive to the parameter K. . . . 65
3.6 Simulated trajectories of the first quartile error, median error, and third quartile error flights under three guidance laws given globally best-fit parameter values. . . . 67
3.7 Different methods of mechanising the estimation of ${}^{\mathcal{I}}\dot{\lambda}$ are represented by different block diagrams. . . . 69
3.8 The effect of swapping the best-fit K between inertial-PNP and background-PNP guidance simulations. . . . 72
3.9 The setup of the pursuit task. . . . 75

4.1 Apparent eye-in-head movement during perch-to-perch trials. . . . 85
4.2 A method for inferring eye-in-head movement between images. . . . 86
4.3 Stages of pursuit. . . . 88
4.4 Eye-in-head motion during the terminal phase of pursuit. . . . 89
4.5 Extending the method for detecting eye-in-head movement. . . . 90
4.6 The nictitating membrane covers the eye during a head saccade. . . . 93

4.7 Timing of leg protraction during terminal pursuit. 94
4.8 Timing of foot extension during intercept. 95
4.9 Protraction of the alulae. 96

B.1 The distribution of τ under different guidance models. 127
B.2 The distribution of the prediction error ϵ and guidance constants under PP, PN, and PN background guidance. 128
B.3 Surface plot of PN guidance. 129
B.4 Histograms of minimum median prediction error found by k-fold cross validation for different guidance models. 129
B.5 The lure, measured bird, and simulated trajectories under three different guidance models for three randomly selected flights. 130

C.1 Eye motion during the terminal phase of one pursuit flight by Drogon. . . 132
C.2 Eye motion during the terminal phase of one pursuit flight by Toothless. . 133
C.3 Eye motion during the terminal phase of one pursuit flight by Charmander. 134
C.4 Eye motion during the terminal phase of one pursuit flight by Ruby. 135
C.5 Image pairs for rectification. 136
C.6 Reference and tangent lines drawn on consecutive frames after Rhaegal catches the target. 136
C.7 Reference and tangent lines drawn on consecutive frames before Rhaegal captures the target. 137
C.8 Reference and tangent lines drawn on consecutive frames after Toothless catches the target. 137
C.9 Charmander draws the nictitating membrane across the eye during a head saccade. 138
C.10 Toothless draws the nictitating membrane across the eye during a head saccade. 138
C.11 Rhaegal draws the nictitating membrane across the eye during a head saccade. 139
C.12 Ruby draws the nictitating membrane across the eye during a head saccade. 139

List of Supplementary Videos

The following supplementary videos pertain to Chapter 2:

1. Supplementary Movie S1 - Raw footage from video camera attached to bird b117ii, trimmed to the period of data analysed and plotted in Figure 2.2.
2. Supplementary Movie S2 - Video demonstrating the steps of the horizon detection algorithm as applied to the raw footage from bird b117ii.
3. Supplementary Movie S3 - Video sequence comparing, for video b16-701, the horizon lines directly output by the horizon detection algorithm (yellow lines) and those manually adjusted after output (green lines).

A seeming change of place may come of movement either of object or observer, or again of unequal movements of the two."

— Nicolas Copernicus *De Revolutionibus Orbium Coelestium* (1543), Chapter V

1 Introduction

Contents

1.1 Disclaimer . . . 1
1.2 Reference frames . . . 2
1.2.1 Inertial Reference Frames . . . 4
1.2.2 Non-inertial reference frames . . . 5
1.3 Modelling in different reference frames . . . 5
1.3.1 Tractability . . . 6
1.3.2 Parsimony . . . 7
1.3.3 Physical meaning . . . 9
1.3.4 Explicability . . . 9
1.4 Modelling biological systems in different reference frames . . . 10
1.4.1 Dynamic soaring . . . 10
1.4.2 Prey pursuit . . . 11
1.5 Conclusion . . . 12
References . . . 12

1.1 Disclaimer

Over the course of this thesis, I variously make reference to the following terms: inertial frame of reference, air-fixed frame of reference, ground-fixed frame of reference, background frame of reference, non-inertial frame of reference, line-of-sight frame of reference, rotating frame of reference, body-fixed frame of reference, camera-fixed frame of reference. This rather begs the question of what is a frame of reference, and what are these different flavours in which it exists? But before I tackle these questions, I feel I must provide a disclaimer. Much as Leonard Bernstein was loathe to present a disclaimer to the audience in advance

of conducting the Brahms D Minor Piano Concerto performed by Glenn Gould at Carnegie Hall in 1962, I am loathe to write one here. But, like Bernstein, I think it appropriate to do so. Though this is a thesis on biology, one that concerns two different dynamic flight behaviours performed by birds – dynamic soaring and prey pursuit – it is the concept of the reference frame that unites the chapters, and it is in the context of physics that the concept of the reference frame was developed. It is also among examples from physics that I think it is clearest to illustrate what a frame of reference is, and the sometimes profound ramifications that modelling physical or biological systems in different reference frames can have. Thus, I start this Introduction by considering reference frames in the context of physics before I arrive at the specific biological systems that are the subject of this thesis.

1.2 Reference frames

A feature of the language of physics is the use of terms that, when employed in the common vernacular, convey somewhat different meanings. For a given word employed both by the physicist and the layman, the meaning for the physicist will inevitably be more concrete and, accompanying a concreteness in meaning, there exists a precise mathematical statement. Thus, in physics, work is the amount of energy that it takes to move a particle along a given path, and the associated equation is:

$$W_P^{(\mathbf{F}_P)}(\mathbf{r}_{P/O};\gamma_P) = \int_{\gamma_P} \mathbf{F}_P \cdot^{\mathcal{I}} d\mathbf{r}_{P/O}, \tag{1.1}$$

where the symbols require careful definition: $W_P^{(\mathbf{F}_P)}(\mathbf{r}_{P/O};\gamma_P)$ is the work, W_P, performed by the force, $\mathbf{F}_p$, on a particle, P, whose position along the path, γ_P, is specified by the vector, $\mathbf{r}_{P/O}$ (Kasdin, 2011). In physics, momentum is the quantity that remains constant in the absence of an external force and is defined mathematically as:

$${}^{\mathcal{I}}\mathbf{p}_{P/O} = m_P {}^{\mathcal{I}}\mathbf{v}_{P/O}, \tag{1.2}$$

where $\mathbf{p}_{P/O}$ is the momentum of particle P, m_P is the mass of P, and $\mathbf{v}_{P/O}$ is the velocity of P. One as yet undissected feature of Equations 1.1 and 1.2 is the caligraphic symbol $\mathcal{I}$. This is connected to another concept in physics that has a counterpart in the vernacular: frame of reference. During the course of my PhD, I have collated instances in which the (synonymous) terms frame of reference and reference frame have been used in the vernacular. To take some choice examples, James Meek, writing in the London Review of

Books, employs the term while describing an interview between himself and Oleh Pilipenko, a man kidnapped by Russian forces at the opening of the 2022 invasion of Ukraine: "[Oleh] used the concepts of 'barbarity' and 'civilisation' as part of the reference frame for his experiences" (Meek, 2022). In 'Get your tongue out of my mouth, I'm kissing you goodbye', Cynthia Heimel laments the female equivalents to the colloquialism 'guy': "when women hear a man say, 'I want a terrific lady', we know we're dealing with someone with a different frame of reference and we talk slower" (Heimel, 1993). Stewart Lee, in the 2018 Southend-on-Sea recording of his touring stand-up routine Content Provider, defends his brother-in-law's inability to appreciate his comedy: "to be fair to him, my bother-in-law, he has no frame of reference whatsoever for my live show, because he has only seen one other thing live in his whole life". James Meek, Cynthia Heimel, and Stewart Lee all use the term frame of reference to argue that a particular set of experiences shapes a person's outlook. Thomas Kuhn more closely approaches the physical definition of reference frame in his 'The Copernican Revolution'. He states that the time of day at which the shadow of a gnomon (a vertical stick used for tracking the sun's motion) is shortest "provided two fundamental frames of reference for all further astronomical measurements", namely North as the direction of the shadow, and noon as the point in time between which the unit of a day is defined (Kuhn, 1957). Here, Kuhn alludes to the importance of having a reference with respect to which one makes measurements. To the physicist, a frame of reference is, qualitatively, "a point of view from which observations and measurements are made regarding the motion of a system" (Kasdin, 2011). More properly, a frame of reference is defined by three orthogonal unit vectors and one point (the origin) (Kasdin, 2011). To assign specific values to mathematical objects like points and vectors, we must decide where our zero-point lies, what the fundamental unit of magnitude is, and what our reference directions are. This is what a reference frame does by providing a zero-point, called the origin, and a set of orthonormal basis vectors whose lengths define the unit length and whose directions define a set of reference directions. To give an example, we can define the reference frame denoted by the caligraphic $\mathcal{I}$ earlier as:

$$F_{\mathcal{I}} = (O, \mathbf{1}_{\boldsymbol{x}}, \mathbf{1}_{\boldsymbol{y}}, \mathbf{1}_{\boldsymbol{z}}), \tag{1.3}$$

where O is the origin that has uniform motion, and $\mathbf{1}_{\boldsymbol{x}}$, $\mathbf{1}_{\boldsymbol{y}}$, and $\mathbf{1}_{\boldsymbol{z}}$ are orthogonal unit vectors that define fixed directions. With a reference frame defined, values can be assigned to physical properties like position, velocity, and acceleration.

1.2.1 Inertial Reference Frames

There are an infinity of possible reference frames. The reference frame defined in Equation 1.5 is, however, among a privileged set known as inertial reference frames. An inertial reference frame is a reference frame whose origin is in uniform (unaccelerated) motion, and whose basis vectors are not rotating (Kasdin, 2011). This begs the question of not accelerating and not rotating relative to what? Newton answered, in relation to absolute space. In Newton's mechanical pantheistic philosophy, time, space, and motion were absolute quantities defined in relation to God and an ethereal medium, these being the stationary, immovable entities of the universe (Mason, 1962). Thus, Newton espoused a privileged viewpoint, this being an observer at rest with respect to the cosmic ether. Galileo, through his mouthpiece Salviati, conducted a thought experiment in his *Dialogue Concerning the Two Chief World Systems* in which a man in a windowless room below deck must judge a ship to be at rest or in uniform motion by the behaviour of animals and dripping water in the room (Galilei, 2013). The man cannot do so, by which Galileo concludes that observers in uniform motion with respect to a rest frame perceive the same laws of motion as those observes in the rest frame. This is the principle of Galilean invariance (Koessler, 2018), and it means that Newton's privileged viewpoint also contains observations made in frames moving uniformly with respect to the rest frame. But how to define the absolute rest frame? Classically, this was the firmament of fixed stars that Copernicus placed as the eighth sphere in his spherical universe (Mason, 1962). Though these stars appear to move, Copernicus accounted for this apparent motion by prescribing a diurnal rotation to the Earth and, as the stars appeared to keep fixed angular distances to each other (Kuhn, 1957), they therefore appeared to describe fixed cosmic directions. However, the search for absolute space and its instantiation as a stationary ether led to its abolition following the experiments of Michelson and Morley, and as part of the Einsteinian revolution. Today, an inertial reference frame is therefore an abstract, axiomatic statement, one in which Newton's Laws hold (Kasdin, 2011). This means that for practical purposes, an inertial reference frame is one whose acceleration is small in comparison to the accelerations of the particles of interest (Kasdin, 2011). Thus, a frame whose origin is moving at 30 km/s (and not 90 miles/s as Eric Idle tells us) with the Earth's centre, and whose basis vectors do not rotate relative to the 'fixed stars', is a

functional inertial reference frame for flight dynamics research, even if the Earth's centre is accelerating on an elliptical orbit (Boiffier, 1998).

1.2.2 Non-inertial reference frames

Consider the following reference frame:

$$F_{\mathcal{A}} = (A, \mathbf{1}_{\boldsymbol{x}}, \mathbf{1}_{\boldsymbol{y}}, \mathbf{1}_{\boldsymbol{z}}), \tag{1.4}$$

whose origin, A, accelerates with respect to the frame $F_{\mathcal{I}}$. Or, consider the frame $F_{\mathcal{R}}$ that shares its origin, O, with the frame $F_{\mathcal{I}}$ but whose $\mathbf{1}_{\boldsymbol{x}'}$ and $\mathbf{1}_{\boldsymbol{y}'}$ basis vectors rotate with respect to the basis vectors of $F_{\mathcal{I}}$:

$$F_{\mathcal{R}} = (R, \mathbf{1}_{\boldsymbol{x}'}, \mathbf{1}_{\boldsymbol{y}'}, \mathbf{1}_{\boldsymbol{z}}), \tag{1.5}$$

Both $F_{\mathcal{A}}$ and $F_{\mathcal{R}}$ are non-inertial reference frames because they are frames that are not in uniform motion with respect to an inertial frame. In non-inertial reference frames Newton's laws do not hold; additional terms must be added to the equation $\mathbf{F} = m\mathbf{a}$ to solve for the trajectory of a particle modelled in a non-inertial frame.

1.3 Modelling in different reference frames

When modelling the dynamics of a system's motion, there is something of a recipe (Kasdin, 2011) for constructing the equations of motion of the system:

1. Choose the coordinates in which to write the motion variables,
2. Choose the reference frame in which to write vectors,
3. Draw a free-body diagram,
4. Use Newton's second law, $\mathbf{F} = m\mathbf{a}$, to construct the vector equation of motion,
5. For accelerations where derivatives have not been taken with respect to the inertial frame, use the transport equation to find the inertial derivative,
6. If vectors need to be expressed in a different basis, apply a change of basis transformation,
7. From the vector equation of motion, form the scalar equations of motion.

Superficially, it may appear that choosing a reference frame in the above recipe is simply a step to ensure that one has an accounting mechanism to keep track of the numbers. And though this is true, the choice of one reference frame among an infinity of others (Koessler, 2018) in which to pose the equations of motion can have varied, and sometimes profound, consequences.

1.3.1 Tractability

An important consequence of reference frame choice is its influence on the tractability of a system. This is well illustrated by the modelling of the simple pendulum. We consider a simple pendulum as a bob, P, of mass m attached to a massless rod of length l. Using Cartesian coordinates to specify the position of the bob in the x-axis and y-axis of an inertial reference frame, the scalar dynamic equations of motion for the pendulum bob are:

$$\frac{F_x}{l} = m\ddot{x}, \tag{1.6}$$

$$\frac{F_y}{l} - mg = m\ddot{y}, \tag{1.7}$$

where F_x is the force exerted by the rod in the x-direction, F_y is the force exerted by the rod in the y-direction, $\ddot{x}$ is the acceleration of the bob in the x-direction, $\ddot{y}$ is the acceleration of the bob in the y-direction, and g is the acceleration due to gravity. From Equations 1.6 and 1.7, one can derive the following scalar kinematic equations of motion knowing that the position of the pendulum bob is constrained by $x^2 + y^2 = l^2$:

$$\ddot{x} = \frac{(-x\dot{x}^2 - x\dot{y}^2 + xyg)}{l^2}, \tag{1.8}$$

$$\ddot{y} = \frac{(-y\dot{x}^2 - y\dot{y}^2 - x^2 g)}{l^2}, \tag{1.9}$$

where $\dot{x}$ is the velocity of the bob in the x-direction, and $\dot{y}$ is the velocity of the bob in the y-direction.

As (Kasdin, 2011) note, solving Equations 1.8 and 1.9 will yield the correct trajectory for the bob, but the problem is in solving it – there is no exact solution. However, if we instead model the pendulum using polar coordinates in an inertial reference frame, we arrive at the following, solvable, dynamic equations of motion:

$$-F\cos\theta + mg = m(-l\ddot{\theta}\sin\theta - l\dot{\theta}^2\cos\theta), \tag{1.10}$$

$$-F\sin\theta = m(l\ddot{\theta}\cos\theta - l\dot{\theta}^2\sin\theta), \tag{1.11}$$

where F is the total force imparted by the rod, and θ is the angle that the rod makes with the y-axis. Alternatively, if we model the pendulum using polar coordinates in a non-inertial frame that rotates such that its x-axis always points along the pendulum rod (called the polar frame), we arrive at the following dynamic equations of motion:

$$-F + mg\cos\theta = -ml\dot{\theta}^2, \tag{1.12}$$

$$-mg\sin\theta = ml\ddot{\theta}, \tag{1.13}$$

This is the most tractable way of modelling the problem; it is immediately clear from Equation 1.13 that the kinematic equation of motion for the pendulum is:

$$\ddot{\theta} = \frac{g}{l}\sin\theta, \tag{1.14}$$

which, when solved, gives the trajectory of the pendulum bob and allows the determination of the system's key behaviours.

1.3.2 Parsimony

The early Greek astronomers produced a conceptual scheme of the universe for predicting the motion of the sun and the stars at different locations on Earth. Their two-sphere cosmology had the following elements:

1. An outer sphere holding the sun and stars,
2. An inner sphere, at the centre of the universe, that is the Earth,
3. The outer sphere is significantly larger than the inner sphere,
4. The poles of the inner and outer spheres are on the same axis, and the equators of the inner and outer sphere lie in the same plane,

5. The outer sphere rotates about the inner sphere once every 23 hours and 56 minutes in a westward direction,

6. The sun moves in an eastward direction on a great circle that is on, and inclined at 23.5° to, the equator of the outer sphere, with a period of approximately 365.25 days,

7. Courtesy of the rotation of the outer sphere, and the sun's motion relative to the outer sphere, the sun reaches the same relative position (such as its zenith) every 24 hours.

Though highly successful at predicting the motion of the sun and the stars, this model struggled to account for the motion of the planets. The problem of the planets was attacked by Eudoxus and Calippus with their homocentric sphere theory. More successfully, Apollonius, Hipparchus, Ptolemy, and others developed the theory of epicycles, eccentrics, and deferents, which now bears the name of the Ptolemaic system. In the Ptolemaic system a series of compound circles were used to account for the motion of the planets around a central, stationary Earth. In total, Ptolemy used approximately 80 circles (Mason, 1962).

Fundamental to Ptolemy's system is the assumption of a central, stationary Earth. In imparting a daily rotation and an orbit to the Earth, and in replacing the Earth with the sun at the centre of the universe, Copernicus reduced the number of compound circles from approximately 80 to 48 (Mason, 1962). Copernicus' move is akin to a switch in the reference frame in which one is modelling the planetary system. With Ptolemy, the solar system is considered from an Earth that is an inertial reference frame in uniform (stationary) motion and defines fixed directions. With Copernicus, the solar system is considered from an Earth that is a non-inertial frame, in non-uniform motion with respect to the sun, and rotating so that it does not define fixed directions. Both the geocentric Ptolemaic system and the heliocentric Copernican system produce the same predictions about planetary motion and are equally successful in this regard, but the Copernican system is more parsimonious.

In breaking the assumption of uniform circular orbits, Kepler reduced the number of planetary orbits to 7. Not only is this the most parsimonious solution to the problem of the planetary motions, but it also yields more accurate predictions.

The greater parsimony of the Copernican and Keplerian descriptions relative to the Ptolemaic reflects the number of underlying degrees-of-freedom of the system. The

complexity of Equations 1.6 and 1.7 in modelling the simple pendulum emerges from using two degrees of freedom to model a one degree-of-freedom system. Similarly, there are far fewer than the approximately 80 degrees-of-freedom used by Ptolemy for the planetary orbits. And, much as a change in reference frame exposed the underlying number of degrees-of-freedom in the pendulum example, so did the shift from a geocentric to heliocentric model of the universe. Experimenting with the reference frame in which to model can expose more parsimonious solutions to a problem; in cases, finding a more parsimonious solution to a problem reveals some underlying structure to the physics.

1.3.3 Physical meaning

The reference frame in which one chooses to model implies something about the physical structure of the system one is representing. In the cosmological example of Section 1.3.2, the switch in reference frame from geocentric to heliocentric is not simply a modelling device (though Copernicus claimed it to be so), but also reflects something deep about the structure of our solar system, namely that the Earth orbits the sun, and rotates daily, and that the sun lies at the centre of the solar system. Thus, choosing an appropriate reference frame to model a system can be more than just making a choice about a numerical accounting method, but also a reflection of the underlying physics.

1.3.4 Explicability

With the pendulum bob modelled with polar coordinates in the polar frame we earlier arrived at the kinematic equation of motion in Equation 1.14. This equation allows one to immediately investigate the behaviour of the system, which the less tractable Equations 1.8 and 1.9 do not. For example, in setting $\ddot{\theta} = 0$, one can investigate the stability behaviour of the pendulum and determine that it has a stable equilibrium at $\theta = 0$ and an unstable equilibrium at $\theta = \pm\pi$. Furthermore, if one makes the small angle assumption that $\theta = \sin\theta$, Equation 1.14 becomes $\ddot{\theta} = \frac{g}{l}\theta$, which is the equation for simple harmonic motion, and one can say that the natural frequency of this system is $f = \sqrt{\frac{g}{l}}$.

1.4 Modelling biological systems in different reference frames

Biological systems are constrained by the laws of physics much as physical systems are, and applying tools developed in the context of physics and engineering to biological problems can be fruitful (Taylor et al., 2014). This is especially true for biomechanical systems, like bird flight. In this thesis, I focus on two dynamic flight behaviours performed by birds – dynamic soaring and prey pursuit. In particular, I explore the energetics and guidance of these behaviours by collecting data from Manx shearwaters (*Puffinus puffinus*) and Harris' hawks (*Parabuteo unicinctus*) and modelling this data in different frames of reference.

1.4.1 Dynamic soaring

Dynamic soaring is a flight technique performed by some birds, notably Procellariiformes (the albatrosses, shearwaters, and petrels), that is defined by persistent harvesting of energy from a wind shear layer (Richardson, 2011; Sachs et al., 2013; Gibb et al., 2017; Bousquet et al., 2017). Though there has been little empirical work formally quantifying dynamic soaring in birds (see Sachs et al. (2013) and Gibb et al. (2017) for exceptions), there has been much theoretical investigation into dynamic soaring in birds and flight vehicles (Rayleigh, 1883; Zhao et al., 2004; Sachs, 2004; Lissaman, 2005; Suryan et al., 2008; Deittert et al., 2009; Richardson, 2011; Bower, 2012; Sukumar et al., 2013; Liu, 2017; Bousquet et al., 2017). Within the literature on dynamic soaring in birds, the concept of reference frame is often discussed. Indeed, two factions emerged supporting different viewpoints on the reference frame in which it is 'correct' to model dynamic soaring (Koessler, 2018). Starting with Sachs (2004), and continuing with Lissaman (2005) and Lissaman (2007), one faction claims that dynamic soaring is 'correctly' understood by modelling the total mechanical energy of a bird in terms of the kinematic kinetic energy, defined relative to the Earth. Starting with Barnes (2004), and continuing with Richardson (2011) and Richardson (2015), another claims that dynamic soaring is 'correctly' understood in terms of the aerodynamic kinetic energy, defined relative to the air around the bird. More recently, a consensus has emerged that one can 'correctly' understand dynamic soaring in both frames of reference (Koessler, 2018; Sachs, 2019) in the sense that in both frames the equations of motion are valid (Koessler, 2018) and neither of the physical mechanisms implied by different definitions of kinetic energy are 'wrong'. Earlier in the conflict, for

example, Sachs et al. (2013) made such statements as, "This means with regard to the theory of wind-gradient soaring that the wind gradient itself is insignificant for the energy gain. Rather, the energy gain is due to the change in the flight direction from windward to leeward in the upper curve". Here, Sachs refers to the fact that, when kinetic energy is defined kinematically, the energy increase phase of dynamic soaring is during the windward turn (Lissaman, 2005), whereas when kinetic energy is defined aerodynamically, the energy increase phase of dynamic soaring is when the bird ascends into the wind gradient and descends with the wind gradient (Taylor et al., 2016). The reality is that both mechanisms are true, but their truth depends on the definition of kinetic energy. Albatross do not harvest aerodynamic kinetic energy in the windward turn, for example, nor do petrels harvest kinematic kinetic energy during upwind ascents. Unfortunately, in the debate over the 'correct' reference frame in which to understand dynamic soaring, more nuanced points on the insights that modelling in different frames of reference can provide has been lost, and I shall return to these in the Discussion, once Chapter 2 on dynamic soaring in the Manx shearwater (*Puffinus puffinus*) has been digested.

1.4.2 Prey pursuit

The stooping of the peregrine falcon (*Falco peregrinus*) is among the most impressive attack trajectories seen in nature (Mills et al., 2018). What's more, we now understand much more about how the peregrine falcon commands steering to guide its attack trajectory (Brighton et al., 2017). Indeed, inspired by the homing missile literature (Palumbo et al., 2010; Shneydor, 2011), it is now increasingly popular to model animal pursuit trajectories in terms of feedback laws that command steering in respose to inputs that reflect the geometry of attacks (Brighton et al., 2017; Fabian et al., 2018; Brighton et al., 2019; Brighton et al., 2021). Where properties of the geometry are measured exocentrically, that is with respect to some external reference, this makes the reference frame concept extremely relevant. In particular, where the input to the feedback law is measured exocentrically, this implies that the attacker has a means to measure the input with respect to some external reference, and that the input need be measured with respect to some reference frame. For animals, this opens up questions on the frame of reference in which they measure sensory information for pursuit. In Chapter 3, I undertake phenomenological modelling of Harris' hawk (*Parabuteo unicinctus*) attack trajectories in different frames of

reference to explore the sensory information with which a hawk could feasibly guide itself to a target. The results of the modelling define requirements to mechanise the feasible feedback laws that a bird could use. In particular, the proportional navigation (PN) law, which I find to be consistent with Harris' hawk trajectories in Chapter 3, implies that if hawks track a target with their heads, then robust mechanisation of the law requires hawk to keep the eyes fixed relative to the head. Thus, in Chapter 4, I attempt to record eye-in-head movement in flying birds to test this requiremnent, a test inspired by thinking about hawk pursuit using the concept of the reference frame.

1.5 Conclusion

The Discussion of this thesis acts like a mirror to the Introduction. Using the work that I present on dynamic soaring and prey pursuit in Chapters 2-4, I shall consider how using difference frames of reference to model these behaviours leads to greater insight into the behaviours than would otherwise be possible. Thus, I approach a set of biological examples much in the same way as I approached the physical examples above.

References

Barnes, J. P. (Nov. 2004). "How Flies the Albatross – the Flight Mechanics of Dynamic Soaring". In: *World Aviation Congress & Exposition*. ISSN: 0148-7191. SAE International. DOI: https://doi.org/10.4271/2004-01-3088.

Boiffier, J.-L. (1998). *The dynamics of flight: the equations*. eng. Chichester: Wiley.

Bousquet, G. D., Triantafyllou, M. S., and Slotine, J.-J. E. (2017). "Optimal dynamic soaring consists of successive shallow arcs". In: *Journal of The Royal Society Interface* 14.135, p. 20170496. DOI: 10.1098/rsif.2017.0496.

Bower, G. C. (2012). "Boundary layer dynamic soaring for autonomous aircraft: Design and validation". thesis. Stanford University.

Brighton, C. H., Chapman, K. E., Fox, N. C., and Taylor, G. K. (Mar. 2021). "Attack behaviour in naive gyrfalcons is modelled by the same guidance law as in peregrine falcons, but at a lower guidance gain". en. In: *Journal of Experimental Biology* 224.5, jeb238493. DOI: 10.1242/jeb.238493.

Brighton, C. H. and Taylor, G. K. (Dec. 2019). "Hawks steer attacks using a guidance system tuned for closepursuit of erratically manoeuvring targets". en. In: *Nature Communications* 10.1, p. 2462. DOI: 10.1038/s41467-019-10454-z.

Brighton, C. H., Thomas, A. L. R., and Taylor, G. K. (Dec. 2017). "Terminal attack trajectories of peregrine falcons are described by the proportional navigation guidance law of missiles". en. In: *Proceedings of the National Academy of Sciences* 114.51, pp. 13495–13500. DOI: 10.1073/pnas.1714532114.

Deittert, M., Richards, A., Toomer, C., and Pipe, A. (2009). "Dynamic Soaring Flight in Turbulence". In: *AIAA Guidance, Navigation, and Control Conference*, pp. 2–5. DOI: 10.2514/6.2009-6012. eprint: https://arc.aiaa.org/doi/pdf/10.2514/6.2009-6012.

Fabian, S. T., Sumner, M. E., Wardill, T. J., Rossoni, S., and Gonzalez-Bellido, P. T. (Oct. 2018). "Interception by two predatory fly species is explained by a proportional navigation feedback controller". en. In: *Journal of The Royal Society Interface* 15.147, p. 20180466. DOI: 10.1098/rsif.2018.0466.

Galilei, G. (2013). *Dialogue concerning the two chief world systems: Ptolemaic and Copernican*. eng. London: The Folio Society.

Gibb, R., Shoji, A., Fayet, A. L., Perrins, C. M., Guilford, T., and Freeman, R. (2017). "Remotely sensed wind speed predicts soaring behaviour in a wide-ranging pelagic seabird". In: *Journal of The Royal Society Interface* 14.132, p. 20170262. DOI: 10.1098/rsif.2017.0262.

Heimel, C. (1993). *Get your tongue out of my mouth, I'm kissing you good-bye*. eng. London: Macmillan.

Kasdin, N. J. (2011). *Engineering dynamics: a comprehensive introduction*. eng. Princeton ; Oxford: Princeton University Press.

Koessler (2018). "Dynamic Soaring UAV Gliders". PhD thesis.

Kuhn, T. S. (1957). *The Copernican revolution: planetary astronomy in the development of Western thought*. eng. Cambridge, Mass.: Harvard University Press.

Lissaman, P. (2005). "Wind Energy Extraction by Birds and Flight Vehicles". en. In: *43rd AIAA Aerospace Sciences Meeting and Exhibit*. Reno, Nevada: American Institute of Aeronautics and Astronautics. DOI: 10.2514/6.2005-241.

Lissaman, P. (2007). "Fundamentals of energy extraction from natural winds". In: *Technical Soaring* 31.2, pp. 36–41.

Liu, D.-N. (2017). "Bio-inspired energy-harvesting mechanisms and patterns of dynamic soaring". In: *Bioinspir. Biomim.* 12, p. 016014.

Mason, S. F. (1962). *A history of the sciences*. eng. New rev. ed. New York: Collier Macmillan.

Meek, J. (Aug. 2022). "Blast Effects". en. In: *London Review of Books* 44.16.

Mills, R., Hildenbrandt, H., Taylor, G. K., and Hemelrijk, C. K. (Apr. 2018). "Physics-based simulations of aerial attacks by peregrine falcons reveal that stooping at high speed maximizes catch success against agile prey". en. In: *PLOS Computational Biology* 14.4. Publisher: Public Library of Science, e1006044. DOI: 10.1371/journal.pcbi.1006044.

Palumbo, N. F., Blauwkamp, R. A., and Lloyd, J. M. (2010). "Basic principles of homing guidance". In: *Johns Hopkins APL Technical Digest* 29.1, pp. 25–41.

Rayleigh, L. (1883). "The Soaring of Birds". In: *Nature* 27, pp. 534–535.

Richardson, P. L. (2011). "How do albatrosses fly around the world without flapping their wings?" In: *Progress in Oceanography* 88.1, pp. 46–58. DOI: 10.1016/j.pocean.2010.08.001.

Richardson, P. L. (Jan. 2015). "Upwind dynamic soaring of albatrosses and UAVs". en. In: *Progress in Oceanography* 130, pp. 146–156. DOI: 10.1016/j.pocean.2014.11.002.

Sachs, G., Traugott, J., Nesterova, A. P., and Bonadonna, F. (2013). "Experimental verification of dynamic soaring in albatrosses". In: *Journal of Experimental Biology* 216.22, pp. 4222–4232. DOI: 10.1242/jeb.085209.

Sachs, G. (2004). "Minimum shear wind strength required for dynamic soaring of albatrosses: Shear wind strength and dynamic soaring". In: *Ibis* 147.1, pp. 1–10. DOI: 10.1111/j.1474-919x.2004.00295.x.

Sachs, G. (2019). "Kinetic Energy in Dynamic Soaring—Inertial Speed and Airspeed". In: *Journal of Guidance, Control, and Dynamics* 42.8. Publisher: American Institute of Aeronautics and Astronautics _eprint: https://doi.org/10.2514/1.G003407, pp. 1812–1821. DOI: 10.2514/1.G003407.

Shneydor, N. A. (2011). *Missile guidance and pursuit: kinematics, dynamics and control*. eng. Oxford: Woodhead Publishing.

Sukumar, P. P. and Selig, M. S. (2013). "Dynamic Soaring of Sailplanes over Open Fields". In: *Journal of Aircraft* 50.5, pp. 1420–1430. DOI: 10.2514/1.C031940.

Suryan, R. M., Anderson, D. J., Shaffer, S. A., Roby, D. D., Tremblay, Y., Costa, D. P., Sievert, P. R., Sato, F., Ozaki, K., Balogh, G. R., and Nakamura, N. (2008). "Wind, Waves, and Wing Loading: Morphological Specialization May Limit Range Expansion of Endangered Albatrosses". In: *PLoS ONE* 3.12. Ed. by S. Humphries, e4016. DOI: 10.1371/journal.pone.0004016.

Taylor, G. and Thomas, A. (2014). *Evolutionary Biomechanics*. eng. Oxford University Press. DOI: 10.1093/acprof:oso/9780198566373.001.0001.

Taylor, G. K., Reynolds, K. V., and Thomas, A. L. R. (2016). "Soaring energetics and glide performance in a moving atmosphere". In: *Philosophical Transactions of the Royal Society B: Biological Sciences* 371.1704, p. 20150398. DOI: 10.1098/rstb.2015.0398.

Zhao, Y. J. and Qi, Y. C. (2004). "Minimum fuel powered dynamic soaring of unmanned aerial vehicles utilizing wind gradients". In: *Optimal Control Applications and Methods* 25.5, pp. 211–233. DOI: 10.1002/oca.744.

2

Optimization of dynamic soaring in a flap-gliding seabird impacts its large-scale distribution at sea

Contents

2.1 Abstract 15
2.2 Introduction 16
2.3 Theoretical Framework 19
2.4 Results 23
2.5 Discussion 34
2.6 Materials and Methods 45
References 49

2.1 Abstract

Dynamic soaring harvests energy from a spatiotemporal wind gradient, allowing albatrosses to glide over vast distances. However, its use is challenging to demonstrate empirically, and has yet to be confirmed in other seabirds. Here we investigate how flap-gliding Manx Shearwaters optimize their flight for dynamic soaring. We do so by deriving a new metric, the horizontal wind effectiveness, that quantifies how effectively flight harvests energy from a shear layer. We evaluate this metric empirically for fine-scale trajectories reconstructed from bird-borne video data using a simplified flight dynamics model. We find that the birds' undulations are phased with their horizontal turning to optimize energy harvesting. We also assess the opportunity for energy harvesting in long-range, GPS-logged

foraging trajectories, and find that Manx Shearwaters optimize their flight to increase the opportunity for dynamic soaring during favourable wind conditions. Our results show how small-scale dynamic soaring impacts large-scale Manx Shearwater distribution at sea.

2.2 Introduction

Wind speed and direction influence the movement ecology of birds across a range of spatiotemporal scales from local flight direction (Åkesson et al., 2002) and timing (Hawkes et al., 2011; Conklin et al., 2011; Åkesson et al., 2000; Schaub et al., 2004; Deppe et al., 2015; Åkesson et al., 2016), through route selection (Åkesson et al., 2016) and drift compensation (Horton et al., 2016; Åkesson et al., 2002; Wynn et al., 2020), to population distribution (Jouventin et al., 1990; Suryan et al., 2008) and migration success (Deppe et al., 2015). Such wind effects have been observed in a wide range of species, but the procellariiform seabirds (Jouventin et al., 1990; Paiva et al., 2010; Weimerskirch et al., 2000; González-Solís et al., 2009; Alerstam et al., 1993), comprising the albatrosses, petrels and shearwaters, differ notably from non-pelagic species in their behavioral responses to wind. In contrast to the tailwind preference of non-pelagic birds (Åkesson et al., 2000; Deppe et al., 2015; Conklin et al., 2011; Åkesson et al., 2016), Procellariiformes typically prefer crosswind or cross-tailwind flight (Paiva et al., 2010; Weimerskirch et al., 2000; Alerstam et al., 1993; Gibb et al., 2017). They are also able to fly huge distances (Croxall, 2005; Guilford et al., 2009; Catry et al., 2004; Jouventin et al., 1990) without having to offset their aerodynamic drag losses fully through flapping (Weimerskirch et al., 2000; Spivey et al., 2014). Both differences may be the product of a specialised flight mode called dynamic soaring (Richardson, 2011), but whereas this is the only plausible explanation of how albatrosses are able to glide immense distances without flapping (Weimerskirch et al., 2000), dynamic soaring is more challenging to demonstrate in species such as shearwaters that routinely flap their wings during their characteristic rising-falling flight (Spivey et al., 2014).

Soaring enables a bird to replace some or all of the aerodynamic kinetic energy that it loses to aerodynamic drag by harvesting energy from the atmosphere (Pennycuick, 2008). Static soaring offsets these drag losses by harvesting gravitational potential energy from rising air currents, whereas dynamic soaring harvests aerodynamic kinetic energy from a spatiotemporal wind gradient (Taylor et al., 2016). This can be most easily understood by noting that a bird flying into the wind experiences an increase in headwind speed as it

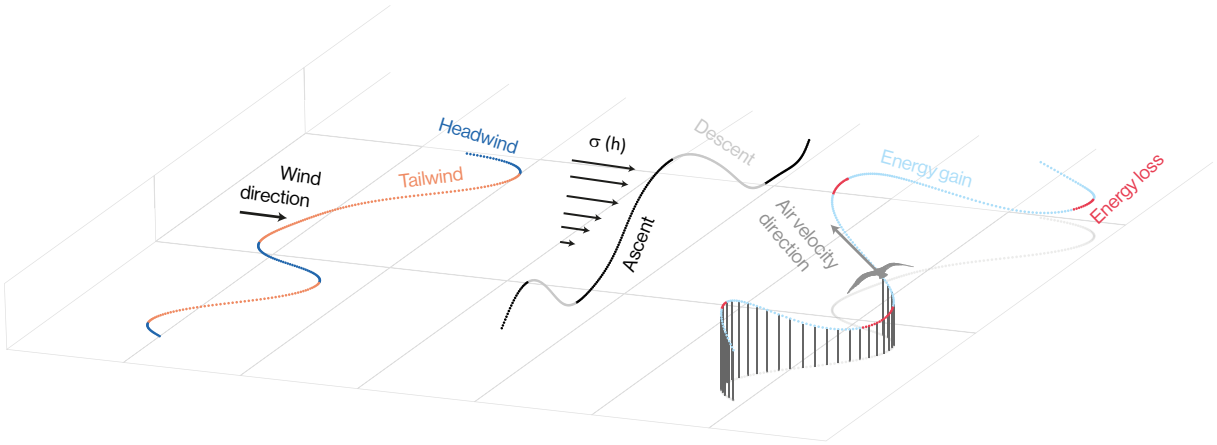


Figure 2.1: Cyclical basis of dynamic soaring. The energetic benefits of dynamic soaring are realised by phasing the horizontal and vertical components of flight to meet the Rayleigh conditions of flying into a strengthening wind and with a weakening wind. In a horizontal wind field, the sequence of headwinds (dark blue) and tailwinds (orange) that the bird experiences is determined only by the horizontal component of its flight trajectory (left). The vertical component (middle) determines whether the bird experiences an increasing or decreasing wind, according to whether it is ascending (black) or descending (light grey) through the shear layer (σ). The pattern of energy harvesting (right) depends on whether the phasing of the horizontal and vertical components of the flight trajectory meets the Rayleigh conditions, as these are what determine whether a bird gains (light blue) or loses (red) energy from the shear layer before taking account of drag losses. How much energy the bird harvests depends on the degree of alignment of the wind vector (black arrow) and the air velocity vector (grey arrow), as well as on the speed of flight and strength of wind shear. The trajectories shown here are reconstructed relative to the air from our empirical data for a part of one flight.

moves from slower to faster moving air. Because the bird's flight dynamics prevent its airspeed from equilibrating instantaneously (Bousquet et al., 2017), it follows that the bird will experience an immediate increase in its airspeed, and hence aerodynamic kinetic energy. Less obviously, perhaps, a similar increase in aerodynamic kinetic energy must also occur when a bird that is flying with the wind moves from faster to slower moving air. In general, dynamic soaring therefore entails flying *into* a strengthening wind and *with* a weakening wind (Taylor et al., 2016). More specifically, because wind speed increases with height above the sea's surface (Bencatel et al., 2013), pelagic dynamic soaring entails ascending *into* the wind and descending *with* the wind (Taylor et al., 2016). We call these criteria the Rayleigh conditions (see Figure 2.1), after their late 19th century discoverer (Rayleigh, 1883).

Although the physical principles of dynamic soaring are well understood, showing empirically that a bird is extracting aerodynamic kinetic energy from a spatiotemporal wind gradient—and hence implementing dynamic soaring—is extremely challenging. Among Procellariiformes, cyclical variation in mechanical energy has been used to assess dynamic soaring for the Wandering Albatross (*Diomedea exulans*) (Sachs et al., 2013) and the Manx

Shearwater (*Puffinus puffinus*) (Gibb et al., 2017) using high-resolution GPS measurements. There is a general difficulty with this approach in that cyclical variation in mechanical energy does not necessarily imply cyclical dynamic soaring. For instance, a bird which is circling at constant airspeed in a uniform wind field displays cyclical variation in its inertial kinetic energy, but is not extracting energy from a spatiotemporal wind gradient. Similarly, intermittent bounding and undulating flight shows cyclical variation in both inertial kinetic energy and gravitational potential energy in the absence of energy harvesting from a spatiotemporal wind gradient (Rayner et al., 2001). The mere occurrence of cyclical variation in mechanical energy is therefore insufficient to prove the use of dynamic soaring. In albatrosses, dynamic soaring has instead been inferred by analysing the distribution of mechanical energy gain with reference to a detailed aerodynamic model (Sachs et al., 2013). Proving that flap-gliding species such as shearwaters use dynamic soaring is even more challenging, however, because the variation in mechanical energy that dynamic soaring entails may not even appear cyclical when changes in mechanical energy due to flapping are superimposed (Gibb et al., 2017).

Here, we address these challenges by deriving a dimensionless metric describing dynamic soaring that we call the horizontal wind effectiveness (ϵ_h). We estimate this empirically for flap-gliding Manx Shearwaters by using a simplified flight dynamics model to reconstruct $n = 9$ detailed flight trajectories from video data (Supplementary Movie S1) collected using bird-borne video loggers (Rutz et al., 2007) attached to $N = 6$ individuals. The horizontal wind effectiveness ϵ_h quantifies how effectively flight in a given instantaneous direction harvests aerodynamic kinetic energy from a wind gradient, where positive values indicate that energy is gained from the shear layer and negative values indicate that energy is lost to it. Its long-term average ($-1 \leq \bar{\epsilon}_h \leq 1$) can therefore be used to assess whether and how a given flight trajectory is optimized for dynamic soaring in relation to the opportunity that the wind direction provides, which we quantify by defining another metric that we call the wind opportunity $\bar{\omega}$. We find that shearwaters phase their vertical sequence of ascent and descent appropriately to gain energy from the shear layer independent of the wind speed W, but only optimize their horizontal turning cycle for dynamic soaring under favourable conditions when the product of wind opportunity and wind speed $\bar{\omega}W$, which we call the crosswind component, is high. We use GPS data from $n = 368$ outbound foraging flights and $n = 368$ return flights, from $N = 201$ individuals, to test whether

this fine-scale behavior is recapitulated at larger spatiotemporal scales. We find that shearwaters tend to fly in a crosswind direction that is favourable for dynamic soaring on their outbound foraging trips, particularly when the wind speed W is high. Return legs are more constrained in their flight direction and do not show any significant crosswind tendency. Besides conclusively demonstrating the use of dynamic soaring by a flap-gliding seabird, the metrics of wind effectiveness, wind opportunity, and crosswind component that we derive offer a framework for analysing dynamic soaring more generally.

2.3 Theoretical Framework

Energetics of dynamic soaring For a bird flying in a steady horizontal wind field with vertical wind shear $\sigma \geq 0$, the mass-specific flow of useful mechanical energy due to dynamic soaring is shown in the Supplementary Text to be:

$$\frac{de}{dt} = -\frac{1}{2}U^2\sigma \sin 2\gamma \cos \eta \tag{2.1}$$

where $U = \|\mathbf{U}\|$ is the bird's airspeed, γ is the aerodynamic flight path angle defined as the elevation of the bird's air velocity $\mathbf{U}$ with respect to the horizontal, signed positive when climbing, and η is the heading-to-wind angle defined as the angle between the wind vector $\mathbf{W}$ and the horizontal component of $\mathbf{U}$. The local shear gradient σ is usually unknown, but it is clear by inspection that the instantaneous rate of energy harvesting is always maximized by flying in an instantaneous direction that maximizes the dimensionless quantity:

$$\epsilon = -\sin 2\gamma \cos \eta \tag{2.2}$$

which we call the total wind effectiveness. Because wind velocity increases with height above a surface, σ is > 0 by definition (see Supplementary Text). Energy is therefore harvested from the wind gradient when $\epsilon > 0$ and lost when $\epsilon < 0$, at a rate proportional to $\|\epsilon\|$.

The aerodynamic flight path angle γ is difficult to measure in an unknown wind field. However, because $-90° \leq \gamma \leq 90°$ by definition, it follows that $\sin 2\gamma$ is positive when $\gamma > 0$, and negative when $\gamma < 0$. The instantaneous rate of energy harvesting is therefore maximized by flying in an instantaneous direction that maximizes the simpler quantity:

$$\epsilon_h = -\operatorname{sgn}(\gamma)\cos\eta \tag{2.3}$$

where sgn denotes the signum or sign function. We call ϵ_h the horizontal wind effectiveness, because its magnitude depends only on the bird's horizontal flight direction with respect to the wind $\eta(t)$, whereas its sign depends on how the bird's vertical motion $\gamma(t)$ is phased with respect to its horizontal motion. Energy is harvested from the wind gradient when $\epsilon_h > 0$ and lost when $\epsilon_h < 0$, at a rate which is proportional to $\|\epsilon_h\|$. The Rayleigh conditions of ascending into a headwind (i.e. flying with $\gamma > 0$ and $\cos\eta < 0$) or descending with a tailwind (i.e. flying with $\gamma < 0$ and $\cos\eta > 0$) are met whenever $\epsilon_h > 0$, but are implemented most effectively as $\epsilon_h \to 1$. Eq. 2.3 therefore emphasises that both the shape of the horizontal flight track and the phasing of its ascent-descent sequence are critical to determining how effectively energy is harvested through dynamic soaring. Eq. 2.3 also implies that making net progress in a useful direction will tend to conflict with dynamic soaring trajectory optimization.

Flight dynamics model Computing the horizontal wind effectiveness ϵ_h requires knowledge of the sign of the aerodynamic flight path angle γ, and measurement of the heading-to-wind angle η (see Eq. 2.3). Identifying the sign of γ is straightforward if the wind field is horizontal, because then $\operatorname{sgn}(\gamma)$ is positive when ascending and negative when descending. We will further assume that $\operatorname{sgn}(\gamma) = \operatorname{sgn}(\theta)$ where θ is the bird's pitch angle (see Materials and Methods). Measuring η is much harder because whereas a bird's flight trajectory is most readily obtained in an Earth-fixed coordinate system using a GPS logger, the heading-to-wind angle η is necessarily measured with respect to the air. Relating these two frames of reference requires knowledge of the local wind velocity, which is problematic in a shear layer. To avoid this difficulty, we instead use a simplified flight dynamics model to predict the turning associated with the bird's pitching and banking motion that we measure by observing the horizon in bird-borne video from a body-fixed camera (Figure 2.2A,B; Supplementary Movies S1–S3; see also (Schoombie et al., 2019)). For this, we specify the bird's orientation using a set of intrinsic Euler angles where ψ is the bird's yaw angle, θ is the bird's pitch angle, and ϕ is the bird's bank angle, defined in that order (see Supplementary Text and Figure 2.2C–E).

We assume that the heading-to-wind angle η is equivalent to the angular difference between the bird's yaw angle ψ and the wind's bearing ζ, such that $\eta = \psi - \zeta$ (Figure 2.2C). This amounts to assuming that the bird's air velocity vector $\mathbf{U}$ is aligned with its longitudinal body axis at all times. We estimate ψ by integrating the following approximate model of unsteady banked turning (see Supplementary Text) on a per-frame basis using trapezoidal integration:

$$\dot{\psi} \approx \frac{g \sin \phi}{U_0 \cos \theta} \tag{2.4}$$

where $g = 9.81$ ms^{-2} is gravitational acceleration and $U_0 = 11.1$ ms^{-1} is the bird's equilibrium airspeed, as estimated in an earlier study of cruising Manx Shearwaters (Spivey et al., 2014). Here, the angles θ and ϕ are the bird's pitch and bank angles (Figure 2.2D,E), estimated from the apparent motion of the horizon (Figure 2.2A,B).

The unsteady banked turn model in Eq. 2.4 is an approximation, insofar as it assumes that the product of the bird's wing area S and lift coefficient C_L remains approximately constant, and assumes that any variation in the airspeed U is small in comparison with the equilibrium airspeed U_0. This is equivalent to assuming approximately constant airspeed $U \approx U_0$, and approximately constant lift L equal to body weight, $L \approx mg$ where m is mass. Eq. 2.4 also neglects the aerodynamic effects of wind shear on the bird's turning, which is reasonable if the bird flies directly with or against the wind as it descends or ascends through the shear layer, as is most efficient for dynamic soaring (see Supplementary Text for detailed discussion). For the purposes of the subsequent statistical analysis, we define dynamic soaring cycles as beginning and ending at peaks in the estimated time history of the bird's yaw angle ψ (Figure 2.2F).

Optimization of dynamic soaring Whilst it is possible in principle to find cyclical trajectories whose wind effectiveness is always non-negative, the optimization of a dynamic soaring trajectory is complicated in practice by the need to progress in a useful direction. The benefits of harvesting energy through dynamic soaring are therefore expected to trade off against the costs of deviating from the desired direction of progress, such that flights can typically be expected to involve alternating periods of negative as well as positive wind effectiveness. Because the rate of return from dynamic soaring is proportional to the wind shear strength σ (see Eq. 2.1), we should not necessarily expect birds to fly trajectories that

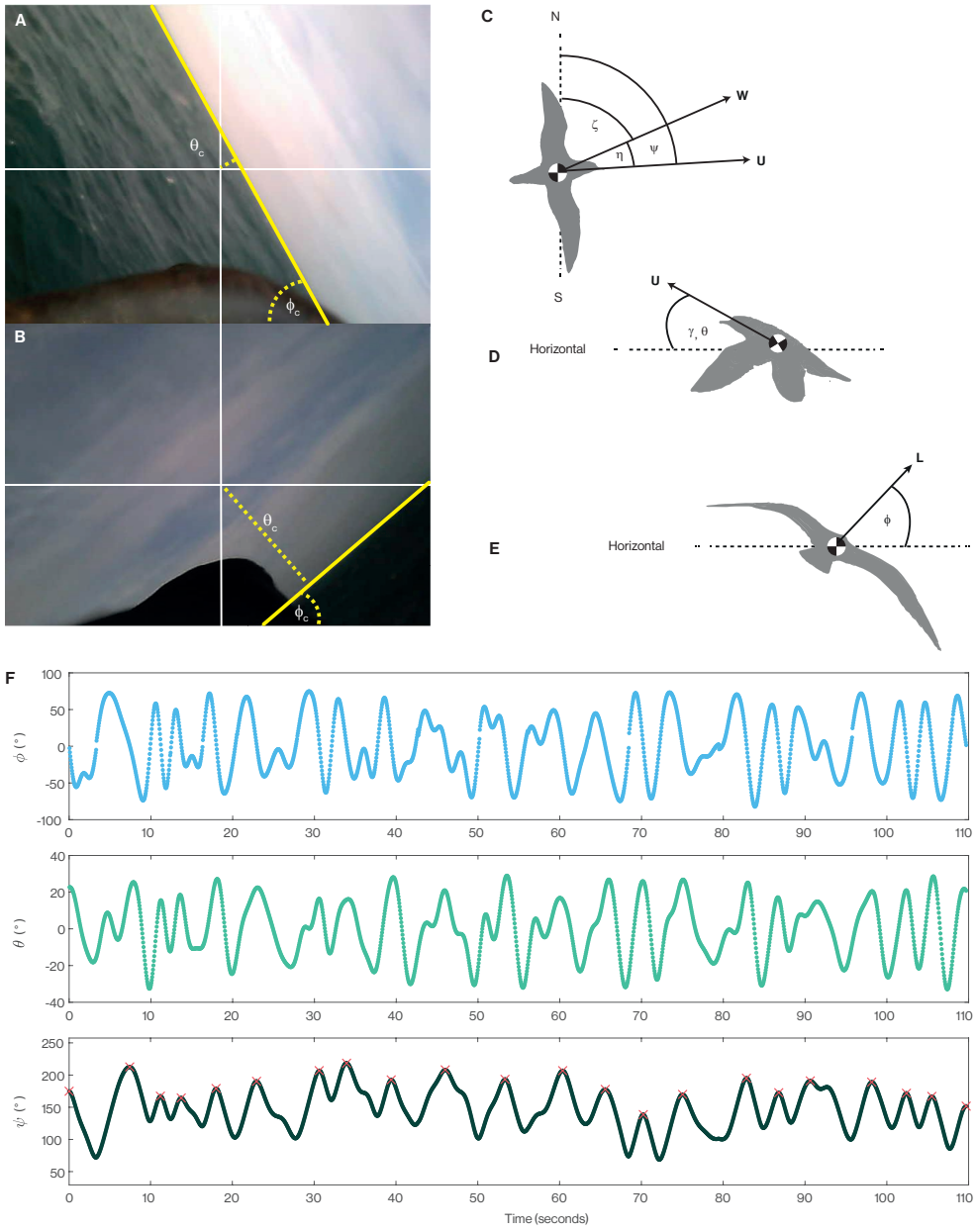


Figure 2.2: Reconstruction of cyclical turning behavior using bird-borne video. **(A,B)** Video from a camera mounted on the back of a Manx Shearwater demonstrates alternating left (A) and right (B) banked turns, coupled with cyclical pitching. The camera bank angle (ϕ_c) is measured as the angle of the horizon line, which we detect automatically (yellow line); the camera pitch angle (θ_c) is measured as the angular distance of the detected horizon line from the image centre (crosshairs); see Materials and Methods. **(C-E)** Angle definitions, shown in three orthogonal views. Overhead view (C): the bird's heading-to-wind angle (η) is defined as the angle between the horizontal wind vector (**W**) and the bird's air velocity vector (**U**) in horizontal projection; this angle η is assumed to equal the angular difference between the bird's yaw angle (ψ) and the wind's azimuth (ζ). Lateral view (D): the bird's flight path angle (γ) is defined as the elevation of **U** with respect to the horizontal; this angle is assumed to equal the bird's pitch angle (θ), which defines the inclination of the lift vector **L** in the bird's symmetry plane. Caudal view (E): the bird's bank angle (ϕ) defines the inclination of **L** in the bird's transverse plane. **(F)** Sample time histories of the estimated bank (ϕ), pitch (θ) and yaw (ψ) angles for flight b117ii-753. Red crosses denote peaks in ψ, corresponding to points where the sign of ϕ changes; these points are used to define the beginning and end of each turning cycle.

maximize the energy they harvest on days with little wind. On such days, there is no prior reason to expect the mean wind effectiveness to be significantly different from zero, which is the null expectation if the bird phases the ascent-descent sequence described by $\gamma(t)$ at random with respect to the pattern of horizontal turning described by $\eta(t)$ (see Eq. 2.3). Conversely, under extremely windy conditions like those exploited by albatrosses flying in the Southern Ocean, it may be possible to harvest more energy than is lost to drag, or than is desirable. Hence, whilst we should certainly expect the mean wind effectiveness to be positive under such favourable conditions, we should not necessarily expect it to be maximized outright, given that such maximization may harvest too much kinetic energy and that this excess kinetic energy cannot be converted to gravitational potential energy when flying close to the surface. In fact, energy harvesting is most likely to be maximized under marginally favourable conditions, when the returns available from dynamic soaring are sufficient to merit deviating from the desired direction of progress, but insufficient to enable flight to be sustained without flapping. These are precisely the conditions that we hypothesise will hold for Manx Shearwaters using flap-gliding flight on windy days.

2.4 Results

Our bird-borne video data (Figure 2.2) show the weaving, undulatory, flap-gliding flight behavior that is characteristic of shearwaters (Spivey et al., 2014). This is evidenced by the cyclical rolling and pitching of the visible horizon (Figure 2.2A,B), upon which are superimposed occasional faster oscillations due to flapping (see Supplementary Movie S1). The weaving component of this behavior is clearly visible in the $n = 9$ horizontal flight trajectories that we reconstructed at a fine scale by using Eq. 2.4 to model the turning associated with the birds' observed rolling and pitching motion (Figure 2.3). Likewise, the coupling of the weaving and undulatory components of this behavior is apparent in the three-dimensional reconstructions (Figure 2.1). This turning behavior occurs on comparatively short timescales (median of mean turning cycle period per flight: 7.0 s), and produces an indirect flight path that must presumably offer some functional benefit to the bird. The reconstructed flight trajectories qualitatively resemble the cyclical trajectories attributed to dynamic soaring in albatrosses (Sachs et al., 2013), and we analyse their suitability for harvesting energy from the shear layer quantitatively below. Nevertheless, as the shearwaters usually flapped their wings as they transitioned from ascending to

descending flight, and as they were sometimes observed flapping at other points in the cycle, such energy as they harvested from the shear layer cannot have been sufficient to offset their drag losses completely. This fine-scale flight behavior is not directly observable in the coarse trajectories that we sampled at 5-minute intervals using GPS loggers, but it is reasonable to assume that the birds would have behaved similarly on these $n = 368$ flights, so we analyse the opportunity that these flights would have provided for dynamic soaring below.

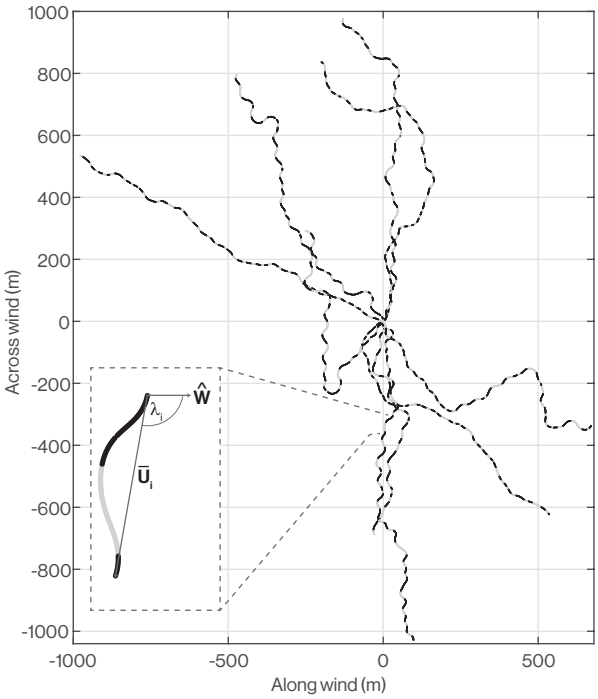


Figure 2.3: Weaving flight of Manx Shearwaters. All $n = 6$ individual Manx Shearwaters that we sampled at fine-scale consistently undertook weaving flight. We reconstructed their $n = 9$ trajectories shown here by using our estimates of the bird's pitch, bank and assumed airspeed to estimate the bird's air relative flight velocity vector $\mathbf{U}$, which we integrated numerically using trapezoidal integration for the purposes of visualisation. Here, these air-relative trajectories are expressed in a coordinate system aligned with the experienced wind direction, such that the overall direction of each flight on the graph indicates the extent to which the bird heads with, against, or across the wind. The angle between the average air velocity vector $\overline{\mathbf{U}}_i$ of cycle i and the wind velocity unit vector $\hat{\mathbf{W}}$ we call λ_i, and we use this for computing the mean wind opportunity metric $\bar{\omega}$ in section 2.4. Each trajectory has been projected into the horizontal plane and sections of ascent are shown in black, while sections of descent are shown in grey.

The weaving flight of shearwaters implements dynamic soaring The sample mean horizontal wind effectiveness $\hat{\bar{\epsilon}}_h$ was positive on all $n = 9$ fine-scale flight trajectories that we collected from $N = 6$ individuals (sign test: $p = 0.004$, $n = 9$; median $\hat{\bar{\epsilon}}_h = 0.167$; bootstrapped 95% CI: 0.042, 0.272). These data comprise a total of 17,457 video frames corresponding to approximately 873 s of flight data, with each recording lasting between 89

s and 114 s. This positive mean horizontal wind effectiveness indicates that the shearwaters flew in a manner expected to harvest energy from the shear layer, but how effectively were their trajectories optimized for dynamic soaring?

To answer this question, it will prove convenient to decompose the mean horizontal wind effectiveness $\bar{\epsilon}_h$ as:

$$\bar{\epsilon}_h = f_R \overline{\|\cos\eta\|}_R - f_{R'} \overline{\|\cos\eta\|}_{R'} \tag{2.5}$$

where f_R represents the frequency with which the Rayleigh conditions are met (i.e. the proportion of frames on which $\epsilon_h > 0$) and $f_{R'} = 1 - f_R$ represents the frequency with which they are not met (i.e. the proportion of frames on which $\epsilon_h \leq 0$). Implicitly, $\overline{\|\cos\eta\|}_R$ and $\overline{\|\cos\eta\|}_{R'}$ denote the mean magnitude of $\cos\eta$ over the corresponding portions of flight. This decomposition emphasises: (i) that the mean horizontal wind effectiveness $\bar{\epsilon}_h$ of a given pattern of turning behavior becomes maximal as $f_R \to 1$, which entails phasing the ascent-descent sequence to meet the Rayleigh conditions; and (ii) that the maximal value of the mean horizontal wind effectiveness is further constrained by the time history of the bird's horizontal flight direction with respect to the wind, because $\bar{\epsilon}_h \to \overline{|\cos\eta|}_R$ as $f_R \to 1$. We will examine these two influences separately, first by assessing the optimality of the observed ascent-descent sequence conditional upon the observed horizontal trajectory, before then assessing the optimality of the observed horizontal trajectory in relation to the observed wind direction.

Shearwaters phase their vertical and horizontal trajectories for dynamic soaring We first compare the sample mean horizontal wind effectiveness $\hat{\bar{\epsilon}}_h$ on each trajectory with the distribution of possible values of $\bar{\epsilon}_h$ given counterfactual phasing of the same ascent-descent sequence. In other words, we compute the distribution of $\bar{\epsilon}_h(\tau)$ by holding the time history of the observed heading-to-wind angle $\eta(t)$ fixed, while time-shifting the aerodynamic flight path angle $\gamma(t)$ by an amount τ such that:

$$f_R = \frac{1}{T}\sum_{t=0}^{T} H\Big[-\operatorname{sgn}\Big(\gamma(t-\tau)\Big)\operatorname{sgn}\Big(\cos\eta(t)\Big)\Big] \tag{2.6}$$

where H is the Heaviside function, which returns $H(x) = 0$ for $x \leq 0$ and $H(x) = 1$ for $x > 0$. Likewise, we have:

$$\overline{\|\cos\eta\|}_R = \frac{1}{f_R T}\sum_{t=0}^{T} H\Big[-\operatorname{sgn}\Big(\gamma(t-\tau)\Big)\operatorname{sgn}\Big(\cos\eta(t)\Big)\Big]\|\cos\eta(t)\| \tag{2.7}$$

$$\overline{\|\cos\eta\|}_{R'} = \frac{1}{f_{R'} T}\sum_{t=0}^{T} \Big(1 - H\Big[-\operatorname{sgn}\Big(\gamma(t-\tau)\Big)\operatorname{sgn}\Big(\cos\eta(t)\Big)\Big]\Big)\|\cos\eta(t)\| \tag{2.8}$$

with $f_{R'} = 1 - f_R$. Evaluating f_R, $f_{R'}$, $\overline{\|\cos\eta\|}_R$ and $\overline{\|\cos\eta\|}_{R'}$ for different time shifts τ and substituting these into Eq. 2.5 generates the desired distribution of $\bar{\epsilon}_h(\tau)$, and recovers the observed value $\hat{\bar{\epsilon}}_h$ when $\tau = 0$. Note that we wrap the time history of each flight when computing these quantities, such that the number of time points that we evaluate is the same for all values of τ. If the birds' ascent-descent sequences were appropriately synchronised with their horizontal flight trajectories, then we would naturally expect $\bar{\epsilon}_h(\tau)$ to peak at $\tau \approx 0$. This was true of the ascent-descent sequences that we observed on all 9 flights (Figure 2.4), each of which was timed to within ± 0.4 s of the optimum, with a median phase shift of $-7°$ relative to the period of a complete turning cycle (1st, 3rd quartiles: $-8°$, $11°$). Moreover, the sample mean horizontal wind effectiveness $\hat{\bar{\epsilon}}_h$ was usually close to the peak value of $\bar{\epsilon}_h(\tau)$, at a median value of 98.4% of the maximum (1st, 3rd quartiles: 94.6, 99.1%). These results demonstrate that the birds synchronised their ascent-descent sequences with their horizontal flight trajectories so as to harvest energy from the shear layer.

This conclusion is based on holding the ascent-descent sequence fixed while varying its timing with respect to the observed horizontal flight trajectory. This is analogous to finding that a piano score harmonizes most closely when its bass and treble clef lines are correctly aligned, which provides evidence that they were jointly composed. To assess whether the ascent-descent sequence is not only well synchronised with the horizontal flight trajectory, but also globally optimal, we therefore evaluate the maximum possible value that $\bar{\epsilon}_h$ could have taken for each horizontal flight trajectory, by finding the optimal permutation of the observed ascent-descent sequence. That is, we find the global optimum $\bar{\epsilon}_{h^*}$, by permuting the observations of $\operatorname{sgn}(\gamma)(t)$ so as to: (i) maximize f_R at $f_R = f_{R^*}$; and (ii) maximize $\overline{\|\cos\eta\|}_R$ given $f_R = f_{R^*}$. This analysis showed that the sample mean horizontal wind effectiveness $\hat{\bar{\epsilon}}_h$ was considerably lower than the global optimum, at a median value of 40.5% of $\bar{\epsilon}_{h^*}$ (1st, 3rd quartiles: 16.2, 59.2%)). We therefore find no evidence that the observed ascent-descent sequence was itself optimal, although it is worth noting that the strength of this conclusion depends on the fidelity of the modelled flight

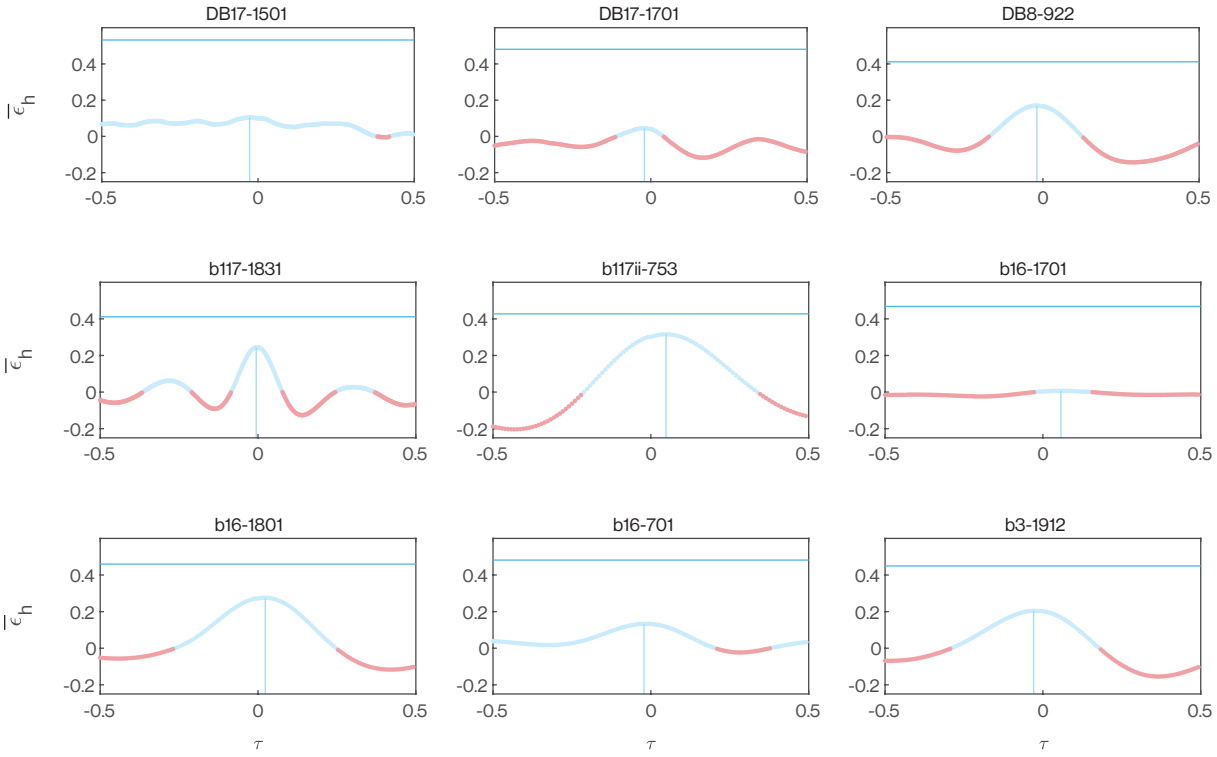


Figure 2.4: Optimization of the phasing of the vertical and horizontal components of each flight. Each panel plots the distribution of mean horizontal wind effectiveness $\bar{\epsilon}_h(\tau)$ computed by holding the horizontal component of one of the $n = 9$ fine-scale flight trajectories fixed whilst varying the phasing of its vertical component by applying a time shift τ. Here $-0.5 \leq \tau \leq 0.5$, where τ is expressed relative to the mean period of one turning cycle. Positive values of $\bar{\epsilon}_h(\tau)$ are shown in blue; negative values in red. The vertical blue line denotes the maximum value of $\bar{\epsilon}_h(\tau)$ for each distribution and its associated value of τ, from which it is clear that the sample mean horizontal wind effectiveness $\hat{\bar{\epsilon}}_h = \bar{\epsilon}_h(0)$ is close to the maximum $\bar{\epsilon}_h(\tau)$ for each trajectory. The horizontal blue line plots the global optimum $\bar{\epsilon}_{h^*}$ obtained by permuting the sequence of ascent and descent to maximize $\bar{\epsilon}$, which is always substantially higher than the maximum $\bar{\epsilon}_h(\tau)$ obtained by phase-shifting the ascent-descent sequence. See text for discussion.

trajectory and assumed wind, and that there is no guarantee that any globally-optimal sequence of ascent and descent would have been physically achievable.

In principle, any sub-optimality of the observed ascent-descent sequence reflects the possibility of reordering it so as to: (i) meet the Rayleigh conditions more frequently; or (ii) meet the Rayleigh conditions at times when the horizontal flight direction was more effective for energy harvesting. To test between these alternatives, we compute a constrained global optimum $\bar{\epsilon}_{h^{*\prime}}$, by permuting the observed sequence of $\mathrm{sgn}(\gamma(t))$ so as to: (i) hold f_R fixed at $f_R = \hat{f}_R$, where $\hat{f}_R$ is the observed value of f_R; and (ii) maximize $\overline{\|\cos\eta\|}_R$ given that $f_R = \hat{f}_R$. This analysis showed that the sample mean horizontal wind effectiveness $\hat{\bar{\epsilon}}_h$ was considerably lower even than the constrained global optimum, at a median value of 56.6% of $\bar{\epsilon}_{h^{*\prime}}$ (1st, 3rd quartiles: 41.2, 74.9%), despite the Rayleigh

conditions still being met with the same frequency $f_R = \hat{f}_R$. This result demonstrates that the sub-optimality of the observed ascent-descent sequences was primarily attributable to the Rayleigh conditions not being met at the most opportune points in the flight, and only secondarily to the frequency with which they were met. This is consistent with our earlier conclusion that the observed ascent-descent sequences were synchronised with the horizontal flight trajectories so as to harvest energy from the shear layer, but suggests that there might have been some room for improvement, subject to the earlier caveats on the fidelity of the modelled flight trajectory, assumed wind, and physical achievability.

Shearwaters optimize their flight trajectories for dynamic soaring in a strong crosswind The analysis so far has explored the optimization of the observed vertical sequence of ascent and descent conditional upon the observed horizontal flight trajectory. Theory predicts that a bird will maximize the energy it can harvest from the shear layer by either flying in a circular loitering pattern or, where constrained to make useful progress over the sea's surface, heading in a net crosswind direction (Sachs, 2004; Liu, 2017; Richardson, 2011; Lissaman, 2005). That energy harvesting is maximized in a net crosswind direction is a natural consequence of the Rayleigh conditions, which state that energy is gained by ascending into the wind and descending with the wind, but lost if this phasing is reversed. Hence, because a bird must on average lose as much height as it gains to remain within the shear layer, any net progress parallel to the wind introduces an asymmetry that reduces the opportunity for energy harvesting. A bird may therefore increase the energy that it can harvest from the shear layer by biasing its flight direction to head across the wind on each cycle. We quantify this by defining the wind opportunity for the ith cycle as $\omega_i = \|\sin \lambda_i\|$ where λ_i is the angle between the bird's mean air velocity vector over that cycle $\overline{\mathbf{U}}_i$ and the wind velocity unit vector $\hat{\mathbf{W}}$ (Figure 2.3). In principle, a flight trajectory that heads across the wind on every cycle has a mean wind opportunity of $\bar{\omega} = 1$, whereas a trajectory that heads into or against the wind on every cycle has a mean wind opportunity of $\bar{\omega} = 0$. In practice, a value $0 < \bar{\omega} < 1$ is expected if the bird changes its net heading across cycles.

To assess how the horizontal flight trajectories were optimized in relation to the observed wind direction, we compare the sample mean horizontal wind effectiveness $\hat{\bar{\epsilon}}_h$ for each trajectory with the corresponding distribution of possible values of $\bar{\epsilon}_h$ given counterfactual wind directions ζ. Specifically, we compute $\bar{\epsilon}_h(\zeta)$ for each flight by holding the time history

of the bird's observed yaw angle $\psi(t)$ fixed, whilst varying ζ in 1° steps around the compass. This operation implicitly varies the mean wind opportunity $\bar{\omega}$ for each flight, which we use to assess the joint distribution of $\bar{\epsilon}_h(\zeta)$ and $\bar{\omega}(\zeta)$. The resulting plots of $\bar{\epsilon}_h(\zeta)$ against $\bar{\omega}(\zeta)$ typically have a symmetric, scissor-like form comprising two looped arms (Figure 2.5). The symmetry of these plots reflects the fact that reversing the wind direction reverses the flow of energy, whereas the looped shape of each arm reflects the asymmetry of the birds' turning cycles (Figure 2.3). In most cases, the maximum value of the wind opportunity $\bar{\omega}(\zeta)$ for any wind direction ζ was close to, but less than, one. This reflects the fact that the birds' cyclical turning behavior was superimposed on a longer-term change in overall flight direction. Nevertheless, as we now show, the scissor-plots in Figure 2.5 provide clear evidence that the birds optimized their horizontal turning cycle for dynamic soaring on flights with higher crosswind components $\hat{\bar{\omega}}W$. Conversely, on days when the crosswind component $\hat{\bar{\omega}}W$ was lower, there is no clear evidence that the horizontal turning cycle was optimized for dynamic soaring—albeit that the vertical sequence of ascent and descent was still timed appropriately to gain rather than lose energy from the shear layer.

The proper phasing of the vertical sequence of ascent and descent to meet the Rayleigh conditions is evident from the fact that the observed point $\left(\hat{\bar{\omega}}, \hat{\bar{\epsilon}}_h\right)$ always lies on the upper arm of the scissor-plot, for which $\hat{\bar{\epsilon}}_h > 0$ (Figure 2.5). Flights for which there is evidence that the detailed horizontal flight trajectory is itself optimized for dynamic soaring are those in which both of the following two conditions are satisfied. First, the maximum value of $\bar{\epsilon}_h(\zeta)$ should coincide with a maximum of $\bar{\omega}(\zeta)$. This implies that the turning cycle is tuned to harvest energy most effectively when the overall flight direction relative to the wind offers the most opportunity for energy harvesting. Second, the observed point $\left(\hat{\bar{\omega}}, \hat{\bar{\epsilon}}_h\right)$ should be located at or close to the joint maximum of $\bar{\epsilon}_h(\zeta)$ and $\bar{\omega}(\zeta)$. This implies that the observed flight trajectory has the greatest potential for harvesting energy when the wind direction is the same as was observed. These conditions hold for the 5 flights falling in the upper 50th percentile for the crosswind component $\hat{\bar{\omega}}W$ (panels **C-E**, **G**, and **I** of Figure 2.5), which are those offering the greatest potential returns from dynamic soaring. Conversely, these conditions do not hold on the 4 flights with crosswind components below the 50th percentile (panels **A-B**, **F**, and **H** of Figure 2.5). This may imply that, when the crosswind component $\hat{\bar{\omega}}W$ is small, birds tune their horizontal flight trajectories by prioritizing flight objectives other than harvesting energy by dynamic soaring. For

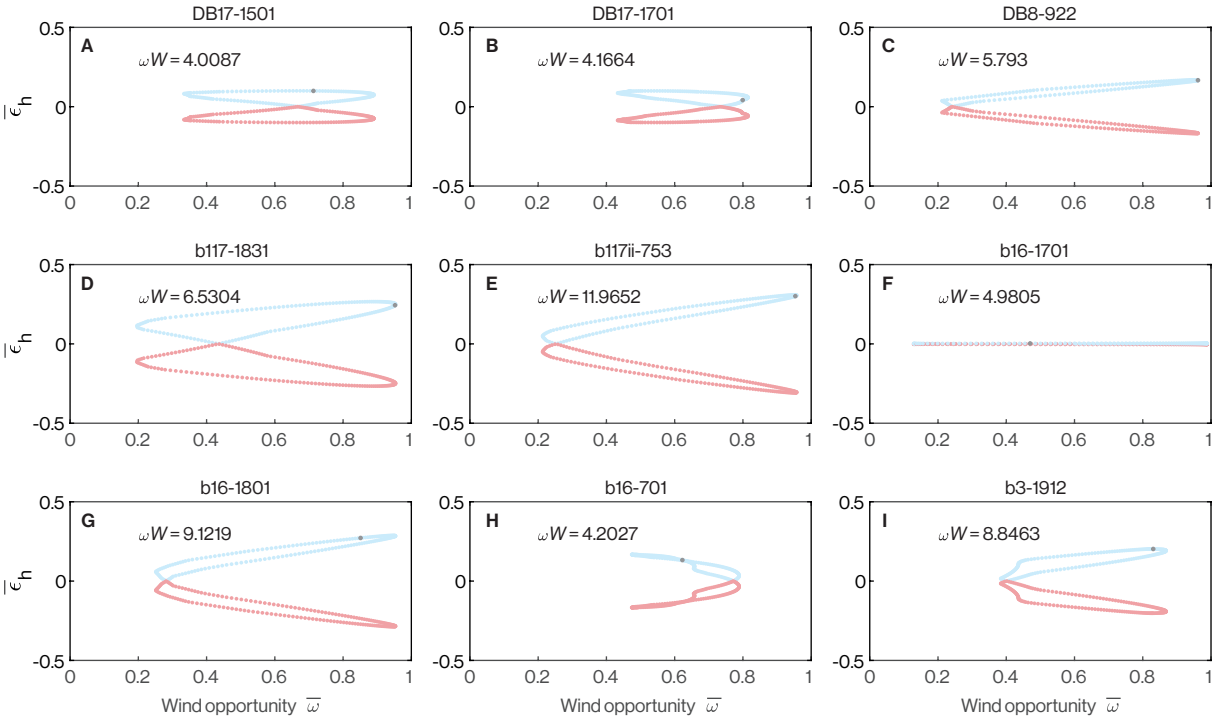


Figure 2.5: Optimization of horizontal flight trajectories with respect to the wind. Each panel plots the distribution of mean horizontal wind effectiveness $\bar{\epsilon}_h(\zeta)$ computed by holding the horizontal and vertical components of one of the $n = 9$ fine-scale flight trajectories fixed whilst varying the assumed wind direction ζ. Both the mean horizontal wind effectiveness $\bar{\epsilon}_h$ and the mean wind opportunity $\bar{\omega}$ vary as the wind direction ζ varies, and plots of $\bar{\epsilon}_h$ against $\bar{\omega}$ have a scissor-like form in most cases. Positive values of $\bar{\epsilon}_h$ are shown in blue; negative values in red. The grey points mark the observed mean horizontal wind effectiveness $\hat{\bar{\epsilon}}_h$ and observed mean wind opportunity $\hat{\bar{\omega}}W$. See text for discussion.

example, our assumption of a steady, horizontal wind field is an idealization, and birds might prioritize flight that harvests energy from vertical wind components such as wave generated updrafts. In summary, the birds only turned in a manner that was tuned to capitalize on the opportunity for dynamic soaring on days when the potential return was high, albeit that they always phased their vertical sequence of ascent and descent to gain rather than lose energy from the shear layer.

Shearwaters bias outbound flight in a crosswind direction favouring dynamic soaring Given the strong association observed between mean horizontal wind effectiveness $\bar{\epsilon}_h$ and mean crosswind component $\bar{\omega}W$ at fine spatiotemporal scales (Figure 2.6C), it is reasonable to expect that Manx Shearwaters might benefit from biasing the heading of their foraging flights across the wind, with possible implications for their large-scale distribution at sea. Depending on the locations of available foraging grounds, crosswind flight may not be possible in all winds on the outbound leg of a flight, and will be even

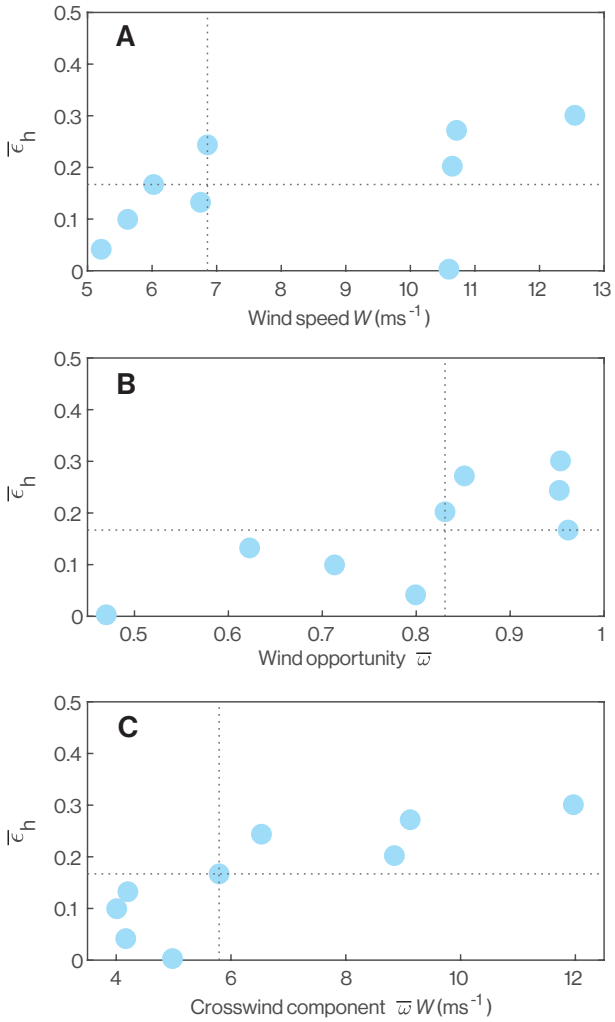


Figure 2.6: Influence of the wind on the effectiveness of dynamic soaring. Each datapoint represents one of the $n = 9$ fine-scale flight trajectories, and plots how the observed mean horizontal wind effectiveness $\bar{\epsilon}_h$ varies as a function of the wind and its interaction with the bird's overall direction of flight. Wind speed W is treated as constant within a trajectory. The mean wind opportunity $\bar{\omega}$ is the average of $\|\sin\lambda_i\|$ over a trajectory where λ_i is the angle between **W** and the bird's average heading over the ith cycle. The crosswind component $\bar{\omega}W$ is the product of the wind speed W and mean wind opportunity $\bar{\omega}$. Vertical and horizontal dashed lines plot the median values of each variable. See text for discussion.

more tightly constrained on the return leg by the unique direction to home. Indeed, pure crosswind flight is impossible to achieve on both the outbound and return legs of a flight, because directing the air velocity vector **U** perpendicular to the wind **W** on the outbound leg will generate a downwind drift requiring correction on the return leg. We might, therefore, expect to see a preference for crosswind flight directions on the outbound legs of foraging trips, which we test here against data from $n = 368$ outbound and $n = 368$ return tracks collected using GPS loggers attached to $N = 201$ individuals from 2016-2019 (Figure 2.7). Note that of the $n = 368$ tracks that we analyse for each direction of flight, 349 comprise the outbound and return legs of the same flights; the

remaining 19 outbound and 19 return flights are not from matched samples. Also note that since departure times in Manx Shearwaters are staggered throughout the night, and shearwaters are not thought to fly in at-sea formations (Guilford et al., 2008; Padget et al., 2019), we assume that birds do not influence the orientation decisions of other birds and hence that each track is an independent data point.

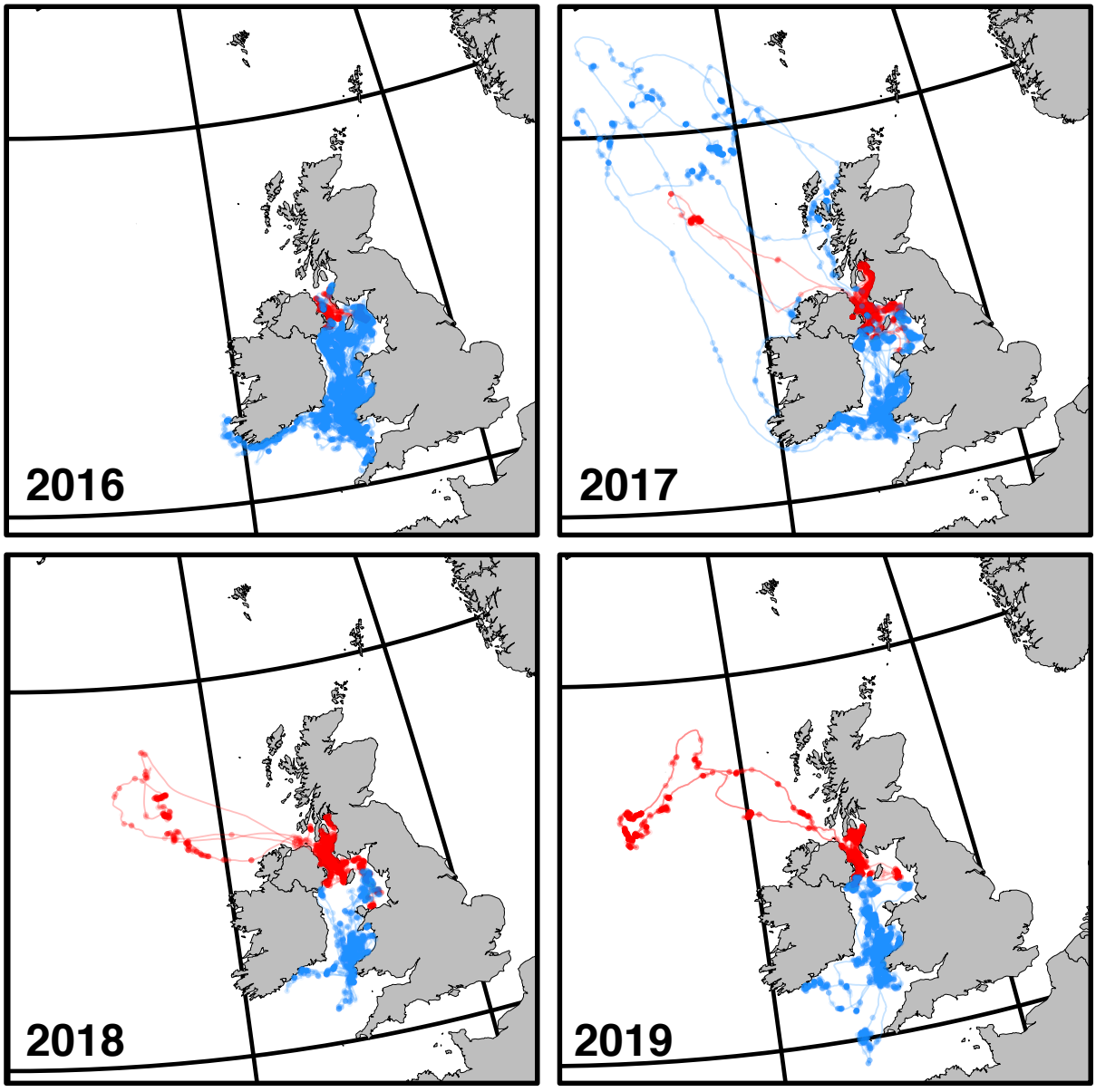


Figure 2.7: At-sea distribution of Manx Shearwaters. Coarse GPS trajectories show $n = 368$ flight tracks from colonies in Northern Ireland (Copeland; red) and southwest Wales (Skomer and Skokholm; blue) recorded from 2016-19. GPS fixes during feeding behavior are highlighted with translucent points (note that when there are multiple fixes during feeding in a similar area, the points appear more opaque); sections of the track spent in directed flight are shown as connecting lines

We calculated the overall heading-to-wind angle λ for each flight leg as the angle between the bird's mean air velocity vector $\overline{\mathbf{U}}$ over the flight leg and the wind velocity

vector $\mathbf{W}$ (Figure 2.8A). As the benefits of heading in a crosswind direction are independent of whether the wind comes from the left or right, we quantified the variation in the overall heading-to-wind angle by computing the sample standard deviation of $\|\lambda\|$ where λ is defined on the interval $[-180°, 180°]$. We then compared this to the population distribution of the same statistic obtained by randomising 100,000 times the pairings of the sample values of $\overline{\mathbf{U}}$ and $\mathbf{W}$ that we used to calculate λ (Figure 2.8B). In this analysis we used all recorded outbound and return trajectories, meaning we included $n = 368$ outbound and $n = 368$ return trajectories (see Methods). We found that the overall heading-to-wind angle was no more conserved than expected by chance on the return legs of the flights ($n = 368$; $p = 0.26$), but was significantly conserved on the outbound legs ($n = 368$; $p < 0.0001$), albeit that the effect size was quite small (s.d. 50.1° on return legs versus 48.2° on outbound legs). The mean absolute heading-to-wind angle on the outbound legs was 81.3° (± 3.13° 95% CI; Figure 2.8A), which is close to the crosswind tendency predicted to maximize the opportunity for dynamic soaring, but with a tailwind bias of 7° appropriate to provide wind assistance on the outbound leg.

To test how the observed crosswind tendency impacted the potential returns from dynamic soaring, we compared the mean wind opportunity $\bar{\omega} = \|\sin\lambda\|$ between the outbound and return legs of the flights. As expected, the mean wind opportunity $\bar{\omega}$ was significantly higher on the outbound journey for flights on which both legs were represented ($n = 349$; paired Mann-Whitney test; $p = 0.0149$), confirming that the birds' tendency to fly across the wind on their outbound flights increased their potential returns from dynamic soaring (Figure 2.9). Furthermore, $\bar{\omega}$ increased significantly with wind speed W on the outbound legs of the flights (Spearman's $\rho = 0.292$; $p < 0.0001$; $n = 368$), but was not significantly associated with wind speed on their return legs (Spearman's $\rho = 0.0508$; $p = 0.331$; $n = 368$). It follows that the birds' tendency to fly across the wind on their outbound flights was stronger on windier days, when the potential returns from dynamic soaring were highest (Figure 2.9). This result could in principle have arisen as an artefact of the prevailing wind coming from a direction promoting crosswind flight. However, we found no evidence that the strongest winds came from a constrained direction when comparing the Rayleigh statistic for the wind directions associated with the top 10% of wind speeds with the population distribution of this statistic after randomising the pairings of wind speed and wind direction ($p = 0.34$). We conclude that the shearwaters' tendency to forage in a

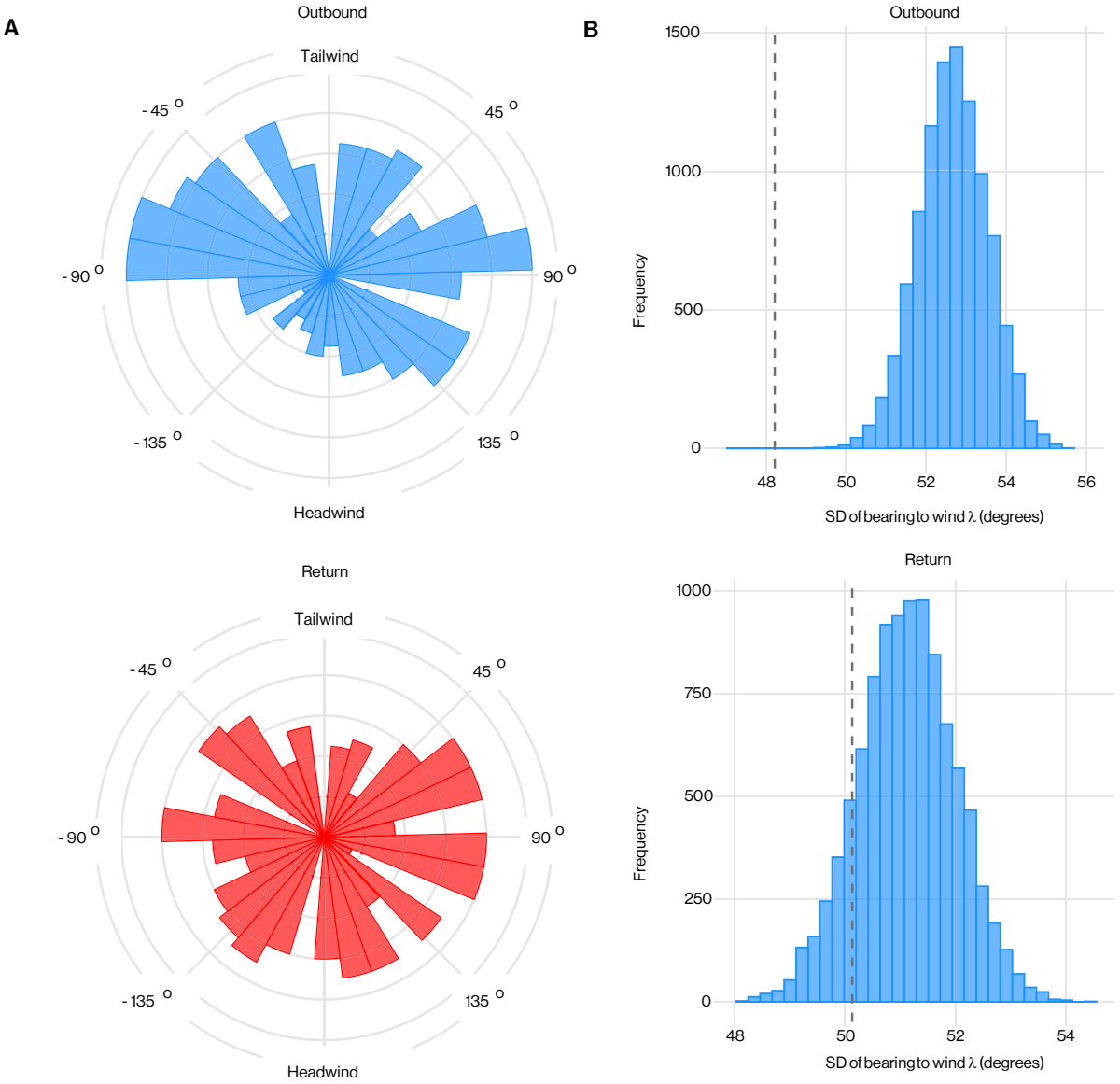


Figure 2.8: Association of wind direction and flight direction in Manx Shearwaters. **(A)** Circular histograms comparing the overall heading-to-wind angle (λ) experienced by shearwaters on outbound (top) and return (bottom) flight. **(B)** Distribution of standard deviation of absolute overall heading-to-wind angle $\|\lambda\|$ computed by randomising the pairings of the sample flight directions and sample wind speeds on outbound (top) and return (bottom) flights; red dashed lines mark sample standard deviations.

more crosswind direction on windier days increases their potential returns from dynamic soaring when conditions are most conducive for harvesting energy from the shear layer.

2.5 Discussion

Here we use bird-borne video loggers to record the fine-scale flight trajectories of flap-gliding Manx Shearwaters, and use GPS loggers to record their coarse-scale movements and distribution at sea. Our data cover spatial scales ranging from less than a metre

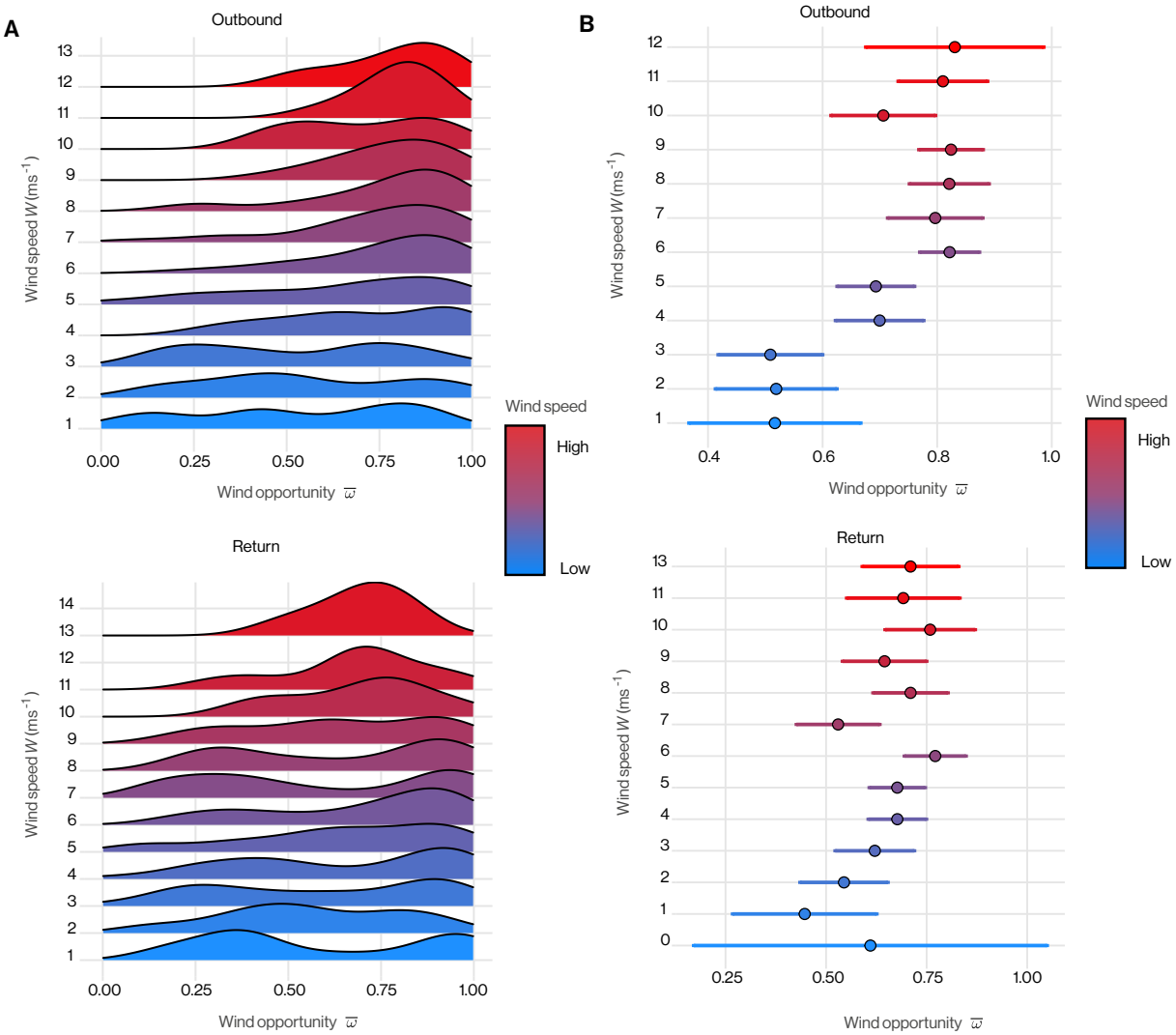


Figure 2.9: Association of wind speed and flight direction in Manx Shearwaters. **(A)** Density curves of mean wind opportunity $\bar{\omega}$ plotted for integer wind speed bins (m s^{-1}). The higher the curve, the greater the density, and hence the more frequently that birds experience that wind opportunity when flying in winds of that speed. **(B)** Mean wind opportunity $\bar{\omega}$ plotted with bootstrapped 95% confidence interval in integer wind speed bins (m s^{-1})

to hundreds of kilometres, and time scales ranging from less than a second to several days. We find that the shearwaters flew trajectories optimized for dynamic soaring, and that they harvested energy from the shear layer more effectively with increasing wind speed. Furthermore, we find that on outbound flights when their destination was less constrained, Manx Shearwaters increased the crosswind component of their flight trajectory to maximize the opportunity for energy harvesting, and did so to a greater extent when the wind speed was higher. We discuss below why such a strategy might be adaptive for these birds, and consider how small-scale flight decisions might influence large-scale feeding distribution at sea.

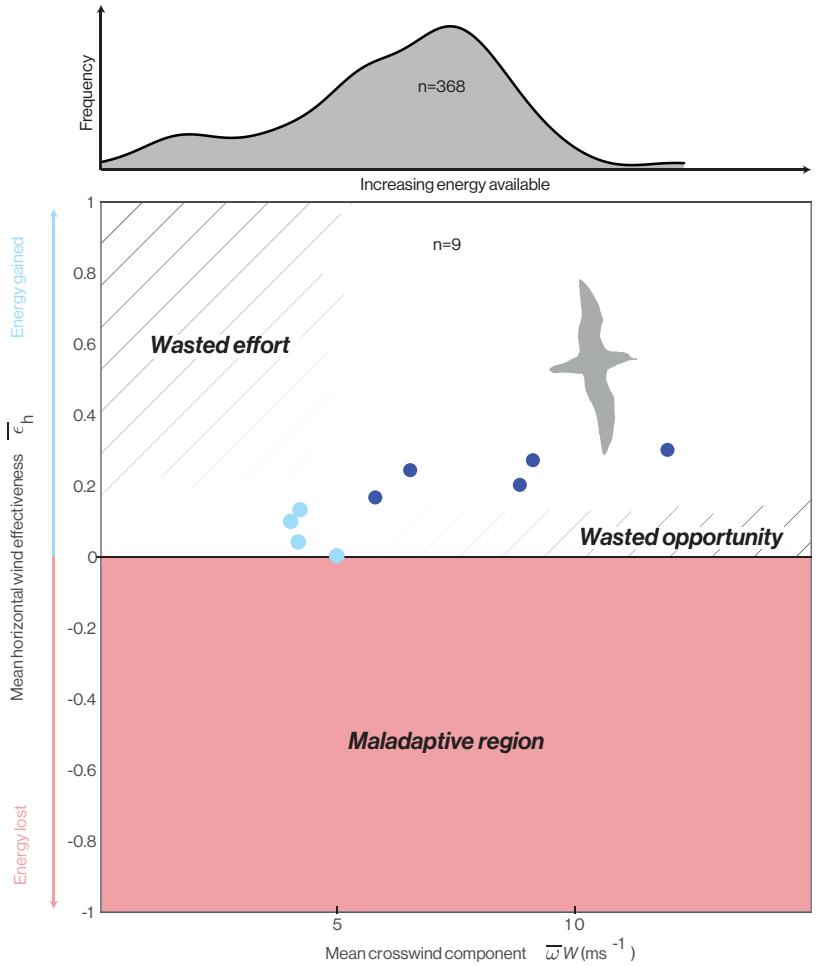


Figure 2.10: Performance space of dynamic soaring. Birds implementing dynamic soaring should fly such that they occupy the white region of the performance space. The pink-shaded area is the region of performance space in which energy is lost to the wind gradient, which is maladaptive in the sense that it is always possible to find alternative ascent-descent sequences that avoid this. Within the upper half of the performance space, trajectories occupying the cross-hatched regions are sub-optimal in the sense that they represent either wasted effort or wasted opportunity. The wasted opportunity region lies to the right hand side of the performance space, as the energy accessible in the wind gradient increases with the mean crosswind component $\bar{\omega}W$. How this bears on our studied shearwaters is illustrated by the histogram at the top of the figure which shows the distribution of mean crosswind component $\bar{\omega}W$ over the $n = 368$ recorded outbound flights. The blue-filled circles plotted in the performance space are the data from Figure 2.6C where those shaded darker correspond to trajectories showing clear evidence of optimization of their horizontal trajectories in relation to the wind (see text for discussion). Note that the range of mean crosswind components over which there is clear evidence of detailed trajectory optimization for dynamic soaring (dark blue) matches the range experienced on the majority of flights (see histogram).

Optimization of dynamic soaring in Manx Shearwaters Pelagic birds harvesting kinetic energy from the shear layer incur an opposing cost because of the weaving and undulating flight trajectory needed to extract energy by dynamic soaring. This increases the path length relative to direct flight, and induces drag through the use of lift to turn (Bousquet et al., 2017). Dynamic soaring behavior therefore represents a trade-off between

maximizing the potential for energy harvesting and minimizing the energy losses due to drag. Assessing both sides of this trade-off is challenging in flap-gliding species because of the difficulty of measuring flight efficiency in a bird using intermittent flapping. We have therefore focused on quantifying how effectively energy is harvested from the shear layer through the mean horizontal wind effectiveness and mean wind opportunity metrics that we have defined. We represent the associated trade-off diagrammatically in the form of a performance space (Taylor et al., 2014) plotting mean horizontal wind effectiveness $\bar{\epsilon}_h$ against mean crosswind component $\bar{\omega}W$ (Figure 2.10).

The lower half of this performance space (i.e. $\bar{\epsilon}_h < 0$) is unambiguously maladaptive, because flight in this region of the graph actively loses energy to the wind gradient (pink shaded region in Figure 2.10). Indeed, the shearwaters avoided this region of the graph on all $n = 9$ trajectories that we recorded at a fine scale (blue points in Figure 2.10). This region of the performance space represents a hazard for any bird ascending or descending through a shear layer, and we call this outcome maladaptive because it should always be possible to avoid. Specifically, for any horizontal trajectory, there will always exist corresponding ascent-descent sequences for which $\bar{\epsilon}_h \geq 0$. Unless there is some countervailing reason to ascend or descend, these should always be adopted in favour of ascent-descent sequences for which $\bar{\epsilon}_h < 0$. The reality of this hazard is demonstrated by the pink-shaded portions of Figures 2.4 and 2.5, which show how the same horizontal trajectory can be maladaptive given counterfactual phasing of its ascent-descent sequence or a counterfactual wind direction. Conversely, even the four flight trajectories experiencing the lowest mean crosswind component $\hat{\bar{\omega}}W$, and hence the least opportunity for energy harvesting, achieved $\bar{\epsilon}_h > 0$ (Figure 2.10). The birds therefore avoided the small energy losses to the wind gradient that they would have experienced had they adopted poorly phased counterfactual ascent-descent sequences.

The upper half of the performance space (i.e. $\bar{\epsilon}_h > 0$) represents the region of the graph in which energy is actively harvested from the shear layer. However, because of the trade-off that exists between harvesting energy from the shear layer and losing energy to drag in the process, it is not equally beneficial to occupy all regions of this upper half of the performance space (Figure 2.10). Specifically, when the mean crosswind component of the trajectory $\hat{\bar{\omega}}W$ is low— whether because of low wind speed W, an unfavourable flight direction resulting in a low mean wind opportunity $\bar{\omega}$, or both—there will be little

energy accessible to harvest in the wind gradient. Increasing path tortuosity to maximize the effectiveness with which this little energy is harvested (i.e. maximizing $\bar{\epsilon}_h$) will not then yield appreciable increases in energy harvesting but will incur appreciable costs. The corresponding portion of the graph is therefore labelled 'wasted effort', referring to the crosshatched region in the top left of the performance space (Figure 2.10). The portion of the performance space labelled 'wasted opportunity' on the right hand side of the graph also represents a sub-optimal execution of the trade-off. In this region of the graph, the mean crosswind component $\bar{\omega}W$ is high, so there is significant energy accessible to harvest in the wind gradient. Trajectories that do not effectively harvest this significant energy, as indicated by their low mean horizontal wind effectiveness $\bar{\epsilon}_h$, are therefore expected to be sub-optimal.

It is clear from Figure 2.10 that the shearwaters broadly conform to these expectations, avoiding the maladaptive region of the performance space altogether, and showing evidence of avoiding those regions of the performance space in which the most opportunity or effort is wasted. This implies that they synchronise their vertical motion appropriately with their horizontal motion so as to meet the Rayleigh conditions of ascending into the wind and descending with it. Nevertheless, using the fine-scale trajectory data that we derive from our bird-borne video footage, we only find evidence that the birds optimized their detailed horizontal trajectories in relation to the wind during flights on which the mean crosswind component $\bar{\omega}W$ was high (Figure 2.5). These flights, marked as dark blue points in Figure 2.10, are those for which the evidence of dynamic soaring is strongest, so it is noteworthy that their mean crosswind components are in the same range as those recorded on the majority of the outbound flights that we sampled at a coarse scale using GPS (see histogram at top of Figure 2.10). In summary the GPS data show that for most of their outbound flights, the birds flew with a crosswind component that the video data show was associated with detailed trajectory optimization for dynamic soaring.

While the value of the mean crosswind component $\bar{\omega}W$ is obviously limited by the wind speed W served on the day, birds can maximize their mean crosswind component subject to this constraint by heading in a direction that maximizes the mean wind opportunity $\bar{\omega}$. It follows that birds can move around the performance space in Figure 2.10 by making fine adjustments to their fine-scale flight trajectories to optimize their wind effectiveness $\bar{\epsilon}_h$, and by making coarse adjustments to their large-scale flight trajectories to optimize

their mean crosswind component $\bar{\omega}W$ which implicitly alters $\bar{\epsilon}_h$. The performance space in Figure 2.10 thereby captures the effects of both fine and large-scale flight behavior.

Using the very large data set of $n = 368$ outbound flights and $n = 368$ return flights that we obtained using bird-borne GPS loggers, we find evidence that Manx Shearwaters tune their flights at this larger scale, by increasing the mean wind opportunity $\bar{\omega}$ that they experience as wind speed W increases. In other words, shearwaters have a stronger tendency to fly in a crosswind direction on days when the wind is strongest (Figures 2.8), although we only observe this tendency during their outbound flights (Figure 2.9). This likely reflects a higher-level trade-off between adopting flight directions that are better for dynamic soaring and those that are better for other ecological reasons. In particular, flight direction is tightly constrained during homing flight because of the necessity to return to the breeding site to provision offspring. In contrast, constraints on flight direction are more relaxed during outbound flight for which the foraging destination is flexible within reason. It is important to note that the birds' stronger tendency to fly across the wind on windier days could reflect headwind avoidance rather than crosswind selection. Nevertheless, as the effect of this large-scale behavior will be to promote dynamic soaring regardless, and as the birds' fine-scale flight trajectories confirm their use of dynamic soaring, it seems reasonable to view the observed crosswind tendency as an adaptation for dynamic soaring on outbound flights.

How might the optimization of atmospheric energy harvesting impact the foraging distributions at-sea? Manx Shearwaters are known to utilise a dual foraging strategy when rearing (Shoji et al., 2015), alternating between short chick-provisioning trips and longer self-provisioning trips to predictable oceanic resources (Dean et al., 2015). It is therefore possible that, within these constraints, decisions relating to choice of foraging site account for flight directions that increase energy extraction from the prevailing wind. Furthermore, given that the wind observed in the Irish Sea has a strong south-westerly bias, it is possible that the overall feeding distribution of shearwaters is contingent on these prevailing winds as a consequence of their use of dynamic soaring.

We have shown soft boundaries to the sub-optimal regions of the performance space to reflect uncertainty over their actual extent in relation to the performance that we observed in Manx Shearwaters (Figure 2.10). It is reasonable to assume that the performance spaces of other Procellariiformes will look broadly similar, but the upper half of the performance

space might differ in detail for albatrosses, whose higher aspect ratio wings enable them to glide continuously over the windier open oceans. For example, for birds like the Wandering Albatross, we might expect the 'wasted effort' region to be narrower with respect to the mean crosswind component $\bar{\omega}W$. This is because the minimum mean crosswind component $\bar{\omega}W$ needed to fly energy-neutral dynamic soaring cycles is lower at the higher lift-to-drag ratios that higher aspect ratio wings enable (Bower, 2012). Moreover, at very high mean crosswind components, it is plausible that albatrosses might benefit from flying trajectories with reduced mean horizontal wind effectiveness $\bar{\epsilon}_h$ to avoid the very high aerodynamic loads associated with building up surplus kinetic energy.

Implications for sensory physiology and behavior Our finding that shearwaters optimize their fine-scale flight behavior for dynamic soaring might be thought to suggest that they require some sense of wind direction to determine when to transition between ascent and descent. In fact, for flight through a thick shear layer, it has been shown theoretically that optimal dynamic soaring trajectories approach a chain of alternating semi-circular turns (Bousquet et al., 2017). Under these conditions, a simple behavioral rule may suffice for the optimal control of dynamic soaring, because for a bird that spends as much time ascending as descending, transitioning between the two at the extremes of each cycle maximizes the energy gain (or loss) for any wind direction. All that is needed, therefore, is to select the binary phasing of ascent versus descent that makes the mean wind effectiveness positive, which only depends on knowing whether the wind is coming from the left or right of the average heading. The optimal transition points themselves are reached when the bird is heading in the same direction as its average heading, so could be sensed with the aid of any compass or other heading indicator, including a magnetic compass, the sun and its attendant cues, or distant landmarks and clouds (Guilford et al., 2014). A detailed sense of wind direction would of course allow for more precise optimization of any trajectory, and might be possible using ventral optic flow cues under some conditions (Serres et al., 2019). In particular, if the bird's longitudinal axis were aligned with its heading vector as assumed here, then any lateral optic flow must be a consequence of wind drift. Vision may therefore be at least as important for wind sensing in Procellariiformes as their tubular nostrils, which have been suggested to function as pitot tubes sensing airspeed during dynamic soaring (Pennycuick, 2002).

Our camera-based method of reconstructing dynamic soaring trajectories also points to the fact that vision may be useful in controlling the turning flight behavior that we observe. When visible, the horizon offers a reliable means of identifying the vertical direction. This could be particularly useful in the control of pitching and banking during dynamic soaring, given that sensing gravitational acceleration is unreliable when aerodynamic accelerations are superimposed during unsteady manoeuvres. In fact, our horizon sensing algorithm calls to mind the specializations of the visual field in Procellariiformes, which possess a horizontal streak where the retinal ganglion density is higher thereby improving resolving power around the horizon (Hayes et al., 1990). Whilst this has traditionally been explained by the 'terrain hypothesis', which invokes the need for detection of objects against a horizon in open terrain (Hughes, 1977)(Martin, 2017), it may also have a function in flight control (Meyer, 1977). Specifically, by stabilising their head with respect to the fixed horizon, our shearwaters would have had an external reference for roll stabilisation from which, via neck proprioception (Bilo, 1992), the angle of the body relative to the head could be inferred to obtain estimates of bank and pitch. This head stabilisation behavior is clearly visible in the videos (see Supplementary Movie S1). These sensing implications are also of interest for marine unmanned air vehicles (UAVs), given the potential to increase their flight time, range, and efficiency by dynamic soaring.

Limitations The horizontal wind effectiveness metric ϵ_h (Eq. 2.3) does not account for the quantitative effect of the bird's flight path angle (γ) on the rate of energy harvesting. This is captured by the total wind effectiveness metric ϵ (Eq. 2.2), which differs from ϵ_h by a factor of $\sin 2\gamma$. We have chosen to evaluate ϵ_h rather than ϵ here on the pragmatic grounds that while it is usually possible to distinguish unambiguously whether a bird is ascending or descending, accurate quantitative estimates of the flight path angle γ relative to the air are difficult to obtain. Furthermore, the sign of the horizontal wind effectiveness ϵ_h is always the same as the total wind effectiveness ϵ, and evaluating the horizontal wind effectiveness metric ϵ_h partitions out the effects of the horizontal components of the flight trajectory, which are what combine to determine the overall flight direction that we analyse on larger spatiotemporal scales.

The mean horizontal wind effectiveness metric $\bar{\epsilon}_h$ is calculated as the unweighted mean of the horizontal wind effectiveness ϵ_h across a flight trajectory. This is appropriate if a given flight direction is equally good at harvesting energy everywhere in the wind field,

but this only strictly holds for a linear wind profile in which the vertical wind gradient is constant. In contrast, theoretical studies of dynamic soaring have variously assumed linear (Zhao et al., 2004), exponential (Sachs, 2004)(Liu, 2017)(Sukumar et al., 2013)(Deittert et al., 2009), or logarithmic (Sachs, 2004)(Liu, 2017)(Sukumar et al., 2013) models of wind shear. Under the nonlinear wind shear models, the wind gradient σ varies with altitude. For example, a logarithmic wind gradient is steepest just above the sea surface, and becomes shallower with height. In this case, the same flight direction and hence same value of ϵ_h would harvest more energy closer to the sea's surface.

The suitability of the mean horizontal wind effectiveness metric $\bar{\epsilon}_h$ as a measure of how effectively a given flight trajectory harvests energy from the wind gradient therefore depends on the nature of the wind gradient, which is usually unknown. If necessary, the calculation of the mean horizontal wind effectiveness $\bar{\epsilon}_h$ could be adjusted to account for the local wind gradient by taking a weighted mean of the horizontal wind effectiveness ϵ_h with weights that vary as a function of height. This operation requires precise knowledge of vertical position, however, which is difficult to achieve, even with GPS loggers. Hence, even in the presence of a nonlinear wind profile, there is utility calculating the mean horizontal wind effectiveness $\bar{\epsilon}_h$ as we have done here, which only requires a binary assessment of whether the bird is ascending or descending.

Although the mean horizontal wind effectiveness $\bar{\epsilon}_h$ is itself a robust metric for assessing the effectiveness of a flight trajectory at harvesting energy from a vertical wind gradient, evaluating $\bar{\epsilon}_h$ empirically requires accurate estimates of the flight path angle γ and yaw angle ψ. Clearly, the estimates that we have made of the bird's pitch angle θ and bank angle ϕ are subject to measurement error, and although we have attempted to calibrate out any systematic bias in these estimates, our method for doing so is itself subject to model error (see Materials and Methods). Specifically, we derive the following exact expression for the yaw angle rate induced by an unsteady banked turn in a steady horizontal wind field of uniform direction with vertical wind shear σ:

$$\dot{\psi} = \frac{L \sin \phi}{mU \cos \theta} + \sigma \sin \psi \tan \theta. \tag{2.9}$$

This expression is exact, subject to the simplifying assumption that the bird's air velocity vector is always aligned with its longitudinal body axis (see Supplementary Text), which

implies either that the bird is perfectly stable in pitch and yaw or that it coordinates its turning to achieve the same weathercock effect. For the purposes of estimating the bird's yaw angle ψ, we have used the approximate model given in Eq. 2.4, which drops the term $\sigma \sin\psi \tan\theta$ describing the weathercock effect of wind shear. This is done on the basis that we know neither the vertical wind shear strength σ, nor the detailed stability properties of the bird that give rise to this term, but is expected to lead to model error (Taylor et al., 2014) if the assumptions of Eq. 2.9 are satisfied.

Dropping this term is equivalent to assuming that the aerodynamic effect of wind shear on the birds' turning is negligible, which is true when the vertical wind shear σ is weak, when the bird is flying with or against the wind such that $\sin\psi$ is small, or when the bird flies a shallow flight path such that $\tan\theta$ is small. These conditions will not always prevail, resulting in a time-varying error in the estimation of $\dot{\psi}$. This will modify the shape of the weaving trajectories predicted under the model (Figure 2.3), but any changes in curvature will have a second-order effect on our estimates of mean horizontal wind effectiveness ϵ_h compared to any first-order integration error, which we remove by calibrating our estimates of ψ against the position of the sun's disc in the video. In making this correction, we correct for camera bank offset, and we correct separately for camera pitch offset impacting our estimates of the flight path angle γ. Eq. 2.4 further assumes near-constant airspeed $U \approx U_0$, and near-constant lift equal to body weight $L \approx mg$. Our constant airspeed assumption was necessary because we were unable to deploy airspeed sensors simultaneously with bird-borne video cameras given the constraints on carried load (Phillips et al., 2003), but we do not expect this to have much effect on our results because airspeed tends to fall in a narrow range. We also find that any statistical tests reported to be significant at $U_0 = 11.1$ m s^{-1} were also significant for alternative assumed airspeed values from 7.5 to 14.0 m s^{-1}.

There is the possibility that behavioral sampling biases could affect the generality of our findings (Webster et al., 2020). We used breeding birds for both GPS and video analysis so that loggers could be retrieved (Guilford et al., 2008). Since both male and female shearwaters provide the same level of chick-rearing effort (Gillies et al., 2021), it is unlikely our results are sex-biased. However, as breeding birds tends to be older than non-breeding birds, our samples will be age-biased. Given that flight behavior optimization in relation to wind has been suggested to develop through learning (e.g.

(Wynn et al., 2020)), it is therefore possible that our results might not generalize to younger, inexperienced shearwaters.

A quantitative framework for identifying dynamic soaring Although it is widely accepted that Procellariiformes use dynamic soaring (Pennycuick, 1982; Alerstam et al., 1993), and whilst the theory of dynamic soaring is well understood, rigorous empirical demonstrations of its utilisation are few and far between. Indeed, dynamic soaring has only previously been demonstrated conclusively in Wandering albatross (Sachs et al., 2013), having been inferred somewhat indirectly in Manx Shearwaters (Gibb et al., 2017). Demonstrating that a bird is implementing dynamic soaring demands showing that the bird is extracting energy actively from a wind gradient. One characteristic of such behavior is its cyclical variation in mechanical energy (see Introduction), but this is neither necessary nor sufficient to demonstrate dynamic soaring. It is not sufficient as mechanical energy may vary cyclically during other flight modes, such as the undulating intermittent flight of European Starlings (*Sturnus vulgaris*) (Rayner et al., 2001). It is not necessary as mechanical energy variation due to drag losses, static soaring, and flapping (see Supplementary Text) may obscure the energetic signature of dynamic soaring altogether, and this is especially problematic in flap-gliding species such as Manx Shearwater (Gibb et al., 2017). The metric of mean horizontal wind effectiveness $\bar{\epsilon}_h$ that we have derived here overcomes these limitations by assessing directly whether a given flight behavior is expected to harvest energy from the shear layer or to lose energy to it. Most importantly, this assessment is independent of other energy flows, such that it is not prone to masking in the way that an assessment of the changes in total mechanical energy would be.

Other observational studies have found no difference between large and small Procellariiformes in the frequency of flights that contain soaring (Pennycuick, 1982), so our demonstration that Manx Shearwaters fly in a manner adapted to harvest energy from the shear layer suggests that dynamic soaring may be important across a broader range of species and environments than has been demonstrated to date. Demonstrating that the mean horizontal wind effectiveness $\bar{\epsilon}_h$ is consistently positive across flights, as we have shown here for Manx Shearwaters, therefore offers a reliable method for diagnosing dynamic soaring in other candidate flap-gliding Procellariiformes such as the Northern Fulmar (*Fulmarus glacialis*). When studied in combination with the other metrics of mean wind opportunity $\bar{\omega}$ and mean crosswind component $\bar{\omega}W$ that we have derived here, the

quantification of horizontal wind effectiveness also permits a fuller consideration of the optimization of dynamic soaring in these species. Furthermore, it could be applied to groups traditionally unassociated with dynamic soaring but known to glide in regions with strong spatiotemporal wind gradients such as Lesser Black-backed Gulls (*Larus fuscus*) flying in cityscapes (Shepard et al., 2016), or Jackdaws (*Corvus monedula*) flying around ridgelines. Finally, our demonstration of dynamic soaring in coastal environments by a flap-gliding bird will be of interest to those working on marine unmanned aerial vehicles (UAVs). Our results illustrate the possibility of marine UAVs using dynamic soaring to decrease power consumption and thereby increase flight range, time and sustainability during facultatively powered flight in the socially important coastal zone.

2.6 Materials and Methods

The theoretical framework that underpins the analysis described in the main text is derived in the Supplementary Text of Appendix A. The following sections describe the empirical methods used to collect and analyse the field data.

Field observations All work was done under ethical approval from the Animal Welfare and Ethical Review Board of the Department of Zoology, Oxford University, under endorsements from the British Trust for Ornithology Unconventional Methods Panel (BTO permit numbers C/5311 (Tim Guilford) and C/6128 (Oliver Padget)), and following approval by the Islands Conservation Advisory Committee.

We captured 146 bird-borne video recordings from Manx Shearwaters *Puffinus puffinus* during fieldwork undertaken 15–28 August 2014 on Skomer Island, Pembrokeshire ($51.74°N$, $5.30°W$). However, as the behavior of interest for this study was cruising flight, we excluded videos containing take-off, landing, and sea-sitting behavior. Likewise, as the sun was needed to calibrate flight direction (see below), we excluded videos in which the sun's disc was not visible, leaving a sample of $n = 9$ videos from $N = 6$ individuals across 6 different days.

Each video was captured using a miniature video logger (VEHO VCC-003 MUVI^{TM} Micro DV Camcorders) (Rutz et al., 2013) attached to the bird's back using water soluble adhesive and TESA(4651) marine tape (Guilford et al., 2008). A custom-designed, microprocessor-controlled timer was used to record two-minute sections of video once

every hour (640 × 480 pixels; RGB24 AVI format; 20 frames per second). Video loggers were inserted into waterproof heat-shrink plastic tubing (Guilford et al., 2008), in which a small incision was made to enable the head of the camera to be positioned upright pointing forwards. The camera head was inserted into a purpose-built Perspex turret, which was waterproofed and held in place by hot-melt glue. The video loggers weighed 17-18 g including battery, which is approximately 4% of body mass (Spivey et al., 2014; Guilford et al., 2008; Phillips et al., 2003).

Shearwaters were also (not simultaneously) tracked at a coarse-scale using iGotU (Mobile Action, Taiwan) GPS devices (mass = 15g (Phillips et al., 2003)) from colonies on Lighthouse Island (Copeland Archipelago; $n = 164$; 54.70°N, 5.52°W), Skomer island ($n = 211$; 51.74°N, 5.30°W) and Skokholm Island (2016 only; $n = 10$; 51.70°N, 5.30°W) from 2016 to 2019. These $n = 368$ tracks were taken from $N = 201$ birds in total. GPS loggers were set to record speed and position at 5-minute intervals, and were interpolated using a cubic spline function to ensure that the position estimates fell at precise 5-minute intervals (Tremblay, 2006). Tracks up to and including those gathered in 2016 were also analysed and published in (Padget et al., 2019).

Video analysis We estimated the camera pitch angle (θ_c) and camera bank angle (ϕ_c) directly from the video footage by writing an automatic horizon detection algorithm in MATLAB (The Mathworks Inc, Natick, MA). The algorithm squares the intensity of the blue channel to obtain a high-contrast grayscale image, to which it applies a Gaussian smoothing kernel with $\sigma = 8$. The algorithm then uses Roberts edge detection to find and mask the outline of the bird, and uses the Hough Transform to detect straight lines outside of this mask. The longest straight line is then taken as the putative horizon (Supplementary Movie S2). We checked all putative horizon lines manually and edited these where necessary to correct any errors (Supplementary Movie S3). The frame was skipped if no horizon line was visible.

We estimated the camera bank angle as $\phi_c = -\arctan(\Delta y/\Delta x)$, where Δx and Δy denote the differences in the image coordinates of the horizon endpoints. Likewise, we estimated the camera pitch angle as $\theta_c = s \times 72/640$, where s is the signed distance in pixels between the horizon line and the midpoint of the image, assuming an equiangular projection model over the measured 72° field of view. We interpolated ϕ_c and θ_c for

skipped frames using a piecewise cubic Hermite interpolating polynomial, and forwards-backwards filtered the signals using a fifth order low-pass Butterworth filter at a cut-off frequency of 0.5 Hz to remove high frequency noise due to measurement error, flapping perturbations, and other camera motion.

The measured pitch angle θ_c and measured bank angle ϕ_c of the camera differ from the true pitch angle θ and true bank angle ϕ of the bird because of camera offset and measurement error. We therefore estimate the bird's pitch angle as $\hat{\theta} = \theta_c - \delta_\theta$, having calibrated the pitch offset δ_θ by enforcing the constraint that $\hat{\theta}$ should average zero over the entire flight. This is justified on the basis that the vertical component of the bird's motion $U \sin\theta$ must average zero for it to remain close to the surface in a horizontal wind field, such that $\sin\theta$ must also average zero if the airspeed U remains approximately constant as assumed.

We estimate the bird's bank angle as $\hat{\phi} = \phi_c - \delta_\phi$, and calibrate out any bank offset δ_ϕ by integrating Eq. 2.4 numerically, having replaced θ and ϕ with their estimates $\hat{\theta} = \theta_c - \delta_\theta$ and $\hat{\phi} = \phi_c - \delta_\phi$. We estimated the bank offset δ_ϕ in piecewise fashion over a flight, by using the sun's disc or a distant cloud as a reference for estimating the change in the camera's azimuth $\Delta\psi_c$ between calibration frames at times t_1 and t_2, and finding the offset δ_ϕ that would satisfy the integral equation:

$$\int_{t_1}^{t_2} \frac{g \sin(\phi_c - \delta_\phi)}{U_0 \cos(\theta_c - \delta_\theta)}\, dt = \Delta\psi_c. \tag{2.10}$$

We measured the apparent azimuthal position of the sun in each calibration frame by measuring the signed distance d in pixels between lines dropped perpendicular to the horizon from the centre of the image and the sun's disc or distant cloud. We then calculated the apparent change in azimuth $\Delta\psi_c$ between calibration frames at times t_1 and t_2 as $\Delta\psi_c = (d_2 - d_1) \times 72/640$ assuming the same equiangular projection model as before. This use of the sun as a compass serves to remove integration drift on each calibration interval, and also provides an external reference for relating the bird's estimated yaw angle ψ to the wind direction ζ via the solar ephemeris. Specifically, we used the NOAA Solar Calculator to find the sun's azimuth at the known date, time and approximate location of each video recording, from which we were able to calibrate the bird's yaw angle relative to true north.

GPS analysis At-sea behavior was identified using a threshold model (Dean et al., 2015) combining information on the bird's flight speed and the standard deviation of its heading recorded over a rolling window of 6 consecutive points. GPS fixes with a recorded ground speed of $> 7ms^{-1}$ were classified as flight; those with a ground speed of $< 7ms^{-1}$ and a rolling standard deviation in heading of $< 18°$ were classified as rafting; the remainder of points were classified as feeding. GPS fixes were only included in the analysis if they were classified as flight behavior.

The return sections of the GPS tracks were identified by moving backward along the track from the colony until the distance from the colony stopped increasing monotonically with respect to the length of the backward path (Padget et al., 2018). Conversely, the outbound section of the track was identified as the continuous section of the track over which the bird's distance from the colony monotonically increased with total path length. To prevent pseudoreplication in the statistical analyses, the outbound and return sections of each track were summarised as single datapoints, with arithmetic mean values taken for wind speed and crosswind component, and with circular mean values taken for wind direction and heading in the air reference frame (see below). In total we included $n = 348$ flights for which both legs were tracked, and $n = 38$ where either the outbound or the return leg was recorded. As such, we include with each result presented in the main text a sample size that relates to the result in question.

Wind measurements Wind velocity was obtained from the NOAA/NCEP Global Forecast System (GFS). GFS data were sampled at a temporal resolution of 3 hours and a spatial resolution of $0.5° \times 0.5°$. Each GPS fix was assigned the nearest wind measurement in time and space, which was used to determine the bird's velocity with respect to the air as well as the ground. For the video-based analyses, the exact location of the shearwaters was unknown, but the wind velocity was found to be quite homogeneous within the known range of incubating shearwaters from Skomer (Dean, 2012) over the period for which the video footage was recorded. Given their known departure and arrival times, we estimate that the birds foraged within a 50 km radius of Skomer. We therefore averaged wind velocity estimates from the Met Office Wavewatch III wave model (one hourly temporal precision, 8km spatial precision, referenced to 10 m altitude) over this radius for the purposes of analysing the bird-borne video data.

References

Åkesson, S. and Hedenström, A. (2000). "Wind selectivity of migratory flight departures in birds". In: *Behavioral Ecology and Sociobiology* 47.3, pp. 140–144.

Åkesson, S., Bianco, G., and Hedenström, A. (2016). "Negotiating an ecological barrier: crossing the Sahara in relation to winds by common swifts". In: *Philosophical Transactions of the Royal Society B: Biological Sciences* 371.1704, p. 20150393. DOI: 10.1098/rstb.2015.0393.

Åkesson, S., Walinder, G., Karlsson, L., and Ehnbom, S. (2002). "Nocturnal migratory flight initiation in reed warblers *Acrocephalus scirpaceus* : effect of wind on orientation and timing of migration". In: *Journal of Avian Biology* 33.4, pp. 349–357. DOI: 10.1034/j.1600-048X.2002.02951.x.

Alerstam, T., Gudmundsson, G. A., and Larrson, B. (1993). "Flight tracks and speeds of Antarctic and Atlantic seabirds: radar and optical measurements". In: *Philosophical Transactions of the Royal Society of London. Series B: Biological Sciences* 340.1291, pp. 55–67. DOI: 10.1098/rstb.1993.0048.

Bencatel, R., Tasso de Sousa, J., and Girard, A. (2013). "Atmospheric flow field models applicable for aircraft endurance extension". In: *Progress in Aerospace Sciences* 61, pp. 1–25. DOI: 10.1016/j.paerosci.2013.03.001.

Bilo, D. (1992). *Optocollic Reflexes and Neck Flexion—Related Activity of Flight Control Muscles in the Airflow-Stimulated Pigeon*. Publication Title: The Head-Neck Sensory Motor System Section: The Head-Neck Sensory Motor System. Oxford University Press.

Bousquet, G. D., Triantafyllou, M. S., and Slotine, J.-J. E. (2017). "Optimal dynamic soaring consists of successive shallow arcs". In: *Journal of The Royal Society Interface* 14.135, p. 20170496. DOI: 10.1098/rsif.2017.0496.

Bower, G. C. (2012). "Boundary layer dynamic soaring for autonomous aircraft: Design and validation". thesis. Stanford University.

Catry, P., Phillips, R. A., and Croxall, J. P. (2004). "Sustained Fast Travel by a Gray-Headed Albatross (Thalassarche chrysostoma) Riding an Antarctic Storm". In: *The Auk* 121.4, pp. 1208–1213.

Conklin, J. R. and Battley, P. F. (2011). "Impacts of wind on individual migration schedules of New Zealand bar-tailed godwits". In: *Behavioral Ecology* 22.4, pp. 854–861. DOI: 10.1093/beheco/arr054.

Croxall, J. P. (2005). "Global Circumnavigations: Tracking Year-Round Ranges of Nonbreeding Albatrosses". In: *Science* 307.5707, pp. 249–250. DOI: 10.1126/science.1106042.

Dean, B., Kirk, H., Fayet, A., Shoji, A., Freeman, R., Leonard, K., Perrins, C., and Guilford, T. (2015). "Simultaneous multi-colony tracking of a pelagic seabird reveals cross-colony utilization of a shared foraging area". In: *Marine Ecology Progress Series* 538, pp. 239–248. DOI: 10.3354/meps11443.

Dean, B. (2012). "The at-sea behaviour of the Manx shearwater". thesis. University of Oxford.

Deittert, M., Richards, A., Toomer, C., and Pipe, A. (2009). "Dynamic Soaring Flight in Turbulence". In: *AIAA Guidance, Navigation, and Control Conference*, pp. 2–5. DOI: 10.2514/6.2009-6012. eprint: https://arc.aiaa.org/doi/pdf/10.2514/6.2009-6012.

Deppe, J. L., Ward, M. P., Bolus, R. T., Diehl, R. H., Celis-Murillo, A., Zenzal, T. J., Moore, F. R., Benson, T. J., Smolinsky, J. A., Schofield, L. N., Enstrom, D. A., Paxton, E. H., Bohrer, G., Beveroth, T. A., Raim, A., Obringer, R. L., Delaney, D., and Cochran, W. W. (2015). "Fat, weather, and date affect migratory songbirds' departure decisions, routes, and time it takes to cross the Gulf of Mexico". In: *Proceedings of the National Academy of Sciences* 112.46, E6331–E6338. DOI: 10.1073/pnas.1503381112.

Gibb, R., Shoji, A., Fayet, A. L., Perrins, C. M., Guilford, T., and Freeman, R. (2017). "Remotely sensed wind speed predicts soaring behaviour in a wide-ranging pelagic seabird". In: *Journal of The Royal Society Interface* 14.132, p. 20170262. DOI: 10.1098/rsif.2017.0262.

Gillies, N., Tyson, C., Wynn, J., Syposz, M., Vansteenberghe, C., and Guilford, T. (2021). "Exploring the mechanisms of coordinated chick provisioning in the Manx shearwater Puffinus puffinus". In: *Journal of Avian Biology*.

González-Solís, J., Felicísimo, A., Fox, J., Afanasyev, V., Kolbeinsson, Y., and Muñoz, J. (2009). "Influence of sea surface winds on shearwater migration detours". In: *Marine Ecology Progress Series* 391, pp. 221–230. DOI: 10.3354/meps08128.

Guilford, T., Meade, J., Willis, J., Phillips, R., Boyle, D., Roberts, S., Collett, M., Freeman, R., and Perrins, C. (2009). "Migration and stopover in a small pelagic seabird, the Manx shearwater *Puffinus puffinus* : insights from machine learning". In: *Proceedings of the Royal Society B: Biological Sciences* 276.1660, pp. 1215–1223. DOI: 10.1098/rspb.2008.1577.

Guilford, T. C., Meade, J., Freeman, R., Biro, D., Evans, T., Bonadonna, F., Boyle, D., Roberts, S., and Perrins, C. M. (2008). "GPS tracking of the foraging movements of Manx Shearwaters Puffinus puffinus breeding on Skomer Island, Wales". In: *Ibis* 150.3, pp. 462–473.

Guilford, T. and Taylor, G. K. (2014). "The sun compass revisited". In: *Animal Behaviour* 97, pp. 135–143. DOI: 10.1016/j.anbehav.2014.09.005.

Hawkes, L. A., Balachandran, S., Batbayar, N., Butler, P. J., Frappell, P. B., Milsom, W. K., Tseveenmyadag, N., Newman, S. H., Scott, G. R., Sathiyaselvam, P., Takekawa, J. Y., Wikelski, M., and Bishop, C. M. (2011). "The trans-Himalayan flights of bar-headed geese (Anser indicus)". In: *Proceedings of the National Academy of Sciences* 108.23, pp. 9516–9519. DOI: 10.1073/pnas.1017295108.

Hayes, B. and Brooke, M. D. L. (1990). "Retinal ganglion cell distribution and behaviour in procellariiform seabirds". In: *Vision Research* 30.9, pp. 1277–1289. DOI: 10.1016/0042-6989(90)90002-3.

Horton, K. G., Van Doren, B. M., Stepanian, P. M., Hochachka, W. M., Farnsworth, A., and Kelly, J. F. (2016). "Nocturnally migrating songbirds drift when they can and compensate when they must". In: *Scientific Reports* 6.1, p. 21249. DOI: 10.1038/srep21249.

Hughes, A. (1977). "The Topography of Vision in Mammals of Contrasting Life Style: Comparative Optics and Retinal Organisation". In: *Handbook of Sensory Physiology VII/5, The Visual System in Vertebrates*. Berlin: Springer-Verlag, pp. 613–756.

Jouventin, P. and Weimerskirch, H. (1990). "Satellite tracking of Wandering albatrosses". In: *Nature* 343.6260, pp. 746–748. DOI: 10.1038/343746a0.

Lissaman, P. (2005). "Wind Energy Extraction by Birds and Flight Vehicles". en. In: *43rd AIAA Aerospace Sciences Meeting and Exhibit*. Reno, Nevada: American Institute of Aeronautics and Astronautics. DOI: 10.2514/6.2005-241.

Liu, D.-N. (2017). "Bio-inspired energy-harvesting mechanisms and patterns of dynamic soaring". In: *Bioinspir. Biomim.* 12, p. 016014.

Martin, G. R. (2017). *The Sensory Ecology of Birds*. Oxford University Press.

Meyer, D. (1977). "The Avian Eye and its Adaptations". In: *Handbook of Sensory Physiology VII/5, The Visual System in Vertebrates*. Berlin: Springer-Verlag, pp. 549–612.

Padget, O., Bond, S. L., Kavelaars, M. M., van Loon, E., Bolton, M., Fayet, A. L., Syposz, M., Roberts, S., and Guilford, T. (Jan. 2018). "In Situ Clock Shift Reveals that the Sun Compass Contributes to Orientation in a Pelagic Seabird". en. In: *Current Biology* 28.2, 275–279.e2. DOI: 10.1016/j.cub.2017.11.062.

Padget, O., Stanley, G., Willis, J. K., Fayet, A. L., Bond, S., Maurice, L., Shoji, A., Dean, B., Kirk, H., Juarez-Martinez, I., et al. (2019). "Shearwaters know the direction and distance home but fail to encode intervening obstacles after free-ranging foraging trips". In: *Proceedings of the National Academy of Sciences* 116.43, pp. 21629–21633.

Paiva, V. H., Guilford, T., Meade, J., Geraldes, P., Ramos, J. A., and Garthe, S. (2010). "Flight dynamics of Cory's shearwater foraging in a coastal environment". In: *Zoology* 113.1, pp. 47–56. DOI: 10.1016/j.zool.2009.05.003.

Pennycuick, C. J. (1982). "The Flight of Petrels and Albatrosses (Procellariiformes), Observed in South Georgia and its Vicinity". In: *Philosophical Transactions of the Royal Society B: Biological Sciences* 300.1098, pp. 75–106. DOI: 10.1098/rstb.1982.0158.

Pennycuick, C. J. (2008). *Modelling the flying bird*. Theoretical ecology series. Amsterdam ; London: Academic Press. xiv+480.

Pennycuick, C. J. (2002). "Gust soaring as a basis for the flight of petrels and albatrosses (Procellariiformes)". In: *Avian Science* 2.1.

Phillips, R. A. and Croxall, J. P. (2003). "Effects of Satellite Transmitters on Albatrosses and Petrels". In: *The Auk* 120.4, pp. 1082–1090. DOI: 10.2307/4090279.

Rayleigh, L. (1883). "The Soaring of Birds". In: *Nature* 27, pp. 534–535.

Rayner, J. M. V., Viscardi, P. W., Ward, S., and Speakman, J. R. (2001). "Aerodynamics and Energetics of Intermittent Flight in Birds". In: *American Zoologist* 41.2, pp. 188–204.

Richardson, P. L. (2011). "How do albatrosses fly around the world without flapping their wings?" In: *Progress in Oceanography* 88.1, pp. 46–58. DOI: 10.1016/j.pocean.2010.08.001.

Rutz, C., Bluff, L. A., Weir, A. A. S., and Kacelnik, A. (2007). "Video Cameras on Wild Birds". In: *Science* 318.5851, pp. 765–765. DOI: 10.1126/science.1146788.

Rutz, C. and Troscianko, J. (2013). "Programmable, miniature video-loggers for deployment on wild birds and other wildlife". In: *Methods in Ecology and Evolution* 4.2. Ed. by D. D. Hodgson, pp. 114–122. DOI: 10.1111/2041-210x.12003.

Sachs, G., Traugott, J., Nesterova, A. P., and Bonadonna, F. (2013). "Experimental verification of dynamic soaring in albatrosses". In: *Journal of Experimental Biology* 216.22, pp. 4222–4232. DOI: 10.1242/jeb.085209.

Sachs, G. (2004). "Minimum shear wind strength required for dynamic soaring of albatrosses: Shear wind strength and dynamic soaring". In: *Ibis* 147.1, pp. 1–10. DOI: 10.1111/j.1474-919x.2004.00295.x.

Schaub, M., Liechti, F., and Jenni, L. (2004). "Departure of migrating European robins, Erithacus rubecula, from a stopover site in relation to wind and rain". In: *Animal Behaviour* 67.2, pp. 229–237. DOI: 10.1016/j.anbehav.2003.03.011.

Schoombie, S., Schoombie, J., Brink, C. W., Stevens, K. L., Jones, C. W., Risi, M. M., and Ryan, P. G. (2019). "Automated extraction of bank angles from bird-borne video footage using open-source software". In: *Journal of Field Ornithology* 90.4, pp. 361–372. DOI: 10.1111/jofo.12313.

Serres, J. R., Evans, T. J., Åkesson, S., Duriez, O., Shamoun-Baranes, J., Ruffier, F., and Hedenström, A. (2019). "Optic flow cues help explain altitude control over sea in freely flying gulls". In: *Journal of The Royal Society Interface* 16.159, p. 20190486. DOI: 10.1098/rsif.2019.0486.

Shepard, E. L. C., Williamson, C., and Windsor, S. P. (2016). "Fine-scale flight strategies of gulls in urban airflows indicate risk and reward in city living". In: *Philosophical Transactions of the Royal Society B: Biological Sciences* 371.1704, p. 20150394. DOI: 10.1098/rstb.2015.0394.

Shoji, A., Aris-Brosou, S., Fayet, A., Padget, O., Perrins, C., and Guilford, T. (2015). "Dual foraging and pair coordination during chick provisioning by Manx shearwaters: empirical evidence supported by a simple model". In: *Journal of Experimental Biology* 218.13, pp. 2116–2123. DOI: 10.1242/jeb.120626.

Spivey, R., Stansfield, S., and Bishop, C. (2014). "Analysing the intermittent flapping flight of a Manx Shearwater, Puffinus puffinus, and its sporadic use of a wave-meandering wing-sailing flight strategy". In: *Progress in Oceanography* 125, pp. 62–73. DOI: 10.1016/j.pocean.2014.04.005.

Sukumar, P. P. and Selig, M. S. (2013). "Dynamic Soaring of Sailplanes over Open Fields". In: *Journal of Aircraft* 50.5, pp. 1420–1430. DOI: 10.2514/1.C031940.

Suryan, R. M., Anderson, D. J., Shaffer, S. A., Roby, D. D., Tremblay, Y., Costa, D. P., Sievert, P. R., Sato, F., Ozaki, K., Balogh, G. R., and Nakamura, N. (2008). "Wind, Waves, and Wing Loading: Morphological Specialization May Limit Range Expansion of Endangered Albatrosses". In: *PLoS ONE* 3.12. Ed. by S. Humphries, e4016. DOI: 10.1371/journal.pone.0004016.

Taylor, G. and Thomas, A. (2014). *Evolutionary Biomechanics*. eng. Oxford University Press. DOI: 10.1093/acprof:oso/9780198566373.001.0001.

Taylor, G. K., Reynolds, K. V., and Thomas, A. L. R. (2016). "Soaring energetics and glide performance in a moving atmosphere". In: *Philosophical Transactions of the Royal Society B: Biological Sciences* 371.1704, p. 20150398. DOI: 10.1098/rstb.2015.0398.

Tremblay, Y. (2006). "Interpolation of animal tracking data in a fluid environment". In: *Journal of Experimental Biology* 209.1, pp. 128–140. DOI: 10.1242/jeb.01970.

Webster, M. M. and Rutz, C. (2020). "How STRANGE are your study animals?" In: *Nature* 582, pp. 337–340.

Weimerskirch, H., Guionnet, T., Martin, J., Shaffer, S. A., and Costa, D. P. (2000). "Fast and fuel efficient? Optimal use of wind by flying albatrosses". In: *Proceedings of the Royal Society of London. Series B: Biological Sciences* 267.1455, pp. 1869–1874. DOI: 10.1098/rspb.2000.1223.

Wynn, J., Collet, J., Prudor, A., Corbeau, A., Padget, O., Guilford, T., and Weimerskirch, H. (2020). "Young frigatebirds learn how to compensate for wind drift". In: *Proceedings of the Royal Society B: Biological Sciences* 287.1937, p. 20201970. DOI: 10.1098/rspb.2020.1970.

Zhao, Y. J. and Qi, Y. C. (2004). "Minimum fuel powered dynamic soaring of unmanned aerial vehicles utilizing wind gradients". In: *Optimal Control Applications and Methods* 25.5, pp. 211–233. DOI: 10.1002/oca.744.

3

Visual guidance by hawks in pursuit of terrestrial prey

Contents

3.1 Abstract 53
3.2 Introduction 54
3.3 Results 57
3.4 Discussion 66
3.5 Materials and Methods 73
References 80

3.1 Abstract

The flight behaviour of predatory birds is often well modelled by a guidance law called proportional navigation, which commands steering in proportion to the angular rate of the line-of-sight from predator to prey. This is defined with respect to an inertial frame of reference, so proportional navigation is classically implemented using visual-inertial sensor fusion. In Harris' hawks, pursuit of terrestrial targets may be even better modelled by a mixed guidance law combining visual-inertial information on the line-of-sight rate with visual information on the deviation angle between the attacker's velocity and the line-of-sight. Here we ask whether there is a variant of the same mixed guidance law that can work using visual information alone. We used motion capture to record $n = 228$ attack flights from $N = 4$ Harris' hawks, confirming that classical proportional navigation and

mixed guidance each model the trajectory data well. We then show that a related form of mixed guidance works just as well when visual-inertial information on the line-of-sight rate is replaced with purely visual information on the apparent motion of the target relative to the ground. All three models can therefore model the behavioural data phenomenologically, but each alternative makes different predictions on the physiological pathways involved.

3.2 Introduction

A hawk pursuing a hare must steer its attack trajectory to achieve capture. Drawing inspiration from missile engineering, an increasingly popular approach to understanding such behaviours is to identify guidance laws that successfully model the turning behaviour of the attacker (Hein et al., 2020). Guidance laws are behavioural algorithms that implement pursuit by commanding turning in response to the relative motion of an attacker and its target (Shneydor, 2011). For example, a guidance law called proportional navigation (PN) has long been used to implement guidance in homing missiles (Palumbo et al., 2010), and commands steering in proportion to the angular rate of the line-of-sight from the attacker to its target. An alternative guidance law called proportional pursuit (PP) involves commanding turning in proportion to the deviation angle between the attacker's velocity and the line-of-sight from the attacker to its target. These different guidance laws predict different pursuit trajectories in response to the same target motion, and whereas PN guidance closely models the steering behaviour of falcons (Brighton et al., 2017; Brighton et al., 2021), bats (Ghose et al., 2006), robber flies (Fabian et al., 2018), and killer flies (Fabian et al., 2018), PP guidance has been found to model the steering of blowflies (Boeddeker et al., 2003), tiger beetles (Haselsteiner et al., 2014) and honeybees (Zhang et al., 1990). Other, more complex, guidance laws are possible. For example, Brighton et al. (2019) found that combining PN and PP guidance linearly in a mixed (PNP) guidance law most successfully modelled the steering behaviour of Harris' hawks (*Parabuteo unicinctus*), which are the subject of this study .

Besides commanding different pursuit trajectories in response to the same target motion, the PN, PP, and PNP guidance laws differ fundamentally in the nature of the sensory cues that they use. PN commands steering in response to the line-of-sight rate ($\dot{\lambda}$), defined as the rate of change in the angle (λ) between the line-of-sight to the target and some external reference direction (Figure 3.1). It follows that the line-of-sight rate $\dot{\lambda}$

is an exocentric cue, because measuring it involves measuring changes in the line-of-sight direction with respect to an external frame of reference. In contrast, PP commands steering in response to the deviation angle, δ, defined as the angle between the line-of-sight to the target and the direction of the attacker's own velocity vector (Figure 3.1). This can be thought of as an egocentric cue, because it involves measuring the line-of-sight direction with respect to the attacker's own self-motion. In missiles, at least, this makes PP guidance simpler to implement than PN guidance (Shneydor, 2011). Finally, the PNP guidance law combines PN and PP elements, and therefore employs a mixture of egocentric and exocentric cues. Nevertheless, as we show below, a related form of the same mixed guidance law can be made to work using egocentric cues alone. As we now discuss, this distinction is important because of the difference it makes to how the respective variables can be measured physiologically.

In homing missiles (Palumbo et al., 2010; Shneydor, 2011), and in studies of animal pursuit (Brighton et al., 2017; Brighton et al., 2021; Fabian et al., 2018), the line-of-sight angle λ is defined with respect to a fixed reference direction. In practice, this means that any agent that employs, or is hypothesised to employ, PN guidance must be able to measure the line-of-sight rate $\dot{\lambda}$ in an inertial frame of reference $\mathcal{F}_{\mathcal{I}}$. A homing missile does this by rotating its target acquisition sensor to keep the target at fixed sensor coordinates, using a gimbaled tracking device called a seeker. The seeker's gyroscopic sensor output can then be used to estimate $\dot{\lambda}$ as the rotation rate of the seeker minus any residual tracking error. Although birds may use head movements to track targets in a similar fashion to a missile seeker, it has not yet been tested whether or how they estimate the line-of-sight rate $\dot{\lambda}$. Vision alone could provide an inertial reference if the background is sufficiently distant that the direction of landmark features does not change appreciably with the attacker's self-motion. It is also plausible that the sun or its attendant cues could provide such a reference when visible (Guilford et al., 2014). However, a hawk chasing a target close to the ground or beneath the canopy will see no distant background against which to measure the target's motion, and the direction of nearby visual features will change quickly as a result of its own self-motion. It therefore seems reasonable to assume that animals implementing PN guidance are likely to do so with the aid of inertial sensors.

Birds possess several inertial sensors that could provide an inertial reference for measuring the line-of-sight rate, including the lumbosacral organ of the body (Stanchak

et al., 2020) and the vestibular system of the inner ear. However, whilst the vestibular system is well set up to sense angular acceleration of the head, it is unclear whether it can also measure the angular rate of the head directly without integration and the error this introduces (Warrick, 2002; Pennycuick, 2008; Muller, 1990; Muller, 2020). Even so, it is reasonable to assume that vestibular output may be used to estimate the tracking rate of the head in response to target motion, analogous to the action of a missile seeker. In addition, vestibular output may be used to stabilize the head in an inertial frame of reference (Benson et al., 2017). Were the head to be stabilised in this manner during prey pursuit, then the visual drift of the target across the retina would become a direct measure of $\dot{\lambda}$. It is not yet clear, however, whether predatory birds keep their head rotationally stabilised during pursuit, or whether they track targets continuously. Peregrine falcons *Falco peregrinus*, for example, appear to intersperse phases of rotational stabilisation of the head with phases of continuous head rotation (Walker, 2018). It is therefore an open question how birds implement PN guidance, though it is reasonable to assume that they do so by fusing visual and inertial information.

In contrast to the line-of-sight rate $\dot{\lambda}$, the deviation angle δ can be measured without an inertial reference. In fact, if the background is suitably close, then the deviation angle δ can be measured purely visually, by taking the vanishing point of the translational optic flow field as the direction of self-motion, and comparing this to the retinal coordinates of the target. Alternatively, the deviation angle could be estimated from the contralateral asymmetry in the translational optic flow field (Ros et al., 2017) produced when a predatory bird looks directly at its target. Hence, the hypothesis that an organism implements PP guidance relies on fundamentally different assumptions regarding the organism's sensory capabilities compared to the hypothesis that an organism implements PN guidance. Clearly, the combination of PN and PP elements in a mixed PNP guidance law relies on different assumptions again. It follows that phenomenological modelling of pursuit behaviour can be informative as to the physiological pathways that may be involved. For instance, Brighton et al. (2019) found that whereas PNP or PN guidance could both successfully model Harris' hawk attack trajectories, PP guidance could not. Given the necessary involvement of a PN element, this result would therefore seem to imply that hawks must be able to measure the line-of-sight rate $\dot{\lambda}$ in an inertial reference frame. However, as we now show, other mixed guidance models that do not imply the ability to measure $\dot{\lambda}$ in an inertial

frame of reference may model Harris' hawk trajectories as well as, or even better than, the PNP guidance law that Brighton et al. (2019) fitted.

Here we describe a new data set comprising $n = 228$ pursuit trajectories flown by $N = 4$ Harris' hawks, which we model using the original PP, PN, and PNP guidance laws described above, together with a new guidance law that we call background-PNP. In background-PNP guidance, the line-of-sight rate is defined in a rotating frame of reference that we call the background frame of reference $\mathcal{F}_{\mathcal{B}}$. As we explain below, this background line-of-sight rate ${}^{\mathcal{B}}\dot{\lambda}$ is effectively just the difference between the retinal drift of the target and the retinal drift of the background. Hence, in contrast to the inertial line-of-sight rate, which we write as ${}^{\mathcal{I}}\dot{\lambda}$ for clarity, the background line-of-sight rate ${}^{\mathcal{B}}\dot{\lambda}$ can be measured without an inertial reference. Having reframed PNP guidance in this way, we test the success of the background-PNP guidance law in explaining the measured hawk trajectories relative to the original PNP guidance law. We find that background-PNP guidance explains the data at least as well as PNP or PN guidance, which has important implications for testing of the sensorimotor pathways involved in implementing pursuit guidance in hawks and other flying animals.

3.3 Results

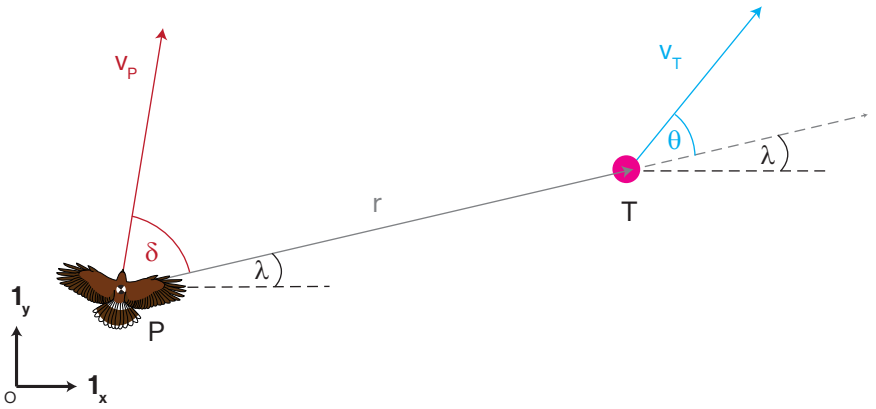


Figure 3.1: Pursuit geometry. The line drawn from the hawk (P) to its target (T) is the line-of-sight vector $\boldsymbol{r}$. The line-of-sight vector $\boldsymbol{r}$ forms the line-of-sight angle λ with the x-axis of an inertial reference frame that we define by the fixed orthonormal basis vectors $\mathbf{1}_{\boldsymbol{x}}$ and $\mathbf{1}_{\boldsymbol{y}}$. The rate of change in the line-of-sight angle in an inertial reference frame, ${}^{\mathcal{I}}\dot{\lambda}$, is the input to the inertial-PN guidance law. The angle that the hawk's velocity vector, $\boldsymbol{v_P}$, forms with $\boldsymbol{r}$ is the target deviation angle, δ, which is the input to the proportional pursuit (PP) guidance law. The inertial-PNP guidance law, which has been found to successfully model Harris' hawk attack trajectories (Brighton et al., 2019), takes ${}^{\mathcal{I}}\dot{\lambda}$ and δ as its two inputs.

Theoretical framework Figure 3.1 shows the geometry of a pursuit involving a hawk chasing a terrestrial target over a flat horizontal surface. We will neglect any vertical displacement of the pursuer, which is assumed to be small in comparison to its horizontal displacement from the target. The line-of-sight vector $\boldsymbol{r}$ is defined as the position vector of the target with respect to the pursuer in an external frame of reference defined by the orthonormal basis vectors $\mathbf{1}_{\boldsymbol{x}}$ and $\mathbf{1}_{\boldsymbol{y}}$. The pursuer's flight path angle γ is defined as the signed angle that its velocity vector $\boldsymbol{v_P}$ makes with the external reference direction $\mathbf{1}_{\boldsymbol{x}}$. Meanwhile, the line-of-sight angle λ is defined as the signed angle that the line-of-sight vector $\boldsymbol{r}$ makes with the reference direction $\mathbf{1}_{\boldsymbol{x}}$, and the deviation angle δ is defined as the signed angle that the line-of-sight vector $\boldsymbol{r}$ makes with the pursuer's velocity vector $\boldsymbol{v_P}$.

It is clear from Figure 3.1 that the deviation angle δ is independent of the choice of external reference direction $\mathbf{1}_{\boldsymbol{x}}$, and in this sense is an egocentric variable. In contrast, both the flight path angle γ and the line-of-sight angle λ depend on the choice of external reference direction $\mathbf{1}_{\boldsymbol{x}}$. We will fix $\mathbf{1}_{\boldsymbol{x}}$ and $\mathbf{1}_{\boldsymbol{y}}$ so that they define an inertial frame of reference $\mathcal{F}_{\mathcal{I}}$, and will use the notation ${}^{\mathcal{I}}\dot{\gamma}$ and ${}^{\mathcal{I}}\dot{\lambda}$ to denote the time derivatives of γ and λ in $\mathcal{F}_{\mathcal{I}}$. With these definitions, the proportional pursuit (PP) guidance law commands turning as:

$$ {}^{\mathcal{I}}\dot{\gamma}(t) = -K\delta(t-\tau), \tag{3.1} $$

where K is a guidance constant and τ is a fixed time delay, whereas the proportional navigation (PN) guidance law commands turning as:

$$ {}^{\mathcal{I}}\dot{\gamma}(t) = N\,{}^{\mathcal{I}}\dot{\lambda}(t-\tau), \tag{3.2} $$

where N is another guidance constant. Finally, the inertial form of the PNP guidance law commands turning as:

$$ {}^{\mathcal{I}}\dot{\gamma}(t) = N\,{}^{\mathcal{I}}\dot{\lambda}(t-\tau) - K\delta(t-\tau), \tag{3.3} $$

where, for sake of simplicity, the same time delay τ is assumed to hold for both elements.

Because we have fixed $\mathbf{1}_{\boldsymbol{x}}$ and $\mathbf{1}_{\boldsymbol{y}}$ with respect to an inertial frame of reference, practical methods of estimating the inertial line-of-sight rate ${}^{\mathcal{I}}\dot{\lambda}$ are expected to involve the fusion of visual and inertial information. One possibility is to track the target visually by turning the head, and to measure the angular rate of the head inertially as a proxy for ${}^{\mathcal{I}}\dot{\lambda}$. An alternative is to stabilise the head inertially, and to measure the retinal drift of the target

visually as a proxy for ${}^{\mathcal{I}}\dot{\lambda}$. However, we may choose to use other sets of basis vectors to define the line-of-sight rate, and in this case the sensory basis of its measurement may differ. For instance, we may choose to define the external reference direction $\mathbf{1}_{x'}$ visually (e.g. as the direction vector of some background feature seen by the pursuer), and may use $\mathbf{1}_{x'}$ and its normal $\mathbf{1}_{y'}$ to define a new background frame of reference $\mathcal{F}_{\mathcal{B}}$. If the background feature used to define $\mathbf{1}_{x'}$ is sufficiently distant (e.g. the sun's disc), then $\mathcal{F}_{\mathcal{B}}$ will approximate an inertial frame of reference. This being so, it is possible to estimate ${}^{\mathcal{I}}\dot{\lambda}$ visually by comparing the retinal drift of the target to the retinal drift of the distant background. On the other hand, if the background feature is close to the pursuer (e.g. contrast on the ground around the target), then $\mathcal{F}_{\mathcal{B}}$ will rotate as the pursuer moves. In this case, the difference between the retinal drift of the target and the retinal drift of the background is no longer a proxy for the inertial line-of-sight rate ${}^{\mathcal{I}}\dot{\lambda}$, but still measures a well-defined quantity that we will call the background line-of-sight rate ${}^{\mathcal{B}}\dot{\lambda}$.

In summary, we therefore have one version of the line-of-sight rate (${}^{\mathcal{I}}\dot{\lambda}$) that is defined in an inertial frame of reference $\mathcal{F}_{\mathcal{I}}$, and another (${}^{\mathcal{B}}\dot{\lambda}$) that is defined with respect to the background frame of reference $\mathcal{F}_{\mathcal{B}}$. In computing the background line-of-sight rate ${}^{\mathcal{B}}\dot{\lambda}$, we will assume that the distance between the target and the background feature used to define $\mathcal{F}_{\mathcal{B}}$ is negligibly small, which is reasonable in the case of a hawk chasing a terrestrial target that is moving over the ground. With this restriction, the background line-of-sight rate describes only the component of the relative motion of the target and pursuer that is due to the target's motion (as we formally show in the Supplementary Text of Appendix B). In contrast, the inertial line-of-sight rate describes the total motion of the target relative to the pursuer, so also contains information on the pursuer's self-motion. Substituting ${}^{\mathcal{B}}\dot{\lambda}$ for ${}^{\mathcal{I}}\dot{\lambda}$ in the PN guidance law therefore loses information on self-motion that is useful for steering an effective intercept. Thus, the following guidance law, which we call background-PN to distinguish it from the inertial form of the PN guidance law described above (which we henceforth call inertial-PN), is unlikely to steer successful attack trajectories:

$$ {}^{\mathcal{I}}\dot{\gamma}(t) = N\,{}^{\mathcal{B}}\dot{\lambda}(t-\tau), \tag{3.4} $$

However, as we discuss in Section 3.4, substituting ${}^{\mathcal{B}}\dot{\lambda}$ for ${}^{\mathcal{I}}\dot{\lambda}$ in the mixed PNP guidance law results in no net loss of information, because of the complementary effect of the

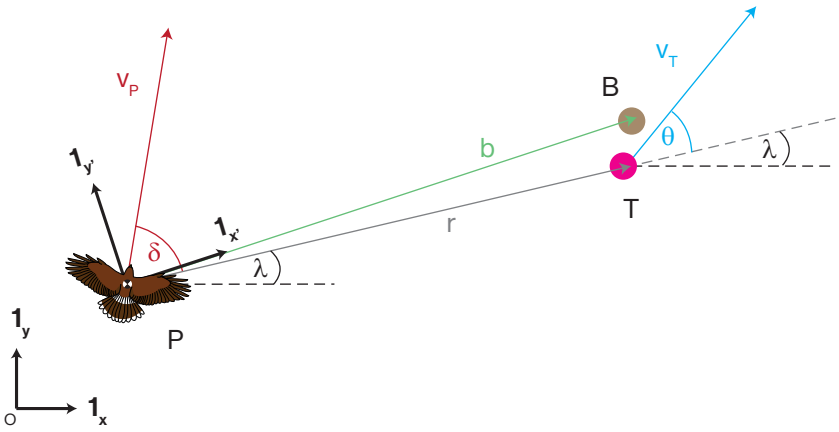


Figure 3.2: Harris' hawk attack geometry with background. We add to the geometry of Figure 3.1 a background patch (B) that lies close to the target (T). This defines a vector, $\boldsymbol{b}$, between the hawk (P) and the background patch. We define the background reference frame, $\mathcal{F}_{\mathcal{B}}$, by the rotating orthonormal basis vectors $\mathbf{1}'_{\boldsymbol{x}}$ and $\mathbf{1}'_{\boldsymbol{y}}$ (where $\mathbf{1}'_{\boldsymbol{x}}$ points in the direction of $\boldsymbol{b}$) which are carried with the bird. Note that $\mathcal{F}_{\mathcal{B}}$ is defined instantaneously by the position of the hawk and the position of the background patch against which it is viewing the target. As such, the background reference frame is constantly updated. The instantaneous angular speed of $\mathcal{F}_{\mathcal{B}}$ defines the angular speed of the background reference frame with respect to $\mathcal{F}_{\mathcal{I}}$.

deviation angle δ. With this in mind, we define the following new guidance law, which commands steering as:

$$^{\mathcal{I}}\dot{\gamma}(t) = N\,{}^{\mathcal{B}}\dot{\lambda}(t-\tau) - K\delta(t-\tau), \tag{3.5}$$

and which we call the background-PNP guidance law to distinguish it from the inertial form of the PNP guidance law described above (which we henceforth call inertial-PNP). Here we ask whether background-PNP guidance can model Harris' hawk attack trajectories as successfully as inertial-PNP, and compare this to the performance of the inertial-PN, background-PN, and PP guidance laws in modelling the same data.

Guidance model simulations We measured hawk and target trajectories across $n = 228$ flight trials in which a Harris' hawk pursued an artificial lure. For each trial, we simulate trajectories using the guidance models in Table 3.1 given the measured lure trajectory, hawk ground speed, and starting hawk position (see Brighton et al. (2017), Brighton et al. (2019), and Brighton et al. (2021) and the Methods and Materials of this paper).

Guidance model comparison First, we find the set of best-fit parameters N, K, and τ for the guidance models in Table 3.1 by finding those parameter values that minimise the prediction error (defined as the root mean squared error between the simulated

Model	Equation	Information
PP	${}^{\mathcal{I}}\dot{\gamma}(t) = -K\delta(t-\tau)$	Visual
inertial-PN	${}^{\mathcal{I}}\dot{\gamma}(t) = N\,{}^{\mathcal{I}}\dot{\lambda}(t-\tau)$	Inertial and visual
background-PN	${}^{\mathcal{I}}\dot{\gamma}(t) = N\,{}^{\mathcal{B}}\dot{\lambda}(t-\tau)$	Visual
inertial-PNP	${}^{\mathcal{I}}\dot{\gamma}(t) = N\,{}^{\mathcal{I}}\dot{\lambda}(t-\tau) - K\delta(t-\tau)$	Inertial and visual
background-PNP	${}^{\mathcal{I}}\dot{\gamma}(t) = N\,{}^{\mathcal{B}}\dot{\lambda}(t-\tau) - K\delta(t-\tau)$	Visual

Table 3.1: Table of fitted models, their respective equations, and the sensory information they imply a hawk would need to implement pursuit guidance

trajectory and measured flight trajectory), ϵ, for each flight individually. We summarise the results of model fitting in Table 3.2.

In Figure 3.3, we compare the simulated trajectories under the median of the best-fit parameters given the inertial-PNP and background-PNP models for an example flight in our dataset. In Figure 3.4, we plot the distribution of ϵ, N, and K under the inertial-PNP and background-PNP guidance models across all $n = 228$ flights, whereas we plot the distribution of ϵ, N, and K under the PP, inertial-PN, and background-PN guidance models in Figure B.2 of Appendix B. Given the median prediction error, $\tilde{\epsilon}$, under the inertial-PNP ($\tilde{\epsilon} = 38$ mm; 95% bootstrapped CI: $28, 51$ mm) and background-PNP ($\tilde{\epsilon} = 38$ mm; 95% bootstrapped CI: $29, 51$ mm) models is the same, we find the two models fit the data equally well. The results cited in Table 3.2 show that the medians of the best-fit

Model	Median prediction error, $\tilde{\epsilon}$	95% CI	Median of best-fit guidance constant(s)	95% CI(s)
PP	135 mm	111, 154 mm	$\tilde{K} = 4.4$ s^{-1}	3.2, 6.1 s^{-1}
inertial-PN	71 mm	54, 90 mm	$\tilde{N} = 0.85$	0.77, 0.91
background-PN	145 mm	113, 203 mm	$\tilde{N} = 0.66$	0.51, 0.82
inertial-PNP	38 mm	28, 51 mm	$\tilde{N} = 0.77$; $\tilde{K} = 0.9$ s^{-1}	0.66, 0.86; 0.51, 1.4 s^{-1}
background-PNP	38 mm	29, 51 mm	$\tilde{N} = 0.66$; $\tilde{K} = 3.4$ s^{-1}	0.51, 0.82; 2.8, 3.8 s^{-1}

Table 3.2: Model fitting results given the individual fitting approach. We summarise the result of model fitting by citing the median prediction error, $\tilde{\epsilon}$, under each model, the 95% bootstrapped confidence interval (CI) around $\tilde{\epsilon}$, the median of the best-fit guidance constant(s) under each model, and the 95% bootstrapped confidence interval(s) around the median value of the best-fit constant(s).

values of N, which we denote $\tilde{N}$, under inertial-PNP ($\tilde{N} = 0.77$; 95% bootstrapped CI: $0.66, 86$) and background-PNP ($\tilde{N} = 0.66$; 95% bootstrapped CI: $0.51, 0.82$) models are similar; the results also show that, under both models, the confidence interval around $\tilde{N}$ is narrow, strengthening our conclusion that the two models fit the data equally well. The median of the best-fit N values under inertial-PNP guidance ($\tilde{N} = 0.7$) in Brighton et al. (2019) is close to our results.

In contrast to N, we find that the distribution of K under inertial-PNP and background-PNP guidance is less well behaved; under both guidance laws, there is no clear mode and the median of the best-fit parameter values, $\tilde{K}$, has a large confidence interval (see Table 3.2). The $\tilde{K}$ value under background-PNP guidance ($\tilde{K} = 3.4$ s^{-1}; 95% bootstrapped CI: $2.8, 3.8$ s^{-1}) is substantially higher than under inertial-PNP guidance ($\tilde{K} = 0.9$ s^{-1}; 95% bootstrapped CI: $0.51, 1.4$ s^{-1}), the value of which is very similar to the $\tilde{K} = 1.0s^{-1}$ found under inertial-PNP guidance by Brighton et al. (2019). We find that the distribution of the delay τ under both guidance models is poorly behaved (Figure B.1 in Appendix B), with no clear central tendency.

Under the individual fitting method it is harder to assess the relative fit of the PNP models to the PP and PN models because, under the PNP models, the total parameter number fit across all flights is substantially larger. Thus, we next take a different model fitting approach to the dataset. Here, we look at how successfully combinations of parameters reproduce all observed trajectories simultaneously, which we call the global fitting approach; we find the three parameter values that minimise $\tilde{\epsilon}$ across all $n = 228$ flight trials simultaneously under the inertial-PNP and background-PNP models. In so doing, we also implicitly find the two parameter values that minimise $\tilde{\epsilon}$ across all $n = 228$ flight trials simultaneously under the PP, inertial-PN, and background-PN models. This is because, when $N = 0$, PP guidance is a special case of both PNP guidance models. Likewise, when $K = 0$, inertial-PN guidance is a special case of the inertial-PNP model, and background-PN guidance is a special case of the background-PNP model. We plot $\tilde{\epsilon}$ as a function of parameter values in Figure 3.5 and we summarise the results of model fitting under the global approach in Table 3.3.

The statistics of Table 3.3 show that the result of the global fitting approach corroborates the result of the individual fitting approach – background-PNP guidance ($\tilde{\epsilon} = 150$ mm; 95% bootstrapped CI: $126, 187$ mm) is as successful as inertial-PNP guidance ($\tilde{\epsilon} = 141$

mm; 95% bootstrapped CI: 123, 189 mm) in modelling Harris' hawk steering behaviour. In addition, the best-fit N under the inertial-PNP ($N = 0.8$; 95% bootstrapped CI: $0.5, 0.9$), and background-PNP guidance ($N = 0.9$; 95% bootstrapped CI: $0.7, 1$) are close to the respective medians of the best-fit N under individual fitting. The same

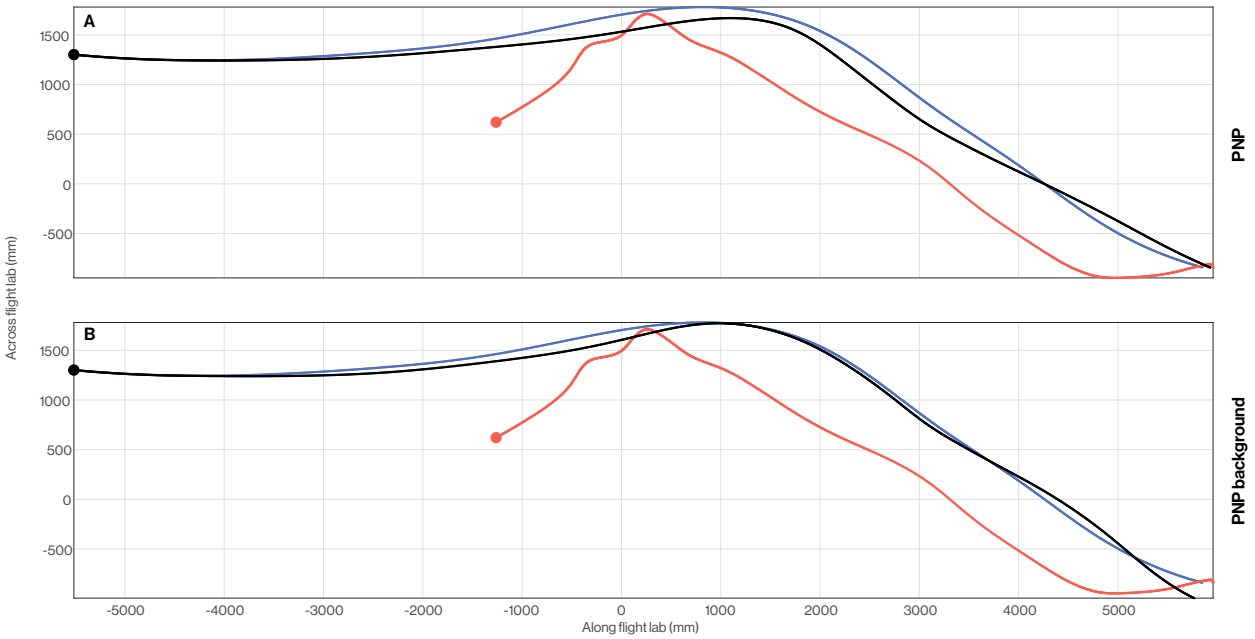


Figure 3.3: Simulated trajectories for a single flight under two different guidance models and optimal parameter values. Given a lure trajectory (red), and a measured hawk trajectory (blue), we plot the best fitting simulated trajectory (black) under different guidance models given best-fit model parameters found with an individual fitting method (see Methods and Materials). Panel **A** shows the best fitting simulation under inertial-PNP guidance for which the line-of-sight rate is measured in an inertial reference frame ($\epsilon = 119$ mm), whereas panel **B** shows the best fitting simulation under background-PNP guidance for which the line-of-sight rate is measured in the background reference frame ($\epsilon = 58$ mm).

Model	**Median prediction error**, $\tilde{\epsilon}$	95% **CI**	**Best-fit guidance constant(s)**	95% **CI(s)**
PP	255 mm	224, 277 mm	$K = 5$ s^{-1}	4.8, 5 s^{-1}
inertial-PN	174 mm	148, 225 mm	$N = 1$	0.9, 1.1
background-PN	523 mm	459, 636 mm	$N = 0.5$	0.3, 0.8
inertial-PNP	141 mm	123, 189 mm	$N = 0.8$; $K = 2.4$ s^{-1}	0.5, 0.9; 0.6, 3.6 s^{-1}
background-PNP	150 mm	126, 187 mm	$N = 0.9$; $K = 3.6$ s^{-1}	0.7, 1.0; 3.0, 3.8 s^{-1}

Table 3.3: Model fitting results given the global fitting approach. We summarise the result of model fitting by citing the median prediction error, $\tilde{\epsilon}$, under each model, the 95% bootstrapped confidence interval (CI) around $\tilde{\epsilon}$, the best-fit guidance constant(s) under each model, and the 95% bootstrapped confidence interval(s) around best-fit constant(s).

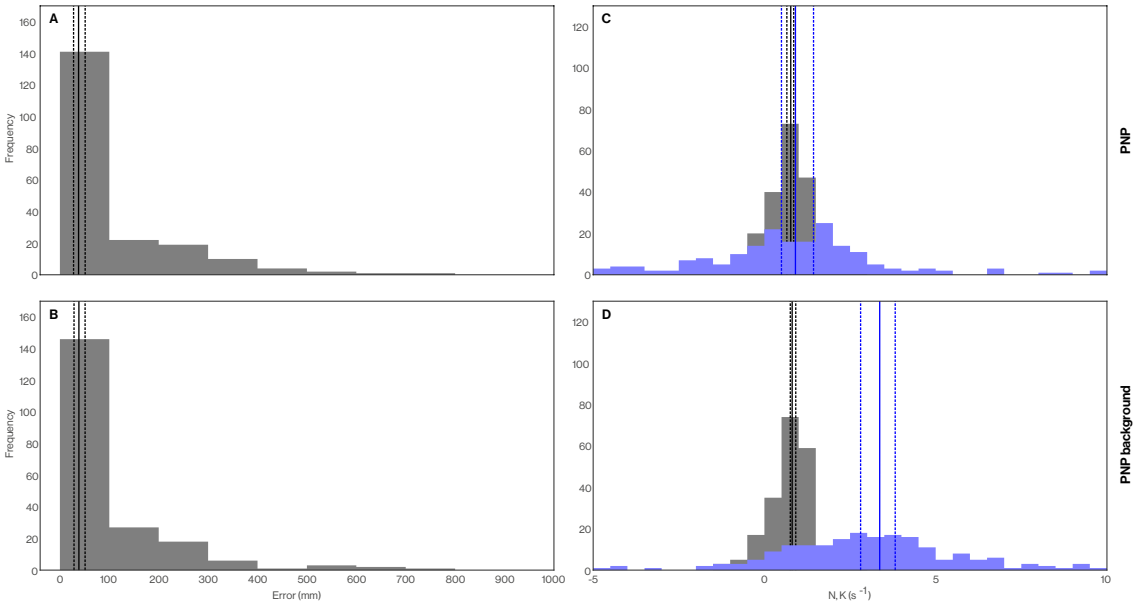


Figure 3.4: Comparison of the prediction error, N, and K distributions under inertial-PNP and background-PNP guidance. A-B display the histograms of the minimum prediction error, ϵ, under individual fitting of different guidance models; the solid vertical line in each panel is the median of the minimum prediction errors, $\tilde{\epsilon}$, while the broken vertical lines display the 95% confidence interval bounds for $\tilde{\epsilon}$; we label the respective guidance laws on the right hand y-axis. **C-D** display the histograms of the values of the guidance constant N (in grey) and the guidance constant K (in blue) that minimise ϵ under individual fitting of different guidance models; the solid black vertical line in each panel is the median of the best-fit N constants, $\tilde{N}$, the solid blue vertical line in each panel is the median of the best-fit K constants, $\tilde{K}$, and broken vertical lines display the 95% confidence intervals around medians.

can be said for the best-fit K under background-PNP guidance ($K = 3.6$ s^{-1}; 95% bootstrapped CI: $3.0, 3.8$ s^{-1}), though under inertial-PNP guidance the globally best-fit K ($K = 2.4$ s^{-1}; 95% bootstrapped CI: $0.6, 3.6$ s^{-1}) is greater than the median of the best-fit K under individual fitting. Nonetheless, the best-fit value of K under background-PNP guidance is still substantially higher than the best-fit value under the inertial-PNP model. Furthermore, by comparing panels **C** and **F** of Figure 3.5**C**, it is clear that the background-PNP model is more sensitive to the value of K than the inertial-PNP model in its ability to successfully model the data. Whereas the inertial-PNP surface is almost flat with respect to K (while keeping the other parameters constant), the background-PNP surface has a negative slope as K increases (while keeping the other parameters constant) for most of the plotted range of K.

When $N = 0$, both inertial-PNP and background-PNP guidance instantiate PP guidance. Corroborating the result of the individual fitting approach, we find that PP guidance does not successfully model ($\tilde{\epsilon} = 255$ mm; 95% bootstrapped CI: $224, 277$

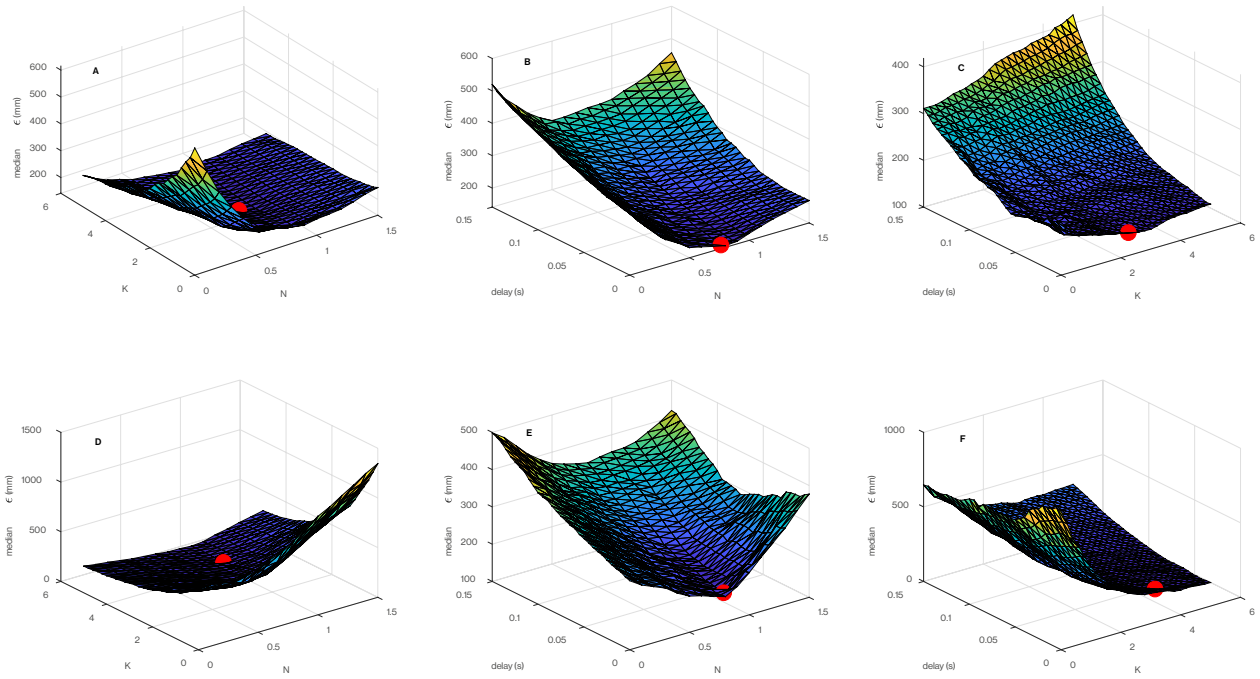


Figure 3.5: Both PNP guidance laws are successful models of the data, but background-PNP is more sensitive to the parameter K. In **A-C** we plot the median prediction error, $\tilde{\epsilon}$, under inertial-PNP guidance as a function of the different two parameter combinations from the three guidance parameters N, K, and τ (where we keep the third parameter constant at its best-fit value). In **D-F** we do the same under background-PNP guidance. Surface colouring represents $\tilde{\epsilon}$, whereas the red dot indicates the parameter combination that minimises $\tilde{\epsilon}$ under the global fit method. background-PNP guidance best fits the data at a higher value of K than PNP guidance; the steeper slope with respect to K in panel **F** compared to panel **D** also shows that the background-PNP model is more sensitive to K than the PNP model in its ability to successfully model the data.

mm) the steering of Harris' hawk attack trajectories when tested with the global fitting approach. Likewise, global fitting shows that background-PN guidance, instantiated by the background-PNP model when $K = 0$, does not successfully model ($\tilde{\epsilon} = 523$ mm; 95% bootstrapped CI: $459, 636$ mm) attack trajectories.

When $K = 0$, inertial-PNP guidance instantiates inertial-PN guidance. Interestingly, we find that the median prediction error, $\tilde{\epsilon}$ under inertial-PN guidance ($\tilde{\epsilon} = 174$ mm; 95% bootstrapped CI: $148, 225$ mm) is not substantially larger than under the inertial-PNP and background-PNP guidance models that have one extra parameter. The best-fit N under PN guidance ($N = 1$; 95% bootstrapped CI: $0.9, 1.1$) is similar to the best-fit N values under inertial-PNP and background-PNP guidance. We plot the surface of $\tilde{\epsilon}$ against N and τ under inertial- PN guidance in Figure B.3 of Appendix B.

The individual and global fitting approaches corroborate that there is no difference between the inertial-PNP and background-PNP guidance models in their fit to the data,

that their best-fit values of the guidance constant N are similar, and that the best-fit value of the parameter K is higher under background-PNP guidance. However, global fitting also suggests that inertial-PN guidance is not appreciably different to the PNP models in its ability to fit the data.

Given the results of the individual and global fitting methods, we carry forward the successful inertial-PNP, background-PNP, and inertial-PN guidance models to a validation step. We validate the models using k-fold cross-validation where $k = 12$ (see Methods and Materials). We measure the predictive ability of a model as the mean of the minimum $\tilde{\epsilon}$, which we denote $\bar{\tilde{\epsilon}}$. We find that the order of model predictive ability mirrors the order of model success under global fitting – inertial-PNP guidance has the best predictive power ($\bar{\tilde{\epsilon}} = 173$ mm), followed by background-PNP guidance ($\bar{\tilde{\epsilon}} = 179$ mm), followed by inertial-PN guidance ($\bar{\tilde{\epsilon}} = 191$ mm) (Figure B.4 in Appendix B). We plot the raw and simulated trajectories under the globally optimal guidance law parameter values for the first quartile error, median error, and third quartile error flights in Figure 3.6.

3.4 Discussion

Proportional navigation guidance models hawk attack trajectories The previous work on Harris' hawk pursuit has argued that inertial-PN is less appropriate than inertial-PNP for modelling hawk attack trajectories (Brighton et al., 2019). In our study, we find that the globally fitted inertial-PN guidance model performs only slightly worse than the globally fitted PNP guidance models, despite having one fewer parameter. We also do not find (Figure B.2 in Appendix B) that the prediction error under a globally fitted inertial-PNP guidance model is smaller than that under individual fitting of the inertial-PN guidance model, the reverse result of which Brighton et al. (2019) used to support their argument that Harris' hawk steering is more appropriately modelled by inertial-PNP guidance. Our results therefore suggest that the inertial-PN guidance model is appropriate to model Harris' hawk steering; the equivalent conclusion was also reached in studies on peregrine falcons (*Falco peregrinus*) (Brighton et al., 2017) and gyr falcons (*Falco rusticolus*) (Brighton et al., 2021). Like Brighton et al. (2019), who find that $\tilde{N} = 0.9$, we find that when Harris' hawk attack trajectories are modelled by inertial-PN guidance, the best-fit N is much lower than in peregrine falcons (median $N = 2.6$) (Brighton et al., 2017). Under the global fit method, we find a best-fit value of $N = 1$ given

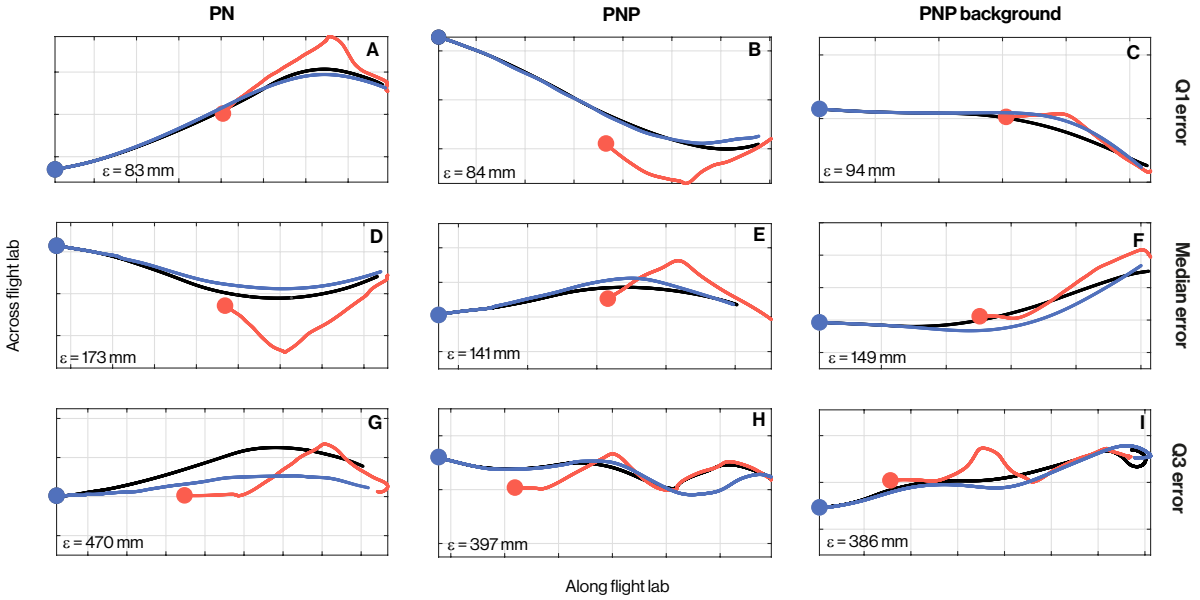


Figure 3.6: Simulated trajectories of the first quartile error, median error, and third quartile error flights under three guidance laws given globally best-fit parameter values. Given a lure trajectory (red), and a measured hawk trajectory (blue), we simulate the best fitting trajectory (black) under different guidance models given their best-fit guidance parameters found using the global fit method. The best-fit parameters under PN guidance are $N = 1.0$ and $\tau = 0.055$, under PNP guidance are $N = 0.8$, $K = 2.4$, and $\tau = 0.005$, and under background-PNP guidance are $N = 0.9$, $K = 3.6$, and $\tau = 0.015$. We plot the flights whose simulations have the prediction error, ϵ, at the first quartile (in **A**-**C**), the median (in **D**-**F**), and the third quartile (in **G**-**I**) of the error distributions under PN (**A**, **D**, **G**), PNP (**B**, **E**, **H**), and background-PNP (**C**, **F**, **I**) guidance. The specific ϵ associated with each flight's simulation is given in the bottom left corner of each panel. Note that all panels are plotted with the same data aspect ratio, but that the axis limits vary.

inertial-PN guidance, exactly the value required to implement the tailchase pursuit that is characteristic of Harris' hawks (Brighton et al., 2019; Shneydor, 2011). Furthermore, the median of the best-fit N values under independent fitting of inertial-PN guidance ($\tilde{N} = 0.85$) is remarkably close to the equivalent result in Brighton et al. (2019), showing a repeatability that is rare for studies in animal research (Frommlet, 2020). Our results therefore corroborate the effectiveness of modelling pursuit dynamics with inertial-PN guidance and support its use as a means to compare pursuit across different animal groups (Brighton et al., 2017; Brighton et al., 2019; Fabian et al., 2018).

Mechanising the inertial-PN guidance law To steer attack trajectories by the inertial-PN law, Harris' hawks would need to estimate the line-of-sight rate in an inertial reference frame, ${}^{\mathcal{I}}\dot{\lambda}$, an ability that hawks may or may not have. In space-stabilised homing missiles, a gimbaled tracking device called a seeker continuously directs its centreline along the line-of-sight, minimising target drift within the seeker coordinate system. The angular

rate of the seeker, which is measured by gyroscopic sensors, is then an estimate of ${}^{\mathcal{I}}\dot{\lambda}$ (Murtaugh et al., 1966; Palumbo et al., 2010). As Shneydor (2011) says, "there is no PN without a gyro". If a hawk were to use its head as a space-stabilised missile seeker, then it would need to keep the target at constant retinal coordinates by continuously rotating the head. The hawk would also need to measure the head's angular rate, which may be possible by the semi-circular canals of the hawk's vestibular system. Though some authors argue that the semi-circular canals can only transduce angular acceleration information (Warrick, 2002; Pennycuick, 2008), modelling suggests that they may also estimate angular velocity (Mayne, 1950; Goldberg et al., 1975; Muller, 2020). Under this mechanisation of PN guidance, the visual system directs inner loop guidance (Hardcastle et al., 2016) to stabilise the target's position in the retinal coordinate system, whereas the vestibular system provides outer loop guidance (see Figure 3.7**B**).

Mechanising inertial-PN by measuring the angular head rate lies at one extreme of a continuum. In strapdown missiles the seeker is fixed to the missile body (Palumbo et al., 2010); target drift in the seeker coordinate system of a rotationally stabilised missile is then an estimate of ${}^{\mathcal{I}}\dot{\lambda}$. If a hawk's head were to act as a strapdown seeker, then the hawk would need to keep the head fixed relative to the body and measure the target's retinal drift when the body is rotationally stabilised. In a more sophisticated mechanisation, the hawk could isolate the head movement from the body, keep the head rotationally stabilised as the body moves, and measure the target retinal drift in this state. Under this mechanisation, the inner ear system acts as the stabilising inner loop, whereas the retinal drift of the target, under the assumption of no eye movement (which research suggests is minimal in birds-of-prey (Steinbach, 1973; O'Rourke et al., 2010)), drives the outer loop (see Figure 3.7**C**).

How hawks move their heads is unclear because there is limited data on the head movements of predatory birds during pursuit. Data on a small number of inexperienced peregrine falcons indicates that these birds use their heads in a manner consistent with both extremes of the mechanisation spectrum. Peregrine falcons appear to mix head stabilisation with saccades during medium-phase pursuit, whereas they keep the target at consistent retinal coordinates during the terminal phase (Walker, 2018). There is more data on predatory insects and non-predatory birds. Among predatory insects, *Laphria* flies rotationally stabilise their head between rapid saccades, whereas dragonflies appear

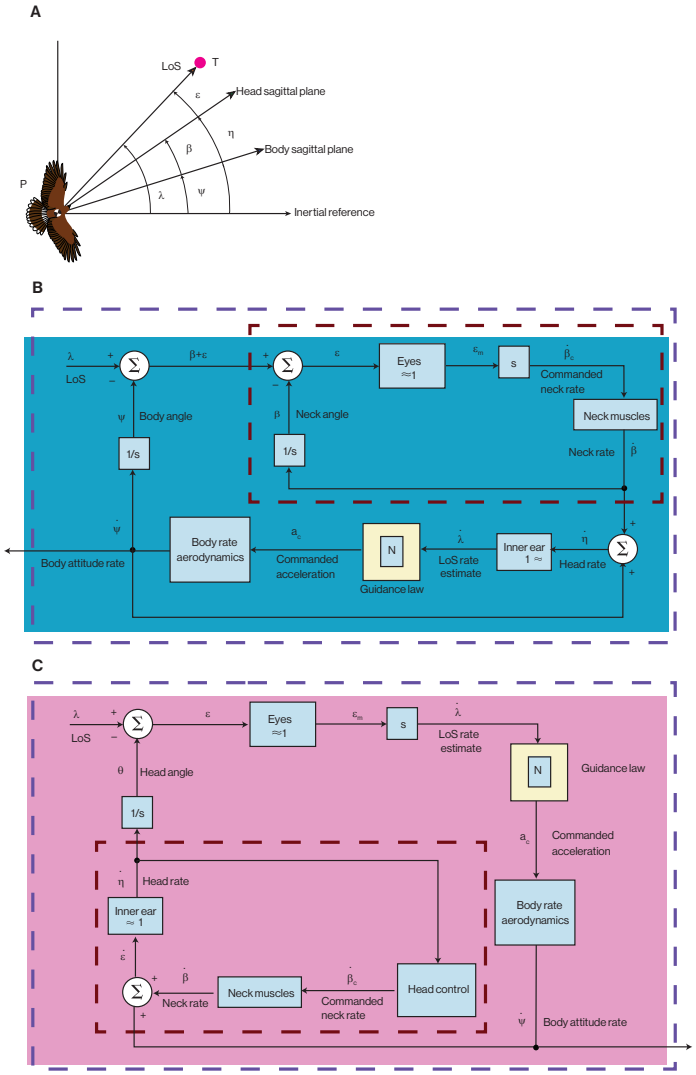


Figure 3.7: Different methods of mechanising the estimation of ${}^{\mathcal{I}}\dot{\lambda}$ are represented by different block diagrams. In **A** we show the relevant angles for mechanising pursuit by inertial-PN guidance. The line-of-sight angle in an inertial frame, λ, is a composite of the body angle, ψ, the neck angle, β, and an error angle, ϵ. The body angle, ψ, is defined as the angle between an inertial reference and the hawk body's sagittal plane, whereas the neck angle, β, is defined as the angle between the body sagittal plane and the hawk head's sagittal plane. The error angle, ϵ, is defined as the angle between the head sagittal plane and the target azimuth in retinal coordinates. Note that the head angle, η is defined as $\psi + \beta$. The inertial line-of-sight rate, ${}^{\mathcal{I}}\dot{\lambda}$, can be reconstructed in different ways. The block diagram in **B** mechanises the estimation of ${}^{\mathcal{I}}\dot{\lambda}$ by measuring the angular rate of the hawk's head, $\dot{\eta}$, as might the bird's semi-circular canals of the vestibular system. Here, the visual system acts as an inner loop (within red dashed line) to command the neck rate, $\dot{\beta}$, so as to minimise the error between the target and a fixed retinal position. The head rate, $\dot{\eta}$, is the sum of $\dot{\beta}$ and the body attitude rate, $\dot{\psi}$. The estimate of ${}^{\mathcal{I}}\dot{\lambda}$ drives outer loop guidance (within blue dashed line) that commands lateral accelerations to control the body attitude rate, $\dot{\psi}$, and hawk steering. In contrast, the block diagram in **C** drives outer loop guidance by estimating ${}^{\mathcal{I}}\dot{\lambda}$ visually as the retinal drift of the target. For this to be an accurate estimate of ${}^{\mathcal{I}}\dot{\lambda}$, the head must be rotationally stabilised such that $\dot{\eta} \approx 0$. Thus, the vestibular system here drives the inner loop (within red dashed line) by commanding $\dot{\beta}$ to neutralise the tendency for the head to turn with a body that is rotating with rate $\dot{\psi}$. This figure is adapted from Palumbo et al. (2010).

to continuously track a target with their head by keeping the target's retinal coordinates approximately constant (Mischiati et al., 2015; Lin et al., 2017). Among non-predatory birds, both the lovebird and the pigeon use a saccade and fixate gaze strategy during turning behaviour (Eckmeier et al., 2008; Kress et al., 2015; Ros et al., 2017). However, unpublished data on the Harris' hawk suggests that they lie at neither extreme of the mechanisation continuum. Instead, Harris' hawks allow their target to drift within about 5° of a fixed retinal location while fixing their head relative to their body. Hawks then saccade the head at upwards of $200°s^{-1}$ to refix the target retinal coordinates (Shelton, unpublished data).

Visual implementation of the mixed guidance law Given that the deviation angle, δ, can be measured purely visually (Ros et al., 2017), proportional pursuit (PP) is a guidance law that can be implemented with vision alone. However, like Brighton et al. (2019), we find that PP does not successfully model Harris' hawk attack trajectories. Nonetheless, we show that another guidance law that can implement guidance by vision alone – the background-PNP model – does successfully model Harris' hawk attack trajectories.

A third guidance law that allows vision only guidance is the background-PN model, which is a special case of the background-PNP law when $K = 0$. However, we find background-PN to be the least successful at simulating Harris' hawk attack trajectories among all fitted models. This shows that the success of the background-PNP model does not extend to background-PN guidance. This is not surprising; in the Supplementary Text of Appendix B we show that, for a Harris' hawk chasing terrestrial prey, the background line-of-sight rate ${}^{\mathcal{B}}\dot{\lambda}$ reflects only the component of the relative motion between hawk and target that is due to the target's motion. Thus, in lacking information on self-motion, the background-PN model cannot successfully command attack trajectories to intercept. How, then, does the background-PNP law successfully model attack trajectories? In the Supplementary Text of Appendix B we show that ${}^{\mathcal{I}}\dot{\lambda}$ can be rewritten as $(v_T \sin\theta - v_P \sin\delta)/r$, and we show that ${}^{\mathcal{B}}\dot{\lambda}$ can be rewritten as $v_T \sin\theta/r$. This means that one can rewrite the equations presented in Table 3.1 for the background-PN, inertial-PNP,

and background-PNP models respectively as:

$$^{\mathcal{I}}\dot{\gamma} = N\frac{v_T \sin\theta}{r}, \tag{3.6}$$

$$^{\mathcal{I}}\dot{\gamma} = N\frac{v_T \sin\theta}{r} - N\frac{v_P \sin\delta}{r} - K\delta, \tag{3.7}$$

$$^{\mathcal{I}}\dot{\gamma} = N\frac{v_T \sin\theta}{r} - K\delta, \tag{3.8}$$

where we have omitted the time dependence of the variables for clarity. The lack of $v_P \sin\delta/r$ in Equations 3.6 and 3.8 reflects the lack of self-motion information in these guidance models. However, whereas the background-PNP model has one term in the variable δ, the background-PN model has none. Thus, the background-PNP model can account for self-motion information lost in the absence of the $v_P \sin\delta/r$ term, whereas the background-PN model cannot. Indeed, Equations 3.7 and 3.8 demonstrate how the background-PNP law, which has similar model fitting success as the inertial-PNP law, must operate at a higher best-fit K. For example, in the case that equal model fitting success (defined here as when the median prediction error under both models is the same) is achieved because both models produce the same steering commands, this means that $N(v_P \sin\delta)/r - K_{\mathcal{I}}\delta = K_{\mathcal{B}}\delta$, where $K_{\mathcal{I}}$ refers to the constant K in the inertial-PNP model and $K_{\mathcal{B}}$ refers to the constant K in the background-PNP model. Given that N tends to be positive (see Figure 3.4), this means that the constraint $N(v_P \sin\delta)/r - K_{\mathcal{I}}\delta = K_{\mathcal{B}}\delta$ is only satisfied when $K_{\mathcal{B}} > K_{\mathcal{I}}$. As a consequence, we see that the effect of swapping the best-fit K values between the inertial-PNP and background-PNP models is to substantially increase the prediction error, ϵ, under background-PNP guidance (Figure 3.8). However, we do not see the same sensitivity under inertial-PNP guidance (as also indicated by Figure 3.5**C**), which is because of the redundancy in δ in Equation 3.7.

Neural encoding of the line-of-sight rate Feature detecting neurons that are tuned to the motion of small targets have been found in many flying insect species (Nordström et al., 2006; Evans et al., 2022). Some neurons among these small target motion dector (STMD) neurons also show properties that imply the ability to estimate $^{\mathcal{I}}\dot{\lambda}$. For example, the STMD responses of hoverflies and dragonflies are unaffected when target motion is projected onto background motion (Nordström et al., 2006; Evans et al., 2022). When treated with octopamine, a neuromodulator that flushes the *Drosophila melanogaster* nervous system during flight, the LC12 and LC15 target detecting neurons of this species

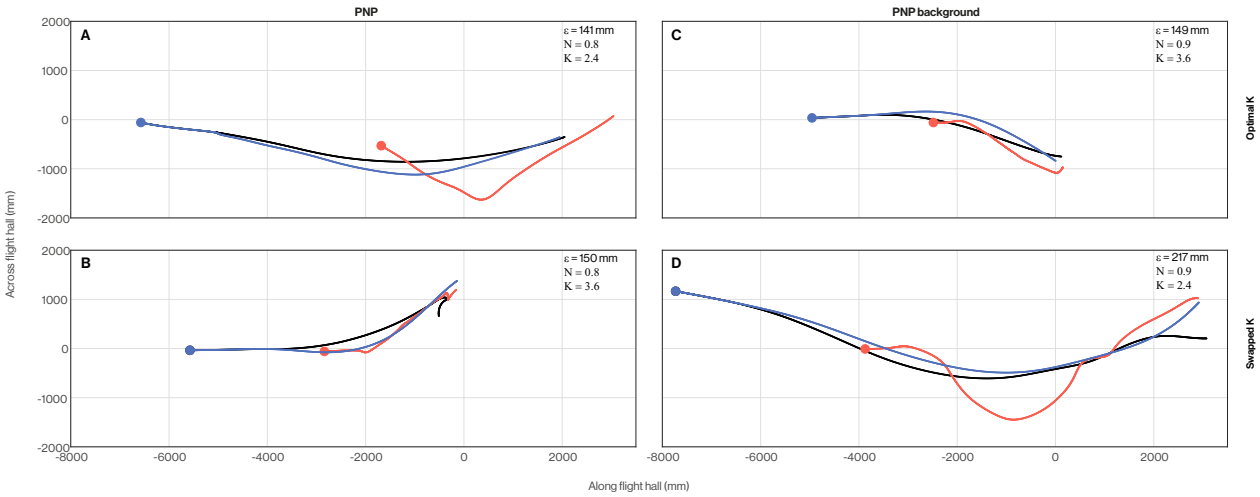


Figure 3.8: The effect of swapping the best-fit K between PNP and background-PNP guidance simulations. Given a lure trajectory (red), and a measured hawk trajectory (blue), we simulate trajectories (black) under PNP (**A-B**) and background-PNP guidance (**C-D**). In **A** we plot the median error trajectory under PNP guidance given this model's globally optimal parameter values $N = 0.8$, $K = 2.4$, and $\tau = 0.005$. In **B** we plot the median error trajectory under background-PNP guidance given this model's globally optimal parameter values $N = 0.9$, $K = 3.6$, and $\tau = 0.015$. To test the impact of swapping the best-fit K parameter values between the two guidance models, we plot the median error trajectory under PNP guidance in **C** given the best-fit $K = 3.6$ under background-PNP guidance, whereas in **D** we plot the median error trajectory under background-PNP guidance given the best-fit $K = 2.4$ under PNP guidance. The prediction error, ϵ, associated with each flight is given is the top right corner of each panel.

are also unaffected by background motion (Städele et al., 2020; Keleş et al., 2020). These examples imply a mechanism, if an insect rotationally stabilises its head, that estimates ${}^{\mathcal{I}}\dot{\lambda}$. In contrast, the response of target sensitive descending neurons (TSDNs) – which lie closer to the motor neurons commanding locomotion (Namiki et al., 2018) – in the hoverfly and the robberfly are affected by background motion (Nicholas et al., 2018; Nicholas et al., 2021). In particular, TSDN response is a function of the relative motion between target and background; under syndirectional target and background motion of the same speed, TSDN response is totally suppressed (Nicholas et al., 2018). TSDN responses suggest that these neurons respond not to the retinal drift of a target but to the retinal drift of the target relative to the retinal drift of the background. They therefore imply a mechanism for estimating ${}^{\mathcal{B}}\dot{\lambda}$. Furthermore, inhibition of TSDNs persists even when the region of syndirectional optic flow is small and restricted to the frontal visual field (Nicholas et al., 2021), the region that contains the background close to the target.

In the bird brain's tectofugal system there are neurons tuned to small object motion (Jassik-Gerschenfeld et al., 1972), much as the STMDs of the hoverfly lobula complex. These tectofugal neurons have directionally selective receptive fields (Frost et al., 1976) and,

of interest to measuring the the line-of-sight rate, this directional senstivity is dependent upon background motion (Frost et al., 1990). As in the TSDN response of hoverflies and robberflies, neurons of the tectofugal system in pigeons are suppressed when object and background motion are syndirectional (Frost, 1978). Furthermore, when the background and object motion are contradirectional, the neuronal output is augmented.

Conclusion We find that the inertial-PN guidance law performs nearly as well as the inertial-PNP and background-PNP guidance laws at modelling the Harris' hawk attack trajectories that we measured. Unlike the background-PNP model, which requires only visual information to implement guidance, the inertial-PN model requires the fusion of visual and inertial information. Visual-only pursuit is also possible under the PP law, but we find that this guidance law does not successfully model the data. Thus, we are left with inertial-PN as the most parsimonious model that implies fusion of visual and inertial information, whereas background-PNP is the only well-fitting candidate for pursuit guidance by vision alone. Of relevance to the background-PNP model, the response properties of some neurons in both insects and pigeons may be amenable to estimate the ${}^{\mathcal{B}}\dot{\lambda}$ input of this model.

3.5 Materials and Methods

Experimental protocol Between January and February 2018 we trained $N = 4$ captive-bred Harris' hawks (*Parabuteo unicinctus*) to perform pursuit of an unpredictably moving artificial lure. We performed 157 training trials and, from February to March 2018, we flew the same $N = 4$ Harris' hawks (one female hawk of 7 years, three males of < 1 year) in 330 test trials. We conducted all flight trials at the John Krebs Field Station (Wytham, Oxford, UK). In each trial, we pulled the lure through an unpredictable, zigzagging course by a tow line attached to two parallel Aerotech ACT140DL linear actuators (Aerotech Limited, Hampshire, UK). We randomised the lure starting position, trajectory, and speed (between 6 and 8 ms^{-1}) across trials to prevent the hawks predicting the target's motion. We created the lure course by guiding the tow line around a system of pulleys. The setup approximated the natural hunting conditions of the Harris' hawk, which principally pursues lagomorphs that jink across the ground (Bednarz, 1988). We conducted the trials in a flight hall with floor dimensions of 20.2 m $\times$ 6.1 m, and with a minimum ceiling

height of 3.8 m. We lit the windowless hall with flicker-free LED lamps that provided lighting at circa 1000 lux, mimicking an overcast day.

Motion capture Between January and February 2018 we trained $N = 4$ captive-bred Harris' hawks (*Parabuteo unicinctus*) to perform pursuit of an unpredictably moving artificial lure. We performed 157 training trials and, from February to March 2018, we flew the same $N = 4$ Harris' hawks (one female hawk of 7 years, three males of < 1 year) in 330 test trials. We conducted all flight trials at the John Krebs Field Station (Wytham, Oxford, UK). In each trial, we pulled the lure through an unpredictable, zigzagging course by a tow line attached to two parallel Aerotech ACT140DL linear actuators (Aerotech Limited, Hampshire, UK), as shown in Figure 3.9**A-B**. We randomised the lure starting position, trajectory, and speed (between 6 and 8 ms^{-1}) across trials to prevent the hawks predicting the target's motion. We created the lure course by guiding the tow line around a system of pulleys. The setup approximated the natural hunting conditions of the Harris' hawk, which principally pursues lagomorphs that jink across the ground (Bednarz, 1988). We conducted the trials in a flight hall with floor dimensions of 20.2 m $\times$ 6.1 m, and with a minimum ceiling height of 3.8 m. We lit the windowless hall with flicker-free LED lamps that provided lighting at circa 1000 lux, mimicking an overcast day.

Motion capture We recorded flight trajectories with twenty motion capture cameras (Vicon Vantage 16, Vicon Motion Systems Ltd, Oxford, UK) positioned 3 m above floor level in the flight hall. The motion capture cameras recorded at 200 Hz under stroboscopic 850 nm infrared illumination. We calibrated the cameras using an Active Calibration Wand (Vicon Motion Systems Ltd, Oxford, UK) that we also used to set the capture volume origin and ground plane. To record flight trajectories, we fitted each hawk with two rigid templates holding 6.4 mm spherical, retroreflective markers (Figure 3.9**C**). We attached one template holding four asymmetrically arranged markers to the back by falconry harness (TrackPack Mounting System, Marshall Radio Telemetry, UT, USA), and another template holding three symetrically arranged markers to the tail by falconry mount (Marshall Aluminium Tail Feather Piece, Marshall Radio Telemetry Ltd, Cumbria, UK). We also attached 3 mm markers to the head, wings, and tail, but do not analyse this data here. To record the lure trajectory, we attached three 6.4 mm markers to each long face of the lure. We also attached markers to the pulley system and the tunnels from which the lure started.

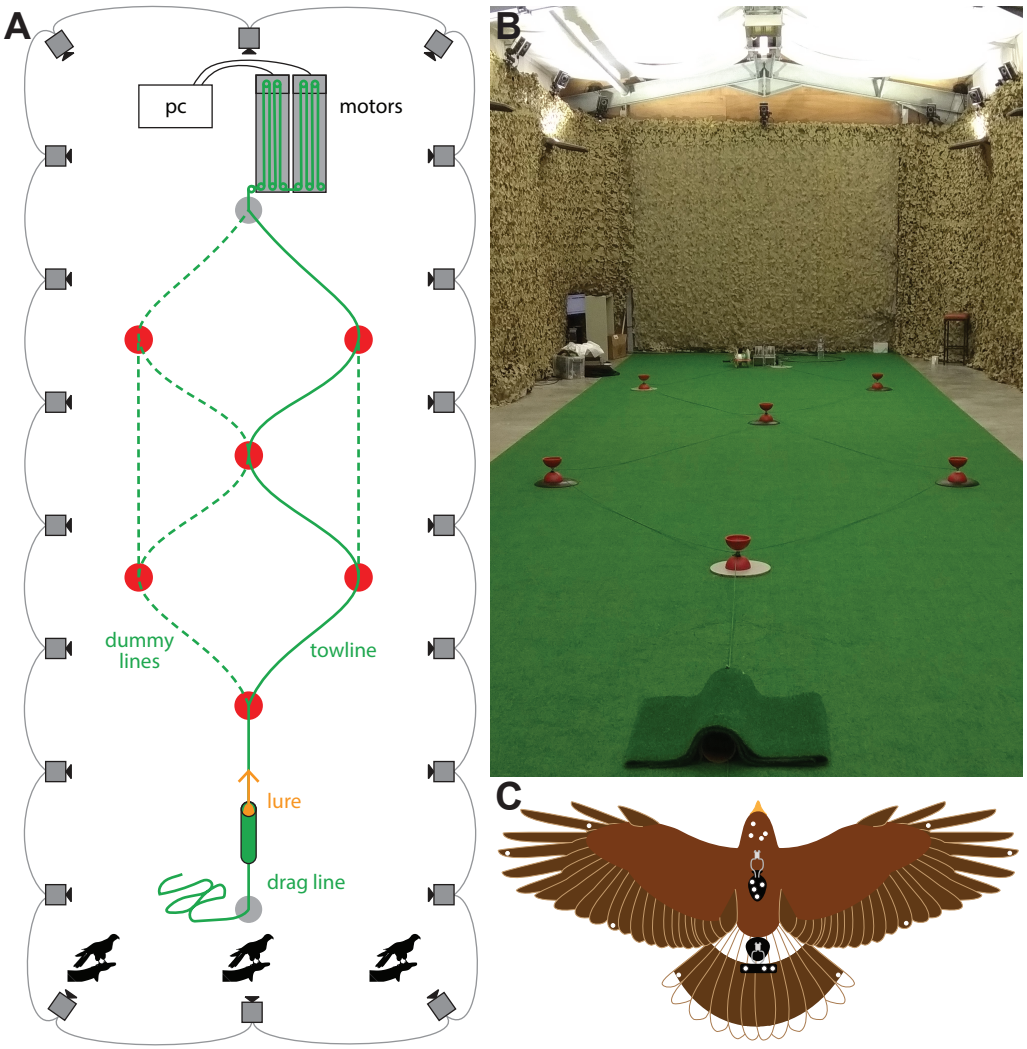


Figure 3.9: The setup of the pursuit task. In **A** we show a schematic of the experimental setup from an overhead view. The approximate (projected) positions of the 20 motion capture cameras are indicated by the camera icons, while the bird icons indicate the three different starting bird positions. We also indicate the approximate positions of the 6 pulleys (red circles), and the 6 possible lure paths (green lines). To prevent the hawks predicting the lure path, we laid dummy tow lines for each trial (dotted green line), in addition to the motor-connected tow line (solid green line). We randomised the lure path between trials. In **B** we show a photo of the same set-up, from the perspective of the middle starting position. In **C** we show an overhead schematic of a Harris' hawk wearing the retroreflective markers (white circles) needed for motion capture and the rigid templates (black) to which we attached some markers.

Data processing We reconstructed marker positions to submillimetre precision, with respect to a coordinate system fixed to the principal axes of the flight hall, using Vicon Nexus 2.7.6 software (Vicon Motion Systems Ltd, Oxford, UK). However, as marker labelling using the Vicon software was unreliable, we wrote a custom marker labelling script in MATLAB R2019a (The Mathworks Inc., MA, USA). This script first pooled those markers that remained within the same 10 mm range for $\geq 60\%$ of the frames and labelled them stationary markers; these are markers on the pulley system and starting tunnels.

The remaining unlabelled markers are either bird or lure markers. We distinguished lure markers as those that exist ≤ 150 mm from the floor plane, given the lure motion over the floor. We define lure position as the mean position over lure markers for each frame. We used the rigid pairwise distances between markers on the back and tail templates to define, search for, and label the respective templates. Due to wear or damage, we occasionally replaced markers and we therefore defined templates on a per-day basis. The pairwise distances between every marker in the same frame were compared against, and matched, with each template with a tolerance of 5 mm to label the bird markers (see also KleinHeerenbrink et al. (2022)). We continued to analyse those flight trials in which back template markers could be reconstructed in $> 50\%$ of frames; having applied this criterion, we proceeded with 274 flight trials.

We used the centroid of the back template markers, tail template markers, and lure markers as our initial estimate of their respective positions. We considered any frames for which fewer than 3 markers were detected for either of the templates or lure as missing data. The trajectory outputs often contained some misidentified outlying points which we filtered out from the raw data using a mean sliding window elimination. We subtracted the smoothed trajectory (with window size of 20 Hz) from the raw data, and removed any remaining points with a distance > 500 mm from the raw data. Having removed the extreme outliers, we removed jitter caused by marker dropout by applying a second mean sliding window to eliminate outliers at a distance threshold of > 75 mm, following the same method as above. We aligned the 'cleaned' raw bird and lure data streams using the frame number, and cropped them to start at the first frame where both bird and lure were visible. To define the position of the hawk, we took the mean position of all markers detected on the back template and tail template for each frame. Of the 274 flight trials, we analysed only those in which an intercept occurred. We defined intercept as that point in which the bird came within ≥ 30 mm of the lure during recording. Following this selection criterion, we continued to analyse $n = 228$ flight trials.

We performed a cubic interpolation to fill in missing data points and fitted a quintic spline to smooth the data, using a tolerance of 0.03 m for the bird data and 0.01 m for the lure data. Finally, we differentiated and evaluated the splines analytically, to estimate the velocity and acceleration of the bird and lure at 20 kHz, resulting in a sufficiently small integration step size for our simulations.

Simulations of guidance behaviour We simulated the measured flight trajectory of a hawk by calculating the hawk's turning rate ${}^{\mathcal{I}}\dot{\gamma}(t)$ under different guidance models. Specifically, we predicted a hawk's turning under (i) the proportional pursuit (PP) guidance law, ${}^{\mathcal{I}}\dot{\gamma}(t) = -K\delta(t-\tau)$, where $\delta = \gamma - \lambda$ is the deviation angle between the hawk's velocity vector v_p and the line-of-sight vector, $\boldsymbol{r}(t)$, K is a guidance constant, and τ is a delay parameter; (ii) the inertial-PN guidance law, ${}^{\mathcal{I}}\dot{\gamma}(t) = N\,{}^{\mathcal{I}}\dot{\lambda}(t-\tau)$, where ${}^{\mathcal{I}}\dot{\lambda}$ is the time rate of change in the line-of-sight angle λ with respect to an inertial reference frame $\mathcal{F}_I$ and N is a guidance constant; (iii) the background-PN guidance law, ${}^{\mathcal{I}}\dot{\gamma}(t) = N\,{}^{\mathcal{B}}\dot{\lambda}(t-\tau)$, where ${}^{\mathcal{B}}\dot{\lambda}$ is the time rate of change in the line-of-sight λ with respect to the background reference frame $\mathcal{F}_B$; (iv) the inertial-PNP guidance law, ${}^{\mathcal{I}}\dot{\gamma}(t) = N\,{}^{\mathcal{I}}\dot{\lambda}(t-\tau) - K\delta(t-\tau)$; and (v) the background-PNP background guidance law, ${}^{\mathcal{I}}\dot{\gamma}(t) = N\,{}^{\mathcal{B}}\dot{\lambda}(t-\tau) - K\delta(t-\tau)$.

To compute the simulated trajectory, we used the initial position and velocity of the hawk, the measured time-history of the lure's position and velocity, and we forced the hawk's ground speed to match that measured. We used only the trajectory data in the horizontal plane for simulations. We calculated the line-of-sight vector, $\boldsymbol{r}(t)$, as:

$$\boldsymbol{r}(t) = \hat{\boldsymbol{r}}_T(t-\tau) - \boldsymbol{r}_P(t-\tau), \tag{3.9}$$

where $\hat{\boldsymbol{r}}_T(t-\tau)$ is the measured lure position at the time $t-\tau$, and $\boldsymbol{r}_P(t-\tau)$ is the simulated hawk position at the time $t-\tau$. We calculated the deviation angle, δ, as:

$$\delta(t) = \cos^{-1}\left(\frac{\boldsymbol{r}(t)\cdot\boldsymbol{v}_P(t-\tau)}{r(t)\hat{v}_P(t-\tau)}\right), \tag{3.10}$$

where $\boldsymbol{v_p}(t-\tau)$ is the hawk's simulated velocity at time $t-\tau$, $r(t)$ is the magnitude of the line-of-sight vector, and $\hat{v}_p(t-\tau)$ is the hawk's measured speed at time $t-\tau$. The angular velocity of $\boldsymbol{r}(t)$ depends on the reference frame in which it is calculated. In the inertial frame, $\mathcal{F}_{\mathcal{I}}$, we have:

$$\boldsymbol{\omega_I}(t) = \frac{\boldsymbol{r}(t)\times\boldsymbol{v}_C(t-\tau)}{r(t)^2}, \tag{3.11}$$

where $\boldsymbol{v}_C(t-\tau) = \hat{\boldsymbol{v}}_T(t-\tau) - \boldsymbol{v}_P(t-\tau)$ is called the closing velocity at time $t-\tau$, $\hat{\boldsymbol{v}}_T(t-\tau)$ is the measured lure velocity at time $t-\tau$, and $\boldsymbol{\omega}_I(t)$ is the simulated angular

velocity of the line-of-sight vector in an inertial reference frame and which is used to command steering at time t. In the background frame, $\mathcal{F}_{\mathcal{B}}$, the angular velocity of the LoS vector, $\boldsymbol{\omega}_B(t)$, used to command steering is:

$$\boldsymbol{\omega_B}(t) = \frac{\boldsymbol{r}(t) \times \boldsymbol{v}_T(t-\tau)}{r(t)^2}, \tag{3.12}$$

which we derive in the Supplementary Text of Appendix B. The background frame of reference, $\mathcal{F}_{\mathcal{B}}$, is defined by the orthonormal basis vectors $\mathbf{1}_{\boldsymbol{x'}}$ and $\mathbf{1}_{\boldsymbol{y'}}$, the former of which always points at a background patch close to the target.

Each guidance model that we test commands a lateral acceleration $\boldsymbol{a}(t)$ at time t. Under the five guidance models, the lateral accelerations are commanded as:

$$\boldsymbol{a}(t) = -K\boldsymbol{\delta}(t) \times \boldsymbol{v}_P(t-1) \tag{3.13}$$

$$\boldsymbol{a}(t) = N\boldsymbol{\omega_I}(t) \times \boldsymbol{v}_P(t-1) \tag{3.14}$$

$$\boldsymbol{a}(t) = N\boldsymbol{\omega_B}(t) \times \boldsymbol{v}_P(t-1) \tag{3.15}$$

$$\boldsymbol{a}(t) = N\boldsymbol{\omega_I}(t) \times \boldsymbol{v}_P(t-1) - K\boldsymbol{\delta}(t) \times \boldsymbol{v}_P(t-1) \tag{3.16}$$

$$\boldsymbol{a}(t) = N\boldsymbol{\omega_B}(t) \times \boldsymbol{v}_P(t-1) - K\boldsymbol{\delta}(t) \times \boldsymbol{v}_P(t-1) \tag{3.17}$$

We simulated the Harris' Hawk trajectories by implementing the preceding continuous time equations in discrete time with the difference equations:

$$\boldsymbol{r}_{P_n} = \boldsymbol{r}_{P_{n-1}} + \Delta t \boldsymbol{v}_{P_{n-1}}, \tag{3.18}$$

$$\boldsymbol{v}_{P_n} = \hat{v}_{P_{n-1}} \frac{\boldsymbol{v}_{P_{n-1}} + \Delta t \boldsymbol{a}_{n-1}}{v_{P_{n-1}} + \Delta t a_{n-1}}, \tag{3.19}$$

where $\boldsymbol{r}_{P_n}$ is the hawk's simulated position vector at time step n, $\boldsymbol{r}_{P_{n-1}}$ is the hawk's simulated position vector at time step $n-1$, $\boldsymbol{v}_{P_n}$ is the hawk's simulated velocity at time step n, $\boldsymbol{v}_{P_{n-1}}$ is the hawk's simulated velocity at time step $n-1$, $v_{P_{n-1}}$ is the hawk's simulated speed at time step $n-1$, $\hat{v}_{P_{n-1}}$ is the hawk's measured speed time at time step $n-1$, $\boldsymbol{a}_{n-1}$ is the hawk's simulated lateral acceleration at time step $n-1$, a_{n-1} is the magnitude of the hawk's simulated lateral acceleration at time step $n-1$, and Δt is the size of the time step.

We implemented Equations 3.18–3.19 to simulate hawk trajectories for each of the guidance models in Equations 3.13–3.17.

Model fitting For each guidance model we simulated each hawk trajectory individually under different values of time delay τ. We varied the time delay τ, where $0 \leq \tau \leq \tau_{max}$ and $\tau_{max} = 0.15$ s, at intervals of 0.005 s (the sampling period of the Vicon system). For each value of τ, we used a Nelder-Mead simplex algorithm to find the values of N or K that minimised the prediction error ϵ between the simulated and measured trajectories, where ϵ is the root mean-squared error:

$$\epsilon = \frac{1}{k}\sqrt{\sum_{n=1}^{k}(\boldsymbol{r}_{p_n} - \hat{\boldsymbol{r}}_{p_n}) \cdot (\boldsymbol{r}_{p_n} - \hat{\boldsymbol{r}}_{p_n})}. \tag{3.20}$$

We found the optimum τ by finding the minimum ϵ across all fitted τ. We call this approach the individual fitting approach.

We also fitted the PNP and background-PNP guidance laws globally across all flights. We found the unique combination of N, K and τ that minimised the median prediction error $\tilde{\epsilon}$ by varying N on the interval $[0, 1.5]$ with 0.1 spacing, K on the interval $[0, 5]$ s^{-1} with 0.2 s^{-1} spacing, and τ on the interval $[0, 0.15]$ s with 0.005 s spacing.

Guidance model comparison For the PNP and background-PNP guidance models, we calculated bootstrapped 95% confidence intervals (CIs) for the median prediction error, $\tilde{\epsilon}$, and median guidance constants, $\tilde{N}$, $\tilde{K}$, and $\tilde{\tau}$, from the $n = 228$ independently fit simulations. We computed the 95 % CIs using the bias-corrected and accelerated percentile method over 10^6 iterations in Matlab v2018b. We also calculated bootstrapped 95% confidence intervals (CIs) for the minimum $\tilde{\epsilon}$ and associated guidance parameters given global fitting. We used the same bias-corrected and accelerated percentile method, but over 10^3 iterations.

To address the predictive power among the PN, PNP, and background-PNP guidance models, we performed a k-fold cross-validation analysis on these models. We split the $n = 228$ flight trials into $k = 12$ data subsets, each of $N = 19$ trials, and applied the global fitting method to the 12 unique combinations of $k - 1$ data subsets. We then calculated $\tilde{\epsilon}$ under the global best-fit parameters found for each guidance model when each model was tested on the excluded data subset for each combination of $k - 1$ subsets.

References

Bednarz, J. C. (1988). "Cooperative Hunting in Harris' Hawks (Parabuteo unicinctus)". en. In: *Science* 239.4847, pp. 1525–1527.

Benson, R. B. J., Starmer-Jones, E., Close, R. A., and Walsh, S. A. (Dec. 2017). "Comparative analysis of vestibular ecomorphology in birds". en. In: *Journal of Anatomy* 231.6, pp. 990–1018. DOI: 10.1111/joa.12726.

Boeddeker, N. and Egelhaaf, M. (Sept. 2003). "Steering a virtual blowfly: simulation of visual pursuit". en. In: *Proceedings of the Royal Society of London. Series B: Biological Sciences* 270.1527, pp. 1971–1978. DOI: 10.1098/rspb.2003.2463.

Brighton, C. H., Chapman, K. E., Fox, N. C., and Taylor, G. K. (Mar. 2021). "Attack behaviour in naive gyrfalcons is modelled by the same guidance law as in peregrine falcons, but at a lower guidance gain". en. In: *Journal of Experimental Biology* 224.5, jeb238493. DOI: 10.1242/jeb.238493.

Brighton, C. H. and Taylor, G. K. (Dec. 2019). "Hawks steer attacks using a guidance system tuned for closepursuit of erratically manoeuvring targets". en. In: *Nature Communications* 10.1, p. 2462. DOI: 10.1038/s41467-019-10454-z.

Brighton, C. H., Thomas, A. L. R., and Taylor, G. K. (Dec. 2017). "Terminal attack trajectories of peregrine falcons are described by the proportional navigation guidance law of missiles". en. In: *Proceedings of the National Academy of Sciences* 114.51, pp. 13495–13500. DOI: 10.1073/pnas.1714532114.

Eckmeier, D., Geurten, B. R. H., Kress, D., Mertes, M., Kern, R., Egelhaaf, M., and Bischof, H.-J. (Dec. 2008). "Gaze Strategy in the Free Flying Zebra Finch (Taeniopygia guttata)". en. In: *PLoS ONE* 3.12. Ed. by E. Greene, e3956. DOI: 10.1371/journal.pone.0003956.

Evans, B. J. E., O'Carroll, D. C., Fabian, J. M., and Wiederman, S. D. (Apr. 2022). "Dragonfly Neurons Selectively Attend to Targets Within Natural Scenes". en. In: *Frontiers in Cellular Neuroscience* 16, p. 857071. DOI: 10.3389/fncel.2022.857071.

Fabian, S. T., Sumner, M. E., Wardill, T. J., Rossoni, S., and Gonzalez-Bellido, P. T. (Oct. 2018). "Interception by two predatory fly species is explained by a proportional navigation feedback controller". en. In: *Journal of The Royal Society Interface* 15.147, p. 20180466. DOI: 10.1098/rsif.2018.0466.

Frommlet, F. (Dec. 2020). "Improving reproducibility in animal research". en. In: *Scientific Reports* 10.1, 19239, s41598–020–76398–3. DOI: 10.1038/s41598-020-76398-3.

Frost, B. (Aug. 1978). "Moving background patterns alter directionally specific responses of pigeon tectal neurons". en. In: *Brain Research* 151.3, pp. 599–603. DOI: 10.1016/0006-8993(78)91093-4.

Frost, B. and DiFranco, D. E. (Jan. 1976). "Motion characteristics of single units in the pigeon optic tectum". en. In: *Vision Research* 16.11, pp. 1229–1234. DOI: 10.1016/0042-6989(76)90046-8.

Frost, B., Wylie, D., and Wang, Y.-C. (Jan. 1990). "The processing of object and self-motion in the tectofugal and accessory optic pathways of birds". en. In: *Vision Research* 30.11, pp. 1677–1688. DOI: 10.1016/0042-6989(90)90152-B.

Ghose, K., Horiuchi, T. K., Krishnaprasad, P. S., and Moss, C. F. (Apr. 2006). "Echolocating Bats Use a Nearly Time-Optimal Strategy to Intercept Prey". en. In: *PLoS Biology* 4.5. Ed. by M. Dickinson, e108. DOI: 10.1371/journal.pbio.0040108.

Goldberg, J. M. and Fernández, C. (1975). "Vestibular Mechanisms". en. In: *Annu. Rev. Physiol.*, p. 34.

Guilford, T. and Taylor, G. K. (2014). "The sun compass revisited". In: *Animal Behaviour* 97, pp. 135–143. DOI: 10.1016/j.anbehav.2014.09.005.

Hardcastle, B. J. and Krapp, H. G. (Oct. 2016). "Evolution of Biological Image Stabilization". en. In: *Current Biology* 26.20, R1010–R1021. DOI: 10.1016/j.cub.2016.08.059.

Haselsteiner, A. F., Gilbert, C., and Wang, Z. J. (June 2014). "Tiger beetles pursue prey using a proportional control law with a delay of one half-stride". en. In: *Journal of The Royal Society Interface* 11.95, p. 20140216. DOI: 10.1098/rsif.2014.0216.

Hein, A. M., Altshuler, D. L., Cade, D. E., Liao, J. C., Martin, B. T., and Taylor, G. K. (June 2020). "An Algorithmic Approach to Natural Behavior". en. In: *Current Biology* 30.11, R663–R675. DOI: 10.1016/j.cub.2020.04.018.

Jassik-Gerschenfeld, D. and Guichard, J. (May 1972). "Visual receptive fields of single cells in the pigeon's optic tectum". en. In: *Brain Research* 40.2, pp. 303–317. DOI: 10.1016/0006-8993(72)90136-9.

Keleş, M. F., Hardcastle, B. J., Städele, C., Xiao, Q., and Frye, M. A. (Feb. 2020). "Inhibitory Interactions and Columnar Inputs to an Object Motion Detector in Drosophila". en. In: *Cell Reports* 30.7, 2115–2124.e5. DOI: 10.1016/j.celrep.2020.01.061.

KleinHeerenbrink, M., France, L. A., Brighton, C. H., and Taylor, G. K. (July 2022). "Optimization of avian perching manoeuvres". en. In: *Nature* 607.7917, pp. 91–96. DOI: 10.1038/s41586-022-04861-4.

Kress, D., van Bokhorst, E., and Lentink, D. (June 2015). "How Lovebirds Maneuver Rapidly Using Super-Fast Head Saccades and Image Feature Stabilization". en. In: *PLOS ONE* 10.6. Ed. by D. Wylie, e0129287. DOI: 10.1371/journal.pone.0129287.

Lin, H.-T. and Leonardo, A. (Apr. 2017). "Heuristic Rules Underlying Dragonfly Prey Selection and Interception". en. In: *Current Biology* 27.8, pp. 1124–1137. DOI: 10.1016/j.cub.2017.03.010.

Mayne, R. (1950). "THE DYNAMIC CHARACTERISTICS OF THE SEMICIRCULAR CANALS". en. In: *J. Comp. Physiol. Psychol.*, p. 11.

Mischiati, M., Lin, H.-T., Herold, P., Imler, E., Olberg, R., and Leonardo, A. (Jan. 2015). "Internal models direct dragonfly interception steering". en. In: *Nature* 517.7534, pp. 333–338. DOI: 10.1038/nature14045.

Muller, M. (1990). "Relationships between semicircular duct radii with some implications for time constants". In: *Netherlands Journal of Zoology* 40, pp. 173–202.

Muller, M. (Oct. 2020). "Mechanical aspects of the semicircular ducts in the vestibular system". en. In: *Biological Cybernetics* 114.4-5, pp. 421–442. DOI: 10.1007/s00422-020-00842-w.

Murtaugh, S. A. and Criel, H. E. (Dec. 1966). "Fundamentals of proportional navigation". en. In: *IEEE Spectrum* 3.12, pp. 75–85. DOI: 10.1109/MSPEC.1966.5217080.

Namiki, S., Dickinson, M. H., Wong, A. M., Korff, W., and Card, G. M. (June 2018). "The functional organization of descending sensory-motor pathways in Drosophila". en. In: *eLife* 7, e34272. DOI: 10.7554/eLife.34272.

Nicholas, S. and Nordström, K. (Sept. 2021). "Facilitation of neural responses to targets moving against optic flow". en. In: *Proceedings of the National Academy of Sciences* 118.38, e2024966118. DOI: 10.1073/pnas.2024966118.

Nicholas, S., Supple, J., Leibbrandt, R., Gonzalez-Bellido, P. T., and Nordström, K. (Dec. 2018). "Integration of Small- and Wide-Field Visual Features in Target-Selective Descending Neurons of both Predatory and Nonpredatory Dipterans". en. In: *The Journal of Neuroscience* 38.50, pp. 10725–10733. DOI: 10.1523/JNEUROSCI.1695-18.2018.

Nordström, K., Barnett, P. D., and O'Carroll, D. C. (Feb. 2006). "Insect Detection of Small Targets Moving in Visual Clutter". en. In: *PLoS Biology* 4.3. Ed. by T. Collett, e54. DOI: 10.1371/journal.pbio.0040054.

O'Rourke, C. T., Hall, M. I., Pitlik, T., and Fernández-Juricic, E. (Sept. 2010). "Hawk Eyes I: Diurnal Raptors Differ in Visual Fields and Degree of Eye Movement". en. In: *PLoS ONE* 5.9. Ed. by E. Warrant, e12802. DOI: 10.1371/journal.pone.0012802.

Palumbo, N. F., Blauwkamp, R. A., and Lloyd, J. M. (2010). "Basic principles of homing guidance". In: *Johns Hopkins APL Technical Digest* 29.1, pp. 25–41.

Pennycuick, C. J. (2008). *Modelling the flying bird*. Theoretical ecology series. Amsterdam ; London: Academic Press. xiv+480.

Ros, I. G. and Biewener, A. A. (Dec. 2017). "Pigeons (C. livia) Follow Their Head during Turning Flight: Head Stabilization Underlies the Visual Control of Flight". In: *Frontiers in Neuroscience* 11. DOI: 10.3389/fnins.2017.00655.

Shneydor, N. A. (2011). *Missile guidance and pursuit: kinematics, dynamics and control*. eng. Oxford: Woodhead Publishing.

Städele, C., Keleş, M. F., Mongeau, J.-M., and Frye, M. A. (July 2020). "Non-canonical Receptive Field Properties and Neuromodulation of Feature-Detecting Neurons in Flies". en. In: *Current Biology* 30.13, 2508–2519.e6. DOI: 10.1016/j.cub.2020.04.069.

Stanchak, K. E., French, C., Perkel, D. J., and Brunton, B. W. (Jan. 2020). "The Balance Hypothesis for the Avian Lumbosacral Organ and an Exploration of Its Morphological Variation". en. In: *Integrative Organismal Biology* 2.1, obaa024. DOI: 10.1093/iob/obaa024.

Steinbach (1973). "Eye Movements of the Owl". In: *Vision*.

Walker, J. A. (2018). "Visual Guidance of Target-Oriented Flight Behaviours in Birds". en. In: *Thesis*, p. 188.

Warrick, D. R. (Feb. 2002). "Bird Maneuvering Flight: Blurred Bodies, Clear Heads". en. In: *Integrative and Comparative Biology* 42.1, pp. 141–148. DOI: 10.1093/icb/42.1.141.

Zhang, S. W., Xiang, W., Zili, L., and Srinivasan, M. V. (Apr. 1990). "Visual tracking of moving targets by freely flying honeybees". en. In: *Visual Neuroscience* 4.4, pp. 379–386. DOI: 10.1017/S0952523800004582.

4

The motion of hawk eyes during dynamic flight behaviour

Contents

4.1 Abstract 83
4.2 Introduction 84
4.3 Results 85
4.4 Discussion 94
4.5 Materials and Methods 99
References 101

4.1 Abstract

Birds can direct their gaze by moving their heads, moving their eyes relative to their heads, or by both. However, most behavioural studies that measure bird gaze direction assume that the eyes are fixed relative to the head. Though measurements from tethered birds show that eye-in-head movement is limited in some species, few studies have recorded the motion of the eye relative to the head in freely moving birds, and none have recorded eye-in-head movement during flight itself. Thus, the fixed eye assumption used to make inferences on a range of visually guided flight behaviours, from obstacle avoidance to prey pursuit, may not be valid. To address this issue, we present preliminary data from a pilot study deploying two methods to record the eye during dynamic flight behaviour. First, we use a miniature head-mounted camera to film the eye of a Harris' hawk during perch-to-

perch flights. Second, we film the eyes of Harris' hawks undertaking terminal pursuit and target capture using high frame rate, high resolution cameras on a moving platform. Our preliminary findings suggest that though eye-in-head movement is small during pursuit, there are larger vergence movements of the eyes during perching behaviour and during prey capture. We comment on the possible benefits of limited eye-in-head movements for prey pursuit, discuss the limitations of the methods used, and we also present observations on the coordination of the eyes, wings, legs, and feet during terminal pursuit and prey capture.

4.2 Introduction

Collecting data on eye-in-head movements during flight is challenging because it is difficult to record a small eye moving at speed. Thus, researchers have tended to study eye movements relative to the head in tethered birds (Steinbach, 1973; O'Rourke et al., 2010; Martin et al., 2003; Troscianko et al., 2012; Wallman et al., 1985). These studies suggest that gaze redirection is principally achieved by the head carrying the eyes, rather than by independent motion of the eyes relative to the head (Land, 2015). In cases, this is because eye-in-head movements appears highly constrained. In the great-horned owl (*Bubo virginianus*) (Steinbach, 1973), the American kestrel (*Falco sparverius*) (O'Rourke et al., 2010), and the barn owl (*Tyto alba*) (du Lac et al., 1990), eye-in-head movements does not exceed 4°; in red-tailed and cooper's hawks, eye-in-head movements do not exceed 8° (O'Rourke et al., 2010). Some birds, however, can more freely move the eye independent of the head. Southern ground hornbills (*Bucorvus leadbeateri*), New Caledonian crows (*Corvus monudeloides*), and tawny frogmouths (*Podargus strigoides*) have all shown eye-in-head movements between 35 and 40° (Martin et al., 2003; Troscianko et al., 2012; Wallman et al., 1985), while Wallman et al. (1985) recorded eye-in-head movements of up to 24° in the little eagle *Hieraaetus morphnoides*.

Because most studies have measured eye-in-head movements in tethered birds, the behavioural relevance of their results is questionable. Only in the Indian peafowl (*Pavo cristatus*) have eye-in-head movements been recorded from freely moving individuals (Yorzinski et al., 2013; Yorzinski et al., 2014; Yorzinski, 2019; Yorzinski et al., 2017; Yorzinski et al., 2015). In these birds it was found that the eyes contribute only 12 % of the gaze shift during large gaze redirections (Yorzinski et al., 2013), similar to the 10-20 % seen in tethered, but head-free, pigeons (Gioanni, 1988). Evidence from tethered

and freely moving birds therefore suggests that birds principally redirect their gaze by head movements. However, no studies have yet been published that record eye-in-head movement during flight itself. Yet, many studies on flight guidance and control take head direction as a proxy for gaze direction, thereby assuming a fixed eye relative to the head during flight (Ros et al., 2017; Kjrsgaard et al., 2008; Erichsen et al., 1989; Miñano et al., 2021; Walker, 2018; Kress et al., 2015; Ohayon et al., 2006). As the fixed eye assumption underlies the behavioural inferences made by these studies, it is therefore important to robustly test the assumption.

To overcome the challenge of recording a small eye moving at high speed for short periods, we recorded the eye-in-head movements of $N = 5$ Harris' hawks (*Parabuteo unicinctus*) using two novel techniques. We first used a lightweight, miniature head-mounted camera in a laboratory setting to image the eye during perch-to-perch flights. We then attached an artificial lure to a moving camera platform to film the hawk eye during pursuit flight using high-speed, high resolution cameras. We present preliminary data from these recordings to demonstrate analytical approaches for measuring eye-in-head movements, and we present tentative findings from the small dataset. Given the wide field of view of the high-speed cameras, we also recorded the bird's flight coordination during terminal pursuit and here briefly present observations on wing, leg, and foot coordination within 0.2 s of prey capture.

4.3 Results

Miniature head-mounted camera We attached a miniature head-mounted camera (ams-OSRAM NanEye wireless camera) to $N = 1$ Harris' hawk (*Parabuteo unicinctus*)



Figure 4.1: Apparent eye-in-head movement during perch-to-perch trials. We imaged the left eye of a Harris' hawk using a miniature head-mounted camera. We show here five consecutive frames from footage recorded during perch-to-perch trials. The numbers in the top left-hand corner of images are frame numbers (as they are in subsequent images). Between frame 4 and frame 5, the bird appears move its eye relative to its head, rotating the eye towards the sagittal plane, as if in a vergence movement.

to film the eye during flight. The 1 mm^2 camera sensor weighed only 1g and projected laterally from the head, imaging one eye. We were prevented from conducting pursuit trials with this set-up given the risks posed to a bird, wearing a sensor so closely to the eye, pursuing a target. Given the sensor size, there was also insufficient light to image the eye in the artificially lit rooms available to us. Thus, we were restricted to flying the hawk in short perch-to-perch trials in a naturally lit aviary. We collected approximately 10400 frames of video during the perch-to-perch trials. In Figure 4.1, we plot an example of an image sequence that, when viewed at the recording frame rate (36 frames per second), appears to show an eye-in-head movement. However, as the camera was not attached to the head in a perfectly rigid manner, it is difficult to distinguish real eye-in-head movements from apparent movements driven by rotation of the head.

To exclude the influence of head rotation and quantify eye-in-head movements, we propose a method that exploits fixed landmarks on the head. We draw a reference line between two head-fixed landmarks, and draw tangent lines to the pupil from the same source point as the reference line (Figure 4.2). The lines form two unsigned angles (α and β), the ratio of which ($r = \alpha/\beta$) is a measure of eye position relative to the head along an axis perpendicular to the reference line. The ratio of r values computed on consecutive frames is then a measure of eye-in-head movement, ρ, between those frames; $\rho = 1$ indicates that the eye is stationary relative to the head. This measure is robust to pupil dilation and contraction and variation in camera-bird distance.

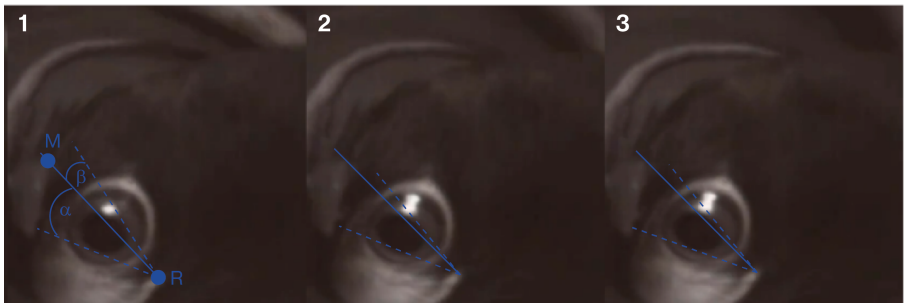


Figure 4.2: A method for inferring eye-in-head movement between images. To infer eye-in-head movements, we plot construction lines on consecutive frames recorded during perch-to-perch trials. The reference line (solid blue) starts at the most posterior point (R) on the rictus, which is the skin at the posterior end of the mouth. The reference line passes through the point (M) at the corner of the head mount. The dotted blue lines are the two lines from R that form a tangent with the pupil. Together, these lines define two angles (α and β), the ratio of which is a measure of eye position relative to the head along an axis perpendicular to the R-M reference line.

Angle (°)	**Frame 1**	**Frame 2**	**Frame 3**
$\boldsymbol{\alpha_n}$	24.6	23.1	25.3
$\boldsymbol{\beta_n}$	11	5.6	5.6
$\boldsymbol{r_n = \alpha_n/\beta_n}$	2.2	4.1	4.5
$\boldsymbol{\rho_n = r_i/r_j}$		1.9	1.1

Table 4.1: Eye-in-head movement data calculated from a miniature head-mounted camera. We define the angles α and β in Figure 4.2. The ratio $r = \alpha/\beta$ is a measure of eye position relative to the axis perpendicular to the R-M reference line. The ratio ρ is a measure of eye-in-head movement; $\rho = 1$ suggests no eye-in-head movement. We compute $\rho_n = r_i/r_j$ across consecutive frames $n-1$ and n, where r_i and r_j are computed on these frames and $r_i \geq r_j$ such that $\rho \geq 1$. Note that the subscript n refers to the n^{th} frame on which an angle or ratio is computed.

In Table 4.1 we calculate ρ between the frames in Figure 4.2. Eyeballing these frames suggests an eye-in-head movement between frame 1 and frame 2, whereas the eye appears stationary relative to the head between frames 2 and 3. The data in Table 4.1 corroborates this appearance in the sense that $\rho_2 > \rho_3$ and ρ_3 is close to 1. However, because we have no second camera synchronised with the head-mounted camera, we do not know what behaviour the bird is performing for any given sequence of video frames. We cannot, therefore, confidently generate a reference dataset that calibrates the absence of eye-in-head movement by calculating ρ over frames where the eye is known to be fixed relative to the head. Thus, it is difficult to know whether a given value of ρ represents real eye-in-head movement or simply noise created by imprecision in placing the reference and tangent lines. Less serious, we were unable to calibrate the camera to convert between pixel distance and angular distance, so we are unable to state the real angular shift in the eye relative to the head.

Camera platform To overcome the deficiencies of the head-mounted camera data, we built a movable camera platform and attached three 4K video cameras (ZCAM E2) in stereo. We recorded $n = 128$ outdoor pursuit trials flown by $N = 5$ Harris' hawks (4 male – Drogon, Rhaegal, Toothless, and Charmander – and 1 female – Ruby) chasing an artificial lure attached to the platform. We fixed the cameras to the same platform as the lure, rather than filming with static cameras, to minimise the relative speed between camera and hawk and thereby minimise the blurriness of the eye in video frames. We used a 1/2000 s^{-1} shutter speed for the same purpose. To one camera we fitted a zoom lens;

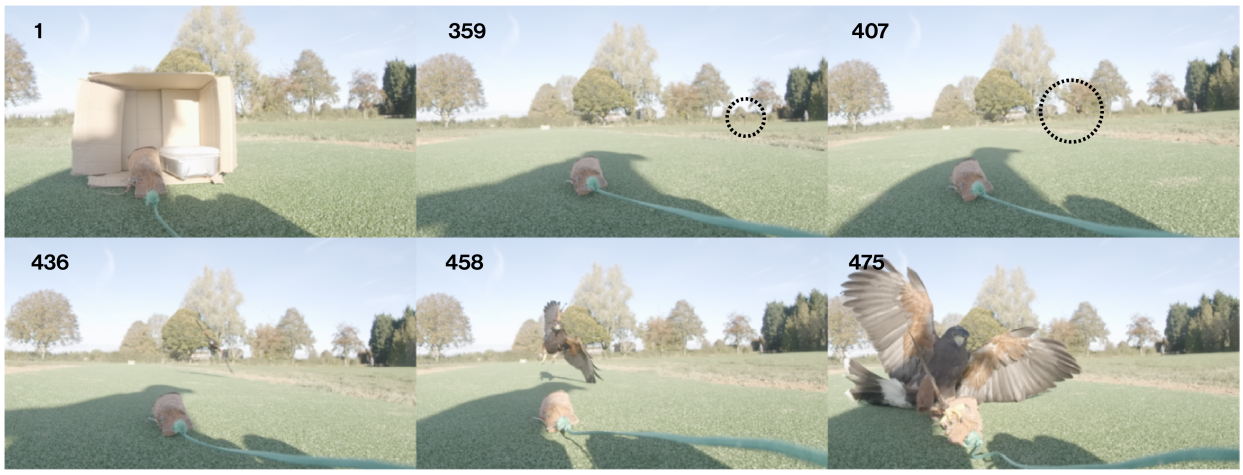


Figure 4.3: Stages of pursuit. At the start of pursuit (frame 1), the artificial lure is hidden behind a box, unseen by the hawk. During the opening and middle phases of pursuit, the hawk flaps to increase speed (bird in mid-flap circled in frame 359). During terminal pursuit, the hawk enters a glide phase (gliding hawk circled in frame 407). About 0.3 seconds before capture, the hawk reaches peak bank angle (frame 436) before completing intercept along a straight line. About 0.15 seconds before intercept, the wing touches the ground, the feet are protracted, and the alulae are raised (frame 458). Intercept occurs in frame 475.

to the other two we fitted fisheye lenses. All cameras recorded at 120 frames per second (fps). We highlight important phases during the pursuit flight in Figure 4.3.

By attaching large cameras to a platform, rather than a small camera to the bird, we were able to film under natural lighting outdoors. We were also able to record the bird's behaviour at the same time as recording the eye. This allows us to identify periods of gaze fixation and thereby form a reference dataset that calibrates an absence of eye-in-head movement across frames. Furthermore, the stereo camera set-up allows us, in principle, to rectify image pairs, generate disparity maps, and thereby produce depth estimates for image coordinates. With depth estimates, one could then build a 3D model of the head and eyes in a given frame and compute real-world eye-in-head movements across frames.

We found that the hawk eye was poorly resolved in images produced by the zoom lens. However, the fisheye lenses produced image sequences in which the eye is well resolved, usually on the order of 10 per trial. Thus, we collected approximately $n_f = 1280$ frames for anlysis. In Figure 4.4 we plot consecutive frames from one camera that depict the eye during the terminal phase of pursuit and capture of the lure. Visual inspection of the frames suggests that there is minimal eye-in-head motion; visual inspection of similar sequences from the other four birds suggests the same (see Supplementary Figures C.1-C.4). However, to quantify eye movement, we attempted to construct a 3D model of the eyes and head using photogrammetric methods.

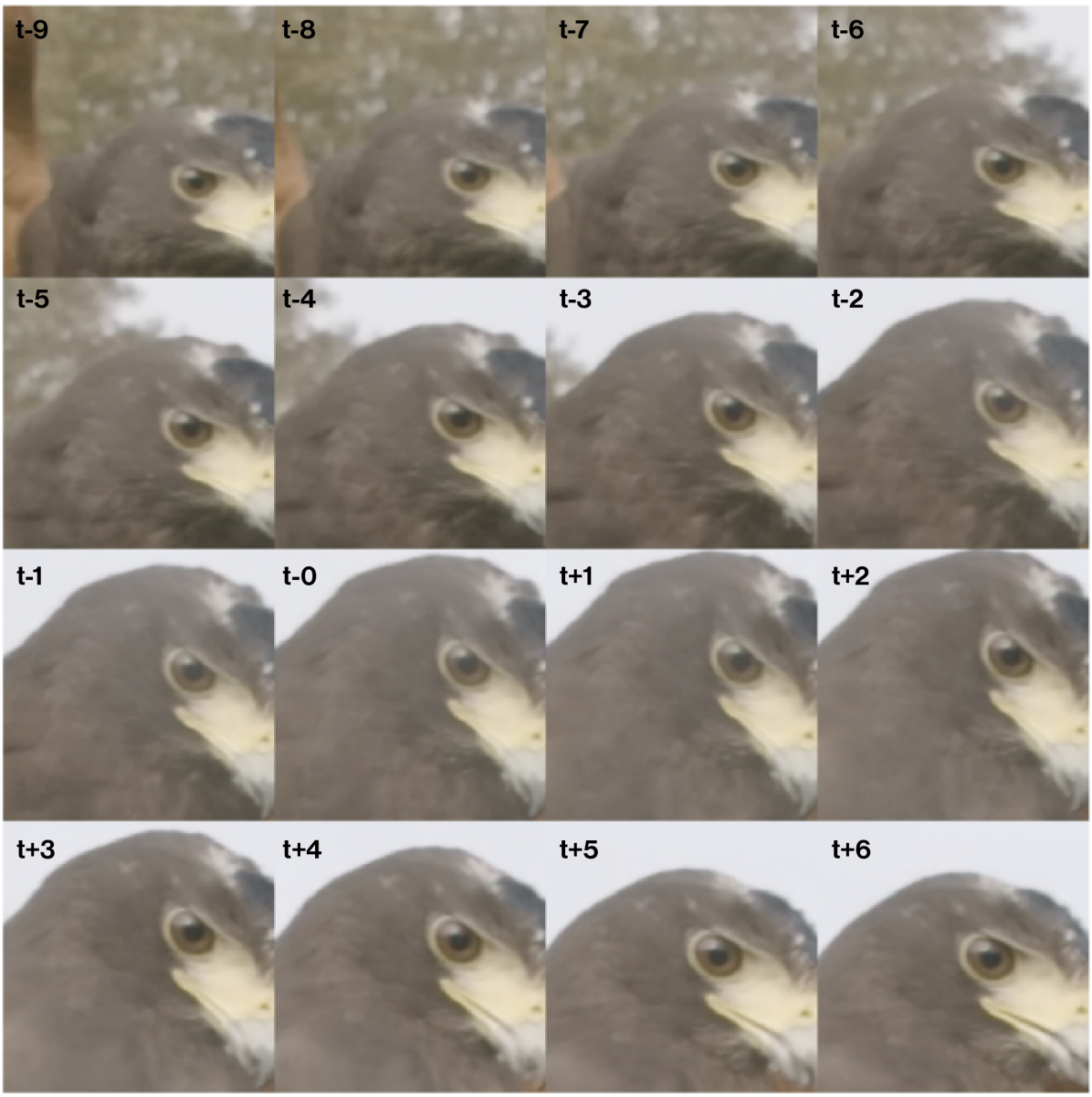


Figure 4.4: Eye-in-head motion during the terminal phase of pursuit. This sequence of 16 frames images the eye before, during, and after prey capture. In the top left-hand corner we note the frame number relative to capture (for example, t-2 indicates the second frame before contact is made with the target). Over the sequence of frames, the eye appears to move minimally.

In Figure C.5 of Appendix C we show the uncropped frames $t + 4$ to $t + 6$ from Figure 4.4 from both fisheye lens cameras as image pairs. To rectify image pairs we first performed monocular camera calibration under a fisheye model using the Matlab (v2018b) single camera calibrator. We obtained the camera instrisic and extrinsic parameters but, unfortunately, Matlab does not provide an option to import these parameters into the stereo camera calibration app. More unfortunately, Matlab does not provide a fisheye model to directly compute the camera intrinsic and extrinsic parameters in the stereo

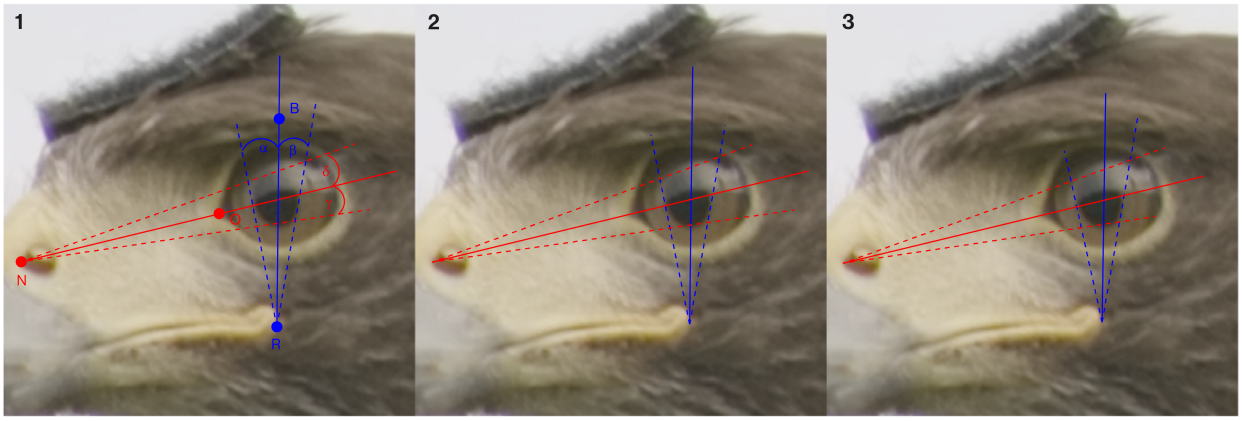


Figure 4.5: Extending the method for detecting eye-in-head movement. We plot reference and tangent lines on three consecutive frames for which the bird has a fixed gaze. The first reference line (solid blue) starts at the most posterior point (R) on the rictus and passes through the point (B) on a repeatably identifiable feather on the brow ridge. The dotted blue lines are the two lines from R that form a tangent with the pupil. Together, these lines define two angles (α and β), the ratio of which is a measure of eye position relative to the head along an axis perpendicular to the R-B reference line. The second reference line (solid red) starts at the most anterior point (N) on the nare and passes through the most anterior point (O) on the orbit. The dotted red lines are the two lines from N that make a tangent with the pupil. Together, these lines define two angles (γ and δ), the ratio of which is a measure of eye position relative to the head along an axis perpendicular to the N-O reference line.

camera calibration app, thereby preventing us from performing image rectification in Matlab. It is possible to perform stereo calibration for fisheye lenses in other software, such as OpenCV, but this was not possible in the timeframe of the thesis. To quantify eye-in-head movement, we therefore use an extension of the method shown in Figure 4.2. We present here example cases of method use on a small subset of the circa $n_f = 1280$ usable frames that we collected, and present preliminary results.

We construct two reference lines and two sets of tangent lines to the pupil, as shown in Figure 4.5. We then compute two sets of angular ratios, one of which is a measure of eye position relative to the head along an axis perpendicular to the R-B reference line, the other of which is a measure of eye position relative to the head along an axis perpendicular to the N-O reference line. Critically, we first do this for a sequence of frames (Figure 4.5) in which the bird has a fixed gaze. This provides a reference datset that calibrates an absence of eye-in-head movement.

In this example calibration dataset we find that ρ lies within the range $[1.0, 1.1]$. In Figure C.7 of Appendix C we draw reference and tangent lines on frames $t-3$ to $t-1$ of Figure 4.4. These frames are taken immediately before target intercept $(t-0)$. Because the pupil is hidden by the brow ridge, we are only able to calculate ρ along an axis perpendicular

Angle (°)	Frame 1	Frame 2	Frame 3
α_n	11.6	12.1	13
β_n	9.1	9.5	9
$r_n = \alpha_n/\beta_n$	1.3	1.3	1.4
$\rho_n = r_i/r_j$		1.0	1.1
γ_n	5.1	5.4	5.1
δ_n	5.9	6.5	6.2
$r_n = \gamma_n/\delta_n$	0.9	0.8	0.8
$\rho_n = r_i/r_j$		1.1	1.0

Table 4.2: Eye-in-head movement data from calibration frames. We cite here the angles defined in Figure 4.5 computed on the frames of the same figure. In Figure 4.5, the bird has fixed its gaze so that the above data is a reference dataset that calibrates an absence of eye-in-head movement.

to the R-B reference line. The computed data (Table 4.3) suggests no eye-in-head movement across these frames as ρ lies either within, or very close to, the calibration range.

In Figure C.6 we apply the construction lines method to frames $t+4$ to $t+6$ of Figure 4.4 where visual inspection suggests there is an eye-in-head movement after prey capture between frames $t+4$ and $t+5$. Similarly, we apply the method to frames $t+6$ to $t+8$ of Figure C.2 in Appendix C, where visual inspection suggests an eye-in-head movement between frames $t+6$ and $t+7$. We show the construction lines in Figure C.8 of Appendix C. We show the computed data in Tables 4.4 – 4.5. We see that, in both cases, there is evidence for eve movement perpendicular to the N-O reference in the expected frames given that ρ lies far from the calibration range line. However, we find little evidence for eye motion perpendicular to the R-B reference line across any frames in the sense that ρ lies within or close to the calibration range.

After target capture, the hawk tended to guard the artificial lure, occasionally scanning the visual scene with its head. To make a scan, the hawk used a saccade and fixate

Angle (°)	Frame 1	Frame 2	Frame 3
α_n	10.6	9.3	9.9
β_n	13.0	13.3	12.7
$r_n = \alpha_n/\beta_n$	0.8	0.7	0.8
$\rho_n = r_i/r_j$		1.2	1.1

Table 4.3: Eye-in-head motion data from during terminal pursuit. We tabulate here the angles defined in Figure C.7 of Appendix C computed on frames $t+3$ to $t+1$ of Figure 4.4, and the values of r_n and ρ_n derived from them. This data comes from a flight by Rhaegal.

Angle (°)	Frame t+4	Frame t+5	Frame t+6
α_n	27.7	25.2	25.5
β_n	3.2	3.2	2.5
$r_n = \alpha_n/\beta_n$	8.7	7.9	10.2
$\rho_n = r_i/r_j$		1.1	1.3
γ_n	5.5	6.3	6.1
δ_n	5.0	4.0	4.2
$r_n = \gamma_n/\delta_n$	1.1	1.6	1.5
$\rho_n = r_i/r_j$		1.5	1.1

Table 4.4: Eye-in-head motion after target capture, part I. We tabulate here the angles defined in Figure C.6 of Appendix C computed on frames $t+4$ to $t+6$ of Figure 4.4 and the values of r_n and ρ_n derived from them. This data comes from a flight by Rhaegal.

Angle (°)	Frame t+4	Frame t+5	Frame t+6
α_n	22.7	22.9	24.9
β_n	5.2	6.4	7.6
$r_n = \alpha_n/\beta_n$	4.4	3.6	3.3
$\rho_n = r_i/r_j$		1.2	1.1
γ_n	4.4	5.8	5.5
δ_n	8.4	6.4	7.6
$r_n = \gamma_n/\delta_n$	0.5	0.9	0.7
$\rho_n = r_i/r_j$		1.8	1.3

Table 4.5: Eye-in-head motion after target capture, part II.. We tabulate here the angles defined in Figure C.8 of Appendix C computed on frames $t+6$ to $t+8$ of Figure C.2 of Appendix C and the values of r_n and ρ_n derived from them. This data comes from a flight by Toothless.

strategy that has been previously reported in many bird species (Eckmeier et al., 2008; Kress et al., 2015; Ros et al., 2017). Noticeable during these saccades was the passing of the nictitating membrane across the eye, which we saw in all five birds (Figure 4.6 and Supplementary Figures C.9 - C.12). We rarely, if ever, saw the nictitating membrane during periods of head fixation, whereas the passing ofthe nictitating membraner across the eye was highly correlated with saccades.

Visual information on the target is used to coordinate other behaviours during prey pursuit and capture. The data collected from the camera platform set-up allows us to make observations on coordination between the body, wings, legs, and feet, which we briefly do here. We find that important changes in the flight condition of the hawk occur within the final 0.2 s of pursuit. For example, birds fly with the legs retracted to minimise aerodynamic drag but, in order to capture prey, hawks must release the legs during



Figure 4.6: The nictitating membrane covers the eye during a head saccade. The hawk saccades the head from a profile position to a frontal position from the point of view of the camera. On initiating the saccade, the bird protracts the nictitating membrane, whereas the bird retracts the membrane towards the end of the saccade. Given a recording frame rate of 120 fps, the passing of the nictitating membrane across the eye takes 0.06 s.

terminal pursuit. In the example flight that we consider in Figure 4.7, the Harris' hawk releases the legs from their retracted position 0.2 s in advance of prey capture. At 0.04 s in advance of prey capture, the Harris' hawk extends the feet to grab the target (Figure 4.8).

The wings provide body stability to coordinate leg and foot extension. Research shows that during slow flight operated at high angles of attack, such as landing, a small structure at the joint between the hand-wing and arm-wing of birds called the alula plays a role to enhance lift and delay stall (Lee et al., 2015). Four out of five of our Harris' hawks stopped on the lure once it was caught (the other bird flew off with the lure), requiring a similar ability to landing. We find that just in advance of prey capture, hawks also raise the alula, as seen in Figure 4.9. In the example flight that we consider in Figure 4.9, we find this happens within 0.2 s of prey capture.

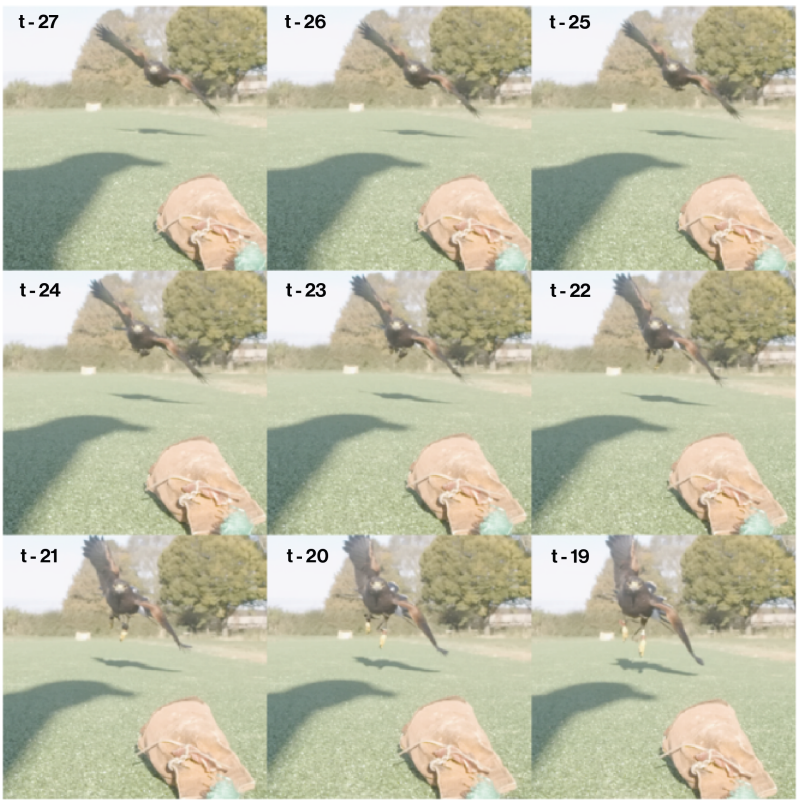


Figure 4.7: Timing of leg protraction during terminal pursuit. A sequence of nine video frames illustrating that the Harris' hawk lowers its feet as it approaches the target, much as a plane lowers its wheels as it approaches the runway. In the top left-hand corner of each frame we specify the frame number in relation to the frame of capture (t-0). Given the recording is at 120 fps, the hawk lowers its legs 0.2 s in advance of capture.

4.4 Discussion

Eye-in-head movement For the frame sequences that we analysed, we find evidence for eye-in-head movement perpendicular to the N-O reference line. In both Figures C.6 and C.8, the bird has intercepted the target and is starting to raise the head away from the target. As the direction perpendicular to the N-O reference line approximately defines the elevation angle of the eye, this may therefore indicate a vergence movement of the eyes towards the feet holding the target as the bird's head rotates upwards. Pigeons show such vergence movements of the eyes when they peck at grain (Martinoya et al., 1984). Pigeons do so to focus the food item on the area dorsalis, a region of high retinal cell density. It is likely that our Harris' hawks, as they lift their heads to include the horizon and sky within their field of view, also make a vergence movement of the eyes towards the feet so that control of the prey item by the feet can be maintained.

In contrast, by visual inspection of image sequences and the application of the reference line method to one sequence of frames, we do not find evidence for eye-in-head motion



Figure 4.8: Timing of foot extension during intercept. In the top left-hand corner of each frame we specify the frame number in relation to the frame of capture (t-0). Given a 120 fps recording frame rate, the hawk does not therefore start to extend its feet until 0.04 s in advance of prey capture.

immediately before pursuit. Nalbach et al. (1990) showed that pigeons maintain active control of the eye-in-head position; one reason that birds may tend to keep the eye at a fixed location relative to the head is to maintain a shared frame of reference between the visual and vestibular systems (Wylie et al., 1998), which may simplify the neural computations for guidance. Limited eye-in-head movement also simplifies the integration of neck proprioceptor information into guidance mechanisation as, with a fixed eye and head, birds can infer body motion via the neck muscles (Groebbels, 1929). The neck then acts as a means to compute a head-to-body coordinate transformation to transform sensory information acquired by the head into motor outputs that steer the body (Ros et al., 2017; Krapp, 2010).

Pursuit guidance mechanisation Falcons and hawks appear to guide themselves to their targets as homing missiles do (Brighton et al., 2017; Brighton et al., 2019; Brighton et al., 2021), steering attack trajectories in a manner that is consistent with the proportional navigation (PN) guidance law used by missiles (Shneydor, 2011). To implement PN guidance, birds-of-prey and missiles alike must measure the rate of change in the line between attacker and target (the line-of-sight) with respect to an inertial reference

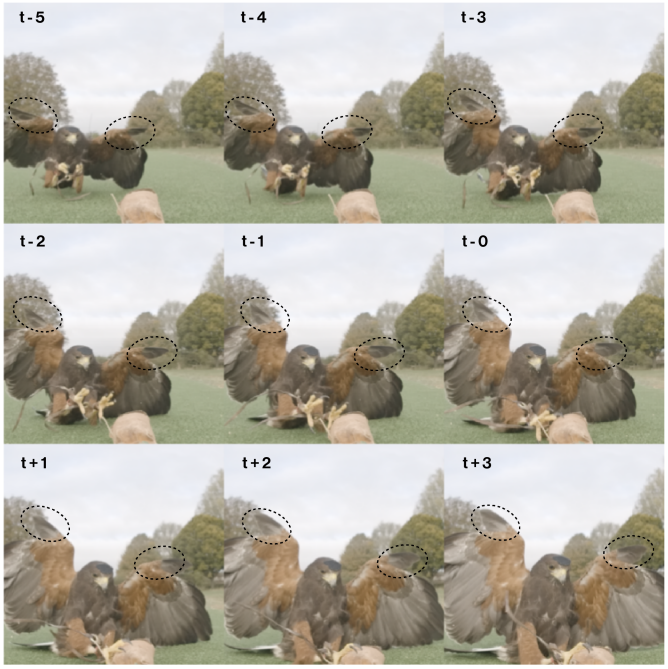


Figure 4.9: Protraction of the alulae. The alula is a small structure between the hand-wing and arm-wing of birds, and we circle the alula of each wing with a black dashed ellipse. In the top left-hand corner of each frame we specify the frame number in relation to the frame of capture (t-0). Given a 120 fps recording frame rate, the alula have already been raised 0.06 s in advance of prey capture.

frame. Space-stabilised homing missiles estimate the inertial line-of-sight rate using a device called a seeker that contains a target acquisition sensor, gimbals, servomotors, and gyroscopic sensors (Palumbo et al., 2010). The acquisition sensor is used to measure the angle between the line-of-sight and the seeker centreline (the boresight). This angle is called the tracking error. Missiles continuously drive the boresight, via the servomotors, towards the line-of-sight to null the tracking error. The seeker's angular rate is then a measure of the line-of-sight rate, and the gyroscopic sensors in the seeker measure the line-of-sight rate (Palumbo et al., 2010).

A hawk's head appears analogous to a seeker. However, a hawk's head only operates like a space-stabilised missile seeker if the hawk smoothly moves its head to maintain a target at a fixed retinal position without moving the eyes relative to the head. Another way of expressing this is to say that the reference frame that instantiates eye motion is the same as that which instantiates head motion (albeit the axis systems will be offset). Walker (2018) finds that peregrine falcons appear to fixate their targets by smoothly moving the head, seemingly like a space-stabilised missile seeker. However, this inference depends on the assumption that the eyes do not move relative to the head. For example, rabbits smoothly

track targets with their head, but they do not keep the target at a fixed retinal position (Collewijn, 1977), whereas humans maintain slowly moving targets at the same retinal position but do so by keeping the head static and continuously moving the eyes relative to the head during smooth pursuit (Collewijn et al., 1984; Kandel et al., 2021). Keeping a target at a fixed retinal position is therefore a necessary but not sufficient condition for an animal head to act like a missile seeker. One must also show that eye-in-head movement is minimal, as the small dataset on terminal pursuit that we anlyse here does.

The nictitating membrane Blinking in animal species is suggested to protect aginst foreign debris and to keep the eye moist (Yorzinski, 2016). Birds possess both an eyelid and a structure called the nictitating membrane to execute blinking. The nictitating membrane is a white sheath that passes laterally across the eye during blinking. Observation of the nictitating membrane has been made across many bird species (Blount, 1927; Kirsten et al., 1983; Cross et al., 2013), but a correlation between gaze shifts and the nictitating membrane is first mentioned by Kirsten et al. (1983) and first explicitly studied by Yorzinski (2016). Across all five hawks studied here, we also see the crossing of the nictitating membrane during gaze shifts.

Limitations In Land's famous study that investigated the eye motion of human subjects making tea, he used a head mounted camera to image the visual scene and eye simultaneously (Land et al., 1999). In the original study to investigate eye-in-head motion in freely moving peahens, Yorzinski et al. (2013) similarly imaged both the visual scene and eye, using two head-mounted cameras. The head-mounted camera set-up used by Yorzinski et al. (2013) weighed 370 g, over half the mass of all our males birds. To overcome the challenge posed by bird-borne sensor mass in measuring eye motion, we trialled a miniature head-mounted camera, with wifi transmission. The total mass of head mount, sensor, chipset, and battery came to 19 g. The principal sacrifice we made in shedding so much weight was the lack of a second, synchronised camera to determine periods when the bird's gaze is fixed. This prevented us from generating a reference dataset that calibrates an absence of eye-in-head movement. Without such a reference dataset, it is difficult to make confident statements about eye movement relative to the head. However, this is not an insurmountable problem. One could conduct behavioural trials before flying the birds

to obtain footage of gaze fixation with the head-mounted camera. For example, when presented with a morsel of food, hawks readily fix their gaze on the food.

The range of flight behaviours that we could anlyse using the miniature head-mounted camera was limited. This is principally because of the risks posed to the hawks by flying aggressively at a target with a sensor worn so closely to the eye. This is a more difficult problem to surmount, and we see no sufficiently safe solution.

To overcome the safety concerns posed by flying with a head-mounted camera, we built a movable camera platform. In being able to move the cameras at speed, we also reduced the difficulty posed by the high speed, short period nature of terminal pursuit by minimising the relative motion between camera and bird eye. However, in detaching the camera from the head, we limit the span of time in which the bird's eye can be resolved in the image. In the case of the fisheye lenses that we used, the eye was not resolvable in the image until about 6 frames in advance of prey capture. In the case of the zoom lens, we could resolve the eye further in advance of prey capture, but the depth of field of the lens was too small for the eye to be sufficiently focused over consecutive frames. Indeed, in many cases, the field of view was too small to even keep the bird in shot over a small sequence of frames. This creates an in principle difficulty with the method for anlysing eye-in-head motion. A possible solution would be to employ an intermediate lens between the fisheye and zoom lenses that we used. For example, a lens that provides sufficient zoom to focus the eye further in advance of prey capture, but not so much zoom that the depth of field is too narrow to focus the eye over consecutive frames, would be the best trade-off. Of course, the ideal solution would be to use a variable zoom lens that was operated by a skilled cameraman to focus the eye over a large timespan, but this is technically extremely difficult.

The method that we use to estimate eye-in-head movements on those frames where the eye is well resolved suffers from its own difficulties. Reliable data requires head fixed landmarks. We are confident that some of the landmarks that we use in this study - the most posterior point on the rictus, the most anterior point on the nare, the most anterior point on the orbit, and the end of the brow ridge – represent truly head-fixed landmarks. The others that we use – the corner point of the head mount, the corner point of the velcro patch, and an identifiable feather on the brow ridge - are not true head-fixed landmarks but, over the small timescale of the image sequences we analysed, they approximate head-fixed landmarks. Reliable data also requires the accurate identification

of the landmarks. Because of bird motion across frames, and changes in lighting across frames, accurate identification of the pixel representing the same landmark is difficult. Similarly, identifying the tangent point for lines drawn tangent to the pupil is difficult because the pupil tends to bleed into the iris in images. Thus, error in the placement of reference and tangent lines means that estimates of ρ contain measurement error that needs to be quantified. This makes the construction of a reference dataset that calibrates an absence of eye-in-head motion particularly improtant. The results that we present here are limited by the small calibration dataset that we present. However, there is not an in principle difficulty in providing a more extensive calibration dataset. One would then calculate an average and standard error for ρ values computed across many image pairs during gaze fixation behaviour, ideally during different lighting conditions, camera-subject orientations, and camera-subject distances. The results that we present are similarly limited by the small test datasets that we anlyse. However, we have an approximately 1270 additional images frames in which the eye is sufficiently resolved to estimate eye-in-head movements. Analysing this data would allow more robust conclusions on eye-in-head movements during terminal pursuit and prey capture.

4.5 Materials and Methods

Miniature head-mounted camera We flew $N = 1$ Harris' hawks (*Parabuteo unicinctus*) in $n = 6$ perch-to-perch trials in January 2019 at the John Krebs Field Station (Wytham, Oxford, UK). We attached a 3D printed head mount to the head of the hawk using velcro and, into the slot of the head mount, we inserted a prototype ams-OSRAM (Premstaetten, Austria) NanEye wireless camera (CAM01) chipset and 3.7 V LiPo battery to power the device. The device uses wireless LAN connectivity (802.11 b/g/n radio, 2.4GHz band) to stream video to a connected computer. We fastened the camera sensor – a 1 mm^2 249×250 square rolling shutter pixel array recording at 36 frames per second (fps) – to an arm of the head mount to stabilise the camera. We operated the sensor at the lowest power supply voltage (1.3 V) to maximise light sensitivity. We intended to conduct pursuit trials in our 20.2 m $\times$ 6.1 $\times$ 3.8 m windowless flight hall, lit by flicker-free LED lamps that provide 4000 K direct lighting and 5000 K indirect lighting at circa 1000 lux. However, even at 1.3 V power supply, there was insufficient light in the flight hall to provide well resolved video data; we also had safety concerns over a hawk chasing a target at speed

with the camera sensor worn so closely to the eye. We therefore conducted perch-to-perch flights in a 3.5 m × 2.5 m × 3.5 m aviary with natural sunlight. We visualised streamed video data in the CAM01 GUI and recorded using OBS studio screen recording software.

Moving camera platform We conducted $n = 128$ outdoor pursuit trials with $N = 5$ Harris' hawks (4 males and 1 female) in October and November 2021 by hand-pulling an artificial lure across a field in Wytham, Oxfordshire (51° 46′ 32.7″ N 1° 18′ 48.1″ W). We attached the lure to a movable camera platform that we called the 'skateboard'. The skateboard was a 1.2 m × 0.4 m wooden plank with fixed front wheels and freely rotating back wheels to encourage straight-line motion. We rigidly attached two ZCAM E2 4K cinema cameras fitted with Olympus M.Zuiko Digital ED 8mm f/1.8 Fisheye PRO lenses to the skateboard with their optical centres 25 cm apart. We also attached one ZCAM E2 4K cinema with Panasonic 14-140mm f/3.5-5.6 Power OIS Micro Four Thirds Lens to the skateboard, though we do not use the data from this camera in this paper because we were unable to resolve the eye in its footage. We hand-pulled the skateboard with mounted cameras and lure in an approximately straight line with a Harris' hawk in pursuit until intercept. We varied the Harris' hawk starting distance and direction on a semi-circle of radius c. 30 m with centre at the skateboard start position. We recorded the flight trials at 4K resolution, f/1.8, ISO 2500, and a shutter speed of 1/2000 s^{-1}. We recorded 111 of these trials at 30 fps using a ZRAW encoder, though we do not use this data in this paper, while we recorded 17 trials at 120 fps using an H.265 encoder and log colour space. We recorded all trials with the two fisheye lens cameras synced by ZCAM E2 sync cables.

To create image sequences of the eye during terminal pursuit and prey capture, we first colour graded the footage using the Auto Basic Correction in Adobe Premiere Pro. We then exported frames to be analysed as .tiff files to Adobe Photoshop. In Photoshop we cropped the extracted frames as desired. To create the 4 × 4 frame montages of the eye, we cropped individual frames to 176 × 176 pixel squares whose bottom edges are defined by the tip of the hawk bill, and whose right edges are defined by the right edge of the nare; we saved these as .tiff files. We then created the 4 × 4 montages of the images in MATLAB R2018b (The Mathworks Inc., Natick, MA). We used the same process to create montages of other behaviour with different crop and frame centering parameters.

References

Blount, W. P. (July 1927). "STUDIES OF THE MOVEMENTS OF THE EYELIDS OF ANIMALS: BLINKING". en. In: *Quarterly Journal of Experimental Physiology* 18.2, pp. 111–125. DOI: 10.1113/expphysiol.1927.sp000426.

Brighton, C. H., Chapman, K. E., Fox, N. C., and Taylor, G. K. (Mar. 2021). "Attack behaviour in naive gyrfalcons is modelled by the same guidance law as in peregrine falcons, but at a lower guidance gain". en. In: *Journal of Experimental Biology* 224.5, jeb238493. DOI: 10.1242/jeb.238493.

Brighton, C. H. and Taylor, G. K. (Dec. 2019). "Hawks steer attacks using a guidance system tuned for closepursuit of erratically manoeuvring targets". en. In: *Nature Communications* 10.1, p. 2462. DOI: 10.1038/s41467-019-10454-z.

Brighton, C. H., Thomas, A. L. R., and Taylor, G. K. (Dec. 2017). "Terminal attack trajectories of peregrine falcons are described by the proportional navigation guidance law of missiles". en. In: *Proceedings of the National Academy of Sciences* 114.51, pp. 13495–13500. DOI: 10.1073/pnas.1714532114.

Collewijn, H. (Apr. 1977). "Eye- and head movements in freely moving rabbits." en. In: *The Journal of Physiology* 266.2, pp. 471–498. DOI: 10.1113/jphysiol.1977.sp011778.

Collewijn, H. and Tamminga, E. P. (June 1984). "Human smooth and saccadic eye movements during voluntary pursuit of different target motions on different backgrounds." en. In: *The Journal of Physiology* 351.1, pp. 217–250. DOI: 10.1113/jphysiol.1984.sp015242.

Cross, D. J., Marzluff, J. M., Palmquist, I., Minoshima, S., Shimizu, T., and Miyaoka, R. (Aug. 2013). "Distinct neural circuits underlie assessment of a diversity of natural dangers by American crows". en. In: *Proceedings of the Royal Society B: Biological Sciences* 280.1765, p. 20131046. DOI: 10.1098/rspb.2013.1046.

Du Lac, S. and Knudsen, E. I. (Jan. 1990). "Neural maps of head movement vector and speed in the optic tectum of the barn owl". en. In: *Journal of Neurophysiology* 63.1, pp. 131–146. DOI: 10.1152/jn.1990.63.1.131.

Eckmeier, D., Geurten, B. R. H., Kress, D., Mertes, M., Kern, R., Egelhaaf, M., and Bischof, H.-J. (Dec. 2008). "Gaze Strategy in the Free Flying Zebra Finch (Taeniopygia guttata)". en. In: *PLoS ONE* 3.12. Ed. by E. Greene, e3956. DOI: 10.1371/journal.pone.0003956.

Erichsen, J. T., Hodos, W., Evinger, C., Bessette, B. B., and Phillips, S. J. (1989). "Head Orientation in Pigeons: Postural, Locomotor and Visual Determinants". en. In: *Brain, Behavior and Evolution* 33.5, pp. 268–278. DOI: 10.1159/000115935.

Gioanni, H. (1988). "Stabilizing gaze reflexes in the pigeon (Columba livia)". en. In: p. 16.

Groebbels, F. (Nov. 1929). "Der Vogel als automatisch sich steuerndes Flugzeug". de. In: *Die Naturwissenschaften* 17.46, pp. 890–893. DOI: 10.1007/BF01506485.

Kandel, E. R., Koester, J., Mack, S., and Siegelbaum, S. (2021). *Principles of neural science*. eng. Sixth edition. New York ; London: McGraw Hill.

Kirsten, S. J. and Kirsten, E. B. (Feb. 1983). "Spontaneous Blink Rates of Birds". en. In: *The Condor* 85.1, pp. 92–93. DOI: 10.2307/1367896.

Kjrsgaard, A., Pertoldi, C., Loeschcke, V., and Witzner Hansen, D. (July 2008). "Tracking the gaze of birds". en. In: *Journal of Avian Biology* 39.4, pp. 466–469. DOI: 10.1111/j.0908-8857.2008.04288.x.

Krapp, H. G. (Mar. 2010). "Sensorimotor transformation: From visual responses to motor commands". en. In: *Current Biology* 20.5, R236–R239. DOI: 10.1016/j.cub.2010.01.008.

Kress, D., van Bokhorst, E., and Lentink, D. (June 2015). "How Lovebirds Maneuver Rapidly Using Super-Fast Head Saccades and Image Feature Stabilization". en. In: *PLOS ONE* 10.6. Ed. by D. Wylie, e0129287. DOI: 10.1371/journal.pone.0129287.

Land, M., Mennie, N., and Rusted, J. (Nov. 1999). "The Roles of Vision and Eye Movements in the Control of Activities of Daily Living". en. In: *Perception* 28.11, pp. 1311–1328. DOI: 10.1068/p2935.

Land, M. F. (Feb. 2015). "Eye movements of vertebrates and their relation to eye form and function". en. In: *Journal of Comparative Physiology A* 201.2, pp. 195–214. DOI: 10.1007/s00359-014-0964-5.

Lee, S.-i., Kim, J., Park, H., Jabłoński, P. G., and Choi, H. (Sept. 2015). "The Function of the Alula in Avian Flight". en. In: *Scientific Reports* 5.1, p. 9914. DOI: 10.1038/srep09914.

Martin, G. R. and Coetzee, H. C. (Dec. 2003). "Visual fields in hornbills: precision-grasping and sunshades: Visual fields in hornbills". en. In: *Ibis* 146.1, pp. 18–26. DOI: 10.1111/j.1474-919X.2004.00211.x.

Martinoya, C., Le Houezec, J., and Bloch, S. (Apr. 1984). "Pigeon's eyes converge during feeding: Evidence for frontal binocular fixation in a lateral-eyed bird". en. In: *Neuroscience Letters* 45.3, pp. 335–339. DOI: 10.1016/0304-3940(84)90248-9.

Miñano, S. and Taylor, G. K. (June 2021). *Through hawks' eyes: reconstructing a bird's visual field in flight to study gaze strategy and attention during perching and obstacle avoidance*. en. preprint. Animal Behavior and Cognition. DOI: 10.1101/2021.06.16.446415.

Nalbach, H.-O., Wolf-Oberhollenzer, F., and Kirschfeld, K. (Jan. 1990). "The pigeon's eye viewed through an ophthalmoscopic microscope: Orientation of retinal landmarks and significance of eye movements". en. In: *Vision Research* 30.4, pp. 529–540. DOI: 10.1016/0042-6989(90)90065-S.

O'Rourke, C. T., Hall, M. I., Pitlik, T., and Fernández-Juricic, E. (Sept. 2010). "Hawk Eyes I: Diurnal Raptors Differ in Visual Fields and Degree of Eye Movement". en. In: *PLoS ONE* 5.9. Ed. by E. Warrant, e12802. DOI: 10.1371/journal.pone.0012802.

Ohayon, S., van der Willigen, R. F., Wagner, H., Katsman, I., and Rivlin, E. (Sept. 2006). "On the barn owl's visual pre-attack behavior: I. Structure of head movements and motion patterns". en. In: *Journal of Comparative Physiology A* 192.9, pp. 927–940. DOI: 10.1007/s00359-006-0130-9.

Palumbo, N. F., Blauwkamp, R. A., and Lloyd, J. M. (2010). "Basic principles of homing guidance". In: *Johns Hopkins APL Technical Digest* 29.1, pp. 25–41.

Ros, I. G. and Biewener, A. A. (Dec. 2017). "Pigeons (C. livia) Follow Their Head during Turning Flight: Head Stabilization Underlies the Visual Control of Flight". In: *Frontiers in Neuroscience* 11. DOI: 10.3389/fnins.2017.00655.

Shneydor, N. A. (2011). *Missile guidance and pursuit: kinematics, dynamics and control*. eng. Oxford: Woodhead Publishing.

Steinbach (1973). "Eye Movements of the Owl". In: *Vision*.

Troscianko, J., von Bayern, A. M., Chappell, J., Rutz, C., and Martin, G. R. (Jan. 2012). "Extreme binocular vision and a straight bill facilitate tool use in New Caledonian crows". en. In: *Nature Communications* 3.1, p. 1110. DOI: 10.1038/ncomms2111.

Walker, J. A. (2018). "Visual Guidance of Target-Oriented Flight Behaviours in Birds". en. In: *Thesis*, p. 188.

Wallman, J. and Pettigrew, J. (June 1985). "Conjugate and disjunctive saccades in two avian species with contrasting oculomotor strategies". en. In: *The Journal of Neuroscience* 5.6, pp. 1418–1428. DOI: 10.1523/JNEUROSCI.05-06-01418.1985.

Wylie, D. R. W., Bischof, W. F., and Frost, B. J. (Mar. 1998). "Common reference frame for neural coding of translational and rotational optic flow". en. In: *Nature* 392.6673, pp. 278–282. DOI: 10.1038/32648.

Yorzinski, J. L. (Oct. 2016). "Eye blinking in an avian species is associated with gaze shifts". en. In: *Scientific Reports* 6.1, p. 32471. DOI: 10.1038/srep32471.

Yorzinski, J. L. (Oct. 2019). "Conjugate eye movements guide jumping locomotion in an avian species". en. In: *Journal of Experimental Biology* 222.20, jeb211565. DOI: 10.1242/jeb.211565.

Yorzinski, J. L., Patricelli, G. L., Babcock, J. S., Pearson, J. M., and Platt, M. L. (Nov. 2013). "Through their eyes: selective attention in peahens during courtship". en. In: *Journal of Experimental Biology* 216.22, pp. 4310–4310. DOI: 10.1242/jeb.098392.

Yorzinski, J. L., Patricelli, G. L., Bykau, S., and Platt, M. L. (Mar. 2017). "Selective attention in peacocks during assessment of rival males". en. In: *Journal of Experimental Biology* 220.6, pp. 1146–1153. DOI: 10.1242/jeb.150946.

Yorzinski, J. L., Patricelli, G. L., Platt, M. L., and Land, M. F. (Jan. 2015). "Eye and head movements shape gaze shifts in Indian peafowl". en. In: *Journal of Experimental Biology*, jeb.129544. DOI: 10.1242/jeb.129544.

Yorzinski, J. L. and Platt, M. L. (May 2014). "Selective attention in peacocks during predator detection". en. In: *Animal Cognition* 17.3, pp. 767–777. DOI: 10.1007/s10071-013-0708-x.

5 Discussion

Contents

5.1 The consequences of reference frame choice 104
5.1.1 Tractability 105
5.1.2 Parsimony 108
5.1.3 Physical meaning 109
5.2 Conclusion 111
References 111

5.1 The consequences of reference frame choice

Now, turning to the reflection. In the Introduction, I discussed how, superficially, the choice of reference frame appears to simply be an accounting method – the choice of reference frames affects the specific numbers one calculates, but little else. I then argued, however, that the frame of reference chosen to model a system influences the tractability of analysing the system, implies physical properties of the system, affects the parsimony of modelling, and influences the explicability of the system's behaviour. I explored these themes with examples from physics, notably the simple pendulum and cosmological models from antiquity and the Renaissance. In light of the research presented in Chapters 2 – 4 of this thesis, I now consider whether and how the biological examples of dynamic soaring by Procellariiformes and pursuit by hawks display the themes of the Introduction.

5.1.1 Tractability

In Chapter 2, I use Equation 2.4 as part of a method to reconstruct Manx shearwater (*Puffinus puffinus*) trajectories and thereby answer questions about dynamic soaring. I arrive at Equation 2.4 from Equation A.31 in Appendix A by making the simplifying assumptions that the shearwater flies at constant airspeed and that the weathercocking effect is negligible. Subject to the assumption that the shearwater always flies in a symmetric flight condition, Equation A.31 is an exact expression for the yaw angle rate induced by an unsteady banked turn in a steady horizontal wind field of uniform direction with vertical wind shear σ. To arrive at this expression, I take the derivative of the bird's kinematic velocity with respect to an Earth-fixed reference frame that, on the timescale of our video recordings, approximates an inertial reference frame. One can take the derivative with respect to any other frame, but this does not allow direct application of Newton's Second Law; as discussed in Chapter 1, Newton's Second Law only holds in an inertial reference frame. By choosing to take the derivative with respect to the inertial frame, I make modelling shearwater trajectories much more tractable. However, it does itself lead to difficulties, as it is difficult to calculate the inertial derivative of the air velocity vector in the same equation. Because I make the assumption that the axes of the body frame of reference are collinear with the axes of the air reference frame, it is much easier to compute the derivative of the air velocity vector with respect to a body frame of reference. Thus, I use the identity ${}^{\mathcal{E}}d\mathbf{U}/dt = {}^{\mathcal{B}}d\mathbf{U}/dt + {}^{\mathcal{E}}\mathbf{\Omega}^{\mathcal{B}} \times \mathbf{U}$ to equate the inertial derivative of the kinematic velocity (needed for application of Newton's Second Law) to the body frame derivative of the aerodynamic velocity (needed to easily compute the aerodynamic acceleration) in Equation A.16.

The second case of choosing a reference frame to increase tractability is to project the vector derivatives of Equation A.19 into the body frame of reference. Given the symmetric flight condition assumption, this choice allows a simple resolution of the force vector and air velocity vector components and the formation of the dynamic equations of motion in Equations A.25 – A.27. From these equations of motion, I arrive at A.31. The model in A.31 is not tractable in the sense that one can find a closed-form solution to the differential equation, as one could with Equation 1.14 that models the simple pendulum, but it does have sufficiently good numerical properties for me to find reconstruct the shearwater trajectories used in Chapter 2. But, the choice of reference frames for modelling

shearwater turning made the system more tractable in the sense of being able to arrive at an expression that can be easily used to reconstruct trajectories.

As foundational to the work of Chapter 2 as Equation A.31 is the derivation of the horizontal wind effectiveness metric, ϵ_h. I derive ϵ_h from Equation A.9, which is the equation for the total rate of change in a bird's useful mechanical energy. Useful mechanical energy is the sum of gravitational potential energy and kinetic energy, where kinetic energy is defined in terms of the aerodynamic velocity vector, $\boldsymbol{U}$. It is also possible to define kinetic energy in terms of the kinematic velocity vector, $\boldsymbol{V}$, from which one defines an alternative form of mechanical energy that I will call kinematic mechanical energy. Thus, one can also derive an equation for the total rate of change in kinematic mechanical energy and, of course, define an analogous measure for ϵ_h. The kinematic form of the ϵ_h measure makes, however, the investigation of dynamic soaring less tractable. The system does not become fundamentally less tractable, as in the case of the simple pendulum, but it becomes less tractable in the sense that it is harder to measure the kinematic form of ϵ_h with current technology. To demonstrate this, I derive the kinematic form of ϵ_h below.

Deriving the kinematic form of ϵ_h We define the total mechanical energy E as the sum of the kinematic kinetic energy $E_k = \frac{1}{2}mV^2 = \frac{1}{2}m(\mathbf{V}\cdot\mathbf{V})$ and gravitational potential energy $E_h = -m\mathbf{g}\cdot\mathbf{x}$ where m is the mass of the bird, $\mathbf{x}$ is the position vector of the bird, $V = ||\mathbf{V}||$, $\mathbf{V}$ is the inertial derivative of the bird's position vector, which we call the inertial velocity, and $\mathbf{g}$ is the acceleration due to gravity. The time rate of change of total mechanical energy $\frac{dE}{dt}$ is then:

$$\frac{dE}{dt} = m(\mathbf{V}\cdot\frac{d\mathbf{V}}{dt}) - m\mathbf{g}\cdot\mathbf{v} \tag{5.1}$$

where $\frac{d\mathbf{V}}{dt}$ is the time derivative of inertial velocity in the inertial frame and is therefore the acceleration of the bird in the inertial frame. We can expand this expression using the identity $\mathbf{V} = \mathbf{U} + \mathbf{W}$ as follows:

$$\frac{dE}{dt} = m(\mathbf{U}+\mathbf{W})\cdot\frac{d\mathbf{V}}{dt} - m\mathbf{g}\cdot\mathbf{v} = \mathbf{F}\cdot\mathbf{U} + m\mathbf{W}\cdot\frac{d\mathbf{V}}{dt} - m\mathbf{g}\cdot\mathbf{v} \tag{5.2}$$

where $\mathbf{F}$ is the total force acting on the bird, $\mathbf{U}$ is the velocity of the bird with respect to the local wind-fixed reference frame, and $\mathbf{W}$ is the velocity of the wind with respect to

the inertial reference frame. We can decompose the total force $\mathbf{F}$ into an aerodynamic force $\mathbf{R}$ and the weight $m\mathbf{g}$. Doing so yields:

$$\frac{dE}{dt} = \mathbf{R} \cdot \mathbf{U} + m\mathbf{g} \cdot \mathbf{U} + m\mathbf{W} \cdot \frac{d\mathbf{V}}{dt} - m\mathbf{g} \cdot \mathbf{v} \tag{5.3}$$

Again using the identity $\mathbf{V} = \mathbf{U} + \mathbf{W}$, we have:

$$\frac{dE}{dt} = \mathbf{R} \cdot \mathbf{U} + m\mathbf{g} \cdot \mathbf{V} - m\mathbf{g} \cdot \mathbf{W} + m\mathbf{W} \cdot \frac{d\mathbf{V}}{dt} - m\mathbf{g} \cdot \mathbf{v} = \mathbf{R} \cdot \mathbf{U} - m\mathbf{g} \cdot \mathbf{W} + m\mathbf{W} \cdot \frac{d\mathbf{V}}{dt} \tag{5.4}$$

The aerodynamic force can be decomposed as the sum of aerodynamic lift $\mathbf{L}$, acting in a direction perpendicular to $\mathbf{U}$, and the net of aerodynamic drag $\mathbf{D}$ acting in the direction opposite $\mathbf{U}$, and thrust $\mathbf{T}$, acting in the direction of $\mathbf{U}$. Therefore we have $\mathbf{U} \cdot \mathbf{R} = (T - D)U$ where T, D, and U are the scalars associated with their respective vector quantities. Since $\mathbf{g}$ points down, only the vertical component of the wind vector (W_z) lies in its direction. Thus, $\mathbf{g} \cdot \mathbf{W} = gW_z$, where W_z is the component of wind in the direction of gravity and g is the scalar value of gravity. We thus arrive at this expression:

$$\frac{dE}{dt} = (T - D)U - mgW_z + m\mathbf{W} \cdot \frac{d\mathbf{V}}{dt} \tag{5.5}$$

The term $m\mathbf{W} \cdot \frac{d\mathbf{V}}{dt}$ is the rate of change of total mechanical energy with respect to the inertial frame as a consequence of dynamic soaring when kinetic energy is defined kinematically. The rate of change of specific mechanical energy due to dynamic soaring, e, is then given as:

$$e = \mathbf{W} \cdot \frac{d\mathbf{V}}{dt} \tag{5.6}$$

which is the specific energy (energy per unit mass) form of the dynamic soaring term of Equation 5.5. As $\frac{d\mathbf{V}}{dt} = \dot{V}\hat{\mathbf{V}} + V\dot{\hat{\mathbf{V}}}$, where $\hat{\mathbf{V}}$ is the unit vector in the direction of the inertial velocity vector and $\dot{\hat{\mathbf{V}}}$ is the rate of change of the direction of this unit vector (the bird's centripetal acceleration), we then have:

$$e = \mathbf{W} \cdot (\dot{V}\hat{\mathbf{V}} + V\dot{\hat{\mathbf{V}}}) = W\dot{V}\hat{\mathbf{W}} \cdot \hat{\mathbf{V}} + WV\hat{\mathbf{W}} \cdot \dot{\hat{\mathbf{V}}} \tag{5.7}$$

Maximising the energy extracted from the vertical wind gradient by dynamic soaring therefore requires maximising e. One contribution to this maximisation comes from the

second term $WV\hat{\mathbf{W}} \cdot \dot{\hat{\mathbf{V}}}$ which we denote ϵ. The term ϵ can never be continually positive as that would demand $\hat{\mathbf{W}} \cdot \dot{\hat{\mathbf{V}}}$ is continually positive which would imply always turning away from the wind. If we assume a horizontal wind field with a vertical wind gradient such that W increases with height, this then implies that a bird should turn with the wind at the higher altitudes of its trajectory and turn into the wind at the lower altitudes. We can write $W = z\sigma(z)$ where z is the altitude of the bird and $\sigma(z)$ is the strength of the vertical wind gradient. We can write $\hat{\mathbf{W}} \cdot \dot{\hat{\mathbf{V}}}$ as $\cos\chi$ where χ is the angle between the wind vector and the bird's centripetal acceleration. We therefore have:

$$\epsilon = z\sigma(z)V\cos\chi \tag{5.8}$$

The inertial velocity depends upon the bird's airspeed, which likely lies in some narrow range around an energy based optimum, and the wind speed, and is therefore less in the control of the bird than its turning behaviour. The wind gradient is outside the bird's control. We therefore suggest that maximising e and therefore ϵ also requires maximising the simpler quantity ϵ_h which we call the horizontal wind effectiveness and looks like:

$$\epsilon_h = z\cos\chi \tag{5.9}$$

With onboard GPS and wind data the angle χ is measurable. In principle, z is also measurable, though herein lies one problem with the kinematic form of ϵ_h. Accuracy in the vertical dimension of readily accessible GPS devices is often poor (Sachs et al., 2013; Gibb et al., 2017) so that estimating the kinematic form of ϵ_h is difficult and makes anlysing dynamic soaring with ϵ_h less tractable.

5.1.2 Parsimony

In the Introduction I discussed how the cosmological models of Hipparchus, Apollonius, Ptolemy, and Copernicus were variously parsimonious in their ability to model planetary motion with the same predictive power. The major shift in model parsimony occurs between the geocentric models of the classical 'scientists' and Copernicus' heliocentric model. The switch from geocentrism to heliocentrism is also a switch in reference frame, and the example illustrates how changes in model parsimony induced by changes in the

reference frame(s) chosen to model a system may be reflective of the physical structure of that system. Fundamentally, this is because a switch in frame can reveal something about the true number of degrees of freedom in a system.

In Chapter 3, I model Harris' hawk (*Parabuteo unicinctus*) pursuit guidance using feedback laws for which I vary the reference frame in which the line-of-sight rate input is measured. A fundamental conclusion of this approach is that proportional navigation (PN) guidance is the most parsimonious model of hawk pursuit, a conclusion that conflicts with an earlier study (Brighton et al., 2019). However, the conclusion corroborates the same result found in other bird and insect species (Brighton et al., 2017; Brighton et al., 2021; Fabian et al., 2018). so that it seems PN guidance may be a phylogenetically deep means of implementing pursuit behaviour. Model parsimony in this case does not reflect the underlying properties of the system in the same way that the parsimony of different cosmological models does; model parsimony here does not reflect something about the underlying degrees of freedom, for example. However, there is an analogy between my approach to Harris' hawk guidance and the cosmological modelling. In both cases by varying the modelling frame, one can judge the likelihood of the implied physical meaning of the frame by means of parsimony.

Of course, parsimony alone is not a sure indicator of the accuracy of a model –one need only consider the number of times flightlessness and gigantism has evolved in the ratite birds (Mitchell et al., 2014) to see so. But, when a more parsimonious model yields similar predictive ability as a less parsimonious one, this is indicative that a more fundamental description of a system is being reached.

5.1.3 Physical meaning

Much as the cosmological models of Ptolemy, Copernicus, and Kepler were phenomenological models, so are the models I present in Chapter 3. In both cases, the models are not derived from underlying physical laws but represent descriptions of the observed phenomena. Notwithstanding this, the reference frame in which a phenomenological model is constructed can imply properties of the system that it is modelling. Thus, whereas the Ptolemaic system implies a stationary Earth at the centre of the universe, the Copernican system implies an Earth that orbits the sun and has a daily rotation. Similarly, the success of the inertial-PN model of pursuit guidance in modelling Harris' hawk attack trajectories

would is consistent with the idea that a bird fuses inertial and visual information, whereas the commensurate success of the background-PNP model is consistent with the idea that visual information alone is sufficient. Copernicus was at pains to state that his model of the universe did not necessarily mean that the Earth was not stationary, the model merely provided an effective means for accounting for planetary motion. In taking this pain, Copernicus certainly saved himself further pain, and I make the analogous claim for the background-PNP model, though for less serious reasons. Just because the background-PNP guidance law successfully models the attack trajectories of Harris' hawks, this does not mean that the Harris' hawk uses only visual information to implement pursuit. The result is rather an in principle one, and in all likelihood Harris' hawks do fuse visual and inertial information to command attack trajectories. However, the finding suggests that one could, for example, implement pursuit guidance in a flight vehicle without the complexities of sensor fusion. Thus, in thinking about reference frames and what they imply about the modelled system, one can reach insights that might otherwise be unreached.

Sometimes the physical meaning implied by modelling a system in different reference frames can cause confusion. As discused in the Introduction, there has been a long running debate within the dynamic soaring literature as to whether the kinetic energy should be defined aerodynamically or kinematically. When defined kinematically, the physical mechanism of energy gain that is implied is one in which energy is harvested during the windward upper turn of the corkscrewing flight, whereas when defined aerodynamically, the physical mechanism of energy gain that is implied is one in which energy is harvested during windward climbs and leeward descents. As also discussed in the Introduction, both interpretations are correct, and a better question is to ask what this means for a dynamic soaring bird. Aerodynamic kinetic energy is 'useful' kinetic energy in the sense that excess aerodynamic kinetic energy can be converted into potential energy (Koessler, 2018; Taylor et al., 2016). In contrast, kinematic kinetic energy cannot necessarily be converted into potential energy, as novice pilots sometimes fatally discover (Pennycuick, 2008). However, this does not necessarily mean that kinematic kinetic energy is not useful. For a falcon turning from windward to leeward over the ridge of a hill, for example, this may provide the ground-reference spped required to catch fleeing quarry. The example of modelling kinetic energy in terms of different reference frames highlights that reference

frame choice does have different physical meaning, but it also highlights that one needs to carefully judge the relevance of implied physical meaning.

5.2 Conclusion

In Hein et al. (2020) the authors suggest that behavioural algorithms "provide a good starting point for studies of natural behaviour". The behavioural algorithm approach underlies the work of Chapter 3 where I use several behavioural algorithms to model Harris' hawk pursuit, and the work of Chapter 3 inspired the work of Chapter 4. However, whether explictly stated or not, the behavioural algorithms with which natural behaviours are modelled will imply whether the input(s) and output(s) are egocentric, exocentric, or both, and therefore whether and which reference frames are relevant. As argued in this thesis, modelling in different reference frames can be fruitful for analysing physical systems, an approach long known to engineers, but it can also be fruitful for modelling biological systems. Thus, I suggest that explicit consideration of the reference frames in which behaviour is modelled, and varying the modelling frame, can be a powerful approach to analysing animal behaviour and biomechanics.

References

Brighton, C. H., Chapman, K. E., Fox, N. C., and Taylor, G. K. (Mar. 2021). "Attack behaviour in naive gyrfalcons is modelled by the same guidance law as in peregrine falcons, but at a lower guidance gain". en. In: *Journal of Experimental Biology* 224.5, jeb238493. DOI: 10.1242/jeb.238493.

Brighton, C. H. and Taylor, G. K. (Dec. 2019). "Hawks steer attacks using a guidance system tuned for closepursuit of erratically manoeuvring targets". en. In: *Nature Communications* 10.1, p. 2462. DOI: 10.1038/s41467-019-10454-z.

Brighton, C. H., Thomas, A. L. R., and Taylor, G. K. (Dec. 2017). "Terminal attack trajectories of peregrine falcons are described by the proportional navigation guidance law of missiles". en. In: *Proceedings of the National Academy of Sciences* 114.51, pp. 13495–13500. DOI: 10.1073/pnas.1714532114.

Fabian, S. T., Sumner, M. E., Wardill, T. J., Rossoni, S., and Gonzalez-Bellido, P. T. (Oct. 2018). "Interception by two predatory fly species is explained by a proportional navigation feedback controller". en. In: *Journal of The Royal Society Interface* 15.147, p. 20180466. DOI: 10.1098/rsif.2018.0466.

Gibb, R., Shoji, A., Fayet, A. L., Perrins, C. M., Guilford, T., and Freeman, R. (2017). "Remotely sensed wind speed predicts soaring behaviour in a wide-ranging pelagic seabird". In: *Journal of The Royal Society Interface* 14.132, p. 20170262. DOI: 10.1098/rsif.2017.0262.

Hein, A. M., Altshuler, D. L., Cade, D. E., Liao, J. C., Martin, B. T., and Taylor, G. K. (June 2020). "An Algorithmic Approach to Natural Behavior". en. In: *Current Biology* 30.11, R663–R675. DOI: 10.1016/j.cub.2020.04.018.

Koessler (2018). “Dynamic Soaring UAV Gliders”. PhD thesis.

Mitchell, K. J., Llamas, B., Soubrier, J., Rawlence, N. J., Worthy, T. H., Wood, J., Lee, M. S. Y., and Cooper, A. (May 2014). “Ancient DNA reveals elephant birds and kiwi are sister taxa and clarifies ratite bird evolution”. en. In: *Science* 344.6186, pp. 898–900. DOI: 10.1126/science.1251981.

Pennycuick, C. J. (2008). *Modelling the flying bird*. Theoretical ecology series. Amsterdam ; London: Academic Press. xiv+480.

Sachs, G., Traugott, J., Nesterova, A. P., and Bonadonna, F. (2013). “Experimental verification of dynamic soaring in albatrosses”. In: *Journal of Experimental Biology* 216.22, pp. 4222–4232. DOI: 10.1242/jeb.085209.

Taylor, G. K., Reynolds, K. V., and Thomas, A. L. R. (2016). “Soaring energetics and glide performance in a moving atmosphere”. In: *Philosophical Transactions of the Royal Society B: Biological Sciences* 371.1704, p. 20150398. DOI: 10.1098/rstb.2015.0398.

Appendices

A

Supplementary Material to Chapter 2

Contents

A.1 Supplementary Text 114
References 122

A.1 Supplementary Text

Energetics of dynamic soaring Here we derive an equation for the rate of change in useful mechanical energy during soaring. This equation demonstrates that one contribution is due to movement through a variable wind field, thereby quantifying the possibility for dynamic soaring. On the time-scale of our video recordings we can assume a flat, non-rotating Earth (Tatum, 1980), such that the Earth-fixed axis system $\mathcal{F}_\mathcal{E} = (O, \hat{\mathbf{x}}_\mathcal{E}, \hat{\mathbf{y}}_\mathcal{E}, \hat{\mathbf{z}}_\mathcal{E})$ with arbitrary origin O and right-handed orthonormal basis vectors $(\hat{\mathbf{x}}_\mathcal{E}, \hat{\mathbf{y}}_\mathcal{E}, \hat{\mathbf{z}}_\mathcal{E})$ with $\hat{\mathbf{z}}_\mathcal{E}$ pointing in the direction of gravity, is an inertial frame of reference. Denoting the centre of mass of the bird G, we call the bird's position vector in this coordinate system $\mathbf{r}_{G/O}$, such that its ground velocity $\mathbf{V}$ is the time-derivative of $\mathbf{r}_{G/O}$ in $\mathcal{F}_\mathcal{E}$, written $\mathbf{V} = {}^\mathcal{E}d\mathbf{r}_{G/O}/dt$. Likewise, if $\mathbf{r}_{W/O}$ is the position of an element of the surrounding fluid barring any influence of the bird, then the local wind velocity $\mathbf{W}$ is the time-derivative of $\mathbf{r}_{W/O}$ in $\mathcal{F}_\mathcal{E}$, written $\mathbf{W} = {}^\mathcal{E}d\mathbf{r}_{W/O}/dt$. Differentiating the identity $\mathbf{r}_{G/O} = \mathbf{r}_{W/O} + \mathbf{r}_{G/W}$ with respect to time in $\mathcal{F}_\mathcal{E}$, we therefore have:

$$\mathbf{V} = \mathbf{W} + \frac{^{\mathcal{E}}d\mathbf{r}_{G/W}}{dt} \tag{A.1}$$

which establishes $\mathbf{U} = {}^{\mathcal{E}}d\mathbf{r}_{G/W}/dt$ as the aerodynamic velocity of the bird, defined as the time-derivative of $\mathbf{r}_{G/W}$ in $\mathcal{F}_{\mathcal{E}}$. We may therefore rewrite Equation A.1 as:

$$\mathbf{V} = \mathbf{W} + \mathbf{U} \tag{A.2}$$

The useful mechanical energy of a bird (E) is the sum of its aerodynamic kinetic energy and its gravitational potential energy, which we may write as:

$$E = \frac{1}{2}m(\mathbf{U} \cdot \mathbf{U}) - m\mathbf{g} \cdot \mathbf{r}_{G/O} \tag{A.3}$$

where m is the bird's mass and $\mathbf{g}$ is the acceleration due to gravity. Hence, since $\mathcal{F}_{\mathcal{E}}$ is an inertial frame, the time-derivative of Equation A.3:

$$\frac{^{\mathcal{E}}dE}{dt} = m\left(\mathbf{U} \cdot \frac{^{\mathcal{E}}d\mathbf{U}}{dt}\right) - m\mathbf{g} \cdot \mathbf{V} \tag{A.4}$$

gives the rate of change of useful mechanical energy in an inertial frame. Taking the derivative of Equation A.2 in $\mathcal{F}_{\mathcal{E}}$ we have:

$$\frac{^{\mathcal{E}}d\mathbf{V}}{dt} = \frac{^{\mathcal{E}}d\mathbf{W}}{dt} + \frac{^{\mathcal{E}}d\mathbf{U}}{dt} \tag{A.5}$$

Then, by substitution of Equations A.2 and A.5 into Equation A.4 , we have:

$$\frac{^{\mathcal{E}}dE}{dt} = m\mathbf{U} \cdot \left[\frac{^{\mathcal{E}}d\mathbf{V}}{dt} - \frac{^{\mathcal{E}}d\mathbf{W}}{dt}\right] - m\mathbf{g} \cdot [\mathbf{U} + \mathbf{W}] \tag{A.6}$$

such that by a rearrangement making use of the distributive property of the scalar product we have:

$$\frac{^{\mathcal{E}}dE}{dt} = \mathbf{U} \cdot \left[m\frac{^{\mathcal{E}}d\mathbf{V}}{dt} - m\mathbf{g}\right] - m\mathbf{g} \cdot \mathbf{W} - m\mathbf{U} \cdot \frac{^{\mathcal{E}}d\mathbf{W}}{dt}. \tag{A.7}$$

By Newton's second law, the first term of this equation is the total force acting on the bird less its weight, which is equivalent to the aerodynamic force $\mathbf{R}$. The vector equation for the total rate of change in useful mechanical energy can therefore be written as:

$$\frac{^{\mathcal{E}}dE}{dt} = \mathbf{U} \cdot \mathbf{R} - m\mathbf{g} \cdot \mathbf{W} - m\mathbf{U} \cdot \frac{^{\mathcal{E}}d\mathbf{W}}{dt} \tag{A.8}$$

The aerodynamic force $\mathbf{R}$ can be decomposed as the sum of aerodynamic lift $\mathbf{L}$, acting in a direction perpendicular to $\mathbf{U}$, and the net of aerodynamic drag $\mathbf{D}$ acting opposite to $\mathbf{U}$, and thrust $\mathbf{T}$ acting in the direction of $\mathbf{U}$. We therefore have $\mathbf{U} \cdot \mathbf{R} = (T - D)U$ where $T = \|\mathbf{T}\|$, $D = \|\mathbf{D}\|$, and $U = \|\mathbf{U}\|$ are the magnitudes of their respective vector quantities. Since $\mathbf{g}$ points down, only the vertical component of the wind vector (W_z) lies in its direction, such that $\mathbf{g} \cdot \mathbf{W} = gW_z$. Here W_z is the component of wind in the direction of gravity and $g = \|\mathbf{g}\|$. We thus arrive at the simpler expression:

$$\frac{^{\mathcal{E}}dE}{dt} = \underbrace{TU - DU}_{\text{power surplus/deficit}} + \underbrace{mgW_z}_{\text{static soaring}} - \underbrace{m\mathbf{U} \cdot \frac{^{\mathcal{E}}d\mathbf{W}}{dt}}_{\text{dynamic soaring}} \tag{A.9}$$

which quantifies all of the energy flows relevant to soaring flight.

The flow of specific energy (e) due to dynamic soaring is:

$$\frac{^{\mathcal{E}}de}{dt} = -\mathbf{U} \cdot \frac{^{\mathcal{E}}d\mathbf{W}}{dt} \tag{A.10}$$

which is just the dynamic soaring term of Equation A.9 normalised by the bird's mass m. Estimating $^{\mathcal{E}}de/dt$ empirically requires precise knowledge of the wind experienced by the bird, which is exceedingly difficult to measure in the natural environment. However, if the wind is assumed to have the same direction everywhere, given by the constant unit vector $\hat{\mathbf{W}} = \mathbf{W}/W$ where $W = ||\mathbf{W}||$ is the wind speed, then $^{\mathcal{E}}d\mathbf{W}/dt = \hat{\mathbf{W}}^{\mathcal{E}}dW/dt$. We will further assume that the wind is steady and horizontal, which implies that only the horizontal component of the bird's air velocity contributes to the scalar product in Equation A.10. These assumptions are those generally employed in modelling dynamic soaring, and we may use them to rewrite Equation A.10 as:

$$\frac{^{\mathcal{E}}de}{dt} = -U \cos\gamma \cos\eta \frac{^{\mathcal{E}}dW}{dt} \tag{A.11}$$

where $U = \|\mathbf{U}\|$ is the bird's airspeed, γ is the aerodynamic flight path angle defined as the elevation of the bird's air velocity $\mathbf{U}$ with respect to the horizontal, and η is the heading-to-wind angle defined as the angle between $\hat{\mathbf{W}}$ and the horizontal component of $\mathbf{U}$. If we further assume that W is only a function of vertical height h above the surface, where $\sigma(h) = {}^{\mathcal{E}}dW/dh$ is the vertical wind shear gradient, then we may make use of the bird's vertical climb rate ${}^{\mathcal{E}}dh/dt = U\sin\gamma$ to write the identity ${}^{\mathcal{E}}dW/dt = \sigma(h)U\sin\gamma$. Equation A.11 then becomes:

$$\frac{{}^{\mathcal{E}}de}{dt} = -U\sigma(h)U\sin\gamma\cos\gamma\cos\eta \tag{A.12}$$

which we may rewrite using the trigonometric identity $\sin 2\gamma = 2\sin\gamma\cos\gamma$ as:

$$\frac{{}^{\mathcal{E}}de}{dt} = -\frac{1}{2}U^2\sigma(h)\sin 2\gamma\cos\eta \tag{A.13}$$

This is the result taken as the starting point of the analysis in the main text, where for simplicity we drop the preceding superscript notation denoting that the derivative is taken in $\mathcal{F}_{\mathcal{E}}$.

Model of unsteady banked turning In a steady wind field, the time derivative of the wind velocity $\mathbf{W}$ that a bird experiences as a result of its own motion relative to the Earth is:

$$\frac{{}^{\mathcal{E}}d\mathbf{W}}{dt} = {}^{\mathcal{E}}\nabla\mathbf{W}\mathbf{V} \tag{A.14}$$

where the preceding superscript notation denotes that the derivative is taken with respect to the Earth-fixed frame of reference $\mathcal{F}_{\mathcal{E}}$. Here, ${}^{\mathcal{E}}\nabla\mathbf{W}$ denotes the gradient of the wind velocity, which is the Jacobian matrix of $\mathbf{W}$. Adding ${}^{\mathcal{E}}d\mathbf{U}/dt$ to both sides and making use of Equation A.5 we may rewrite Equation A.14 as:

$$\frac{{}^{\mathcal{E}}d\mathbf{V}}{dt} = \frac{{}^{\mathcal{E}}d\mathbf{U}}{dt} + {}^{\mathcal{E}}\nabla\mathbf{W}\mathbf{V} \tag{A.15}$$

All of the equations to this point have been written in the Earth-fixed axis system $\mathcal{F}_{\mathcal{E}}$, but for the purposes of modelling the bird's turning behaviour, we define a set of body axes $\mathcal{F}_{\mathcal{B}} = (G, \hat{\mathbf{x}}_{\mathcal{B}}, \hat{\mathbf{y}}_{\mathcal{B}}, \hat{\mathbf{z}}_{\mathcal{B}})$. Here, $(\hat{\mathbf{x}}_{\mathcal{B}}, \hat{\mathbf{y}}_{\mathcal{B}}, \hat{\mathbf{z}}_{\mathcal{B}})$ is a set of right-handed orthonormal basis

vectors with their origin at the bird's centre of mass G. The vector $\hat{\mathbf{x}}_{\mathcal{B}}$ denotes the bird's longitudinal body axis, and is aligned with its aerodynamic velocity vector $\mathbf{U}$ at equilibrium; the vector $\hat{\mathbf{z}}_{\mathcal{B}}$ also lies within the bird's plane of symmetry and points ventrally. The orientation of the body axes with respect to the Earth axes is specified by a set of intrinsic Euler angles (ψ, θ, ϕ) defined in a z-y-x rotation sequence, where ψ is called the yaw angle, θ is called the pitch angle, and ϕ is called the bank angle.

The time derivative of $\mathbf{U}$ in the Earth-fixed axis system is related to the time derivative of $\mathbf{U}$ in the body axis system by the identity ${}^{\mathcal{E}}d\mathbf{U}/dt = {}^{\mathcal{B}}d\mathbf{U}/dt + {}^{\mathcal{E}}\boldsymbol{\Omega}^{\mathcal{B}} \times \mathbf{U}$, where the preceding superscript denotes the axis system in which the derivative is taken, and where ${}^{\mathcal{E}}\boldsymbol{\Omega}^{\mathcal{B}}$ is the angular velocity of the body axes relative to the Earth axes. Using Equation A.2 to write ${}^{\mathcal{E}}\nabla\mathbf{W}\mathbf{V} = {}^{\mathcal{E}}\nabla\mathbf{W}\mathbf{U} + {}^{\mathcal{E}}\nabla\mathbf{W}\mathbf{W}$, we may therefore rewrite the bird's inertial acceleration as:

$$\frac{{}^{\mathcal{E}}d\mathbf{V}}{dt} = \frac{{}^{\mathcal{B}}d\mathbf{U}}{dt} + {}^{\mathcal{E}}\boldsymbol{\Omega}^{\mathcal{B}} \times \mathbf{U} + {}^{\mathcal{E}}\nabla\mathbf{W}\mathbf{U} + {}^{\mathcal{E}}\nabla\mathbf{W}\mathbf{W}. \tag{A.16}$$

We will restrict further analysis to the special case of a steady vertical wind gradient in which the wind is constrained to the horizontal plane and has the same direction everywhere. If we further specify that the otherwise arbitrary horizontal basis vector of the Earth axes, $\hat{\mathbf{x}}_{\mathcal{E}}$, is aligned with the wind, then the Jacobian becomes:

$${}^{\mathcal{E}}\nabla\mathbf{W} = \begin{bmatrix} 0 & 0 & -\sigma(h) \\ 0 & 0 & 0 \\ 0 & 0 & 0 \end{bmatrix} \tag{A.17}$$

where $\sigma(h) = -\partial W/\partial z_{\mathcal{E}}$ denotes the vertical wind shear gradient with respect to height h above the surface. Given our assumptions on the wind, the ${}^{\mathcal{E}}\nabla\mathbf{W}\mathbf{W}$ term in Equation A.16 therefore vanishes, because:

$${}^{\mathcal{E}}\nabla\mathbf{W}\mathbf{W} = \begin{bmatrix} 0 & 0 & -\sigma(h) \\ 0 & 0 & 0 \\ 0 & 0 & 0 \end{bmatrix} \begin{bmatrix} W(h) \\ 0 \\ 0 \end{bmatrix} = 0. \tag{A.18}$$

where $W(h)$ is the wind speed at height h above the surface. Rewriting Equation A.16 therefore yields the equation:

$$\frac{^{\mathcal{E}}d\mathbf{V}}{dt} = \frac{^{\mathcal{B}}d\mathbf{U}}{dt} + {}^{\mathcal{E}}\Omega^{\mathcal{B}} \times \mathbf{U} + {}^{\mathcal{E}}\nabla\mathbf{W}\mathbf{U} \tag{A.19}$$

describing the bird's acceleration in an inertial frame of reference for a steady horizontal wind field of uniform direction with vertical wind gradient.

Having defined the frame of reference in which each derivative is taken, we are free to resolve the vector components of Equation A.19 in whatever axis system we choose. It will prove convenient to do so in the body axes defined by $\mathcal{F}_{\mathcal{B}}$. We write this as:

$$\left[\frac{^{\mathcal{E}}d\mathbf{V}}{dt}\right]_{\mathcal{B}} = \left[\frac{^{\mathcal{B}}d\mathbf{U}}{dt}\right]_{\mathcal{B}} + \left[{}^{\mathcal{E}}\Omega^{\mathcal{B}} \times \mathbf{U}\right]_{\mathcal{B}} + \left[{}^{\mathcal{E}}\nabla\mathbf{W}\mathbf{U}\right]_{\mathcal{B}} \tag{A.20}$$

where the subscript notation indicates the axes into which the quantities contained in square brackets are projected. We now make the key simplifying assumption that the bird always flies in a symmetric flight condition with its aerodynamic velocity vector $\mathbf{U}$ aligned with its longitudinal body axis $\hat{\mathbf{x}}_{\mathcal{B}}$. This amounts to assuming that the bird is perfectly stable in pitch and yaw, or to assuming that it coordinates its turning to achieve the same effect. With this simplifying assumption, we may write out Equation A.20 as:

$$\left[\frac{^{\mathcal{E}}d\mathbf{V}}{dt}\right]_{\mathcal{B}} = \begin{bmatrix}\dot{U}\\0\\0\end{bmatrix} + \begin{bmatrix}0 & -r & q\\ r & 0 & -p\\ -q & p & 0\end{bmatrix}\begin{bmatrix}U\\0\\0\end{bmatrix} + \mathbb{T}_{BE}\begin{bmatrix}0 & 0 & -\sigma(h)\\ 0 & 0 & 0\\ 0 & 0 & 0\end{bmatrix}\mathbb{T}_{EB}\begin{bmatrix}U\\0\\0\end{bmatrix} \tag{A.21}$$

where $\dot{U}$ is the rate of change of the bird's airspeed $U = \|\mathbf{U}\|$, where (p, q, r) are the bird's angular velocity components about $(\hat{\mathbf{x}}_{\mathcal{B}}, \hat{\mathbf{y}}_{\mathcal{B}}, \hat{\mathbf{z}}_{\mathcal{B}})$, and where $\mathbb{T}_{BE} = [\mathbb{T}_{EB}]^T$ is the change-of-basis matrix transforming from the Earth axes to the body axes:

$$\mathbb{T}_{BE} = \begin{bmatrix}\cos\psi\cos\theta & \sin\psi\cos\theta & -\sin\theta\\ -\sin\psi\cos\phi + \cos\psi\sin\theta\sin\phi & \cos\psi\cos\phi + \sin\psi\sin\theta\sin\phi & \cos\theta\sin\phi\\ \sin\psi\sin\phi + \cos\psi\sin\theta\cos\phi & -\sin\phi\cos\psi + \sin\psi\sin\theta\cos\phi & \cos\theta\cos\phi\end{bmatrix}. \tag{A.22}$$

Finally, after completing the matrix multiplications and simplifying, Equation A.21 can be rewritten:

$$\left[\frac{^{\mathcal{E}}d\mathbf{V}}{dt}\right]_{\mathcal{B}} = \begin{bmatrix}\dot{U}\\0\\0\end{bmatrix} + U\begin{bmatrix}0\\r\\-q\end{bmatrix} - U\sigma(h)\begin{bmatrix}-\cos\psi\sin\theta\cos\theta\\ \sin\psi\sin\theta\cos\phi - \cos\psi\sin^2\theta\sin\phi\\ -\sin\psi\sin\theta\sin\phi - \cos\psi\sin^2\theta\cos\phi\end{bmatrix} \tag{A.23}$$

which represents the bird's acceleration in an inertial frame of reference, projected onto its body axes. It remains to relate this acceleration to the forces that produce it, through a straightforward application of Newton's second law.

Because the bird's air velocity vector $\mathbf{U}$ is assumed to be aligned with $\hat{\mathbf{x}}_{\mathcal{B}}$, the net thrust-drag force $\mathbf{T}-\mathbf{D}$ acts along $\hat{\mathbf{x}}_{\mathcal{B}}$, whilst the lift force $\mathbf{L}$ acts opposite to $\hat{\mathbf{z}}_{\mathcal{B}}$. The total external force ($\mathbf{F}$) is therefore:

$$[\mathbf{F}]_{\mathcal{B}} = \begin{bmatrix} T - D - mg\sin\theta \\ mg\cos\theta\sin\phi \\ mg\cos\theta\cos\phi - L \end{bmatrix} \tag{A.24}$$

when resolved in the body axes. Using Newton's second law to relate Equations A.23 and A.24 as $[\mathbf{F}]_{\mathcal{B}} = m\left[{}^{\mathcal{E}}d\mathbf{V}/dt\right]_{\mathcal{B}}$, we therefore have the component equations:

$$T - D - mg\sin\theta = m\dot{U} + mU\sigma(h)\cos\psi\sin\theta\cos\theta \tag{A.25}$$

$$mg\cos\theta\sin\phi = mUr - mU\sigma(h)\sin\psi\sin\theta\cos\phi + mU\sigma(h)\cos\psi\sin^2\theta\sin\phi \tag{A.26}$$

$$mg\cos\theta\cos\phi - L = -mUq + mU\sigma(h)\sin\psi\sin\theta\sin\phi + mU\sigma(h)\cos\psi\sin^2\theta\cos\phi \tag{A.27}$$

describing the dynamics of flight in a steady shear layer for a bird that is perfectly stable in pitch and yaw. Rearranging equations A.26 and A.27 we arrive at the following expressions for the angular velocity components:

$$q = \frac{L}{mU} - \frac{g\cos\theta\cos\phi}{U} + \sigma(h)\sin\psi\sin\theta\sin\phi + \sigma(h)\cos\psi\sin^2\theta\cos\phi \tag{A.28}$$

$$r = \frac{g\cos\theta\sin\phi}{U} + \sigma(h)\sin\psi\sin\theta\cos\phi - \sigma(h)\cos\psi\sin^2\theta\sin\phi \tag{A.29}$$

The rate of change in the bird's yaw angle ψ is kinematically related to its angular velocity as:

$$\dot{\psi} = \frac{q\sin\phi + r\cos\phi}{\cos\theta}. \tag{A.30}$$

Substituting Equations A.29–A.28 into Equation A.30 and simplifying finally yields the general equation:

$$\dot{\psi} = \frac{L\sin\phi}{mU\cos\theta} + \sigma(h)\sin\psi\tan\theta \tag{A.31}$$

describing coordinated turning in a shear layer.

The first term on the right hand side of Equation A.31 captures how the bird's bank (ϕ) and pitch (θ) changes the horizontal direction of its longitudinal body axis. The second term captures the aerodynamic effect of the shear layer on the bird's turning, which arises because of our simplifying assumption that the bird is perfectly stable in pitch and yaw, or coordinates its flight to be so. This assumption implies that any sideslip that would otherwise arise as a result of the change in wind speed that the bird experiences as it ascends or descends through the shear layer is immediately trimmed out by weathercocking. It is clear by inspection that the effect of weathercocking is expected to be negligible if the bird ascends or descends through the shear layer in a headwind or tailwind direction, such that $\sin\psi$ is small, but that the effect of weathercocking could be significant otherwise.

The aerodynamic lift L on the wings is given by the lift equation $L = \rho U^2 S C_L/2$, where ρ is air density, S is wing area, and C_L is the lift coefficient, which is a function of the aerodynamic angle of attack. However, as the bird's air velocity vector $\mathbf{U}$ is assumed to coincide with its longitudinal body axis $\hat{\mathbf{x}}_{\mathcal{B}}$, the product SC_L will remain constant if we assume that the bird holds its wings fixed. Defining a reference airspeed U_0 as the airspeed associated with steady level flight at lift equal to body weight, it follows that the lift at airspeed U is $L = mgU^2/U_0^2$. We may therefore rewrite Equation (A.31) as:

$$\dot{\psi} = \frac{g \sin\phi(1 + \Delta U/U_0)}{U_0 \cos\theta} + \sigma(h) \sin\psi \tan\theta \tag{A.32}$$

where $U = U_0 + \Delta U$. Assuming that ΔU is small in comparison with U_0 such that $\frac{\Delta U}{U_0} \ll 1$, which is reasonable on the basis that any excess aerodynamic kinetic energy is expected to be converted to gravitational potential energy, it follows that we may approximate the bird's horizontal turn rate as:

$$\dot{\psi} \approx \frac{g \sin\phi}{U_0 \cos\theta} + \sigma(h) \sin\psi \tan\theta \tag{A.33}$$

which is the same approximation obtained directly by assuming constant airspeed $U = U_0$, and constant lift equal to body weight $L = mg$ in Eq. A.31.

The local shear gradient $\sigma(h)$ that a bird experiences is exceedingly difficult to measure empirically. Furthermore, as this term arises through weathercocking, it is

heavily dependent on the yaw stability of the bird, which is usually unknown. We have already established that its effect on the bird's turning will be small if the bird transits the shear layer whilst heading with or against the wind. These are the same flight directions as maximize the instantaneous rate of energy harvesting in dynamic soaring (see Eq. A.13). Hence, as a first approximation applicable to birds harvesting energy efficiently from the shear layer, we may adopt the simpler model:

$$\dot{\psi} \approx \frac{g \sin \phi}{U_0 \cos \theta} \tag{A.34}$$

which is the model of unsteady banked turning used in the main text. More generally, Equation A.34 provides a reasonable approximation of turn rate if:

$$\frac{\| \sin \phi \|}{\| \sin \theta \sin \psi \|} \gg \sigma(h) \frac{U_0}{g} \tag{A.35}$$

where we have made use of the trigonometric identity $\tan \theta = \sin \theta / \cos \theta$.

References

Tatum, J. B. (1980). "The Effect of the Coriolis Force on the Flight of a Bird". In: *The Auk* 97, pp. 99–117.

B

Supplementary Material to Chapter 3

Contents

B.1 Supplementary Text 123
B.2 Supplementary Figures 127
References 127

B.1 Supplementary Text

The line-of-sight rate in the background reference frame is equivalent to the component of the line-of-sight rate in the inertial frame due to the target's motion We define an inertial frame of reference, $\mathcal{F}_{\mathcal{I}} = (O, \mathbf{1}_{\boldsymbol{x}}, \mathbf{1}_{\boldsymbol{y}}, \mathbf{1}_{\boldsymbol{\omega}})$, by its origin, O, and its orthonormal basis vectors $(\mathbf{1}_{\boldsymbol{x}}, \mathbf{1}_{\boldsymbol{y}}, \mathbf{1}_{\boldsymbol{\omega}})$. The vector $\boldsymbol{r_T}$ represents the position vector, as a function of time, of a target, T, considered as a point mass in the frame $\mathcal{F}_{\mathcal{I}}$. The vector $\boldsymbol{r_P}$ represents the position vector, as a function of time, of a hawk, P, considered as a point mass in the frame $\mathcal{F}_{\mathcal{I}}$. By vector addition, we have the relative position vector, $\boldsymbol{r} = \boldsymbol{r_T} - \boldsymbol{r_P}$, which we call the line-of-sight vector. We call the time derivative of $\boldsymbol{r}$ with respect to $\mathcal{F}_I$ the relative velocity, $\boldsymbol{v}$.

We define the line-of-sight frame of reference $\mathcal{F}_{\mathcal{L}} = (P, \mathbf{1}_{\boldsymbol{r}}(t), \mathbf{1}_{\boldsymbol{n}}(t), \mathbf{1}_{\boldsymbol{\omega}}(t))$ by its origin P, which is at the centre of mass of the hawk, and its orthonormal basis vectors $(\mathbf{1}_{\boldsymbol{r}}(t), \mathbf{1}_{\boldsymbol{n}}(t), \mathbf{1}_{\boldsymbol{\omega}}(t))$. The $\mathbf{1}_{\boldsymbol{r}}(t)$ basis vector always points in the direction of $\boldsymbol{r}$, the $\mathbf{1}_{\boldsymbol{n}}(t)$ basis vector is always normal to $\mathbf{1}_{\boldsymbol{r}}(t)$ in the plane instantaneously spanned by $\mathbf{1}_{\boldsymbol{r}}(t)$ and

$\boldsymbol{v}$, and $\mathbf{1}_{\boldsymbol{\omega}}(t) = \mathbf{1}_{\boldsymbol{r}}(t) \times \mathbf{1}_{\boldsymbol{n}}(t)$. The time derivative of $\boldsymbol{r}$ with respect to $\mathcal{F}_{\mathcal{L}}$ is related to the time derivative with respect to $\mathcal{F}_{\mathcal{I}}$ by the equation:

$$\begin{aligned}
{}^{\mathcal{I}}\frac{d\boldsymbol{r}}{dt} = \boldsymbol{v} &= {}^{\mathcal{L}}\frac{d\boldsymbol{r}}{dt} + {}^{I}\boldsymbol{\omega}^{L} \times \boldsymbol{r} \\
&= \dot{r}\mathbf{1}_{\boldsymbol{r}} + {}^{I}\boldsymbol{\omega}^{L} \times \boldsymbol{r} \\
&= \dot{r}\mathbf{1}_{\boldsymbol{r}} + r\,{}^{I}\boldsymbol{\omega}^{L} \times \mathbf{1}_{\boldsymbol{r}},
\end{aligned}$$

where ${}^{I}\boldsymbol{\omega}^{L}$ is the angular velocity of the frame $\mathcal{F}_{\mathcal{L}}$ with respect to the frame $\mathcal{F}_{\mathcal{I}}$. Taking the cross product with $\boldsymbol{r}$, we then have:

$$\begin{aligned}
\boldsymbol{r} \times \boldsymbol{v} &= \boldsymbol{r} \times \dot{r}\mathbf{1}_{\boldsymbol{r}} + \boldsymbol{r} \times (r\,{}^{I}\boldsymbol{\omega}^{L} \times \mathbf{1}_{\boldsymbol{r}}) \\
&= r^{2}\mathbf{1}_{\boldsymbol{r}} \times ({}^{I}\boldsymbol{\omega}^{L} \times \mathbf{1}_{\boldsymbol{r}}) \\
&= r^{2}\,{}^{I}\boldsymbol{\omega}^{L} \\
\therefore\ {}^{I}\boldsymbol{\omega}^{L} &= {}^{\mathcal{I}}\dot{\lambda}\mathbf{1}_{\boldsymbol{\omega}} = \frac{\boldsymbol{r} \times \boldsymbol{v}}{r^{2}},
\end{aligned} \tag{B.1}$$

where ${}^{\mathcal{I}}\dot{\lambda}$ is the magnitude of the angular velocity of the frame $\mathcal{F}_{\mathcal{L}}$ with respect to the frame $\mathcal{F}_{\mathcal{I}}$, and therefore also the magnitude of the angular velocity of the relative position vector $\boldsymbol{r}$ with respect to $\mathcal{F}_{\mathcal{I}}$.

As the pursuit is planar, all position and velocity vectors lie in the same plane, and we can decompose the angular velocity vector as:

$$\begin{aligned}
\frac{\boldsymbol{r} \times \boldsymbol{v}}{r^{2}} &= \frac{\boldsymbol{r} \times (\boldsymbol{v_T} - \boldsymbol{v_P})}{r^{2}} \\
&= \frac{\boldsymbol{r} \times \boldsymbol{v_T}}{r^{2}} - \frac{\boldsymbol{r} \times \boldsymbol{v_P}}{r^{2}} && \text{(B.2)} \\
&= \boldsymbol{\omega_T} - \boldsymbol{\omega_P} && \text{(B.3)} \\
\therefore\ {}^{\mathcal{I}}\dot{\lambda}\mathbf{1}_{\boldsymbol{\omega}} &= \dot{\lambda}_{T}\mathbf{1}_{\boldsymbol{\omega}} - \dot{\lambda}_{P}\mathbf{1}_{\boldsymbol{\omega}} \\
\therefore\ {}^{\mathcal{I}}\dot{\lambda} &= \dot{\lambda}_{T} - \dot{\lambda}_{P}, && \text{(B.4)}
\end{aligned}$$

where $\boldsymbol{\omega_T}$ is the angular velocity component of ${}^{I}\boldsymbol{\omega}^{L}$ due to the target's motion, $\dot{\lambda}_{T}$ is the angular speed of this component, $\boldsymbol{\omega_P}$ is the angular velocity component of ${}^{I}\boldsymbol{\omega}^{L}$ due to the pursuer's motion, and $\dot{\lambda}_{P}$ is the angular speed of this component. Computing the cross products of Equation B.2, we have:

$${}^{\mathcal{I}}\dot{\lambda} = \frac{v_{T}\sin\theta}{r} - \frac{v_{P}\sin\delta}{r}, \tag{B.5}$$

where the deviation angle δ is the angle between $\boldsymbol{v_P}$ and $\boldsymbol{r}$, and the aspect angle θ is the angle between $\boldsymbol{v_T}$ and $\boldsymbol{r}$.

Proportional navigation (PN) commands lateral accelerations perpendicular to the pursuer velocity vector by:

$$\boldsymbol{a_c} = N^I\boldsymbol{\omega}^L \times \boldsymbol{v_P}, \tag{B.6}$$

where $\boldsymbol{a_c}$ is the lateral acceleration commanded normal to $\boldsymbol{v_p}$ (Shneydor, 2011) and N is the guidance constant. Computing the cross product in Equation B.6, we have:

$$\boldsymbol{a_c} = N{v_p}^{\mathcal{I}}\dot{\lambda}\sin\beta\mathbf{1_u}, \tag{B.7}$$

where β is the angle between $\mathbf{1}_{\boldsymbol{\omega}}$ and $\boldsymbol{v_p}$ and $\mathbf{1_u}$ is the unit vector normal to these two vectors, which lies in the plane of pursuit. For planar pursuit $\beta = \frac{\pi}{2}$ and therefore $a_c = N{v_p}^{\mathcal{I}}\dot{\lambda}$. Using the classic result from circular mechanics that $a_c = v\dot{\gamma}$, we have:

$$a_c = v_p\dot{\gamma} = N{v_p}^{\mathcal{I}}\dot{\lambda} \tag{B.8}$$

$$\therefore\ \dot{\gamma} = N^{\mathcal{I}}\dot{\lambda}, \tag{B.9}$$

where $\dot{\gamma}$ is the rate of change of direction of the path angle, γ, the angle that $\boldsymbol{v_p}$ makes with $\mathbf{1_x}$. Equation B.9 is the classical result for proportional navigation in planar pursuit. Given the planar engagement and given Equation (B.4), we can rewrite Equation (B.9) as:

$$\dot{\gamma} = N(\dot{\lambda}_T - \dot{\lambda}_P), \tag{B.10}$$

which emphasises the different components of angular speed that influence guidance.

In Figure 3.2 we consider a three particle system containing P, T, and a background patch, B. In the modelling we present in the main text, we assume that the distance between the target and the background patch is negligibly small. We here suspend this assumption for the time being and consider a background patch that can move in an inertial frame and need not be at a negligibly small distance from T. We call the background position vector $\boldsymbol{r_B}$ such that there is a background line-of-sight vector $\boldsymbol{b} = \boldsymbol{r_B} - \boldsymbol{r_P}$ between P and B. We define a background frame of reference $\mathcal{F}_{\mathcal{B}} = (P, \mathbf{1}_{x'}, \mathbf{1}_{y'}, \mathbf{1}_{\omega})$ which shares an origin P with $\mathcal{F}_L$. The basis vector $\mathbf{1}_{x'}$ always points along $\boldsymbol{b}$. The time derivative

of $\boldsymbol{b}$ in the frame $\mathcal{F}_\mathcal{I}$ is the velocity $\boldsymbol{v_b}$. The time derivative of $\boldsymbol{b}$ in the frame $\mathcal{F}_\mathcal{I}$ is related to the time derivative of $\boldsymbol{b}$ in the frame $\mathcal{F}_\mathcal{B}$ by:

$$\begin{aligned}\boldsymbol{v_b} &= {}^{\mathcal{B}}\frac{d\boldsymbol{b}}{dt} + {}^{I}\boldsymbol{\omega}^{B} \times \boldsymbol{b} \\ &= \dot{b}\mathbf{1}_{\boldsymbol{x'}} + {}^{I}\boldsymbol{\omega}^{B} \times \boldsymbol{b} \\ &= \dot{b}\mathbf{1}_{\boldsymbol{x'}} + b^{I}\boldsymbol{\omega}^{B} \times \mathbf{1}_{\boldsymbol{x'}},\end{aligned}$$

where ${}^{I}\boldsymbol{\omega}^{B}$ is the angular velocity of $\mathcal{F}_\mathcal{B}$ with respect to $\mathcal{F}_\mathcal{I}$ and therefore also of $\boldsymbol{b}$ in $\mathcal{F}_\mathcal{I}$. We derive an expression for this angular velocity as:

$$\begin{aligned}\boldsymbol{b} \times \boldsymbol{v_b} &= \boldsymbol{b} \times \dot{b}\mathbf{1}_{\boldsymbol{x'}} + \boldsymbol{b} \times (b^{I}\boldsymbol{\omega}^{B} \times \mathbf{1}_{\boldsymbol{x'}}) \\ &= b^2\mathbf{1}_{\boldsymbol{x'}} \times ({}^{I}\boldsymbol{\omega}^{B} \times \mathbf{1}_{\boldsymbol{x'}}) \\ &= b^{2I}\boldsymbol{\omega}^{B} \\ \therefore {}^{I}\boldsymbol{\omega}^{B} &= \dot{\lambda}_b\dot{\lambda}\mathbf{1}_{\boldsymbol{\omega}} = \frac{\boldsymbol{b} \times \boldsymbol{v_b}}{b^2},\end{aligned} \tag{B.11}$$

where $\dot{\lambda}_b$ is the angular speed of the frame $\mathcal{F}_\mathcal{B}$ with respect to $\mathcal{F}_\mathcal{I}$, and also the angular speed of $\boldsymbol{b}$ in $\mathcal{F}_\mathcal{I}$. Given the form of Equation B.5, we can write $\dot{\lambda}_b$ as:

$${}^{\mathcal{B}}\dot{\lambda} = \frac{v_B \sin\alpha}{b} - \frac{v_P \sin\delta_b}{b}, \tag{B.12}$$

where α is the angle between between the background velocity vector $\boldsymbol{v_b}$ and $\boldsymbol{b}$, and δ_b is the deviation angle between P's velocity vector, $\boldsymbol{v_P}$, and $\boldsymbol{b}$. We have derived the angular speeds of $\mathcal{F}_\mathcal{L}$ and $\mathcal{F}_\mathcal{B}$ relative to $\mathcal{F}_\mathcal{I}$ such that, given the relation ${}^{0}\omega^{2} - {}^{0}\omega^{1} = {}^{1}\omega^{2}$, we can determine the angular speed of $\mathcal{F}_\mathcal{L}$ relative to $\mathcal{F}_\mathcal{B}$. Given Equations B.5 and B.12, we therefore have:

$${}^{\mathcal{B}}\dot{\lambda} = \frac{v_T \sin\theta}{r} - \frac{v_P \sin\delta}{r} - \left(\frac{v_b \sin\alpha}{b} - \frac{v_P \sin\delta_b}{b}\right), \tag{B.13}$$

where ${}^{\mathcal{B}}\dot{\lambda}$ is the angular speed of $\mathcal{F}_\mathcal{L}$ relative to $\mathcal{F}_\mathcal{B}$ or, equivalently, the angular speed of $\boldsymbol{r}$ relative to $\boldsymbol{b}$. Equation B.13 is the general formula for the angular rate of a target with respect to a given background patch. Now, if we assume the background patch is stationary in the inertial frame (i.e. $v_b = 0$), Equation B.13 reduces to:

$${}^{\mathcal{B}}\dot{\lambda} = \frac{v_T \sin\theta}{r} - \frac{v_P \sin\delta}{r} + \frac{v_P \sin\delta_b}{b} \tag{B.14}$$

As $b \to \infty$, $\dot{\lambda}_b \to 0$, and $(v_T \sin\theta)/r - (v_P \sin\delta)/r + (v_P \sin\delta_b)/b \to (v_T \sin\theta)/r - (v_P \sin\delta)/r$ such that ${}^{\mathcal{B}}\dot{\lambda} \to {}^{\mathcal{I}}\dot{\lambda}$. In contrast, when the background patch is close to the target, as we model in the main text, $r \approx b$ and $\delta_b \approx \delta$, such that:

$$ {}^{\mathcal{B}}\dot{\lambda} \approx \frac{v_T \sin\theta}{r} \approx \dot{\lambda}_T \tag{B.15} $$

thereby justifying our equation for ${}^{\mathcal{B}}\dot{\lambda}$ given in Equation 3.12 of the Methods and Materials.

B.2 Supplementary Figures

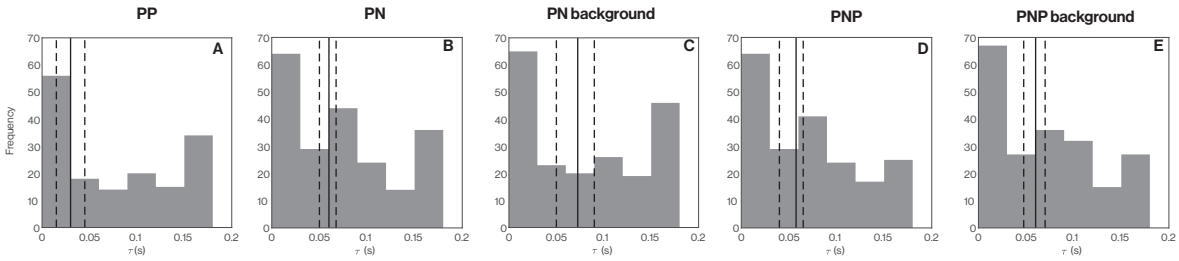


Figure B.1: The distribution of τ under different guidance models. We plot the distribution of the best-fit τ parameter found by the individual fitting method (see Methods and Materials) under **A** PP guidance ($\tilde{\epsilon} = 0.030$ s; 95% bootstrapped CI: 0.015, 0.045 s), **B** PN guidance ($\tilde{\epsilon} = 0.060$ s; 95% bootstrapped CI: 0.050, 0.068 s), **C** PN background guidance ($\tilde{\epsilon} = 0.073$ s; 95% bootstrapped CI: 0.050, 0.090 s), **D** PNP guidance ($\tilde{\epsilon} = 0.058$ s; 95% bootstrapped CI: 0.040, 0.065 s), and **E** PNP background guidance ($\tilde{\epsilon} = 0.060$ s; 95% bootstrapped CI: 0.048, 0.070 s). In none of the histograms does the distribution of τ show a strong central tendency.

References

Shneydor, N. A. (2011). *Missile guidance and pursuit: kinematics, dynamics and control.* eng. Oxford: Woodhead Publishing.

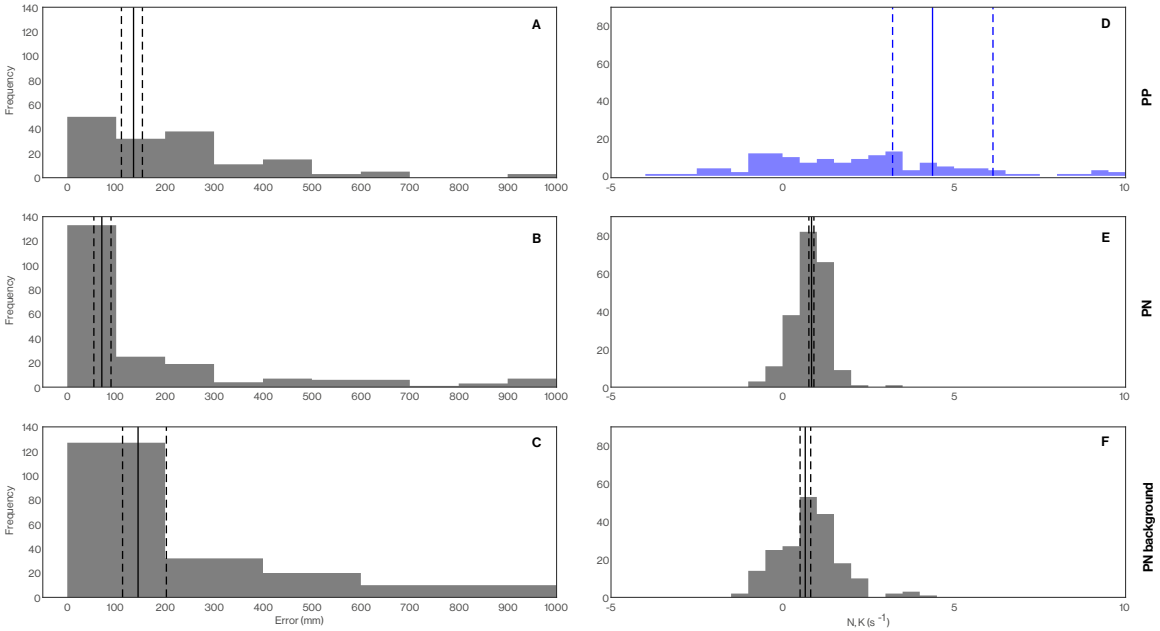


Figure B.2: The distribution of the prediction error ϵ and guidance constants under PP, PN, and PN background guidance. In **A-C** we plot the distribution of the prediction error ϵ under the PP ($\tilde{\epsilon} = 135$ mm; 95% bootstrapped CI: 111, 154 mm), PN ($\tilde{\epsilon} = 71$ mm; 95% bootstrapped CI: 54, 90 mm), and PN background ($\tilde{\epsilon} = 145$ mm; 95% bootstrapped CI: 113, 203 mm) guidance models given the individual fitting method applied to $n = 228$ flight trials (see Methods and Materials). In **D** we plot the distribution of the best-fit parameter K under PP guidance ($\tilde{K} = 4.4$ s^{-1}; 95% bootstrapped CI: 3.2, 6.1 s^{-1}), whereas in **E-F** we plot the distribution of the best-fit parameter N under PN ($\tilde{N} = 0.85$; 95% bootstrapped CI: 0.77, 0.91) and PN background guidance ($\tilde{N} = 0.66$; 95% bootstrapped CI: 0.51, 0.82).

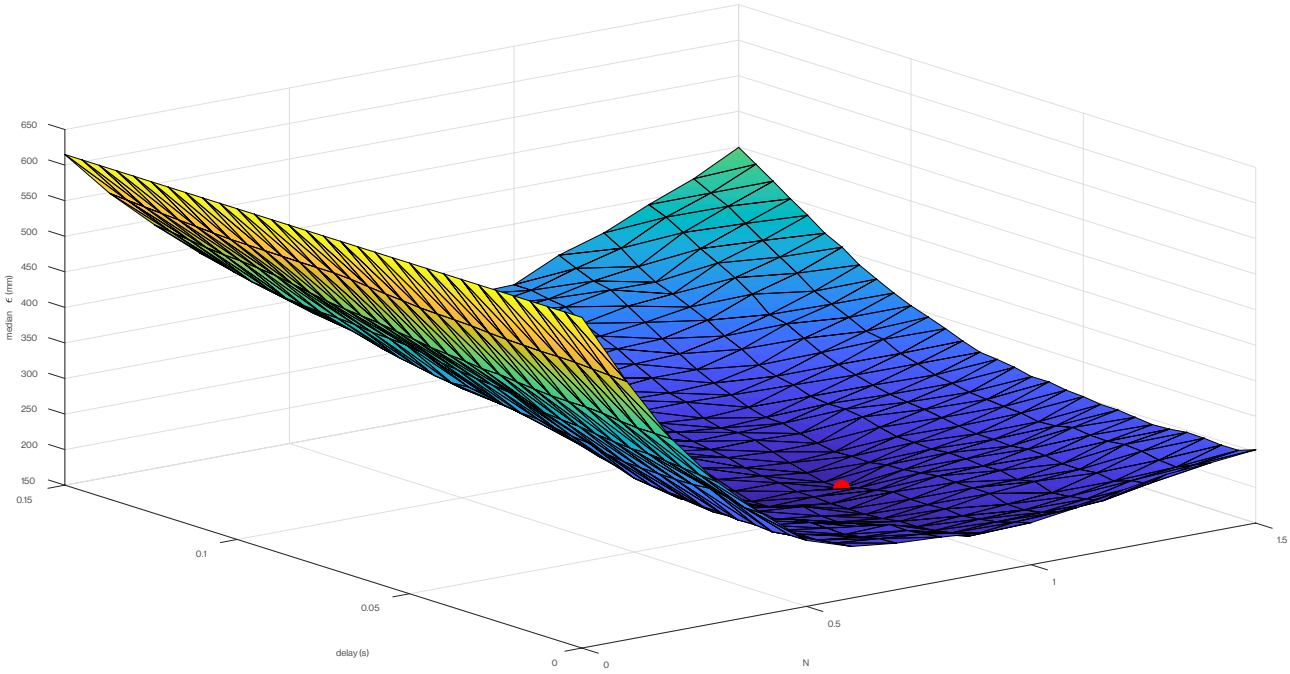


Figure B.3: Surface plot of PN guidance. The surface plot displays how the median prediction error $\tilde{\epsilon}$ under PN guidance varies across the parameter space of τ and N. The colouring indicates surface height (and therefore median prediction error $\tilde{\epsilon}$) and the red dot the optimum parameter combination that minimises the median prediction error $\tilde{\epsilon}$, as found under the global fit method.

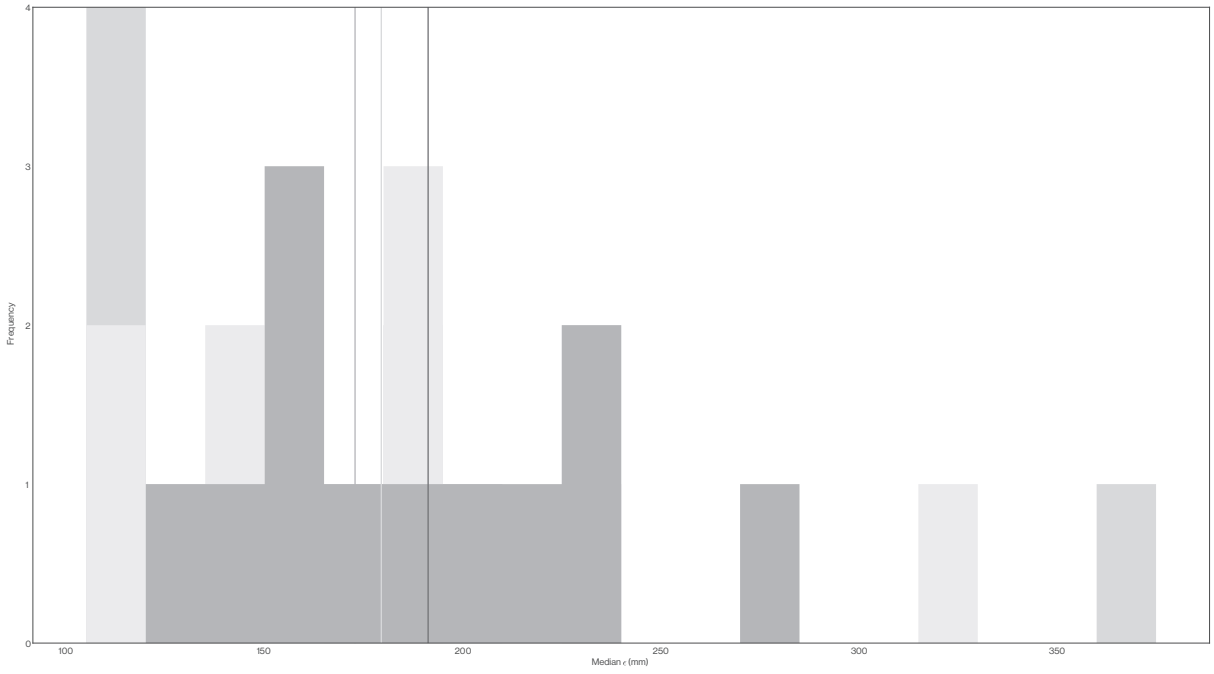


Figure B.4: Histograms of minimum median prediction error found by k-fold cross validation for different guidance models. We plot the histogram of minimum median prediction error $\tilde{\epsilon}$ under PN guidance (dark grey), PNP background guidance (light grey), and PNP guidance (medium grey) found using the k-fold cross validation technique where $k = 12$ (see Methods and Materials). Vertical lines represent the mean minimum median prediction error $\bar{\tilde{\epsilon}}$ under the respective guidance laws.

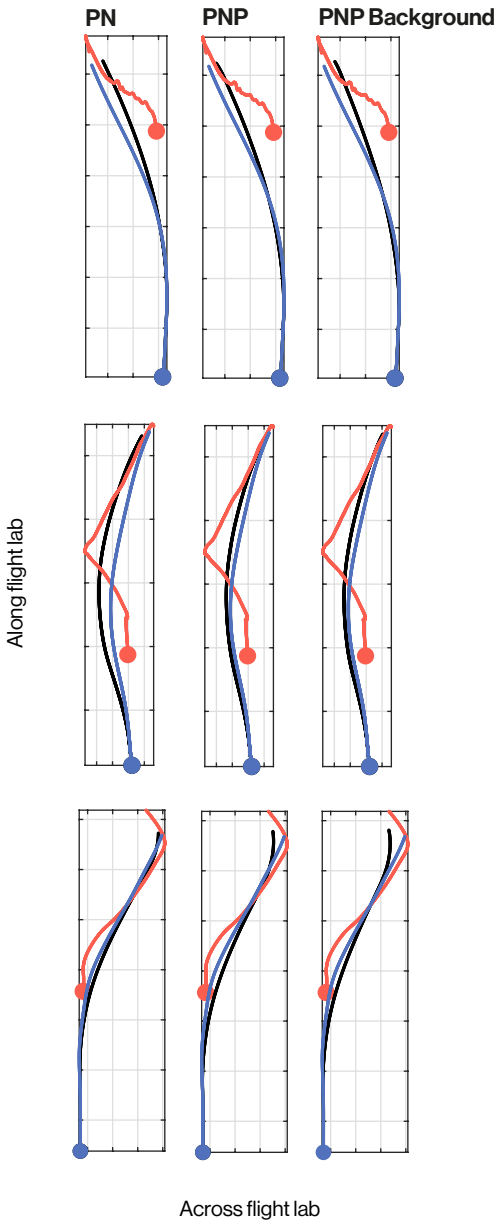


Figure B.5: The lure, measured bird, and simulated trajectories under three different guidance models for three randomly selected flights. Given a lure trajectory (red), and a measured hawk trajectory (blue), we simulate the best fitting trajectory (black) under the PN (first column), PNP (second column) and PNP background (third column) guidance models using the given the best-fit parameters found under the global fitt approach.

C

Supplementary Material to Chapter 4

Contents

C.1 Supplementary Figures 131

C.1 Supplementary Figures

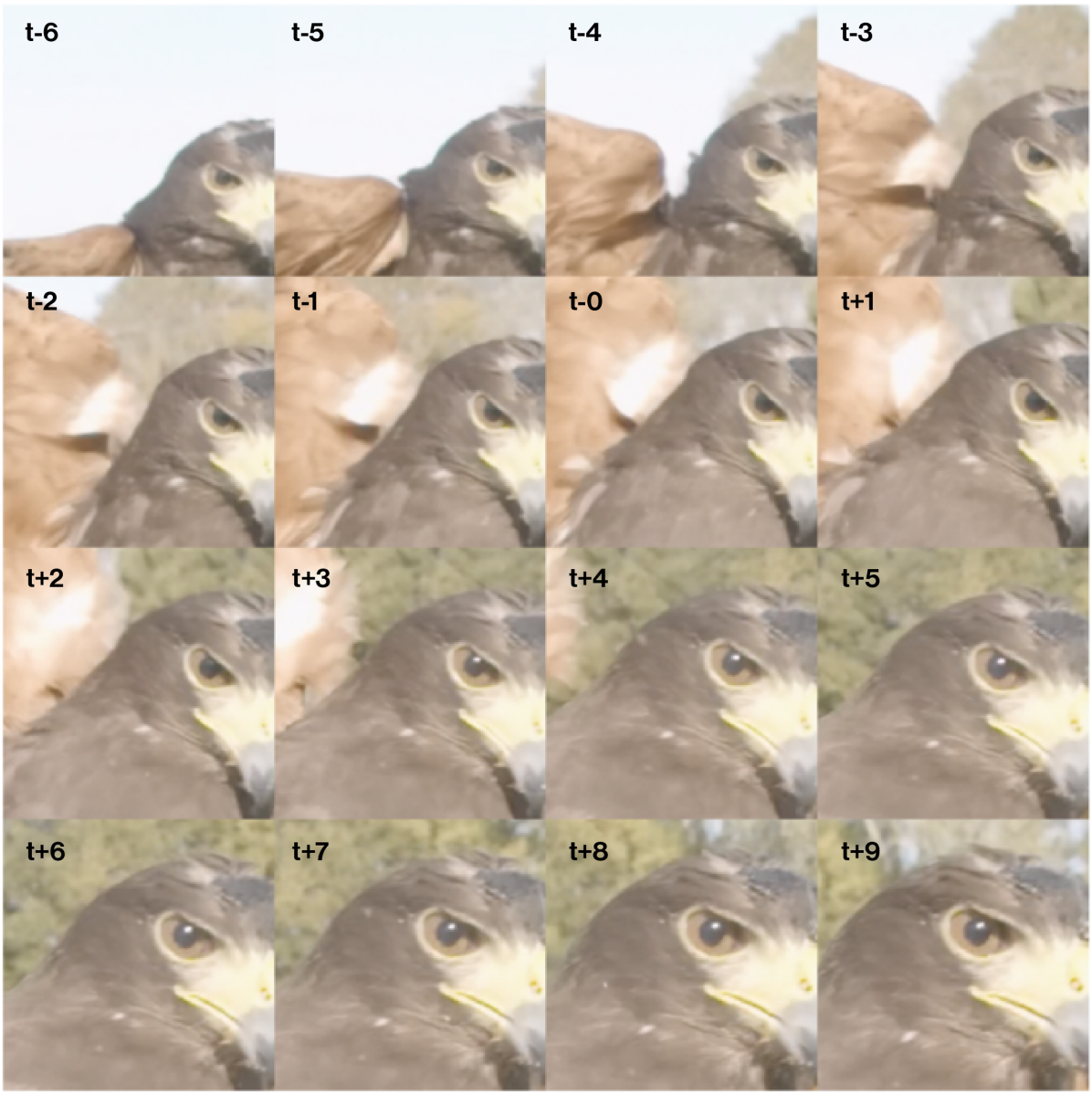


Figure C.1: Eye motion during the terminal phase of one pursuit flight by Drogon. This sequence of 16 frames images the eye before, during and after prey capture. In the top left-hand corner we note the frame number relative to capture (for example, t-2 indicates the second frame before contact is made with the target).

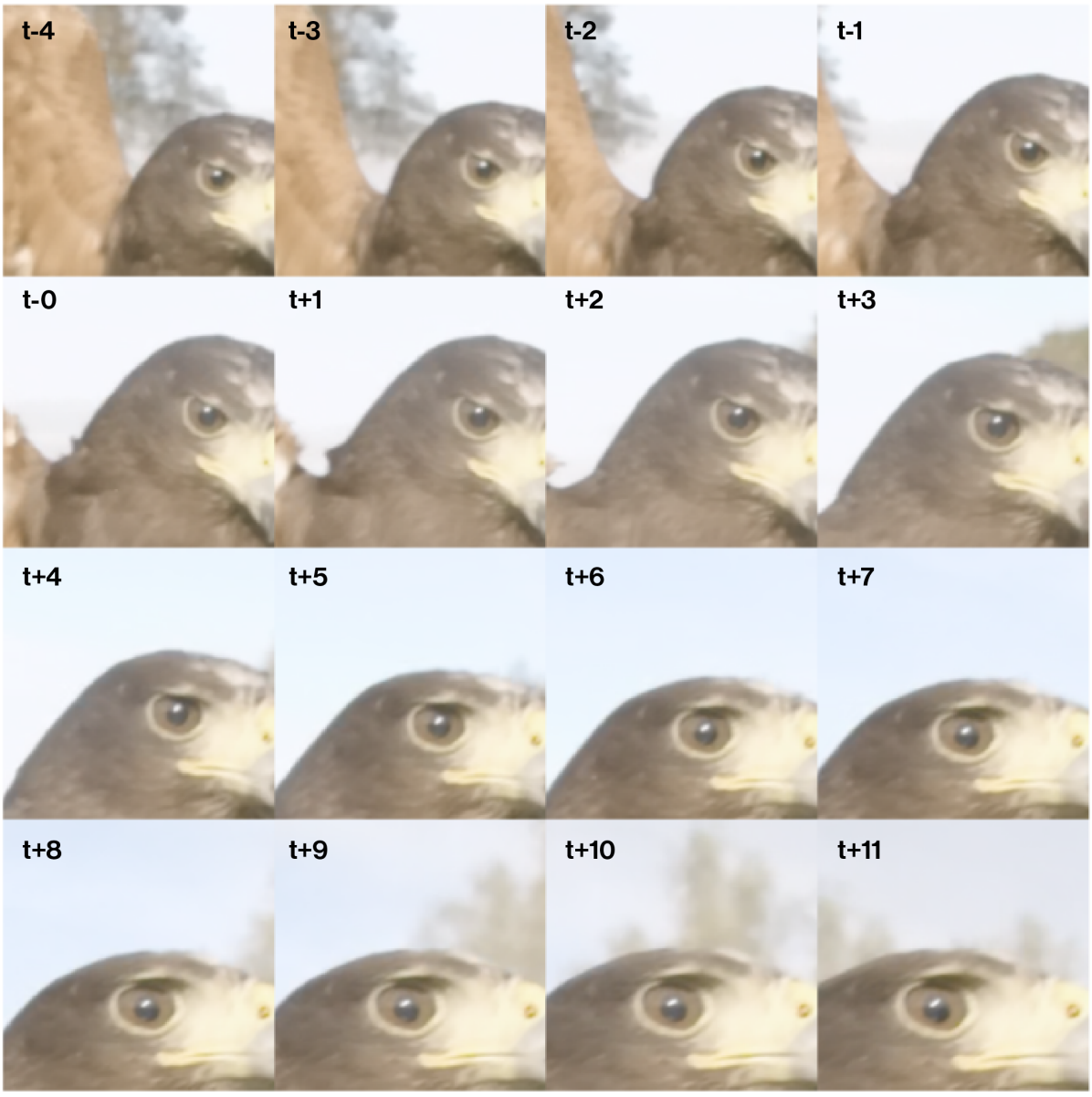


Figure C.2: Eye motion during the terminal phase of one pursuit flight by Toothless.

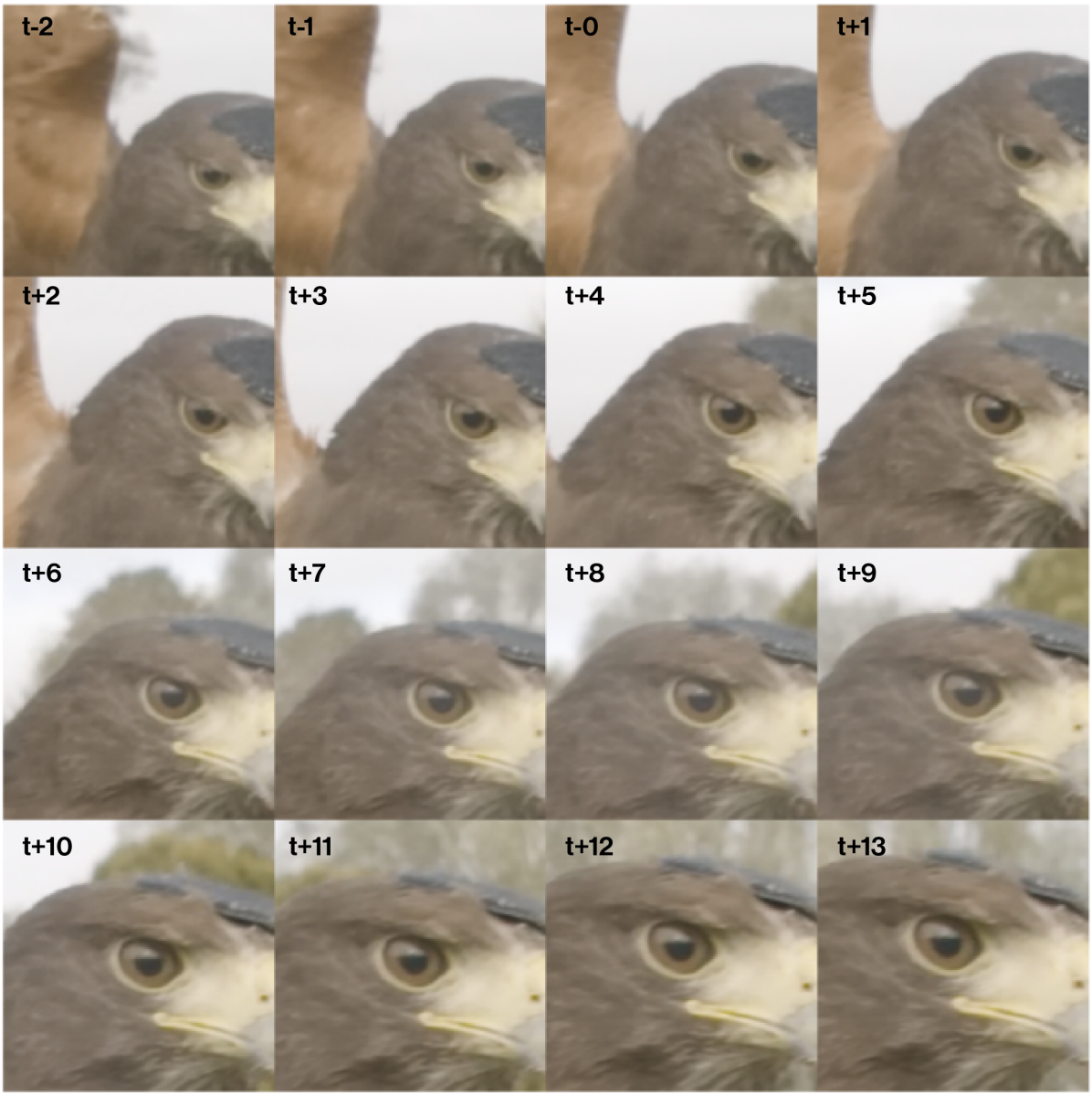


Figure C.3: Eye motion during the terminal phase of one pursuit flight by Charmander.



Figure C.4: Eye motion during the terminal phase of one pursuit flight by Ruby.

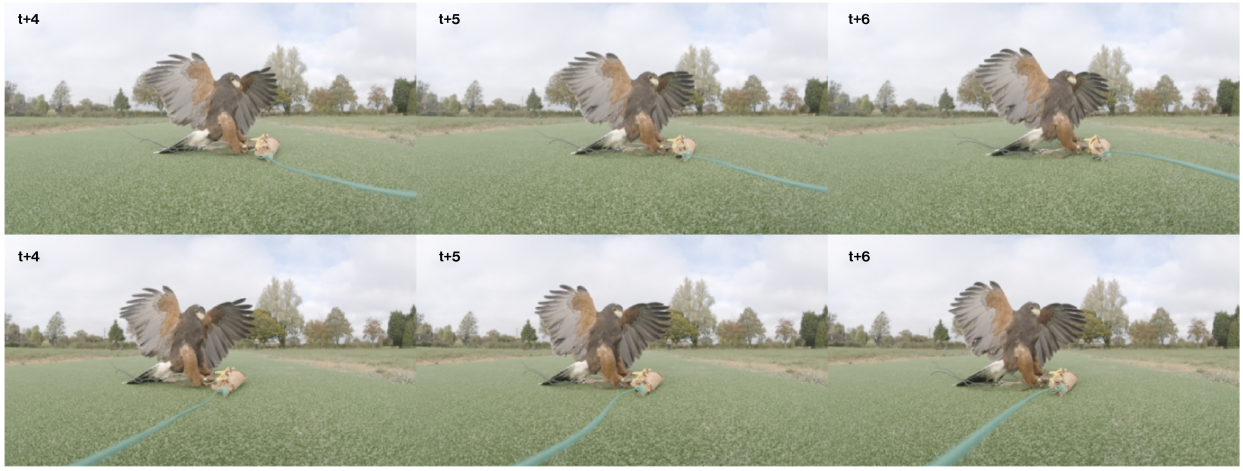


Figure C.5: Image pairs for rectification. Frames t+4 to t+6 in Figure 4.4 are cropped versions of the frames in the first row above. The bottom row of frames above are images taken at the same moment in time as the top row of frames but from the second fisheye camera. With these paired images, one can perform image rectification to create disparity maps. With disparity maps, once can build a 3D model of the head and eyes at each moment in time. One can then infer head and eye-in-head movements between frames.

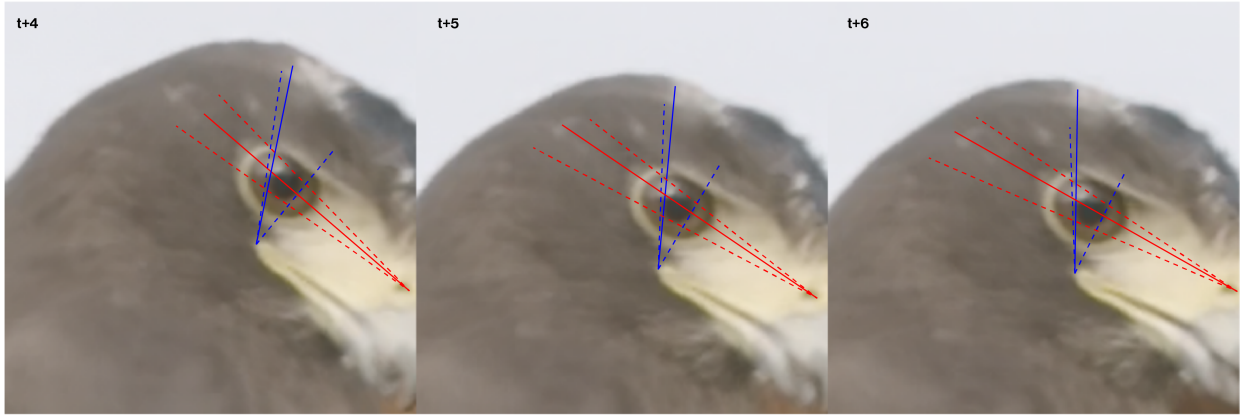


Figure C.6: Reference and tangent lines drawn on consecutive frames after Rhaegal catches the target. We define the solid red reference line as in Figure 4.5. Here, the solid blue reference line starts at the most posterior point (R) on the rictus and passes through the point (B) at the end of the brow ridge. The dotted lines are, as in Figure 4.5, tangent lines to the pupil.

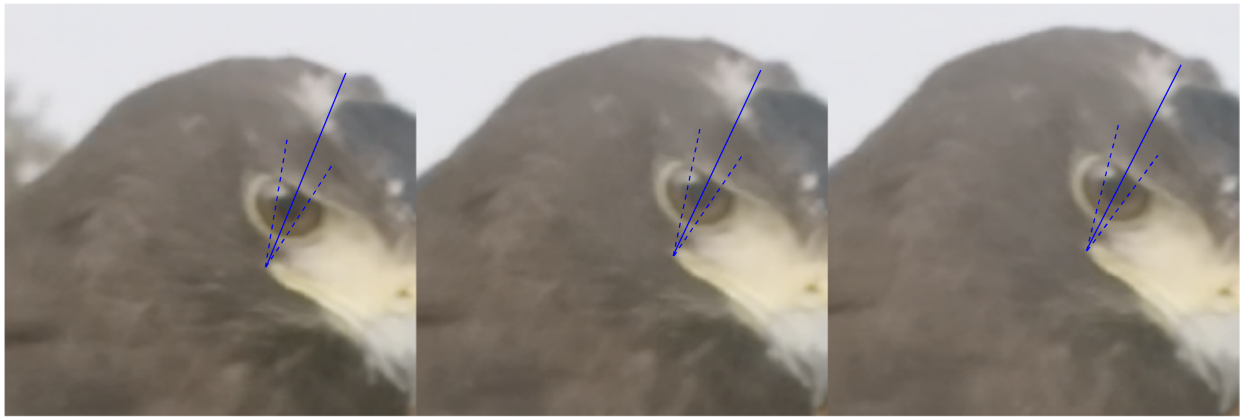


Figure C.7: Reference and tangent lines drawn on consecutive frames before Rhaegal captures the target. Here, the solid blue reference line starts at the most posterior point (R) on the rictus and passes through the point (B) at the corner of the head velcro patch. The dotted lines are, as in Figure 4.5, tangent lines to the pupil.

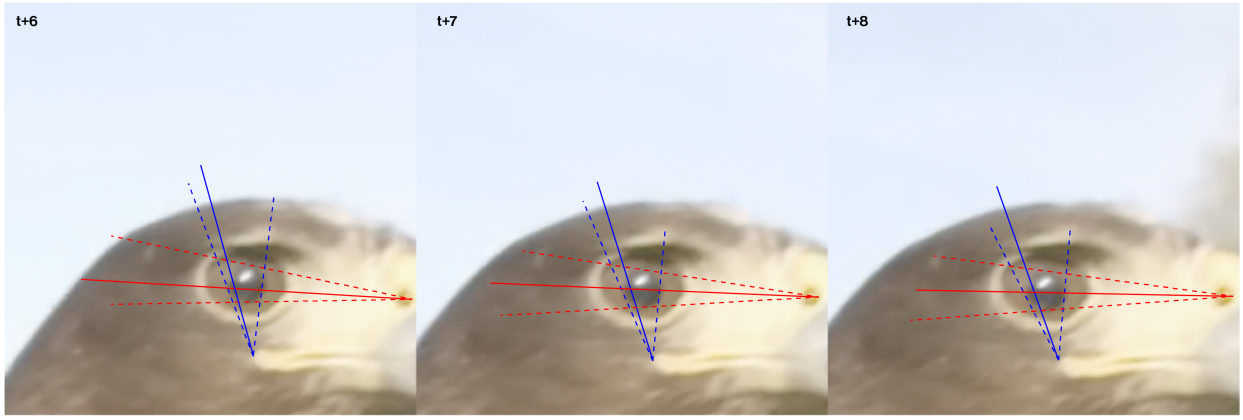


Figure C.8: Reference and tangent lines drawn on consecutive frames after Toothelss catches the target.



Figure C.9: Charmander draws the nictitating membrane across the eye during a head saccade. Given a 120 fps recording frame rate, the protraction and retraction of the nictitating membrane takes 0.05 s.



Figure C.10: Toothless draws the nictitating membrane across the eye during a head saccade. Given a 120 fps recording frame rate, the protraction and retraction of the nictitating membrane takes 0.05 s.



Figure C.11: Rhaegal draws the nictitating membrane across the eye during a head saccade. Given a 120 fps recording frame rate, the protraction and retraction of the nictitating membrane takes 0.05 s. Note that Rhaegal was on a creance.



Figure C.12: Ruby draws the nictitating membrane across the eye during a head saccade. Given a 120 fps recording frame rate, the protraction and retraction of the nictitating membrane takes 0.05 s. Note that Ruby was on a creance.

D

Published version of Chapter 2

ORGANISMAL BIOLOGY

Optimization of dynamic soaring in a flap-gliding seabird affects its large-scale distribution at sea

James A. Kempton[1]*†, Joe Wynn[1,2]†, Sarah Bond[3], James Evry[1,4], Annette L. Fayet[1,5], Natasha Gillies[1], Tim Guilford[1], Marwa Kavelaars[6], Ignacio Juarez-Martinez[1], Oliver Padget[1], Christian Rutz[7], Akiko Shoji[8], Martyna Syposz[1]‡, Graham K. Taylor[1]*

Copyright © 2022 The Authors, some rights reserved; exclusive licensee American Association for the Advancement of Science. No claim to original U.S. Government Works. Distributed under a Creative Commons Attribution License 4.0 (CC BY).

Dynamic soaring harvests energy from a spatiotemporal wind gradient, allowing albatrosses to glide over vast distances. However, its use is challenging to demonstrate empirically and has yet to be confirmed in other seabirds. Here, we investigate how flap-gliding Manx shearwaters optimize their flight for dynamic soaring. We do so by deriving a new metric, the horizontal wind effectiveness, that quantifies how effectively flight harvests energy from a shear layer. We evaluate this metric empirically for fine-scale trajectories reconstructed from bird-borne video data using a simplified flight dynamics model. We find that the birds' undulations are phased with their horizontal turning to optimize energy harvesting. We also assess the opportunity for energy harvesting in long-range, GPS-logged foraging trajectories and find that Manx shearwaters optimize their flight to increase the opportunity for dynamic soaring during favorable wind conditions. Our results show how small-scale dynamic soaring affects large-scale Manx shearwater distribution at sea.

INTRODUCTION

Wind speed and direction influence the movement ecology of birds across a range of spatiotemporal scales from local flight direction (*1*) and timing (*2*–*7*), through route selection (*6*) and drift compensation (*1*, *8*, *9*), to population distribution (*10*, *11*) and migration success (*5*). Such wind effects have been observed in a wide range of species, but the procellariiform seabirds (*10*, *12*–*15*), comprising the albatrosses, petrels, and shearwaters, differ notably from nonpelagic species in their behavioral responses to wind. In contrast to the tailwind preference of nonpelagic birds (*2*, *5*–*7*), Procellariiformes typically prefer crosswind or cross-tailwind flight (*12*, *13*, *15*, *16*). They are also able to fly huge distances (*10*, *17*–*19*) without having to offset their aerodynamic drag losses fully through flapping (*13*, *20*). Both differences may be the product of a specialized flight mode called dynamic soaring (*21*), but although this is the only plausible explanation of how albatrosses are able to glide immense distances without flapping (*13*), dynamic soaring is more challenging to demonstrate in species such as shearwaters that routinely flap their wings during their characteristic rising-falling flight (*20*).

Soaring enables a bird to replace some or all of the aerodynamic kinetic energy that it loses to aerodynamic drag by harvesting energy from the atmosphere (*22*). Static soaring offsets these drag losses by harvesting gravitational potential energy from rising air currents, whereas dynamic soaring harvests aerodynamic kinetic energy from a spatiotemporal wind gradient (*23*). This can be most easily understood by noting that a bird flying into the wind experiences an increase in headwind speed as it moves from slower to faster moving air. Because the bird's flight dynamics prevent its airspeed from equilibrating instantaneously (*24*), it follows that the bird will experience an immediate increase in its airspeed and hence aerodynamic kinetic energy. Less obviously, perhaps, a similar increase in aerodynamic kinetic energy must also occur when a bird that is flying with the wind moves from faster to slower moving air. In general, dynamic soaring therefore entails flying into a strengthening wind and with a weakening wind (*23*). More specifically, because wind speed increases with height above the sea's surface (*25*), pelagic dynamic soaring entails ascending into the wind and descending with the wind (*23*). We call these criteria the Rayleigh conditions (see Fig. 1), after their late 19th century discoverer (*26*).

Although the physical principles of dynamic soaring are well understood, showing empirically that a bird is extracting aerodynamic kinetic energy from a spatiotemporal wind gradient—and hence implementing dynamic soaring—is extremely challenging. Among Procellariiformes, cyclical variation in mechanical energy has been used to assess dynamic soaring for the wandering albatross (*Diomedea exulans*) (*27*) and the Manx shearwater (*Puffinus puffinus*) (*16*) using high-resolution GPS measurements. There is a general difficulty with this approach in that cyclical variation in mechanical energy does not necessarily imply cyclical dynamic soaring. For instance, a bird that is circling at constant airspeed in a uniform wind field displays cyclical variation in its inertial kinetic energy but is not extracting energy from a spatiotemporal wind gradient. Similarly, intermittent bounding and undulating flight shows cyclical variation in both inertial kinetic energy and gravitational potential energy in the absence of energy harvesting from a spatiotemporal wind gradient (*28*). The mere occurrence of cyclical variation in mechanical energy is therefore insufficient to prove the use of dynamic soaring. In albatrosses, dynamic soaring has instead been inferred by analyzing the distribution of mechanical energy gain with reference to a detailed aerodynamic model (*27*). Proving that flap-gliding species such as shearwaters use dynamic soaring is even more challenging, however, because the variation in mechanical energy that dynamic soaring entails may

[1]Department of Zoology, University of Oxford, Oxford OX1 3SZ, UK. [2]Institut für Vogelforschung, 26386 Wilhelmshaven, Germany. [3]School of Ocean Sciences, Bangor University, Menai Bridge LL59 5AB, UK. [4]Costello Medical, Cambridge CB1 2JH, UK. [5]Norwegian Institute for Nature Research, PO Box 5685 Torgarden, 7485 Trondheim, Norway. [6]Behavioral Ecology and Ecophysiology, University of Antwerp, 2610 Antwerp, Belgium. [7]School of Biology, University of St Andrews, St Andrews KY16 9TH, UK. [8]Graduate School of Life and Environmental Sciences, University of Tsukuba, Ibaraki 305-8572, Japan.
*Corresponding author. Email: james.kempton@zoo.ox.ac.uk (J.A.K.); graham.taylor@zoo.ox.ac.uk (G.K.T.)
†These authors contributed equally to this work as co–first authors.
‡Present address: Department of Vertebrate Ecology and Zoology, University of Gdańsk, 80-308 Gdańsk, Poland.

Downloaded from https://www.science.org at University of Newcastle on June 08, 2022

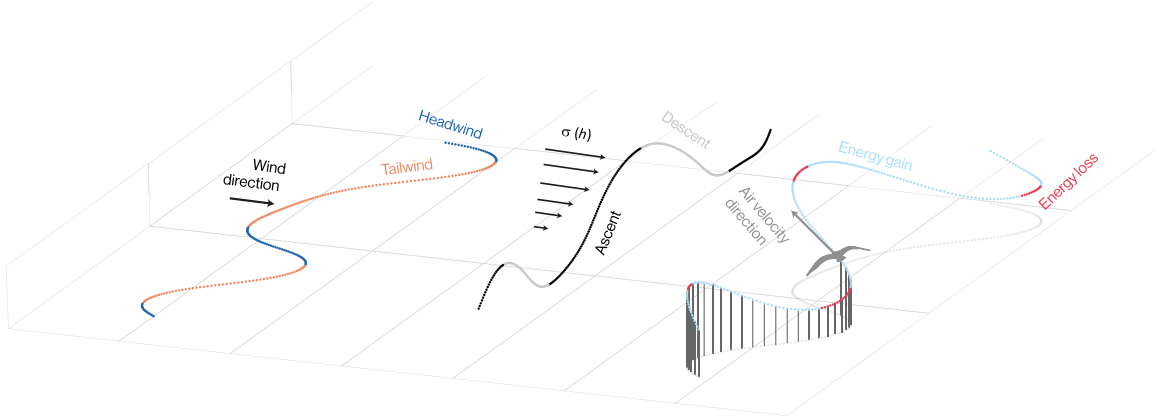


Fig. 1. Cyclical basis of dynamic soaring. The energetic benefits of dynamic soaring are realized by phasing the horizontal and vertical components of flight to meet the Rayleigh conditions of flying into a strengthening wind and with a weakening wind. In a horizontal wind field, the sequence of headwinds (dark blue) and tailwinds (orange) that the bird experiences is determined only by the horizontal component of its flight trajectory (**left**). The vertical component (**middle**) determines whether the bird experiences an increasing or decreasing wind, according to whether it is ascending (black) or descending (light gray) through the shear layer [$\sigma(h)$]. The pattern of energy harvesting (**right**) depends on whether the phasing of the horizontal and vertical components of the flight trajectory meets the Rayleigh conditions, as these are what determine whether a bird gains (light blue) or loses (red) energy from the shear layer before taking account of drag losses. How much energy the bird harvests depends on the degree of alignment of the wind vector (black arrow) and the air velocity vector (gray arrow), as well as on the speed of flight and strength of wind shear. The trajectories shown here are reconstructed relative to the air from our empirical data for a part of one flight.

not even appear cyclical when changes in mechanical energy due to flapping are superimposed (*16*).

Here, we address these challenges by deriving a dimensionless metric describing dynamic soaring that we call the horizontal wind effectiveness (ϵ_h). We estimate this empirically for flap-gliding Manx shearwaters by using a simplified flight dynamics model to reconstruct $n = 9$ detailed flight trajectories from video data (movie S1) collected using bird-borne video loggers (*29*) attached to $N = 6$ individuals. The horizontal wind effectiveness ϵ_h quantifies how effectively flight in a given instantaneous direction harvests aerodynamic kinetic energy from a wind gradient, where positive values indicate that energy is gained from the shear layer and negative values indicate that energy is lost to it. Its long-term average ($-1 \leq \bar{\epsilon}_h \leq 1$) can therefore be used to assess whether and how a given flight trajectory is optimized for dynamic soaring in relation to the opportunity that the wind direction provides, which we quantify by defining another metric that we call the mean wind opportunity $\bar{\omega}$. We find that shearwaters phase their vertical sequence of ascent and descent appropriately to gain energy from the shear layer independent of the wind speed W but only optimize their horizontal turning cycle for dynamic soaring under favorable conditions when the product of mean wind opportunity and wind speed $\bar{\omega}W$, which we call the crosswind component, is high. We use GPS data from $n = 368$ outbound foraging flights and $n = 368$ return flights, from $N = 201$ individuals, to test whether this fine-scale behavior is recapitulated at larger spatiotemporal scales. We find that shearwaters tend to fly in a crosswind direction that is favorable for dynamic soaring on their outbound foraging trips, particularly when the wind speed W is high. Return legs are more constrained in their flight direction and do not show a crosswind tendency. Besides conclusively demonstrating the use of dynamic soaring by a flap-gliding seabird, the metrics of horizontal wind effectiveness, wind opportunity, and crosswind component that we derive offer a framework for analyzing dynamic soaring more generally.

RESULTS

Energetics of dynamic soaring

For a bird flying in a steady horizontal wind field with vertical wind shear $\sigma \geq 0$, the mass-specific flow of useful mechanical energy due to dynamic soaring is shown in Supplementary Text to be

$$\frac{de}{dt} = -\frac{1}{2}U^2\sigma \sin 2\gamma \cos \eta \quad (1)$$

where $U = \|\mathbf{U}\|$ is the bird's airspeed, γ is the aerodynamic flight path angle defined as the elevation of the bird's air velocity $\mathbf{U}$ with respect to the horizontal, signed positive when climbing, and η is the heading-to-wind angle defined as the angle between the wind vector $\mathbf{W}$ and the horizontal component of $\mathbf{U}$. The local shear gradient σ is usually unknown, but it is clear by inspection that the instantaneous rate of energy harvesting is always maximized by flying in an instantaneous direction that maximizes the dimensionless quantity

$$\epsilon = -\sin 2\gamma \cos \eta \quad (2)$$

which we call the total wind effectiveness. Because wind velocity increases with height above a surface, σ is >0 by definition (see Supplementary Text). Energy is therefore harvested from the wind gradient when $\epsilon > 0$ and lost when $\epsilon < 0$, at a rate proportional to $\|\epsilon\|$.

The aerodynamic flight path angle γ is difficult to measure in an unknown wind field. However, because $-90^\circ \leq \gamma \leq 90^\circ$ by definition, it follows that $\sin 2\gamma$ is positive when $\gamma > 0$ and negative when $\gamma < 0$. The instantaneous rate of energy harvesting is therefore maximized by flying in an instantaneous direction that maximizes the simpler quantity

$$\epsilon_h = -\mathrm{sgn}(\gamma) \cos \eta \quad (3)$$

where sgn denotes the signum or sign function. We call ϵ_h the horizontal wind effectiveness, because its magnitude depends only on

Downloaded from https://www.science.org at University of Newcastle on June 08, 2022

the bird's horizontal flight direction with respect to the wind $\eta(t)$, whereas its sign depends on how the bird's vertical motion $\gamma(t)$ is phased with respect to its horizontal motion. Energy is harvested from the wind gradient when $\epsilon_h > 0$ and lost when $\epsilon_h < 0$, at a rate that is proportional to $\|\epsilon_h\|$. The Rayleigh conditions of ascending into a headwind (i.e., flying with $\gamma > 0$ and $\cos\eta < 0$) or descending with a tailwind (i.e., flying with $\gamma < 0$ and $\cos\eta > 0$) are met whenever $\epsilon_h > 0$ but are implemented most effectively as $\epsilon_h \to 1$. Equation 3 therefore emphasizes that both the shape of the horizontal flight track and the phasing of its ascent-descent sequence are critical to determining how effectively energy is harvested through dynamic soaring. Equation 3 also implies that making net progress in a useful direction will tend to conflict with dynamic soaring trajectory optimization.

Flight dynamics model

Computing the horizontal wind effectiveness ϵ_h requires knowledge of the sign of the aerodynamic flight path angle γ and measurement of the heading-to-wind angle η (see Eq. 3). Identifying the sign of γ is straightforward if the wind field is horizontal, because then sgn (γ) is positive when ascending and negative when descending. We will further assume that sgn (γ) = sgn (θ), where θ is the bird's pitch angle (see Materials and Methods). Measuring η is much harder because whereas a bird's flight trajectory is most readily obtained in an Earth-fixed coordinate system using a GPS logger, the heading-to-wind angle η is necessarily measured with respect to the air. Relating these two frames of reference requires knowledge of the local wind velocity, which is problematic in a shear layer. To avoid this difficulty, we instead use a simplified flight dynamics model to predict the turning associated with the bird's pitching and banking motion that we measure by observing the horizon in a bird-borne video from a body-fixed camera [Fig. 2, A and B, and movies S1 to S3; see also (*30*)]. For this, we specify the bird's orientation using a set of intrinsic Euler angles where ψ is the bird's yaw angle, θ is the bird's pitch angle, and ϕ is the bird's bank angle, defined in that order (see Fig. 2, C to E, and Supplementary Text).

We assume that the heading-to-wind angle η is equivalent to the angular difference between the bird's yaw angle ψ and the wind's bearing ζ such that $\eta = \psi - \zeta$ (Fig. 2C). This amounts to assuming that the bird's air velocity vector $\mathbf{U}$ is aligned with its longitudinal body axis at all times. We estimate ψ by integrating the following approximate model of unsteady banked turning (see Supplementary Text) on a per-frame basis using trapezoidal integration

$$\dot{\psi} \approx \frac{g \sin\phi}{U_0 \cos\theta} \tag{4}$$

where $g = 9.81$ m s^{-2} is gravitational acceleration and $U_0 = 11.1$ m s^{-1} is the bird's equilibrium airspeed, as estimated in an earlier study of cruising Manx shearwaters (*20*). Here, the angles θ and ϕ are the bird's pitch and bank angles (Fig. 2, D and E), estimated from the apparent motion of the horizon (Fig. 2, A and B).

The unsteady banked turn model in Eq. 4 is an approximation, insofar as it assumes that the product of the bird's wing area S and lift coefficient C_L remains approximately constant, and assumes that any variation in the airspeed U is small in comparison with the equilibrium airspeed U_0. This is equivalent to assuming approximately constant airspeed $U \approx U_0$ and approximately constant lift L equal to body weight, $L \approx mg$, where m is mass. Equation 4 also neglects the aerodynamic effects of wind shear on the bird's turning, which is reasonable if the bird flies directly with or against the wind as it descends or ascends through the shear layer, as is most efficient for dynamic soaring (see Supplementary Text for detailed discussion). For the purposes of the subsequent statistical analysis, we define dynamic soaring cycles as beginning and ending at peaks in the estimated time history of the bird's yaw angle ψ (Fig. 2F).

Optimization of dynamic soaring

While it is possible in principle to find cyclical trajectories whose wind effectiveness is always non-negative, the optimization of a dynamic soaring trajectory is complicated in practice by the need to progress in a useful direction. The benefits of harvesting energy through dynamic soaring are therefore expected to trade off against the costs of deviating from the desired direction of progress such that flights can typically be expected to involve alternating periods of negative and positive wind effectiveness. Because the rate of return from dynamic soaring is proportional to the wind shear strength σ (see Eq. 1), we should not necessarily expect birds to fly trajectories that maximize the energy they harvest on days with little wind. On such days, there is no prior reason to expect the mean horizontal wind effectiveness to be significantly different from zero, which is the null expectation if the bird phases the ascent-descent sequence described by $\gamma(t)$ at random with respect to the pattern of horizontal turning described by $\eta(t)$ (see Eq. 3). Conversely, under extremely windy conditions like those exploited by albatrosses flying in the Southern Ocean, it may be possible to harvest more energy than is lost to drag, or than is desirable. Hence, while we should certainly expect the mean horizontal wind effectiveness to be positive under such favorable conditions, we should not necessarily expect it to be maximized outright, given that such maximization may harvest too much kinetic energy and that this excess kinetic energy cannot be converted to gravitational potential energy when flying close to the surface. Energy harvesting is most likely to be maximized under marginally favorable conditions, when the returns available from dynamic soaring are sufficient to merit deviating from the desired direction of progress, but insufficient to enable flight to be sustained without flapping. These are precisely the conditions that we hypothesize will hold for Manx shearwaters using flap-gliding flight on windy days.

Fine-scale flight trajectories of shearwaters

Our bird-borne video data (Fig. 2) show the weaving, undulatory, flap-gliding flight behavior that is characteristic of shearwaters (*20*). This is evidenced by the cyclical rolling and pitching of the visible horizon (Fig. 2, A and B), upon which are superimposed occasional faster oscillations due to flapping (see movie S1). The weaving component of this behavior is clearly visible in the $n = 9$ horizontal flight trajectories that we reconstructed at a fine scale by using Eq. 4 to model the turning associated with the birds' observed rolling and pitching motion (Fig. 3). Likewise, the coupling of the weaving and undulatory components of this behavior is apparent in the three-dimensional reconstructions (Fig. 1). This turning behavior occurs on comparatively short time scales (median of mean turning cycle period per flight, 7.0 s) and produces an indirect flight path that must presumably offer some functional benefit to the bird. The reconstructed flight trajectories qualitatively resemble the cyclical trajectories attributed to dynamic soaring in albatrosses (*27*), and we analyze their suitability for harvesting energy from the shear layer quantitatively below. Nevertheless, as the shearwaters usually flapped their wings as they transitioned from ascending to descending

Downloaded from https://www.science.org at University of Newcastle on June 08, 2022

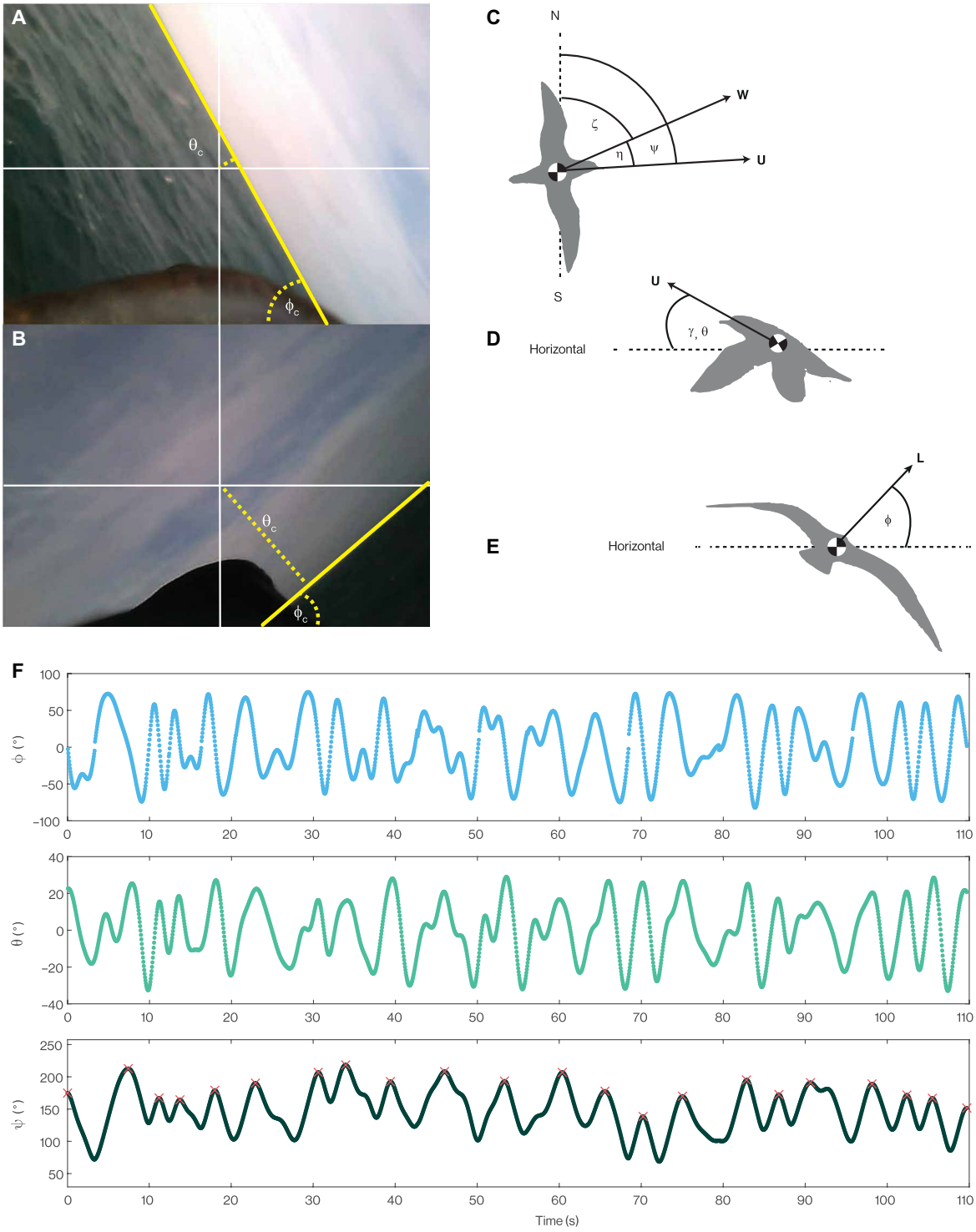


Fig. 2. Reconstruction of cyclical turning behavior using bird-borne video. (**A** and **B**) Video from a camera mounted on the back of a Manx shearwater demonstrates alternating left (A) and right (B) banked turns, coupled with cyclical pitching. The camera bank angle (ϕ_c) is measured as the angle of the horizon line, which we detect automatically (yellow line); the camera pitch angle (θ_c) is measured as the angular distance of the detected horizon line from the image center (crosshairs); see Materials and Methods. (**C** to **E**) Angle definitions, shown in three orthogonal views. Overhead view (C): The bird's heading-to-wind angle (η) is defined as the angle between the horizontal wind vector (**W**) and the bird's air velocity vector (**U**) in horizontal projection; this angle η is assumed to equal the angular difference between the bird's yaw angle (ψ) and the wind's azimuth (ζ). Lateral view (D): The bird's flight path angle (γ) is defined as the elevation of **U** with respect to the horizontal; this angle is assumed to equal the bird's pitch angle (θ), which defines the inclination of the lift vector **L** in the bird's symmetry plane. Caudal view (E): The bird's bank angle (ϕ) defines the inclination of **L** in the bird's transverse plane. (**F**) Sample time histories of the estimated bank (ϕ), pitch (θ), and yaw (ψ) angles for flight b117ii-753. Red crosses denote peaks in ψ, corresponding to points where the sign of ϕ changes; these points are used to define the beginning and end of each turning cycle.

Downloaded from https://www.science.org at University of Newcastle on June 08, 2022

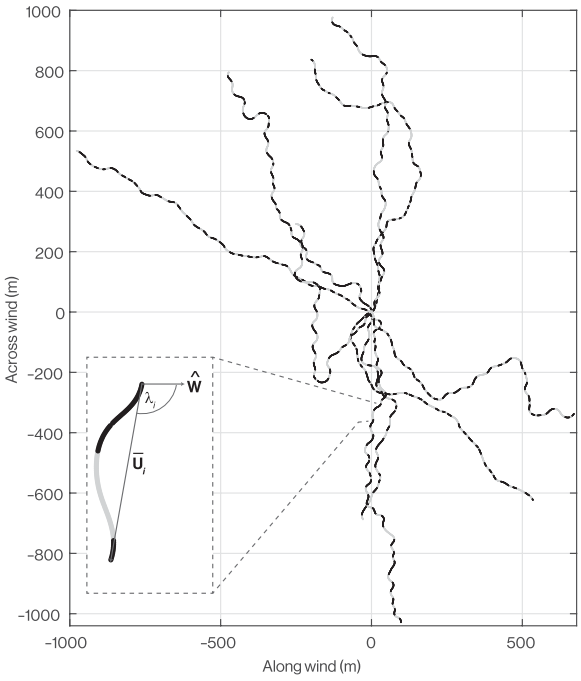


Fig. 3. Weaving flight of Manx shearwaters. All $N = 6$ individual Manx shearwaters that we sampled at fine scale consistently undertook weaving flight. We reconstructed their $n = 9$ trajectories shown here by using our estimates of the bird's pitch, bank, and assumed airspeed to estimate the bird's air relative flight velocity vector **U**, which we integrated numerically using trapezoidal integration for the purposes of visualization. Here, these air-relative trajectories are expressed in a coordinate system aligned with the experienced wind direction such that the overall direction of each flight on the graph indicates the extent to which the bird heads with, against, or across the wind. The angle between the average air velocity vector $\bar{\mathbf{U}}_i$ of cycle i and the wind velocity unit vector $\hat{\mathbf{W}}$ we call λ_i, and we use this for computing the mean wind opportunity metric $\bar{\omega}$. Each trajectory has been projected into the horizontal plane, and sections of ascent are shown in black, while sections of descent are shown in gray.

flight, and as they were sometimes observed flapping at other points in the cycle, such energy as they harvested from the shear layer cannot have been sufficient to offset their drag losses completely. This fine-scale flight behavior is not directly observable in the coarse trajectories that we sampled at 5-min intervals using GPS loggers, but it is reasonable to assume that the birds would have behaved similarly on these $n = 368$ flights, so we analyze the opportunity that these flights would have provided for dynamic soaring below.

The weaving flight of shearwaters implements dynamic soaring

The sample mean horizontal wind effectiveness $\hat{\bar{\epsilon}}_h$ was positive on all $n = 9$ fine-scale flight trajectories that we collected from $N = 6$ individuals [sign test: $P = 0.004$, $n = 9$; median $\hat{\bar{\epsilon}}_h = 0.167$; bootstrapped 95% confidence interval (CI): 0.042, 0.272]. These data comprise a total of 17,457 video frames corresponding to approximately 873 s of flight data, with each recording lasting between 89 and 114 s. This positive mean horizontal wind effectiveness indicates that the shearwaters flew in a manner expected to harvest energy from the shear layer, but how effectively were their trajectories optimized for dynamic soaring?

To answer this question, it will prove convenient to decompose the mean horizontal wind effectiveness $\bar{\epsilon}_h$ as

$$\bar{\epsilon}_h = f_R \overline{\|\cos\eta\|}_R - f_{R'} \overline{\|\cos\eta\|}_{R'} \quad (5)$$

where f_R represents the frequency with which the Rayleigh conditions are met (i.e., the proportion of frames on which $\epsilon_h > 0$) and $f_{R'} = 1 - f_R$ represents the frequency with which they are not met (i.e., the proportion of frames on which $\epsilon_h \leq 0$). Implicitly, $\overline{\|\cos\eta\|}_R$ and $\overline{\|\cos\eta\|}_{R'}$ denote the mean magnitude of cos η over the corresponding portions of flight. This decomposition emphasizes (i) that the mean horizontal wind effectiveness $\bar{\epsilon}_h$ of a given pattern of turning behavior becomes maximal as $f_R \to 1$, which entails phasing the ascent-descent sequence to meet the Rayleigh conditions, and (ii) that the maximal value of the mean horizontal wind effectiveness is further constrained by the time history of the bird's horizontal flight direction with respect to the wind, because $\bar{\epsilon}_h \to \overline{\|\cos\eta\|}_R$ as $f_R \to 1$. We will examine these two influences separately, first by assessing the optimality of the observed ascent-descent sequence conditional upon the observed horizontal trajectory, before then assessing the optimality of the observed horizontal trajectory in relation to the observed wind direction.

Shearwaters phase their vertical and horizontal trajectories for dynamic soaring

We first compare the sample mean horizontal wind effectiveness $\hat{\bar{\epsilon}}_h$ on each trajectory with the distribution of possible values of $\bar{\epsilon}_h$ given counterfactual phasing of the same ascent-descent sequence. In other words, we compute the distribution of $\bar{\epsilon}_h(\tau)$ by holding the time history of the observed heading-to-wind angle $\eta(t)$ fixed while time-shifting the aerodynamic flight path angle $\gamma(t)$ by an amount τ such that

$$f_R = \frac{1}{T}\sum_{t=0}^{T} H[-\mathrm{sgn}(\gamma(t-\tau))\,\mathrm{sgn}(\cos\eta(t))] \quad (6)$$

where H is the Heaviside function, which returns $H(x) = 0$ for $x \leq 0$ and $H(x) = 1$ for $x > 0$. Likewise, we have

$$\overline{\|\cos\eta\|}_R = \frac{1}{f_R T}\sum_{t=0}^{T} H[-\mathrm{sgn}(\gamma(t-\tau))\,\mathrm{sgn}(\cos\eta(t))]\,\|\cos\eta(t)\| \quad (7)$$

$$\overline{\|\cos\eta\|}_{R'} = \frac{1}{f_{R'} T}\sum_{t=0}^{T} (1 - H[-\mathrm{sgn}(\gamma(t-\tau))\,\mathrm{sgn}(\cos\eta(t))])\,\|\cos\eta(t)\| \quad (8)$$

with $f_{R'} = 1 - f_R$. Evaluating f_R, $f_{R'}$, $\overline{\|\cos\eta\|}_R$, and $\overline{\|\cos\eta\|}_{R'}$ for different time shifts τ and substituting these into Eq. 5 generates the desired distribution of $\bar{\epsilon}_h(\tau)$ and recovers the observed value $\hat{\bar{\epsilon}}_h$ when $\tau = 0$. Note that we wrap the time history of each flight when computing these quantities such that the number of time points that we evaluate is the same for all values of τ. If the birds' ascent-descent sequences were appropriately synchronized with their horizontal flight trajectories, then we would naturally expect $\bar{\epsilon}_h(\tau)$ to peak at $\tau \approx 0$. This was true of the ascent-descent sequences that we observed on all nine flights (Fig. 4), each of which was timed to within ±0.4 s of the optimum, with a median phase shift of −7° relative to the period of a complete turning cycle (first and third quartiles: −8° and 11°). Moreover, the sample mean horizontal wind effectiveness $\hat{\bar{\epsilon}}_h$ was usually close to the peak value of $\bar{\epsilon}_h(\tau)$, at a median value of 98.4% of the maximum (first and third quartiles: 94.6 and 99.1%). These results demonstrate that the birds synchronized their ascent-descent sequences

Downloaded from https://www.science.org at University of Newcastle on June 08, 2022

with their horizontal flight trajectories so as to harvest energy from the shear layer.

This conclusion is based on holding the ascent-descent sequence fixed while varying its timing with respect to the observed horizontal flight trajectory. This is analogous to finding that a piano score harmonizes most closely when its bass and treble clef lines are correctly aligned, which provides evidence that they were jointly composed. To assess whether the ascent-descent sequence is not only well synchronized with the horizontal flight trajectory but also globally optimal, we evaluate the maximum possible value that $\bar{\epsilon}_h$ could have taken for each horizontal flight trajectory by finding the optimal permutation of the observed ascent-descent sequence. That is, we find the global optimum $\bar{\epsilon}_{h^*}$ by permuting the observations of $\mathrm{sgn}(\gamma(t))$ so as to (i) maximize f_R at $f_R = f_R{}^*$ and (ii) maximize $\overline{\|\cos\eta\|}_R$ given $f_R = f_R{}^*$. This analysis showed that the sample mean horizontal wind effectiveness $\hat{\bar{\epsilon}}_h$ was considerably lower than the global optimum, at a median value of 40.5% of $\bar{\epsilon}_{h^*}$ (first and third quartiles: 16.2 and 59.2%). We therefore find no evidence that the observed ascent-descent sequence was itself optimal, although it is worth noting that the strength of this conclusion depends on the fidelity of the modeled flight trajectory and assumed wind and that there is no guarantee that any globally optimal sequence of ascent and descent would have been physically achievable.

In principle, any suboptimality of the observed ascent-descent sequence reflects the possibility of reordering it so as to (i) meet the Rayleigh conditions more frequently or (ii) meet the Rayleigh conditions at times when the horizontal flight direction was more effective for energy harvesting. To test between these alternatives, we compute a constrained global optimum $\bar{\epsilon}_{h^{*'}}$ by permuting the observed sequence of $\mathrm{sgn}(\gamma(t))$ so as to (i) hold f_R fixed at $f_R = \hat{f}_R$, where $\hat{f}_R$ is the observed value of f_R, and (ii) maximize $\overline{\|\cos\eta\|}_R$ given that $f_R = \hat{f}_R$. This analysis showed that the sample mean horizontal wind effectiveness $\hat{\bar{\epsilon}}_h$ was considerably lower even than the constrained global optimum, at a median value of 56.6% of $\bar{\epsilon}_{h^{*'}}$ (first and third quartiles: 41.2 and 74.9%), despite the Rayleigh conditions still being met with the same frequency $f_R = \hat{f}_R$. This result demonstrates that the suboptimality of the observed ascent-descent sequences was primarily attributable to the Rayleigh conditions not being met at the most opportune points in the flight and only secondarily to the frequency with which they were met. This is consistent with our earlier conclusion that the observed ascent-descent sequences were synchronized with the horizontal flight trajectories so as to harvest

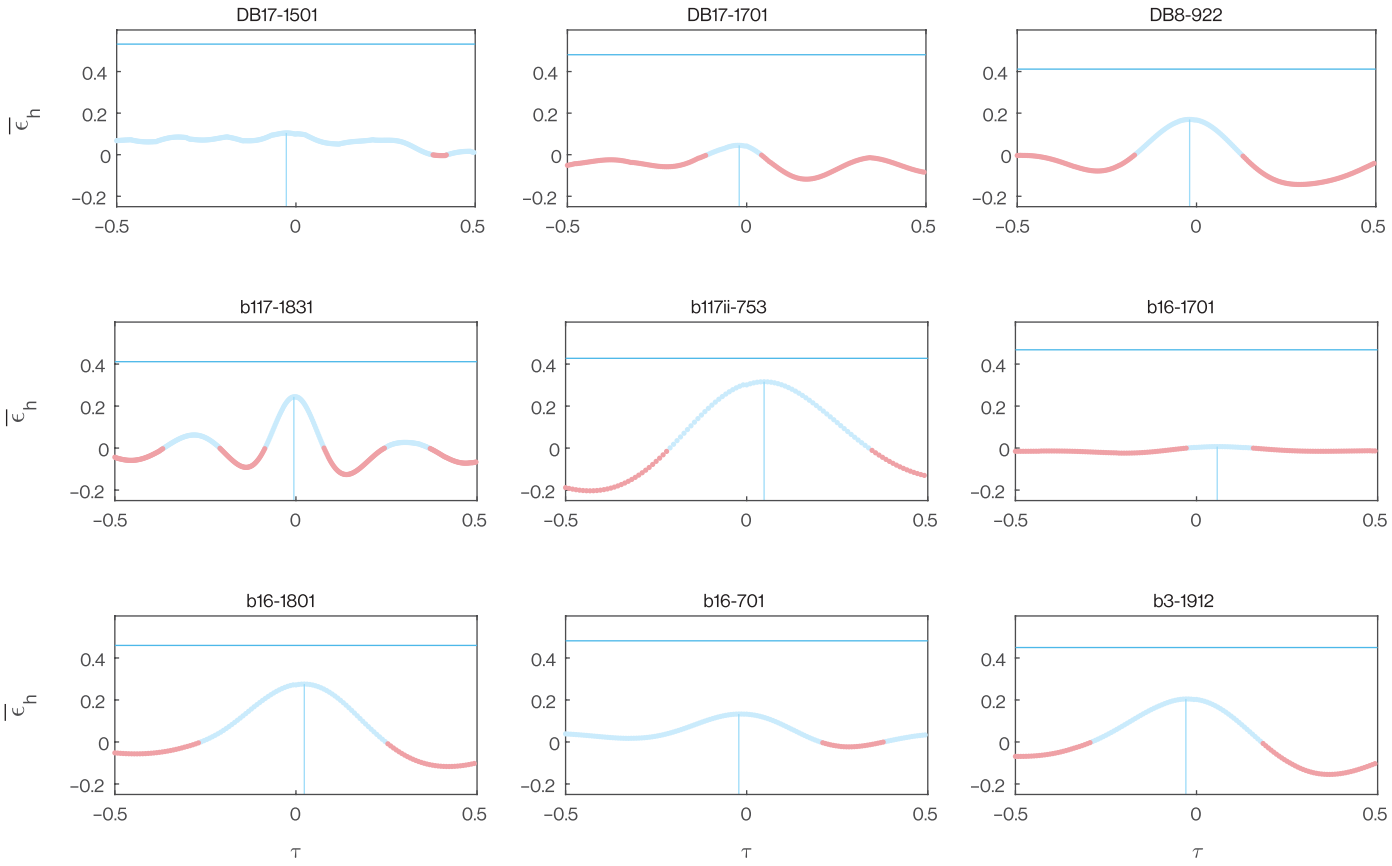


Fig. 4. Optimization of the phasing of the vertical and horizontal components of each flight. Each panel plots the distribution of mean horizontal wind effectiveness $\bar{\epsilon}_h(\tau)$ computed by holding the horizontal component of one of the $n = 9$ fine-scale flight trajectories fixed while varying the phasing of its vertical component by applying a time shift τ. Here, $-0.5 \le \tau \le 0.5$, where τ is expressed relative to the mean period of one turning cycle. Positive values of $\bar{\epsilon}_h(\tau)$ are shown in blue, and negative values in red. The vertical blue line denotes the maximum value of $\bar{\epsilon}_h(\tau)$ for each distribution and its associated value of τ, from which it is clear that the sample mean horizontal wind effectiveness $\hat{\bar{\epsilon}}_h = \bar{\epsilon}_h(0)$ is close to the maximum $\bar{\epsilon}_h(\tau)$ for each trajectory. The horizontal blue line plots the global optimum $\bar{\epsilon}_{h^*}$ obtained by permuting the sequence of ascent and descent to maximize $\bar{\epsilon}_h$, which is always substantially higher than the maximum $\bar{\epsilon}_h(\tau)$ obtained by phase shifting the ascent-descent sequence. See text for discussion.

Downloaded from https://www.science.org at University of Newcastle on June 08, 2022

energy from the shear layer but suggests that there might have been some room for improvement, subject to the earlier caveats on the fidelity of the modeled flight trajectory, assumed wind, and physical achievability.

Shearwaters optimize their flight trajectories for dynamic soaring in a strong crosswind

The analysis so far has explored the optimization of the observed vertical sequence of ascent and descent conditional upon the observed horizontal flight trajectory. Theory predicts that a bird will maximize the energy it can harvest from the shear layer by either flying in a circular loitering pattern or, where constrained to make useful progress over the sea's surface, heading in a net crosswind direction (*21*, *31*–*33*). That energy harvesting is maximized in a net crosswind direction is a natural consequence of the Rayleigh conditions, which state that energy is gained by ascending into the wind and descending with the wind, but lost if this phasing is reversed. Hence, because a bird must, on average, lose as much height as it gains to remain within the shear layer, any net progress parallel to the wind introduces an asymmetry that reduces the opportunity for energy harvesting. A bird may therefore increase the energy that it can harvest from the shear layer by biasing its flight direction to head across the wind on each cycle. We quantify this by defining the wind opportunity for the ith cycle as $\omega_i = \| \sin \lambda_i \|$, where λ_i is the angle between the bird's mean air velocity vector over that cycle $\overline{\mathbf{U}}_i$ and the wind velocity unit vector $\widehat{\mathbf{W}}$ (Fig. 3). In principle, a flight trajectory that heads across the wind on every cycle has a mean wind opportunity of $\bar{\omega} = 1$, whereas a trajectory that heads into or against the wind on every cycle has a mean wind opportunity of $\bar{\omega} = 0$. In practice, a value of $0 < \bar{\omega} < 1$ is expected if the bird changes its net heading across cycles.

To assess how the horizontal flight trajectories were optimized in relation to the observed wind direction, we compare the sample mean horizontal wind effectiveness $\hat{\bar{\epsilon}}_h$ for each trajectory with the corresponding distribution of possible values of $\bar{\epsilon}_h$ given counterfactual wind directions ζ. Specifically, we compute $\bar{\epsilon}_h(\zeta)$ for each flight by holding the time history of the bird's observed yaw angle $\psi(t)$ fixed while varying ζ in 1° steps around the compass. This operation implicitly varies the mean wind opportunity $\bar{\omega}$ for each flight, which we use to assess the joint distribution of $\bar{\epsilon}_h(\zeta)$ and $\bar{\omega}(\zeta)$. The resulting plots of $\bar{\epsilon}_h(\zeta)$ against $\bar{\omega}(\zeta)$ typically have a symmetric, scissor-like form comprising two looped arms (Fig. 5). The symmetry of these plots reflects the fact that reversing the wind direction reverses the flow of energy, whereas the looped shape of each arm reflects the asymmetry of the birds' turning cycles (Fig. 3). In most cases, the maximum value of the mean wind opportunity $\bar{\omega}(\zeta)$ for any wind direction ζ was close to, but less than, one. This reflects the fact that the birds' cyclical turning behavior was superimposed on a longer-term change in overall flight direction. Nevertheless, as we now show, the scissor plots in Fig. 5 provide clear evidence that the birds optimized their horizontal turning cycle for dynamic soaring on flights with higher mean crosswind components $\hat{\bar{\omega}}W$. Conversely, on days when the mean crosswind component $\hat{\bar{\omega}}W$ was lower, there is no clear evidence that the horizontal turning cycle was optimized for dynamic soaring, albeit the vertical sequence of ascent and descent was still timed appropriately to gain rather than lose energy from the shear layer.

The proper phasing of the vertical sequence of ascent and descent to meet the Rayleigh conditions is evident from the fact that the observed point $(\hat{\bar{\omega}}, \hat{\bar{\epsilon}}_h)$ always lies on the upper arm of the scissor plot, for which $\hat{\bar{\epsilon}}_h > 0$ (Fig. 5). Flights for which there is evidence that the detailed horizontal flight trajectory is itself optimized for dynamic soaring are those in which both of the following two conditions are satisfied. First, the maximum value of $\bar{\epsilon}_h(\zeta)$ should coincide with a maximum of $\bar{\omega}(\zeta)$. This implies that the turning cycle is tuned to harvest energy most effectively when the overall flight direction relative to the wind offers the most opportunity for energy harvesting. Second, the observed point $(\hat{\bar{\omega}}, \hat{\bar{\epsilon}}_h)$ should be located at or close to the joint maximum of $\bar{\epsilon}_h(\zeta)$ and $\bar{\omega}(\zeta)$. This implies that the observed flight trajectory has the greatest potential for harvesting energy when the wind direction is the same as was observed. These conditions hold for the five flights falling in the upper 50th percentile for the mean crosswind component $\hat{\bar{\omega}}W$ (Fig. 5, C to E, G, and I), which are those offering the greatest potential returns from dynamic soaring. Conversely, these conditions do not hold on the four flights with crosswind components below the 50th percentile (Fig. 5, A, B, F, and H). This may imply that, when the mean crosswind component $\hat{\bar{\omega}}W$ is small, birds tune their horizontal flight trajectories by prioritizing flight objectives other than harvesting energy by dynamic soaring. For example, our assumption of a steady, horizontal wind field is an idealization, and birds might prioritize flight that harvests energy from vertical wind components such as wave-generated updrafts. In summary, the birds only turned in a manner that was tuned to capitalize on the opportunity for dynamic soaring on days when the potential return was high, albeit they always phased their vertical sequence of ascent and descent to gain rather than lose energy from the shear layer.

Shearwaters bias outbound flight in a crosswind direction favoring dynamic soaring

Given the strong association observed between mean horizontal wind effectiveness $\bar{\epsilon}_h$ and mean crosswind component $\bar{\omega}W$ at fine spatiotemporal scales (Fig. 6C), it is reasonable to expect that Manx shearwaters might benefit from biasing the heading of their foraging flights across the wind, with possible implications for their large-scale distribution at sea. Depending on the locations of available foraging grounds, crosswind flight may not be possible in all winds on the outbound leg of a flight and will be even more tightly constrained on the return leg by the unique direction to home. Pure crosswind flight is impossible to achieve on both the outbound and return legs of a flight, because directing the air velocity vector $\mathbf{U}$ perpendicular to the wind $\mathbf{W}$ on the outbound leg will generate a downwind drift requiring correction on the return leg. We might, therefore, expect to see a preference for crosswind flight directions on the outbound legs of foraging trips, which we test here against data from $n = 368$ outbound and $n = 368$ return tracks collected using GPS loggers attached to $N = 201$ individuals from 2016 to 2019 (Fig. 7). Note that of the $n = 368$ tracks that we analyze for each direction of flight, 349 comprise the outbound and return legs of the same flights; the remaining 19 outbound and 19 return flights are not from matched samples. Also note that since departure times in Manx shearwaters are staggered throughout the night, and shearwaters are not thought to fly in at-sea formations (*34*, *35*), we assume that birds do not influence the orientation decisions of other birds and hence that each track is an independent data point.

We calculated the overall heading-to-wind angle λ for each flight leg as the angle between the bird's mean air velocity vector $\overline{\mathbf{U}}$ over the flight leg and the wind velocity vector $\mathbf{W}$ (Fig. 8A). As the benefits

Downloaded from https://www.science.org at University of Newcastle on June 08, 2022

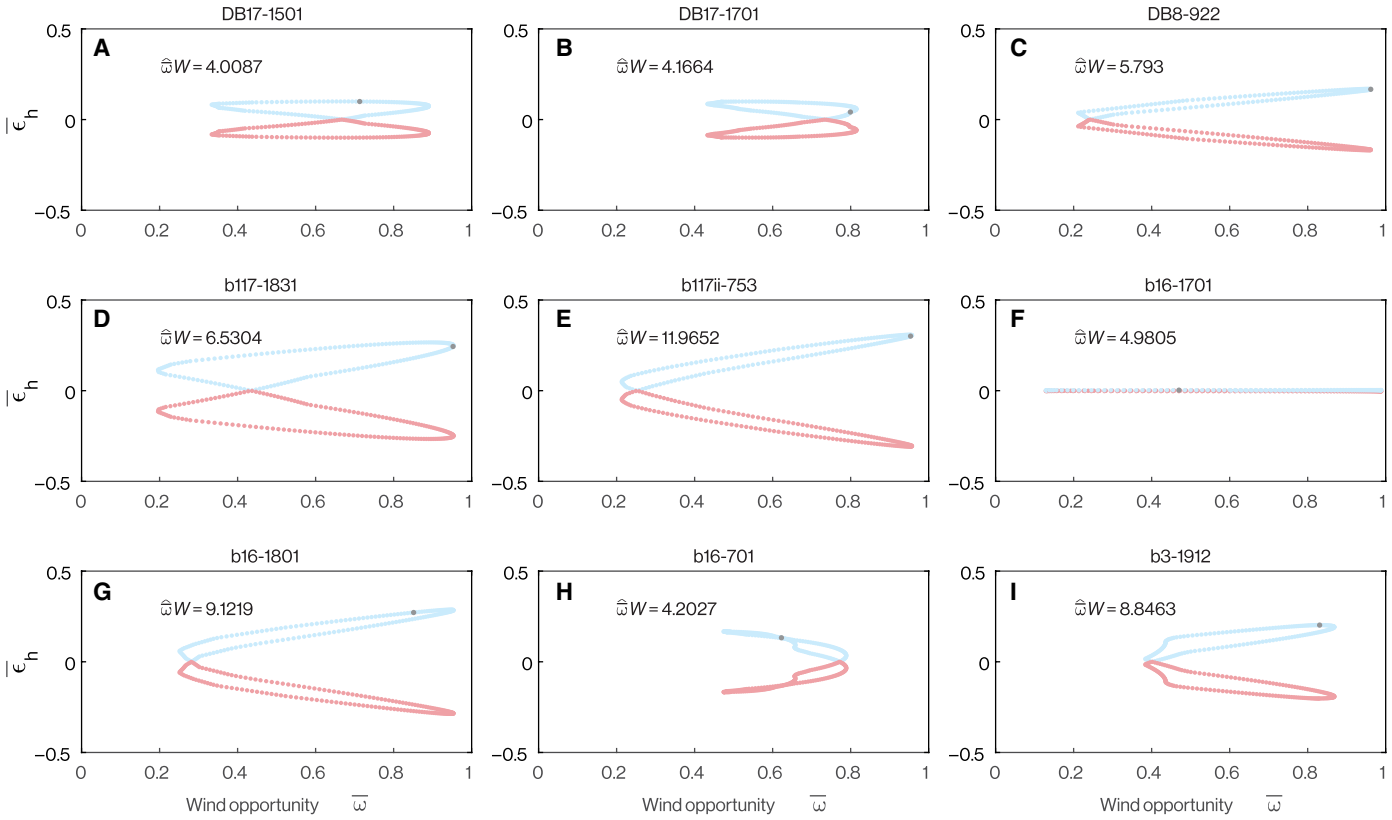


Fig. 5. Optimization of horizontal flight trajectories with respect to the wind. (**A** to **I**) Each panel plots the distribution of mean horizontal wind effectiveness $\bar{\epsilon}_h(\zeta)$ computed by holding the horizontal and vertical components of one of the $n = 9$ fine-scale flight trajectories fixed while varying the assumed wind direction ζ. Both the mean horizontal wind effectiveness $\bar{\epsilon}_h$ and the mean wind opportunity $\bar{\omega}$ vary as the wind direction ζ varies, and plots of $\bar{\epsilon}_h$ against $\bar{\omega}$ have a scissor-like form in most cases. Positive values of $\bar{\epsilon}_h$ are shown in blue, and negative values in red. The gray points mark the observed mean horizontal wind effectiveness $\hat{\bar{\epsilon}}_h$ and observed mean wind opportunity $\hat{\bar{\omega}}W$. See text for discussion.

of heading in a crosswind direction are independent of whether the wind comes from the left or right, we quantified the variation in the overall heading-to-wind angle by computing the sample SD of $\|\lambda\|$, where λ is defined on the interval [0°,180°]. We then compared this to the population distribution of the same statistic obtained by randomizing 100,000 times the pairings of the sample values of $\overline{\mathbf{U}}$ and $\mathbf{W}$ that we used to calculate λ (Fig. 8B). In this analysis, we used all recorded outbound and return trajectories, meaning we included $n = 368$ outbound and $n = 368$ return trajectories (see Materials and Methods). We found that the overall heading-to-wind angle was no more conserved than expected by chance on the return legs of the flights ($n = 368$; $P = 0.26$) but was significantly conserved on the outbound legs ($n = 368$; $P < 0.0001$), albeit the effect size was quite small (SD, 50. 1° on return legs versus 48. 2° on outbound legs). The mean absolute heading-to-wind angle on the outbound legs was 81. 3° (±3.13° 95% CI; Fig. 8A), which is close to the crosswind tendency predicted to maximize the opportunity for dynamic soaring, but with a tailwind bias of 7° appropriate to provide wind assistance on the outbound leg.

To test how the observed crosswind tendency affected the potential returns from dynamic soaring, we compared the mean wind opportunity $\bar{\omega} = \|\sin\lambda\|$ between the outbound and return legs of the flights. As expected, the mean wind opportunity $\bar{\omega}$ was significantly higher on the outbound journey for flights on which both legs were represented ($n = 349$; paired Mann-Whitney test, $P = 0.0149$), confirming that the birds' tendency to fly across the wind on their outbound flights increased their potential returns from dynamic soaring (Fig. 9). Furthermore, $\bar{\omega}$ increased significantly with wind speed W on the outbound legs of the flights (Spearman's $\rho = 0.292$; $P < 0.0001$; $n = 368$) but was not significantly associated with wind speed on their return legs (Spearman's $\rho = 0.0508$; $P = 0.331$; $n = 368$). It follows that the birds' tendency to fly across the wind on their outbound flights was stronger on windier days, when the potential returns from dynamic soaring were highest (Fig. 9). This result could, in principle, have arisen as an artifact of the prevailing wind coming from a direction promoting crosswind flight. However, we found no evidence that the strongest winds came from a constrained direction when comparing the Rayleigh statistic for the wind directions associated with the top 10% of wind speeds with the population distribution of this statistic after randomizing the pairings of wind speed and wind direction ($P = 0.34$). We conclude that the shearwaters' tendency to forage in a more crosswind direction on windier days increases their potential returns from dynamic soaring when conditions are most conducive for harvesting energy from the shear layer.

DISCUSSION

Here, we use bird-borne video loggers to record the fine-scale flight trajectories of flap-gliding Manx shearwaters and use GPS loggers to record their coarse-scale movements and distribution at sea. Our

Downloaded from https://www.science.org at University of Newcastle on June 08, 2022

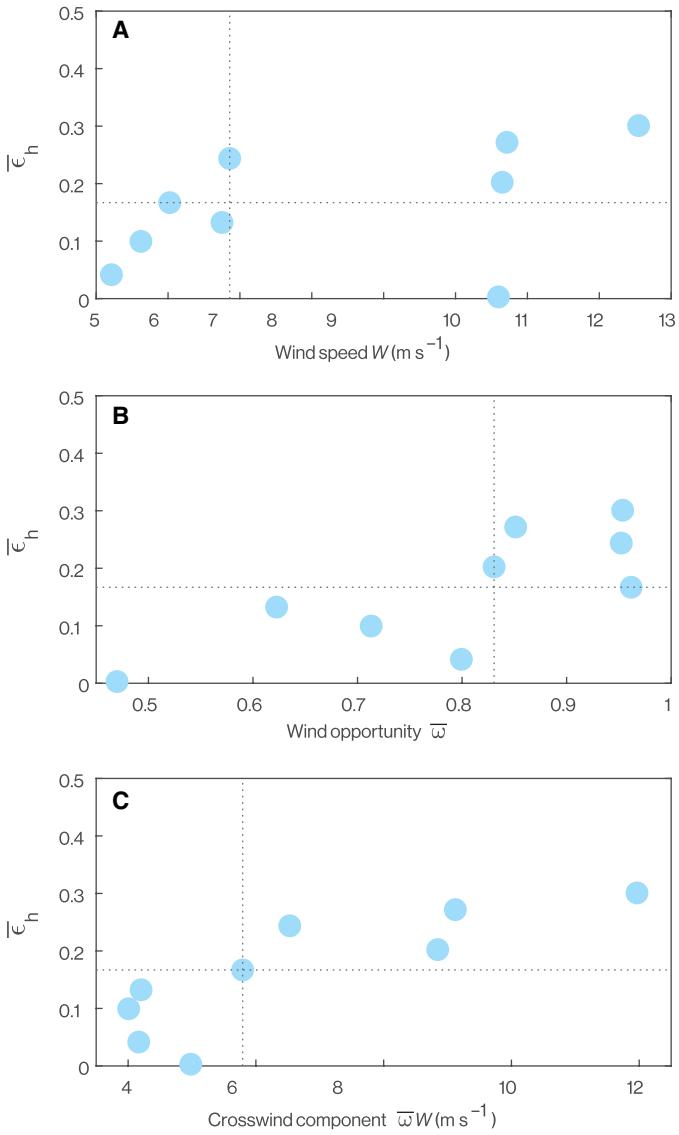


Fig. 6. Influence of the wind on the effectiveness of dynamic soaring. (**A** to **C**) Each data point represents one of the $n = 9$ fine-scale flight trajectories and plots how the observed mean horizontal wind effectiveness $\bar{\epsilon}_h$ varies as a function of the wind and its interaction with the bird's overall direction of flight. Wind speed W is treated as constant within a trajectory. The mean wind opportunity $\bar{\omega}$ is the average of $\|\sin \lambda_i\|$ over a trajectory where λ_i is the angle between **W** and the bird's average heading over the ith cycle. The crosswind component $\bar{\omega}W$ is the product of the wind speed W and mean wind opportunity $\bar{\omega}$. Vertical and horizontal dashed lines plot the median values of each variable. See text for discussion.

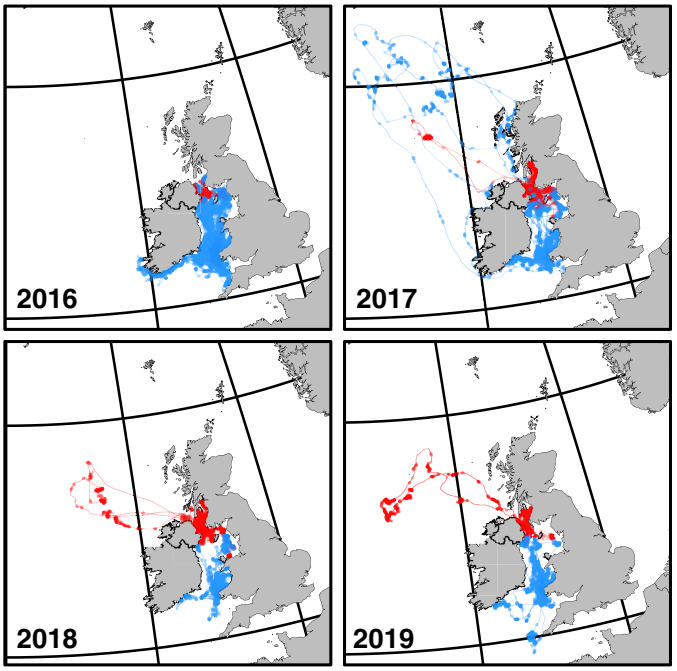


Fig. 7. At-sea distribution of Manx shearwaters. Coarse GPS trajectories show $n = 368$ flight tracks from colonies in Northern Ireland (Copeland; red) and southwest Wales (Skomer and Skokholm; blue) recorded from 2016 to 2019. GPS fixes during feeding behavior are highlighted with translucent points (note that when there are multiple fixes during feeding in a similar area, the points appear more opaque); sections of the track spent in directed flight are shown as connecting lines.

data cover spatial scales ranging from less than a meter to hundreds of kilometers and time scales ranging from less than a second to several days. We find that the shearwaters flew trajectories optimized for dynamic soaring and that they harvested energy from the shear layer more effectively with increasing wind speed. Furthermore, we find that on outbound flights when their destination was less constrained, Manx shearwaters increased the crosswind component of their flight trajectory to maximize the opportunity for energy harvesting, and did so to a greater extent when the wind speed was higher. We discuss below why such a strategy might be adaptive for these birds, and consider how small-scale flight decisions might influence large-scale feeding distribution at sea.

Optimization of dynamic soaring in Manx shearwaters

Pelagic birds harvesting kinetic energy from the shear layer incur an opposing cost because of the weaving and undulating flight trajectory needed to extract energy by dynamic soaring. This increases the path length relative to direct flight and induces drag through the use of lift to turn (*24*). Dynamic soaring behavior therefore represents a trade-off between maximizing the potential for energy harvesting and minimizing the energy losses due to drag. Assessing both sides of this trade-off is challenging in flap-gliding species because of the difficulty of measuring flight efficiency in a bird using intermittent flapping. We have therefore focused on quantifying how effectively energy is harvested from the shear layer through the mean horizontal wind effectiveness and mean wind opportunity metrics that we have defined. We represent the associated trade-off diagrammatically in the form of a performance space (*36*) plotting the mean horizontal wind effectiveness $\bar{\epsilon}_h$ against the mean crosswind component $\bar{\omega}W$ (Fig. 10).

The lower half of this performance space (i.e., $\bar{\epsilon}_h < 0$) is unambiguously maladaptive, because flight in this region of the graph actively loses energy to the wind gradient (pink shaded region in Fig. 10). The shearwaters avoided this region of the graph on all $n = 9$ trajectories that we recorded at a fine scale (blue points in Fig. 10). This region of the performance space represents a hazard for any bird ascending or descending through a shear layer, and we call this outcome maladaptive because it should always be possible to avoid.

Downloaded from https://www.science.org at University of Newcastle on June 08, 2022

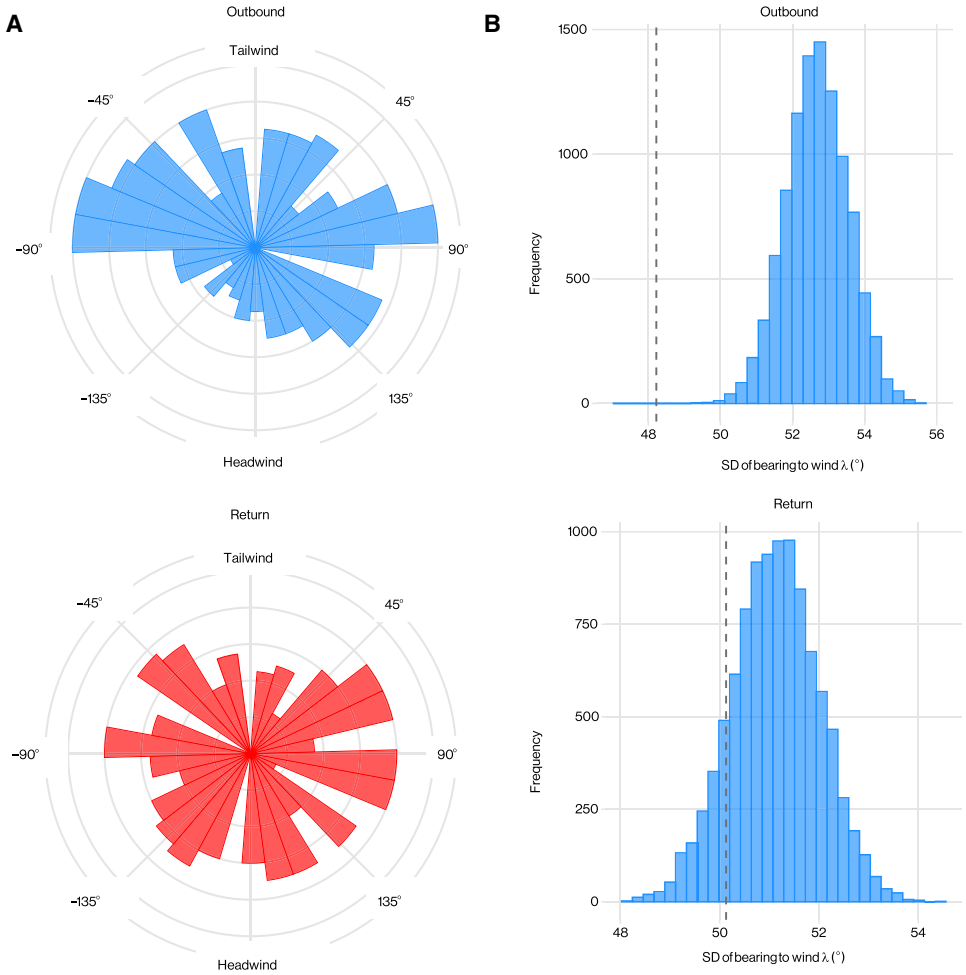


Fig. 8. Association of wind direction and flight direction in Manx shearwaters. (**A**) Circular histograms comparing the overall heading-to-wind angle (λ) experienced by shearwaters on outbound (top) and return (bottom) flight. (**B**) Distribution of SD of absolute overall heading-to-wind angle $\|\lambda\|$ computed by randomizing the pairings of the sample flight directions and sample wind speeds on outbound (top) and return (bottom) flights; gray dashed lines mark sample SDs.

Specifically, for any horizontal trajectory, there will always exist corresponding ascent-descent sequences for which $\bar{\epsilon}_h \geq 0$. Unless there is some countervailing reason to ascend or descend, these should always be adopted in favor of ascent-descent sequences for which $\bar{\epsilon}_h < 0$. The reality of this hazard is demonstrated by the pink-shaded portions of Figs. 4 and 5, which show how the same horizontal trajectory can be maladaptive given counterfactual phasing of its ascent-descent sequence or a counterfactual wind direction. Conversely, even the four flight trajectories experiencing the lowest mean crosswind component $\hat{\bar{\omega}}W$, and hence the least opportunity for energy harvesting, achieved $\hat{\bar{\epsilon}}_h > 0$ (Fig. 10). The birds therefore avoided the small energy losses to the wind gradient that they would have experienced had they adopted poorly phased counterfactual ascent-descent sequences.

The upper half of the performance space (i.e., $\bar{\epsilon}_h > 0$) represents the region of the graph in which energy is actively harvested from the shear layer. However, because of the trade-off that exists between harvesting energy from the shear layer and losing energy to drag in the process, it is not equally beneficial to occupy all regions of this upper half of the performance space (Fig. 10). Specifically, when the mean crosswind component of the trajectory $\hat{\bar{\omega}}W$ is low—whether because of low wind speed W, an unfavorable flight direction resulting in a low mean wind opportunity $\bar{\omega}$, or both—there will be little energy accessible to harvest in the wind gradient. Increasing path tortuosity to maximize the effectiveness with which this little energy is harvested (i.e., maximizing $\bar{\epsilon}_h$) will not then yield appreciable increases in energy harvesting but will incur appreciable costs. The corresponding portion of the graph is therefore labeled "wasted effort," referring to the crosshatched region in the top left of the performance space (Fig. 10). The portion of the performance space labeled "wasted opportunity" on the right-hand side of the graph also represents a suboptimal execution of the trade-off. In this region of the graph, the mean crosswind component $\bar{\omega}W$ is high, so there is significant energy accessible to harvest in the wind gradient. Trajectories that do not effectively harvest this significant energy, as indicated by their low mean horizontal wind effectiveness $\bar{\epsilon}_h$, are therefore expected to be suboptimal.

It is clear from Fig. 10 that the shearwaters broadly conform to these expectations, avoiding the maladaptive region of the performance space altogether and showing evidence of avoiding those regions of the performance space in which the most opportunity or effort is wasted. This implies that they synchronize their vertical motion appropriately

Downloaded from https://www.science.org at University of Newcastle on June 08, 2022

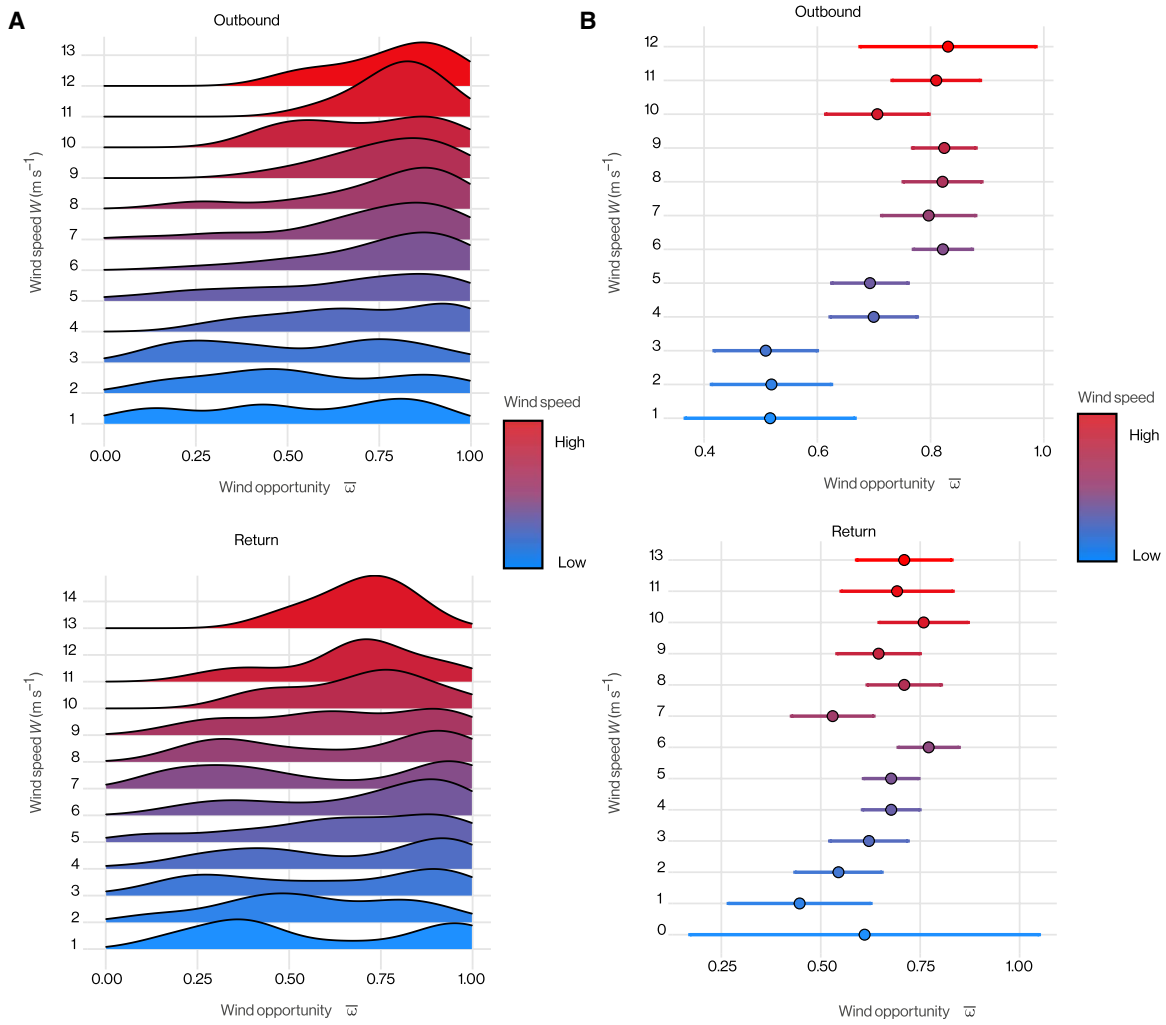


Fig. 9. Association of wind speed and flight direction in Manx shearwaters. (**A**) Density curves of mean wind opportunity $\bar{\omega}$ plotted for integer wind speed bins (meters per second). The higher the curve, the greater the density, and hence the more frequently that birds experience that wind opportunity when flying in winds of that speed. (**B**) Mean wind opportunity $\bar{\omega}$ plotted with bootstrapped 95% CI in integer wind speed bins (meters per second).

with their horizontal motion so as to meet the Rayleigh conditions of ascending into the wind and descending with it. Nevertheless, using the fine-scale trajectory data that we derive from our bird-borne video footage, we only find evidence that the birds optimized their detailed horizontal trajectories in relation to the wind during flights on which the mean crosswind component $\bar{\omega}W$ was high (Fig. 5). These flights, marked as dark blue points in Fig. 10, are those for which the evidence of dynamic soaring is strongest, so it is noteworthy that their mean crosswind components are in the same range as those recorded on most of the outbound flights that we sampled at a coarse scale using GPS (see histogram at the top of Fig. 10). In summary, the GPS data show that for most of their outbound flights, the birds flew with a mean crosswind component that the video data show was associated with detailed trajectory optimization for dynamic soaring.

While the value of the mean crosswind component $\bar{\omega}W$ is obviously limited by the wind speed W served on the day, birds can maximize their mean crosswind component subject to this constraint by heading in a direction that maximizes the mean wind opportunity $\bar{\omega}$. It follows that birds can move around the performance space in Fig. 10 by making fine adjustments to their fine-scale flight trajectories to optimize their wind effectiveness $\bar{\epsilon}_h$ and by making coarse adjustments to their large-scale flight trajectories to optimize their mean crosswind component $\bar{\omega}W$, which implicitly alters $\bar{\epsilon}_h$. The performance space in Fig. 10 thereby captures the effects of both fine- and large-scale flight behavior.

Using the very large dataset of $n = 368$ outbound flights and $n = 368$ return flights that we obtained using bird-borne GPS loggers, we find evidence that Manx shearwaters tune their flights at this larger scale, by increasing the mean wind opportunity $\bar{\omega}$ that they experience as wind speed W increases. In other words, shearwaters have a stronger tendency to fly in a crosswind direction on days when the wind is strongest (Fig. 8), although we only observe this tendency during their outbound flights (Fig. 9). This likely reflects a higher-level trade-off between adopting flight directions that are better for dynamic soaring and those that are better for other ecological reasons. In particular, flight direction is tightly constrained during homing flight because of the necessity to return to the breeding site to provision offspring. In contrast, constraints on flight direction are

Downloaded from https://www.science.org at University of Newcastle on June 08, 2022

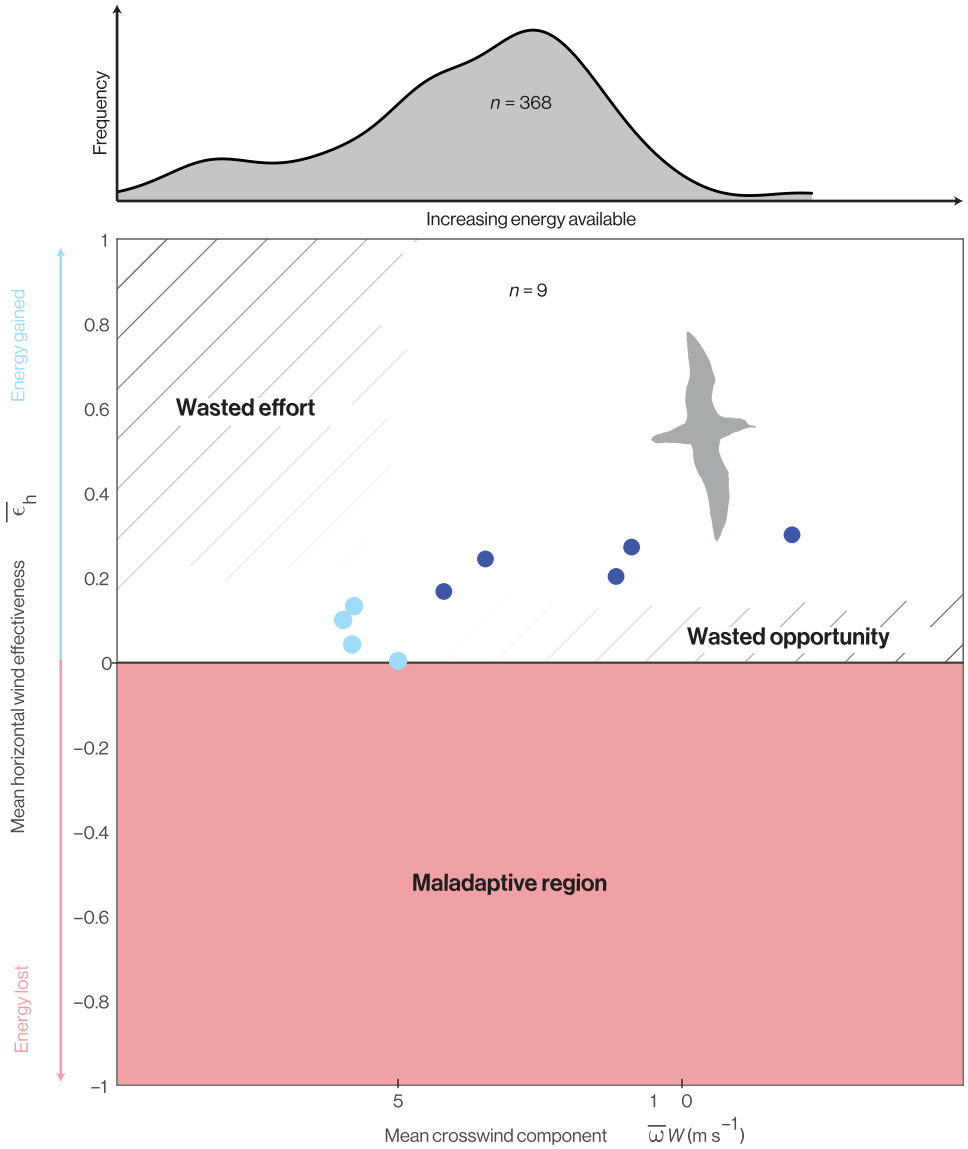


Fig. 10. Performance space of dynamic soaring. Birds implementing dynamic soaring should fly such that they occupy the white region of the performance space. The pink-shaded area is the region of performance space in which energy is lost to the wind gradient, which is maladaptive in the sense that it is always possible to find alternative ascent-descent sequences that avoid this. Within the upper half of the performance space, trajectories occupying the crosshatched regions are suboptimal in the sense that they represent either wasted effort or wasted opportunity. The wasted opportunity region lies to the right-hand side of the performance space, as the energy accessible in the wind gradient increases with the mean crosswind component $\bar{\omega}W$. How this bears on our studied shearwaters is illustrated by the histogram at the top of the figure, which shows the distribution of mean crosswind component $\bar{\omega}W$ over the $n = 368$ recorded outbound flights. The blue-filled circles plotted in the performance space are the data from Fig. 6C where those shaded darker correspond to trajectories showing clear evidence of optimization of their horizontal trajectories in relation to the wind (see text for discussion). Note that the range of mean crosswind components over which there is clear evidence of detailed trajectory optimization for dynamic soaring (dark blue) matches the range experienced on most flights (see histogram).

more relaxed during outbound flight for which the foraging destination is flexible within reason. Note that the birds' stronger tendency to fly across the wind on windier days could reflect headwind avoidance rather than crosswind selection. Nevertheless, as the effect of this large-scale behavior will be to promote dynamic soaring regardless, and as the birds' fine-scale flight trajectories confirm their use of dynamic soaring, it seems reasonable to view the observed crosswind tendency as an adaptation for dynamic soaring on outbound flights.

How might the optimization of atmospheric energy harvesting affect the foraging distributions at sea? Manx shearwaters are known to use a dual-foraging strategy when rearing (*37*), alternating between short chick-provisioning trips and longer self-provisioning trips to predictable oceanic resources (*38*). It is therefore possible that, within these constraints, decisions relating to choice of foraging site account for flight directions that increase energy extraction from the prevailing wind. Furthermore, given that the wind observed in the Irish Sea has a strong southwesterly bias, it is possible that the overall

Downloaded from https://www.science.org at University of Newcastle on June 08, 2022

feeding distribution of shearwaters is contingent on these prevailing winds as a consequence of their use of dynamic soaring.

We have shown soft boundaries to the suboptimal regions of the performance space to reflect uncertainty over their actual extent in relation to the performance that we observed in Manx shearwaters (Fig. 10). It is reasonable to assume that the performance spaces of other Procellariiformes will look broadly similar, but the upper half of the performance space might differ in detail for albatrosses, whose higher aspect ratio wings enable them to glide continuously over the windier open oceans. For example, for birds like the wandering albatross, we might expect the wasted effort region to be narrower with respect to the mean crosswind component $\bar{\omega}W$. This is because the minimum mean crosswind component $\bar{\omega}W$ needed to fly energy-neutral dynamic soaring cycles is lower at the higher lift-to-drag ratios that higher aspect ratio wings enable (*39*). Moreover, at very high mean crosswind components, it is plausible that albatrosses might benefit from flying trajectories with reduced mean horizontal wind effectiveness $\bar{\epsilon}_h$ to avoid the very high aerodynamic loads associated with building up surplus kinetic energy.

Implications for sensory physiology and behavior

Our finding that shearwaters optimize their fine-scale flight behavior for dynamic soaring might be thought to suggest that they require some sense of wind direction to determine when to transition between ascent and descent. For flight through a thick shear layer, it has been shown theoretically that optimal dynamic soaring trajectories approach a chain of alternating semicircular turns (*24*). Under these conditions, a simple behavioral rule may suffice for the optimal control of dynamic soaring, because for a bird that spends as much time ascending as descending, transitioning between the two at the extremes of each cycle maximizes the energy gain (or loss) for any wind direction. All that is needed, therefore, is to select the binary phasing of ascent versus descent that makes the mean wind effectiveness positive, which only depends on knowing whether the wind is coming from the left or right of the average heading. The optimal transition points themselves are reached when the bird is heading in the same direction as its average heading, so could be sensed with the aid of any compass or other heading indicator, including a magnetic compass, the sun and its attendant cues, or distant landmarks and clouds (*40*). A detailed sense of wind direction would, of course, allow for more precise optimization of any trajectory and might be possible using ventral optic flow cues under some conditions (*41*). In particular, if the bird's longitudinal axis were aligned with its heading vector as assumed here, then any lateral optic flow must be a consequence of wind drift. Vision may therefore be at least as important for wind sensing in Procellariiformes as their tubular nostrils, which have been suggested to function as pitot tubes sensing airspeed during dynamic soaring (*42*).

Our camera-based method of reconstructing dynamic soaring trajectories also points to the fact that vision may be useful in controlling the turning flight behavior that we observe. When visible, the horizon offers a reliable means of identifying the vertical direction. This could be particularly useful in the control of pitching and banking during dynamic soaring, given that sensing gravitational acceleration is unreliable when aerodynamic accelerations are superimposed during unsteady maneuvers. Our horizon sensing algorithm calls to mind the specializations of the visual field in Procellariiformes, which have a horizontal streak where the retinal ganglion density is higher, thereby improving resolving power around the horizon (*43*). While this has traditionally been explained by the "terrain hypothesis," which invokes the need for detection of objects against a horizon in open terrain (*44*, *45*), it may also have a function in flight control (*46*). Specifically, by stabilizing their head with respect to the fixed horizon, our shearwaters would have had an external reference for roll stabilization from which, via neck proprioception (*47*), the angle of the body relative to the head could be inferred to obtain estimates of bank and pitch. This head stabilization behavior is clearly visible in the videos (see movie S1). These sensing implications are also of interest for marine unmanned air vehicles (UAVs), given the potential to increase their flight time, range, and efficiency by dynamic soaring.

Limitations

The horizontal wind effectiveness metric ϵ_h (Eq. 3) does not account for the quantitative effect of the bird's flight path angle (γ) on the rate of energy harvesting. This is captured by the total wind effectiveness metric ϵ (Eq. 2), which differs from ϵ_h by a factor of $\sin 2\gamma$. We have chosen to evaluate ϵ_h rather than ϵ here on the pragmatic grounds that, while it is usually possible to distinguish unambiguously whether a bird is ascending or descending, accurate quantitative estimates of the flight path angle γ relative to the air are difficult to obtain. Furthermore, the sign of the horizontal wind effectiveness ϵ_h is always the same as the total wind effectiveness ϵ, and evaluating the horizontal wind effectiveness metric ϵ_h partitions out the effects of the horizontal components of the flight trajectory, which are what combine to determine the overall flight direction that we analyze on larger spatiotemporal scales.

The mean horizontal wind effectiveness metric $\bar{\epsilon}_h$ is calculated as the unweighted mean of the horizontal wind effectiveness ϵ_h across a flight trajectory. This is appropriate if a given flight direction is equally good at harvesting energy everywhere in the wind field, but this only strictly holds for a linear wind profile in which the vertical wind gradient is constant. In contrast, theoretical studies of dynamic soaring have variously assumed linear (*48*), exponential (*31*, *32*, *49*, *50*), or logarithmic (*31*, *32*, *49*) models of wind shear. Under the nonlinear wind shear models, the wind gradient σ varies with altitude. For example, a logarithmic wind gradient is steepest just above the sea surface and becomes shallower with height. In this case, the same flight direction and hence the same value of ϵ_h would harvest more energy closer to the sea's surface.

The suitability of the mean horizontal wind effectiveness metric $\bar{\epsilon}_h$ as a measure of how effectively a given flight trajectory harvests energy from the wind gradient therefore depends on the nature of the wind gradient, which is usually unknown. If necessary, the calculation of the mean horizontal wind effectiveness $\bar{\epsilon}_h$ could be adjusted to account for the local wind gradient by taking a weighted mean of the horizontal wind effectiveness ϵ_h with weights that vary as a function of height. This operation requires precise knowledge of vertical position, however, which is difficult to achieve, even with GPS loggers. Hence, even in the presence of a nonlinear wind profile, there is utility calculating the mean horizontal wind effectiveness $\bar{\epsilon}_h$ as we have done here, which only requires a binary assessment of whether the bird is ascending or descending.

Although the mean horizontal wind effectiveness $\bar{\epsilon}_h$ is itself a robust metric for assessing the effectiveness of a flight trajectory at harvesting energy from a vertical wind gradient, evaluating $\bar{\epsilon}_h$ empirically requires accurate estimates of the flight path angle γ and yaw angle ψ. The estimates that we have made of the bird's pitch

Downloaded from https://www.science.org at University of Newcastle on June 08, 2022

angle θ and bank angle ϕ are subject to measurement error, and although we have attempted to calibrate out any systematic bias in these estimates, our method for doing so is itself subject to model error (see Materials and Methods). Specifically, we derive the following exact expression for the yaw angle rate induced by an unsteady banked turn in a steady horizontal wind field of uniform direction with vertical wind shear σ

$$\dot{\psi} = \frac{L \sin \phi}{mU \cos \theta} + \sigma \sin \psi \tan \theta \quad (9)$$

This expression is exact, subject to the simplifying assumption that the bird's air velocity vector is always aligned with its longitudinal body axis (see Supplementary Text), which implies either that the bird is perfectly stable in pitch and yaw or that it coordinates its turning to achieve the same weathercock effect. For the purposes of estimating the bird's yaw angle ψ, we have used the approximate model given in Eq. 4, which drops the term σ sin ψ tan θ describing the weathercock effect of wind shear. This is done on the basis that we know neither the vertical wind shear strength σ nor the detailed stability properties of the bird that give rise to this term, but is expected to lead to model error (*36*) if the assumptions of Eq. 9 are satisfied.

Dropping this term is equivalent to assuming that the aerodynamic effect of wind shear on the birds' turning is negligible, which is true when the vertical wind shear σ is weak, when the bird is flying with or against the wind such that sin ψ is small, or when the bird flies a shallow flight path such that tan θ is small. These conditions will not always prevail, resulting in a time-varying error in the estimation of $\dot{\psi}$. This will modify the shape of the weaving trajectories predicted under the model (Fig. 3), but any changes in curvature will have a second-order effect on our estimates of mean horizontal wind effectiveness $\bar{\epsilon}_h$ compared to any first-order integration error, which we remove by calibrating our estimates of ψ against the position of the sun's disc in the video. In making this correction, we correct for camera bank offset, and we correct separately for camera pitch offset, affecting our estimates of the flight path angle γ. Equation 4 further assumes near-constant airspeed $U \approx U_0$ and near-constant lift equal to body weight $L \approx mg$. Our constant airspeed assumption was necessary because we were unable to deploy airspeed sensors simultaneously with bird-borne video cameras given the constraints on carried load (*51*), but we do not expect this to have much effect on our results because airspeed tends to fall in a narrow range. We also find that any statistical tests reported to be significant at $U_0 = 11.1$ m s^{-1} were also significant for alternative assumed airspeed values from 7.5 to 14.0 m s^{-1}.

There is the possibility that behavioral sampling biases could affect the generality of our findings (*52*). We used breeding birds for both GPS and video analysis so that loggers could be retrieved (*34*). Since both male and female shearwaters provide the same level of chick-rearing effort (*53*), it is unlikely that our results are sex biased. However, as breeding birds tend to be older than nonbreeding birds, our samples will be age biased. Given that flight behavior optimization in relation to wind has been suggested to develop through learning [e.g., (*9*)], it is therefore possible that our results might not generalize to younger, inexperienced shearwaters.

A quantitative framework for identifying dynamic soaring

Although it is widely accepted that Procellariiformes use dynamic soaring (*15*, *54*), and while the theory of dynamic soaring is well understood, rigorous empirical demonstrations of its utilization are few and far between. Dynamic soaring has only previously been demonstrated conclusively in wandering albatross (*27*), having been inferred somewhat indirectly in Manx shearwaters (*16*). Demonstrating that a bird is implementing dynamic soaring demands showing that the bird is extracting energy actively from a wind gradient. One characteristic of such behavior is its cyclical variation in mechanical energy (see Introduction), but this is neither necessary nor sufficient to demonstrate dynamic soaring. It is not sufficient as mechanical energy may vary cyclically during other flight modes, such as the undulating intermittent flight of European starlings (*Sturnus vulgaris*) (*28*). It is not necessary as mechanical energy variation due to drag losses, static soaring, and flapping (see Supplementary Text) may obscure the energetic signature of dynamic soaring altogether, and this is especially problematic in flap-gliding species such as Manx shearwater (*16*). The metric of mean horizontal wind effectiveness $\bar{\epsilon}_h$ that we have derived here overcomes these limitations by assessing directly whether a given flight behavior is expected to harvest energy from the shear layer or to lose energy to it. This assessment is independent of other energy flows such that it is not prone to masking in the way that an assessment of the changes in total mechanical energy would be.

Other observational studies have found no difference between large and small Procellariiformes in the frequency of flights that contain soaring (*54*), so our demonstration that Manx shearwaters fly in a manner adapted to harvest energy from the shear layer suggests that dynamic soaring may be important across a broader range of species and environments than has been demonstrated to date. Demonstrating that the mean horizontal wind effectiveness $\bar{\epsilon}_h$ is consistently positive across flights, as we have shown here for Manx shearwaters, therefore offers a reliable method for diagnosing dynamic soaring in other candidate flap-gliding Procellariiformes such as the northern fulmar (*Fulmarus glacialis*). When studied in combination with the other metrics of mean wind opportunity $\bar{\omega}$ and mean crosswind component $\bar{\omega}W$ that we have derived here, the quantification of horizontal wind effectiveness also permits a fuller consideration of the optimization of dynamic soaring in these species. Furthermore, it could be applied to groups traditionally unassociated with dynamic soaring but known to glide in regions with strong spatiotemporal wind gradients such as lesser black-backed gulls (*Larus fuscus*) flying in cityscapes (*55*) or jackdaws (*Corvus monedula*) flying around ridgelines. Last, our demonstration of dynamic soaring in coastal environments by a flap-gliding bird will be of interest to those working on marine UAVs. Our results illustrate the possibility of marine UAVs using dynamic soaring to decrease power consumption and thereby increase flight range, time, and sustainability during facultatively powered flight in the socially important coastal zone.

MATERIALS AND METHODS

The theoretical framework that underpins the analysis described in the main text is derived in Supplementary Text. The following sections describe the empirical methods used to collect and analyze the field data.

Field observations

All work was done under ethical approval from the Animal Welfare and Ethical Review Board of the Department of Zoology, Oxford

Downloaded from https://www.science.org at University of Newcastle on June 08, 2022

University, under endorsements from the British Trust for Ornithology Unconventional Methods Panel [BTO permit numbers C/5311 (T.G.) and C/6128 (O.P.)], and following approval by the Islands Conservation Advisory Committee. We captured 146 bird-borne video recordings from Manx shearwaters *P. puffinus* during fieldwork undertaken from 15 to 28 August 2014 on Skomer Island, Pembrokeshire (51.74°N, 5.30°W). However, as the behavior of interest for this study was cruising flight, we excluded videos containing takeoff, landing, and sea-sitting behavior. Likewise, as the sun was needed to calibrate flight direction (see below), we excluded videos in which the sun's disc was not visible, leaving a sample of $n = 9$ videos from $N = 6$ individuals across six different days.

Each video was captured using a miniature video logger (VEHO VCC-003 MUVI Micro DV Camcorders) (*56*) attached to the bird's back using water-soluble adhesive and TESA (4651) marine tape (*34*). A custom-designed, microprocessor-controlled timer was used to record 2-min sections of video once every hour (640 × 480 pixels; RGB24 AVI format; 20 frames per second). Video loggers were inserted into waterproof heat-shrink plastic tubing (*34*), in which a small incision was made to enable the head of the camera to be positioned upright pointing forward. The camera head was inserted into a purpose-built Perspex turret, which was waterproofed and held in place by hot-melt glue. The video loggers weighed 17 to 18 g including battery, which is approximately 4% of body mass (*20*, *34*, *51*).

Shearwaters were also (not simultaneously) tracked at a coarse scale using iGotU (Mobile Action, Taiwan) GPS devices [mass = 15 g (*51*)] from colonies on Lighthouse Island (Copeland Archipelago; $n = 164$; 54.70°N, 5.52°W), Skomer Island ($n = 211$; 51.74°N, 5.30°W), and Skokholm Island (2016 only; $n = 10$; 51.70°N, 5.30°W) from 2016 to 2019. These $n = 368$ tracks were taken from $N = 201$ birds in total. GPS loggers were set to record speed and position at 5-min intervals and were interpolated using a cubic spline function to ensure that the position estimates fell at precise 5-min intervals (*57*). Tracks up to and including those gathered in 2016 were also analyzed and published in (*35*).

Video analysis

We estimated the camera pitch angle (θ_c) and camera bank angle (ϕ_c) directly from the video footage by writing an automatic horizon detection algorithm in MATLAB (The Mathworks Inc., Natick, MA). The algorithm squares the intensity of the blue channel to obtain a high-contrast grayscale image, to which it applies a Gaussian smoothing kernel with $\sigma = 8$. The algorithm then uses Roberts edge detection to find and mask the outline of the bird, and uses the Hough Transform to detect straight lines outside of this mask. The longest straight line is then taken as the putative horizon (movie S2). We checked all putative horizon lines manually and edited these where necessary to correct any errors (movie S3). The frame was skipped if no horizon line was visible.

We estimated the camera bank angle as $\phi_c = -\arctan(\Delta y/\Delta x)$, where Δx and Δy denote the differences in the image coordinates of the horizon end points. Likewise, we estimated the camera pitch angle as $\theta_c = s \times 72/640$, where s is the signed distance in pixels between the horizon line and the midpoint of the image, assuming an equiangular projection model over the measured 72° field of view. We interpolated ϕ_c and θ_c for skipped frames using a piecewise cubic Hermite interpolating polynomial and forward-backward filtered the signals using a fifth-order low-pass Butterworth filter at a cutoff frequency of 0.5 Hz to remove high-frequency noise due to measurement error, flapping perturbations, and other camera motion.

The measured pitch angle θ_c and the measured bank angle ϕ_c of the camera differ from the true pitch angle θ and the true bank angle ϕ of the bird because of camera offset and measurement error. We therefore estimate the bird's pitch angle as $\hat{\theta} = \theta_c - \delta_\theta$, having calibrated the pitch offset δ_θ by enforcing the constraint that $\hat{\theta}$ should average zero over the entire flight. This is justified on the basis that the vertical component of the bird's motion $U \sin\theta$ must average zero for it to remain close to the surface in a horizontal wind field such that $\sin\theta$ must also average zero if the airspeed U remains approximately constant as assumed.

We estimate the bird's bank angle as $\hat{\phi} = \phi_c - \delta_\phi$ and calibrate out any bank offset δ_ϕ by integrating Eq. 4 numerically, having replaced θ and ϕ with their estimates $\hat{\theta} = \theta_c - \delta_\theta$ and $\hat{\phi} = \phi_c - \delta_\phi$. We estimated the bank offset δ_ϕ in piecewise fashion over a flight by using the sun's disc or a distant cloud as a reference for estimating the change in the camera's azimuth $\Delta\psi_c$ between calibration frames at times t_1 and t_2 and finding the offset δ_ϕ that would satisfy the integral equation

$$\int_{t_1}^{t_2} \frac{g \sin(\phi_c - \delta_\phi)}{U_0 \cos(\theta_c - \delta_\theta)} dt = \Delta\psi_c \quad (10)$$

We measured the apparent azimuthal position of the sun in each calibration frame by measuring the signed distance d in pixels between lines dropped perpendicular to the horizon from the center of the image and the sun's disc or distant cloud. We then calculated the apparent change in azimuth $\Delta\psi_c$ between calibration frames at times t_1 and t_2 as $\Delta\psi_c = (d_2 - d_1) \times 72/640$, assuming the same equiangular projection model as before. This use of the sun as a compass not only serves to remove integration drift on each calibration interval but also provides an external reference for relating the bird's estimated yaw angle ψ to the wind direction ζ via the solar ephemeris. Specifically, we used the National Oceanic and Atmospheric Administration (NOAA) Solar Calculator to find the sun's azimuth at the known date, time, and approximate location of each video recording, from which we were able to calibrate the bird's yaw angle relative to true north.

GPS analysis

At-sea behavior was identified using a threshold model (*38*) combining information on the bird's flight speed and the SD of its heading recorded over a rolling window of six consecutive points. GPS fixes with a recorded ground speed of >7 m s^{-1} were classified as flight; those with a ground speed of <7 m s^{-1} and a rolling SD in heading of <18° were classified as rafting; the remainder of points were classified as feeding. GPS fixes were only included in the analysis if they were classified as flight behavior.

The return sections of the GPS tracks were identified by moving backward along the track from the colony until the distance from the colony stopped increasing monotonically with respect to the length of the backward path (*58*). Conversely, the outbound section of the track was identified as the continuous section of the track over which the bird's distance from the colony monotonically increased with total path length. To prevent pseudoreplication in the statistical analyses, the outbound and return sections of each track were summarized as single data points, with arithmetic mean values taken for wind speed and crosswind component, and with circular

Downloaded from https://www.science.org at University of Newcastle on June 08, 2022

mean values taken for wind direction and heading in the air reference frame (see below). In total, we included $n = 349$ flights for which both legs were tracked and $n = 38$ where either the outbound or the return leg was recorded. Hence, we include with each result presented in the main text a sample size that relates to the result in question.

Wind measurements

Wind velocity was obtained from the NOAA/National Centers for Environmental Prediction (NCEP) Global Forecast System (GFS). GFS data were sampled at a temporal resolution of 3 hours and a spatial resolution of $0.5^{\circ} \times 0.5^{\circ}$. Each GPS fix was assigned the nearest wind measurement in time and space, which was used to determine the bird's velocity with respect to the air and the ground. For the video-based analyses, the exact location of the shearwaters was unknown, but the wind velocity was found to be quite homogeneous within the known range of incubating shearwaters from Skomer (*59*) over the period for which the video footage was recorded. Given their known departure and arrival times, we estimate that the birds foraged within a 50-km radius of Skomer. We therefore averaged wind velocity estimates from the Met Office Wavewatch III wave model (one hourly temporal precision, 8-km spatial precision, referenced to 10-m altitude) over this radius for the purposes of analyzing the bird-borne video data.

SUPPLEMENTARY MATERIALS

Supplementary material for this article is available at https://science.org/doi/10.1126/sciadv.abo0200

View/request a protocol for this paper from *Bio-protocol*.

REFERENCES AND NOTES

1. S. Åkesson, G. Walinder, L. Karlsson, S. Ehnbom, Nocturnal migratory flight initiation in reed warblers *Acrocephalus scirpaceus*: Effect of wind on orientation and timing of migration. *J. Avian Biol.* **33**, 349–357 (2002).
2. S. Åkesson, A. Hedenström, Wind selectivity of migratory flight departures in birds. *Behav. Ecol. Sociobiol.* **47**, 140–144 (2000).
3. M. Schaub, F. Liechti, L. Jenni, Departure of migrating European robins, *Erithacus rubecula*, from a stopover site in relation to wind and rain. *Anim. Behav.* **67**, 229–237 (2004).
4. L. A. Hawkes, S. Balachandran, N. Batbayar, P. J. Butler, P. B. Frappell, W. K. Milsom, N. Tseveenmyadag, S. H. Newman, G. R. Scott, P. Sathiyaselvam, J. Y. Takekawa, M. Wikelski, C. M. Bishop, The trans-Himalayan flights of bar-headed geese (*anser indicus*). *Proc. Natl. Acad. Sci. U.S.A.* **108**, 9516–9519 (2011).
5. J. L. Deppe, M. P. Ward, R. T. Bolus, R. H. Diehl, A. Celis-Murillo, T. J. Zenzal Jr., F. R. Moore, T. J. Benson, J. A. Smolinsky, L. N. Schofield, D. A. Enstrom, E. H. Paxton, G. Bohrer, T. A. Beveroth, A. Raim, R. L. Obringer, D. Delaney, W. W. Cochran, Fat, weather, and date affect migratory songbirds' departure decisions, routes, and time it takes to cross the Gulf of Mexico. *Proc. Natl. Acad. Sci. U.S.A.* **112**, E6331–E6338 (2015).
6. S. Åkesson, G. Bianco, A. Hedenström, Negotiating an ecological barrier: Crossing the Sahara in relation to winds by common swifts. *Philos. Trans. R. Soc. B Biol. Sci.* **371**, 20150393 (2016).
7. J. R. Conklin, P. F. Battley, Impacts of wind on individual migration schedules of New Zealand bar-tailed godwits. *Behav. Ecol.* **22**, 854–861 (2011).
8. K. G. Horton, B. M. van Doren, P. M. Stepanian, W. M. Hochachka, A. Farnsworth, J. F. Kelly, Nocturnally migrating songbirds drift when they can and compensate when they must. *Sci. Rep.* **6**, 21249 (2016).
9. J. Wynn, J. Collet, A. Prudor, A. Corbeau, O. Padget, T. Guilford, H. Weimerskirch, Young frigatebirds learn how to compensate for wind drift. *Proc. R. Soc. B Biol. Sci.* **287**, 20201970 (2020).
10. P. Jouventin, H. Weimerskirch, Satellite tracking of wandering albatrosses. *Nature* **343**, 746–748 (1990).
11. R. M. Suryan, D. J. Anderson, S. A. Shaffer, D. D. Roby, Y. Tremblay, D. P. Costa, P. R. Sievert, F. Sato, K. Ozaki, G. R. Balogh, N. Nakamura, Wind, waves, and wing loading: Morphological specialization may limit range expansion of endangered albatrosses. *PLOS ONE* **3**, e4016 (2008).
12. V. H. Paiva, T. Guilford, J. Meade, P. Geraldes, J. A. Ramos, S. Garthe, Flight dynamics of cory's shearwater foraging in a coastal environment. *Fortschr. Zool.* **113**, 47–56 (2010).
13. H. Weimerskirch, T. Guionnet, J. Martin, S. A. Shaffer, D. P. Costa, Fast and fuel efficient? Optimal use of wind by flying albatrosses. *Proc. R. Soc. Lond. B Biol. Sci.* **267**, 1869–1874 (2000).
14. J. González-Solís, A. Felicísimo, J. W. Fox, V. Afanasyev, Y. Kolbeinsson, J. Muñoz, Influence of sea surface winds on shearwater migration detours. *Mar. Ecol. Prog. Ser.* **391**, 221–230 (2009).
15. T. Alerstam, G. A. Gudmundsson, B. Larrson, Flight tracks and speeds of Antarctic and Atlantic seabirds: Radar and optical measurements. *Philos. Trans. R. Soc. Lond. B Biol. Sci.* **340**, 55–67 (1993).
16. R. Gibb, A. Shoji, A. L. Fayet, C. M. Perrins, T. Guilford, R. Freeman, Remotely sensed wind speed predicts soaring behaviour in a wide-ranging pelagic seabird. *J. R. Soc. Interface* **14**, 20170262 (2017).
17. J. P. Croxall, J. R. D. Silk, R. A. Phillips, V. Afanasyev, D. R. Briggs, Global circumnavigations: Tracking year-round ranges of nonbreeding albatrosses. *Science* **307**, 249–250 (2005).
18. T. Guilford, J. Meade, J. Willis, R. A. Phillips, D. Boyle, S. Roberts, M. Collett, R. Freeman, C. M. Perrins, Migration and stopover in a small pelagic seabird, the manx shearwater *Puffinus puffinus*: Insights from machine learning. *Proc. R. Soc. B Biol. Sci.* **276**, 1215–1223 (2009).
19. P. Catry, R. A. Phillips, J. P. Croxall, Sustained fast travel by a gray-headed albatross (*Thalassarche chrysostoma*) riding an antarctic storm. *Auk* **121**, 1208–1213 (2004).
20. R. Spivey, S. Stansfield, C. Bishop, Analysing the intermittent flapping flight of a manx shearwater, *Puffinus puffinus*, and its sporadic use of a wave-meandering wing-sailing flight strategy. *Prog. Oceanogr.* **125**, 62–73 (2014).
21. P. L. Richardson, How do albatrosses fly around the world without flapping their wings? *Prog. Oceanogr.* **88**, 46–58 (2011).
22. C. J. Pennycuick, *Modelling the Flying Bird* (Theoretical Ecology Series, Academic Press, 2008).
23. G. K. Taylor, K. V. Reynolds, A. L. R. Thomas, Soaring energetics and glide performance in a moving atmosphere. *Philos. Trans. R. Soc. B Biol. Sci.* **371**, 20150398 (2016).
24. G. D. Bousquet, M. S. Triantafyllou, J.-J. E. Slotine, Optimal dynamic soaring consists of successive shallow arcs. *J. R. Soc. Interface* **14**, 20170496 (2017).
25. R. Bencatel, J. Tasso de Sousa, A. Girard, Atmospheric flow field models applicable for aircraft endurance extension. *Prog. Aerosp. Sci.* **61**, 1–25 (2013).
26. L. Rayleigh, The soaring of birds. *Nature* **27**, 534–535 (1883).
27. G. Sachs, J. Traugott, A. P. Nesterova, F. Bonadonna, Experimental verification of dynamic soaring in albatrosses. *J. Exp. Biol.* **216**, 4222–4232 (2013).
28. J. M. V. Rayner, P. W. Viscardi, S. Ward, J. R. Speakman, Aerodynamics and energetics of intermittent flight in birds. *Am. Zool.* **41**, 188–204 (2001).
29. C. Rutz, L. A. Bluff, A. A. S. Weir, A. Kacelnik, Video cameras on wild birds. *Science* **318**, 765 (2007).
30. S. Schoombie, J. Schoombie, C. W. Brink, K. L. Stevens, C. W. Jones, M. M. Risi, P. G. Ryan, Automated extraction of bank angles from bird-borne video footage using open-source software. *J. Field Ornithol.* **90**, 361–372 (2019).
31. G. Sachs, Minimum shear wind strength required for dynamic soaring of albatrosses. *Ibis* **147**, 1–10 (2005).
32. D.-N. Liu, Bio-inspired energy-harvesting mechanisms and patterns of dynamic soaring. *Bioinspir. Biomim.* **12**, 016014 (2017).
33. P. Lissaman, *43rd AIAA Aerospace Sciences Meeting and Exhibit* (American Institute of Aeronautics and Astronautics, 2005).
34. T. C. Guilford, J. Meade, R. Freeman, D. Biro, T. Evans, F. Bonadonna, D. Boyle, S. Roberts, C. M. Perrins, GPS tracking of the foraging movements of manx shearwaters *Puffinus puffinus* breeding on Skomer Island, Wales. *Ibis* **150**, 462–473 (2008).
35. O. Padget, G. Stanley, J. K. Willis, A. L. Fayet, S. Bond, L. Maurice, A. Shoji, B. Dean, H. Kirk, I. Juarez-Martinez, R. Freeman, M. Bolton, T. Guilford, Shearwaters know the direction and distance home but fail to encode intervening obstacles after free-ranging foraging trips. *Proc. Natl. Acad. Sci. U.S.A.* **116**, 21629–21633 (2019).
36. G. Taylor, A. Thomas, *Evolutionary Biomechanics* (Oxford Univ. Press, 2014).
37. A. Shoji, S. Aris-Brosou, A. Fayet, O. Padget, C. Perrins, T. Guilford, Dual foraging and pair coordination during chick provisioning by manx shearwaters: Empirical evidence supported by a simple model. *J. Exp. Biol.* **218**, 2116–2123 (2015).
38. B. Dean, H. Kirk, A. Fayet, A. Shoji, R. Freeman, K. Leonard, C. M. Perrins, T. Guilford, Simultaneous multi-colony tracking of a pelagic seabird reveals cross-colony utilization of a shared foraging area. *Mar. Ecol. Prog. Ser.* **538**, 239–248 (2015).
39. G. C. Bower, "Boundary layer dynamic soaring for autonomous aircraft: Design and validation," thesis, Stanford University (2012).
40. T. Guilford, G. K. Taylor, The sun compass revisited. *Anim. Behav.* **97**, 135–143 (2014).
41. J. R. Serres, T. J. Evans, S. Åkesson, O. Duriez, J. Shamoun-Baranes, F. Ruffier, A. Hedenström, Optic flow cues help explain altitude control over sea in freely flying gulls. *J. R. Soc. Interface* **16**, 20190486 (2019).

Downloaded from https://www.science.org at University of Newcastle on June 08, 2022

42. C. J. Pennycuick, Gust soaring as a basis for the flight of petrels and albatrosses (*Procellariiformes*). *Avian Sci.* **2**, 1–12 (2002).
43. B. Hayes, M. D. L. Brooke, Retinal ganglion cell distribution and behaviour in procellariiform seabirds. *Vision Res.* **30**, 1277–1289 (1990).
44. A. Hughes, *Handbook of Sensory Physiology VII/5, The Visual System in Vertebrates* (Springer-Verlag, 1977), pp. 613–756.
45. G. R. Martin, *The Sensory Ecology of Birds* (Oxford Univ. Press, 2017).
46. D. Meyer, *Handbook of Sensory Physiology VII/5, The Visual System in Vertebrates* (Springer-Verlag, 1977), pp. 549–612.
47. D. Bilo, Optocollic reflexes and neck flexion–related activity of flight control muscles in the airflow-stimulated pigeon, in *The Head-Neck Sensory Motor System* (Oxford Univ. Press, 1992).
48. Y. J. Zhao, Y. C. Qi, Minimum fuel powered dynamic soaring of unmanned aerial vehicles utilizing wind gradients. *Optim. Control Appl. Methods* **25**, 211–233 (2004).
49. P. P. Sukumar, M. S. Selig, Dynamic soaring of sailplanes over open fields. *J. Aircr.* **50**, 1420–1430 (2013).
50. M. Deittert, A. Richards, C. Toomer, A. Pipe, Dynamic soaring flight in turbulence, in *AIAA Guidance, Navigation, and Control Conference* (American Institute of Aeronautics and Astronautics, 2009), pp. 2–5.
51. R. A. Phillips, J. C. Xavier, J. P. Croxall, Effects of satellite transmitters on albatrosses and petrels. *Auk* **120**, 1082–1090 (2003).
52. M. M. Webster, C. Rutz, How strange are your study animals? *Nature* **582**, 337–340 (2020).
53. N. Gillies, C. Tyson, J. Wynn, M. Syposz, C. Vansteenberghe, T. Guilford, Exploring the mechanisms of coordinated chick provisioning in the manx shearwater *Puffinus puffinus*. *J. Avian Biol.* (2022).
54. C. J. Pennycuick, The flight of petrels and albatrosses (Procellariiformes), observed in South Georgia and its vicinity. *Philos. Trans. R. Soc. B Biol. Sci.* **300**, 75–106 (1982).
55. E. L. C. Shepard, C. Williamson, S. P. Windsor, Fine-scale flight strategies of gulls in urban airflows indicate risk and reward in city living. *Philos. Trans. R. Soc. B Biol. Sci.* **371**, 20150394 (2016).
56. C. Rutz, J. Troscianko, Programmable, miniature video-loggers for deployment on wild birds and other wildlife. *Methods Ecol. Evol.* **4**, 114–122 (2013).
57. Y. Tremblay, S. A. Shaffer, S. L. Fowler, C. E. Kuhn, B. I. McDonald, M. J. Weise, C.-A. Bost, H. Weimerskirch, D. E. Crocker, M. E. Goebel, D. P. Costa, Interpolation of animal tracking data in a fluid environment. *J. Exp. Biol.* **209**, 128–140 (2006).
58. O. Padget, S. L. Bond, M. M. Kavelaars, E. Loon, M. Bolton, A. L. Fayet, M. Syposz, S. Roberts, T. Guilford, In situ clock shift reveals that the sun compass contributes to orientation in a pelagic seabird. *Curr. Biol.* **28**, 275–279.e2 (2018).
59. B. Dean, "The at-sea behaviour of the manx shearwater," thesis, University of Oxford (2012).
60. J. B. Tatum, The effect of the Coriolis force on the flight of a bird. *Auk* **97**, 99–117 (1980).

Acknowledgments: We thank members of the Oxford Navigation Group and Oxford Flight Group for insightful comments and Glenn Wagner for help in deriving the model for an unsteady banked turn in a vertical wind gradient. **Funding:** This work was supported by the University of Oxford Christopher Welch Scholarship (to J.A.K.); ASAB Undergraduate Project Scholarship (to J.A.K.); UKRI BBSRC scholarship grant number BB/M011224/1 (to J.W. and N.G.); The Queen's College, University of Oxford (to A.L.F.); Junior Research Fellowship at St. John's College, University of Oxford (to O.P.); Merton College, University of Oxford (to T.G.); Mary Griffiths Award (to T.G.); BBSRC David Phillips Fellowship grant numbers BB/G023913/1 and BB/G023913/2 (to C.R.); and Jesus College, University of Oxford (to G.K.T.). This project has received funding from the European Research Council (ERC) under the European Union's Horizon 2020 research and innovation programme (grant agreement no. 682501) (to G.K.T.).
Author contributions: Authors other than the co–first authors are listed alphabetically. Individual contributions are as follows: Conceptualization: J.A.K., J.W., T.G., and G.K.T. Formal analysis: J.A.K., J.W., and G.K.T. Investigation: J.A.K., S.B., J.E., A.L.F., N.G., T.G., M.K., I.J.-M., O.P., C.R., A.S., and M.S. Methodology: J.A.K., J.W., T.G., O.P., C.R., and G.K.T. Supervision: T.G. and G.K.T. Visualization: J.A.K. and J.W. Writing—original draft: J.A.K., J.W., and G.K.T. All authors reviewed and commented on the original draft. **Competing interests:** The authors declare that they have no relevant financial or nonfinancial interests to disclose. **Data and materials availability:** Raw video data and GPS tracks have been uploaded to figshare, together with the processed GPS and video data needed to replicate the analyses. The doi for the data is 10.6084/m9.figshare.18019454.

Submitted 11 January 2022
Accepted 13 April 2022
Published 1 June 2022
10.1126/sciadv.abo0200

Downloaded from https://www.science.org at University of Newcastle on June 08, 2022

ScienceAdvances

Optimization of dynamic soaring in a flap-gliding seabird affects its large-scale distribution at sea

James A. KemptonJoe WynnSarah BondJames EvryAnnette L. FayetNatasha GilliesTim GuilfordMarwa KavelaarsIgnacio Juarez-MartinezOliver PadgetChristian RutzAkiko ShojiMartyna SyposzGraham K. Taylor

Sci. Adv., 8 (22), eabo0200. • DOI: 10.1126/sciadv.abo0200

View the article online
https://www.science.org/doi/10.1126/sciadv.abo0200
Permissions
https://www.science.org/help/reprints-and-permissions

Downloaded from https://www.science.org at University of Newcastle on June 08, 2022

Use of this article is subject to the Terms of service

Science Advances (ISSN) is published by the American Association for the Advancement of Science. 1200 New York Avenue NW, Washington, DC 20005. The title *Science Advances* is a registered trademark of AAAS.
Copyright © 2022 The Authors, some rights reserved; exclusive licensee American Association for the Advancement of Science. No claim to original U.S. Government Works. Distributed under a Creative Commons Attribution License 4.0 (CC BY).